Ge-on-Si Light-Emitting Materials and Devices for Silicon Photonics

by
Xiaochen Sun

B.S. Physics
Peking University, 2004

Submitted to the Department of Materials Science and Engineering in Partial Fulfillment of the Requirements for the Degree of

Doctor of Philosophy in Materials Science and Engineering
at the
Massachusetts Institute of Technology

June 2009

Signature of Author: _____
Department of Materials Science and Engineering
April 23rd, 2009

Certified by: _____
Lionel C. Kimerling
Thomas Lord Professor of Materials Science and Engineering
Thesis Supervisor

Accepted by: _____
Christine Ortiz
Professor of Materials Science and Engineering
Chair, Departmental Committee on Graduate Students

Ge-on-Si Light-Emitting Materials and Devices for Silicon Photonics

by

Xiaochen Sun

Submitted to the Department of Materials Science and Engineering on April 23rd, 2009 in Partial Fulfillment of the Requirements for the Degree of Doctor of Philosophy in Materials Science and Engineering at the Massachusetts Institute of Technology

ABSTRACT

The rapid growing needs for high data transmission bandwidth challenge the metal interconnection technology in every area from chip-level interconnects to long distance communication. Silicon photonics is an ideal platform for the implementation of optical interconnection capable of high bandwidth and low power consumption by integrating electronic and photonic devices on silicon. Many optical components in silicon photonics have been extensively studied, among which a silicon-based laser is arguably the most challenging element. This thesis mainly focuses on using engineered germanium as the optically active material for silicon-based light emitters with many potential benefits: Si-CMOS compatibility (both material and processing), electrical injection capability, and direct gap emission at technologically important 1.55 μm telecommunication band.

Tensile-strained n^+ germanium is capable of behaving like a direct band gap material owing to the direct band gap shrinkage upon tensile strain and the state-filling in the indirect L valleys with extrinsic electrons from n-type dopants. Our theoretical calculation using a direct band-to-band transition model has shown great benefit of tensile strain and n-type doping on the direct gap optical gain characteristics. By considering free carrier absorption which dominates the optical loss we have proven net gain can be achieved in 0.25% tensile-strained Ge with n-type doping concentration in a range of 10^{19} to mid-10^{20} cm^{-3}. The injection threshold of the net gain is about 10^{18} cm^{-3} which can readily be achieved with either optical pumping or electrical pumping. The net gain is in favor of the raise of temperature in a large injection range (threshold to mid-10^{19} cm^{-3}) because of the increased number of high energy electrons in the direct Γ valley contributing to the direct band-to-band radiative recombination.

We have successfully grown single crystalline germanium epitaxially on silicon with a two-step approach. Tensile strain between 0.2% and 0.25% is formed in germanium upon cooling from high growth temperature (or post-growth annealing temperature) to room temperature because of the larger thermal expansion coefficient of germanium compared to that of silicon. Phosphorus are in situ doped in germanium as n-type dopants during the epitaxial growth. By carefully adjusting the growth condition, we have obtained active doping concentration

as high as 2×10^{19} cm^{-3}. An in situ doping model built by considering the transportation processes and the reactions of phosphorus-containing species well explains the temperature dependence of the doping concentration. The deviation from the model while analyzing the influence of other growth parameters indicates possible compensation of the dopants.

We used photoluminescence (PL) measurement to study to the optical properties of tensile-strained n^+ germanium. Room temperature PL was observed from the epitaxial Ge-on-Si films near the direct gap wavelength of 1600nm. The direct gap PL spectrum exhibits Ge direct band-to-band optical transition properties. The direct gap PL intensity increases with n-type doping concentration as a result of the indirect valley state filling effect which increases the Fermi level leading to higher excited electron density in the direct Γ valley. The direct gap PL intensity also increases with temperature because of the increased number of high energy direct Γ valley electrons thermally activated from the indirect L valleys. This effect make germanium light emission robust to inevitable heating effects during operation in practice. The "unusual" n-type doping and temperature dependences of PL are unique properties of the direct gap emission from indirect bandgap Ge. There effects are predicted by our theory, and the observation of these effect in experiments is a strong evidence of validity of the theory.

In order to study the electrical injection in Ge, we fabricated Si/Ge/Si heterojunction light emitting diodes (LEDs). Room temperature direct gap electroluminescence (EL) are observed from these diodes. It is the first observation of EL from Ge. The direct gap EL spectrum matches the PL spectrum underlying the same injection mechanism in both electrical pumping and optical pumping. The direct gap EL intensity increases superlinearly with injection current because of the raised quasi Fermi level leading to the increased fraction of the injected electrons in the direct Γ valley. The internal quantum efficiency of the LEDs is on the order of 10^{-3} consistent with the finite-element simulation results. This EL efficiency can be improved to 10^{-1} if doping germanium active region with n-type. The design of n^+Ge based heterojunction diodes has been simulated, and an optimal design has been proposed based on the simulation.

We used pump-probe spectroscopy to measure material gain of the tensile-strained n^+ germanium. We have observed an optical bleaching effect, the reduction of absorption under pumping and the prelude of optical gain, above the direct band gap energy from the engineered Ge. The population inversion factor increases with the n-type doping concentration in Ge, as predicted by the theory. By increasing the injection level using a Ge micro-mesa structure carrier confinement, we have successfully demonstrated the net gain, i.e. population inversion. A peak gain of 50 ± 25 cm^{-1} at 1605 nm has been obtained from the experiment. It is the first report of observing net gain from germanium.

Thesis Supervisor: Lionel C. Kimerling

Title: Thomas Lord Professor of Materials Science and Engineering

Acknowledgement

I came to the U.S. to pursue my Ph.D. program in 2004. At the end of this great journey, I find it is so difficult to say goodbye. Studying and doing research at MIT is a life-changing experience. I can't express how much I loved the life here in the past five years, and I can't imagine how much I'll miss it for the rest of my life. I would like to thank many people for their helps during these years. Without your helps, I won't be where I am!

I'm deeply in gratitude to my advisor, Prof. Lionel C. Kimerling ("Kim"). Kim is the wise, fearless captain of EMAT. The kindness of him in our first meeting greatly encouraged me to join EMAT. And I never regret my decision. Kim gave me the chance to explore the exciting silicon photonics field. I learned many things in this field from scratch in Kim's class and from conversations with him. He not only taught me the knowledge itself, also shown me the way to think, to investigate, and to accomplish. The knowledge and methodology I learned from him will benefit my whole scientific career. Thank you very much for your continuous guidance.

Jurgen Michel is my second thesis advisor. Jurgen directly supervised me the most part of my thesis, Ge laser project. Jurgen's help to my research is tremendous. Jurgen's door is always open. I learned so much from him through his daily guidance. His advices can be found in nearly every publication and presentation of mine. Thank you! Anuradha ("Anu") Agarwal supervised me on the MIDAS project for my first year and half. Anu's kindness and help gave me a pleasant research experience. I would also like to thank the advices from two other members of my thesis committee: Prof. Eugene Fitzgerald and Franz Kaertner.

EMAT is a family. This family has magic to attract its members forever even they left years ago. Prof. Kazumi Wada and Xiaoman Duan always came to our offices once they were in town. Kazumi taught me how to think out of box. I learned many from talking with him in the office as well as in the conferences. Xiaoman took motherly care of every student in EMAT. She always showed up whenever we have troubles. Mark Beals helped me organize the MURI weekly meeting among eight universities for over a year. He assured the normal operation of our UHVCVD reactor that is critical for my research. Anat Eshed had us well trained for using vacuum systems. Mindy Baughman and Lisa Page made sure EMAT in a good shape.

Jifeng Liu was my mentor when I first joined EMAT. Jifeng is very knowledgeable even as a graduate student by then. I learned many things in materials and photonics from him. I feel so lucky working closely with him in Ge laser project for the past three years. Jifeng and I share the mutual interest in Chinese history and had many fun conversations. Jifeng is also a leader in Chinese community. Through him and the activities he organized, I got to know many friends. Juejun Hu is my classmate, labmate and officemate. We shared almost five years in the same office. He is a sharp-minded scientist. I enjoyed numerous discussions with him on both science and life. It's always inspiring listening to his daily new ideas and debating physical puzzles with him. Rong Sun, the passive device expert, Juejun and I followed your

every step from thesis proposal to defense. Rong, Juejun and I shared a lot of classes, and we were always the team for projects. Your friendship made my five years full of fun. Ching-yin Hong helped me many times on fabrication processes in my research. Yasha Yi, Ningning Feng and Sajan Saini educated me with their expertises. Jianfei Wang, Jing Cheng, Kevin McComber have been great collaborators and friends. And it's my pleasure to know so many friends in EMAT: Donghwan Ahn, David Danielson, Lirong Zeng, Samerkhae ("Nok") Jongthammanurak, Victor Nguyen, Jae Hyung Yi, Winnie Ye, Wojciech Giziewicz, Sarah Bernardis, Suguru Akiyama, Michiel Vanhoutte, Xing Sheng, Rodolfo Camacho-Aguilera and Tim Zens. Rodolfo, I'm lucky to have you as my successor for the Ge laser project. I would also like to thank the people helped me with the work in MTL: Kurt Broderick, Eric Lim and Gary Riggott. Kurt is also a very good friend of mine. During these five years, I met a lot of friends in MIT: Lei Wang, Hui Zhou, Yu Bai, Lin Han, Shuodan Chen, Miao Ye, Irene Chang, Amy Shi, Pengwei Zhuang, Ying Chen, and many others. Thank you all for making my life at MIT more colorful.

Finally, my family. I am grateful for my parents who have treated me as adult and friend since my high school. They respected my decisions and did everything they could for me to chase my dream. Their early education encouraged me to explore the scientific world leading to my career now. And my wife, Wei Kang. We've been loving each other ever since we met eight years ago. She sacrificed her career and came to the U.S. to join me in 2005. She has always been so supportive to my study and she took good care of me everyday. I can't imagine the life without her. Thank you so much for your love and support all these years! I'll try my best to make us the happiest couple in the world for the rest of my life.

Contents

List of Figures

List of Tables

Chapter 1

Introduction

Integrated circuits (ICs, also known as microchips or microcircuits) have been revolutionizing the world ever since they were invented in mid-20th-century. ICs are used in almost all electronic equipments and devices in use today and are the foundation of the current generation of computers. An IC is a miniaturized electronic circuit consisting of computing elements (or active components mainly made of semiconductor materials, e.g. transistors) as well as interconnects elements (or passive components made of conducting materials) that has been manufactured in the surface of a thin substrate of semiconductor material. Among all these semiconductors, silicon (Si) is absolutely the most important and widely used materials in the IC and semiconductor industry owing to its superior properties and low fabrication cost.

1.1 Beyond Scaling

Before 2005, Si IC had been developed in an extraordinary pace for almost four decades, known as Moores law that the number of transistors in an integrated circuit doubles roughly every eighteen months [14]. Upon the increase of the number of transistors, each transistor also get smaller, faster and cheaper. The scalability is the main reason of the tremendous success of many Si IC based technologies [19], such as Si complimentary metal oxide semiconductor (CMOS) technology, which is used to fabricate the central processing unit (CPU) of modern computers.

The scalability of Si-CMOS technology is not only about the shrinkage of the dimensions

of the devices, but also a number of other factors for maintaining the power density while boosting the performance. For an ideal constant-field scaling [20], upon the shrinkage of all the physical dimensions by α (scaling factor), the depletion depth d also has to be shrunk by α to assure the device works properly. The reduction of the depletion depth requires the increase of doping N_d and the decrease of the applied voltage V by a same factor α since $d \sim \sqrt{N_d \cdot V}$.

A direct consequence of the scaling is the increased circuit density by α^2 which dramatically reduce the manufacturing costs. A second important result is the increase of the circuit speed due to both the reduced transit time in transistors and the capacitance in RC delay. In principle, the speed increases by the same factor of α with scaling. In the meantime, the power density of the circuit remains constant. All of these benefits from the CMOS scaling lead to the blossom of IC and computer industry since 1970s.

However, the applied voltage is found to be impossible to scale by α as continuously shrinking the dimensions because of constraints on the threshold bias in order to avoid rising standby power in the "off" state. Eventually, the applied voltage can not be scaled anymore, which, unfortunately, already occurred a couple of years ago. This results in the increase of the electric field with the scaling, leading to the increase of the power density of the circuit by α^2 (assuming the speed is scaled by α). Moreover, the subthreshold leakage current has been forced to relax in order to maintain the performance, which makes the power consumption in the passive components increase even faster than the active counterparts. It has been shown that the passive power density becomes dominant below the device dimension of 130-65 nm regime [19], which effectively halts traditional scaling in CMOS.

In 2005, "for the first time in thirty five years, the clock speed of the fastest commercial computer chips has not increased" [21], because of the reasons explained above: the huge power dissipation, especially in passive interconnects components which leads to severe heating problems, prohibits the further increase of the clock speed. It's possible to overclock the CPU frequency over 8 GHz with real-time liquid nitrogen cooling [22]. However, it is obviously implausible in practice. In 2006, Intel had plans to develop a 9 GHz CPU operating at 70 ^{o}C based on a modified Pentium 4 Cedar Mill architecture with copper and low-K dielectric interconnects [23]. But these plans were eventually scrapped due to the power and

heating issues and were replaced by multi-core architectures shifting towards parallelism.

In order to further increase the clock frequency without the help of the scaling, the entire architecture has to be re-examined and revolutionized. In today's CMOS technology, the intrinsic speed of the transistor is way beyond the speed in any other components of the circuit. The intrinsic frequency of a commercial logic circuit transistor is in the order of 10^2 GHz [24], while other technologies can easily achieve even higher speed, such as a silicon-germanium (SiGe) transistor at 500 GHz [25] and an indium-phosphide (InP) based III-V transistor at over 1000 GHz (1THz) [26].

Therefore, the speed bottleneck of the ICs results from propagation delay in the passive components, which is dominated by RC (resistance-capacitance) delay. How to design a new interconnects system in ICs becomes the key to further enhancement of the speed. A couple of approaches have been investigated to replace the predominant aluminium (for electrical conduction) and silicon oxide (SiO_2, for electrical insulation) interconnects including the use of copper and low-k dielectric materials (such as doped SiO_2 or polymeric dielectrics) to reduce the RC product. Among all these attempts, the optical interconnect design implemented by silicon photonics is extremely promising and can be the potentially ultimate solution to this problem. The reasons are explained in the next section.

1.2 Silicon Photonics

photonics is about the science and the technology of generating, manipulating, and detecting photons. Silicon, while dominating the semiconductor electronics for decades, is on the verge of becoming a superior choice for photonics in many communication applications [27]. Silicon photonics offers a promising platform for the monolithic integration of optics and microelectronics on silicon chips [28], aiming for many applications including the optical interconnects solution to the microelectronics bottleneck [29]. Because of its importance and rapid growth, a roadmap of silicon photonics, assessed by academic scholars and industrial experts, has been proposed [1] and organized by the Microphotonics Center at the Massachusetts Institute of Technology (MIT) [30].

1.2.1 Optical Communication

Photon has been used to transmit information for over three decades, mainly by using optical fibers to form optical interconnection between places in distance. There are many advantages of the optical transmission of information: (1) High speed or bandwidth owing to the lack of RC delay issue existed in the traditional electrical interconnection. In addition, photons with different wavelengths (or energies) do not interact with each other *. Thus multiply wavelengths can co-exist in the same communication channel leading to much higher bandwidth capacity. This technique is called wavelength multiplexing (WDM). (2) Low attenuation due to low optical losses in fibers compared to severe power dissipation through heat generation in metal cables, especially in long distance. (3) Low cost of the transmission medium results from the use of silica and polymer materials instead of expensive metal materials. Therefore, the replacement of the electrical interconnection with optical interconnection revolutionized the long haul telecommunication and enables the fast development of the global information exchange such as the internet.

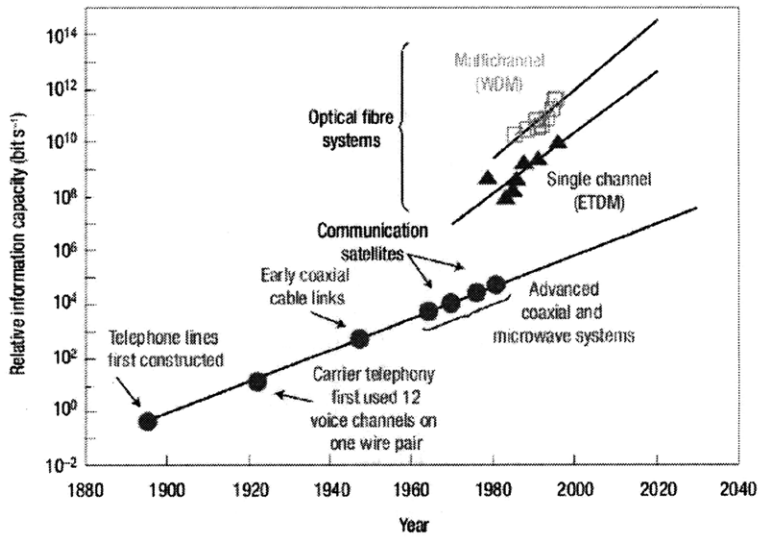

Figure 1.1: Trend in the information-carrying capacity of a single line (wire or optical fibre) with time and technology. (WDM: wavelength-division multiplexing; ETDM: electronic time-division multiplexing). (After Kirchain and Kimerling [1]).

The revolution of technology is always driven by demands. Fig. 1.1 summarizes the

*The interaction between photons with different wavelengths can occur at very high energy densities, which is rare for most of the applications, due to non-linear effects.

history of the information communication, with both electrical wire/cable and optical fiber technologies, since the industrialization. We can see a threshold for the commercial displacement of the electrical interconnection by the optical interconnection, which is described by a figure of merit (FOM) given by the product of the transmission bandwidth and distance, and the threshold occurs at Mbit/s with kilometer scale for telecommunication. For a smaller chip scale of centimeters, the threshold is in the order of 10^2Gbit/s to 1 Tbit/s. Modern signal processing IC chips are calling for such transmission capacity. The optical interconnection at smaller scales has been seriously explored as an option to achieve this capacity and has been included in the International Technology Roadmap for Semiconductors [21].

Besides the long haul optical fiber telecommunications and depending on the various distances of the applications, the optical interconnection can be deployed in rack-to-rack (1-100 m), board-to-board (0.5-1 m), chip-to-chip (or interchip, 1-50 cm) and on-chip (or intrachip, $<$ 1 cm) [31,32].

The rack-to-rack and the board-to-board applications can generally benefit from using the mature long-haul optical fiber technology at a smaller scale. All the electronic and optical components and the communication architecture can be readily applied with some necessary modifications. It has been seriously investigated for connecting a large number of clusters in high performance supercomputer applications [33,34,35]. The optical interconnection will be used in many future peta-flops (10^{15} floating-point operations per second) supercomputers including the next generation, 20 peta-flops IBM BlueGene system (codename: Sequoia) [36] and the Honeywell&Intel Touchstone supercomputer project [37].

On the other hand, chip-to-chip and on-chip applications are more challenging because the entire optical interconnection system has to be redesigned for the integration with the silicon microelectronic devices on silicon chips. All the macroscopic components used in the optical fiber or rack-to-rack communications systems have to be miniaturized thereby leading to dramatic change in material, design and fabrication. The ultimate goal is to replace every metallic bus interconnection with photonic counterparts. Since the architecture is built on the intercommunication and integration of both the electronics and the photonics, it is also called electronic-photonic integrated circuits (EPICs), integrated photonics or integrated optoelectronics.

In these applications, especially for rack-to-rack and board-to-board, many traditional optical components used in optical fiber telecommunication such as III-V semiconductor based devices have been first considered and investigated. However, silicon-based photonics is a natural choice for these applications, since all the materials and fabrication techniques in use aim for the complete compatibility with the Si-CMOS IC technology, which is required for a low cost solution and a smooth convergence between the electronics and the photonics. A number of discrete silicon photonic devices have been demonstrated commercially including the eight-channel variable optical attenuator (VOA) manufactured by Kotura Corporation [38] and the four-chnnel WDM transceiver reported by Luctera Corporation [39].

The advantages of silicon photonics based optical interconnection, compared to other implementations, become more essential as the capacity and the complexity of the integration with electronics grow in chip-to-chip and on-chip applications. In the next section, the discussion of the optical interconnects is focused on the these chip scale applications.

1.2.2 Optical Interconnects

As we point out in the previous section, because of the failure of further scaling † due to server power issues, the speed of the modern signal-processing ICs is limited by the interconnection components.

The total circuit delays with different interconnection technologies are shown in Fig. 1.2. The circuit propagation delay is the combination of the gate delay and the interconnects RC delay ‡. We can see that the RC delay becomes dominant and increases with the shrinkage of the physical dimension in both the current predominant aluminum/SiO_2 technology and the new copper/low-k technology below approximately 200 nm linewidth. On the other hand, the propagation delay of the optical interconnects, which are not subject to the RC delay, is basically the same as the gate delay which decreases with the dimension.

The optical interconnection can be deployed at different levels ranging from the chip-

†Not only the scaling of the physical dimensions, but also the applied voltage, doping profile and other factors, as explained previously.

‡The transmission time of electrical or optical signal from one terminal to the other is not counted in the propagation delay since it can be eliminated by proper circuit designs (e.g. symmetric H-tree design) thus only leading to the latency issue. The propagation delay, on the other hand, is the measure of the delay of AC signals thereby determining the system performance.

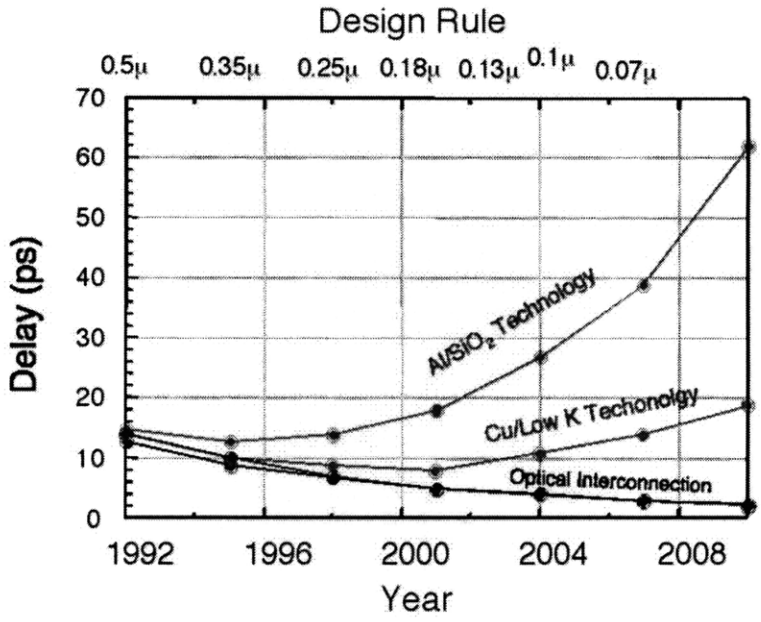

Figure 1.2: Trend in circuit propagation delay (1 cm length) with technology linewidth and time for traditional aluminium (Al) metal and SiO_2 insulator; projected copper (Cu) and low-k dielectric; and projected optical interconnection technologies. (After Wada et al. [2])

to-chip front side bus to the on-chip H-tree clocking bus. Besides the benefit from less propagation delay, optical interconnects offer more capacity per unit area by deploying the dense wavelength division multiplexing (DWDM) technology which succeeds in the optical fiber telecommunication. DWDM allows multiply wavelengths co-exist in the same channel without interaction. Therefore the whole interconnection design is also revolutionized. Many works have been done to investigate and optimize the architecture of the optical interconnection at a system level [40, 41, 42].

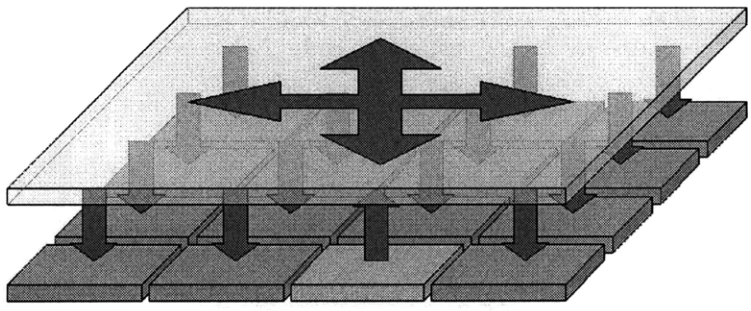

Figure 1.3: Schematic of the broadcasting optical interconnects in the application of multi-core parallel processing.

As the parallelism becomes the future of computing, the overall parallel performance and the number of cores become the new measures of the development in IC industry. But the rapidly increased number of cores challenges the interconnection more than ever, not only because of the propagation delay and power issue, but also the complexity of mutual communications between all the cores. DWDM enabled optical interconnect can simplify the problem by assigning each core a pre-selected specific wavelength and broadcasting all the wavelength in the interconnection layer, as shown in Fig. 1.3. Thus the retrieval of information from a given core is completed by dropping the specific wavelength associated with that core. It is a neat and scalable approach that benefits both the hardware design and the software programming.

1.2.3 Electronic-Photonic Convergence

The realization of optical interconnects requires a number of optical and optoelectronic components, while serving similar functionalities as their counterparts in the optical fiber telecommunication. But the need for the integration with electronics results in dramatic changes in material, design and fabrication.

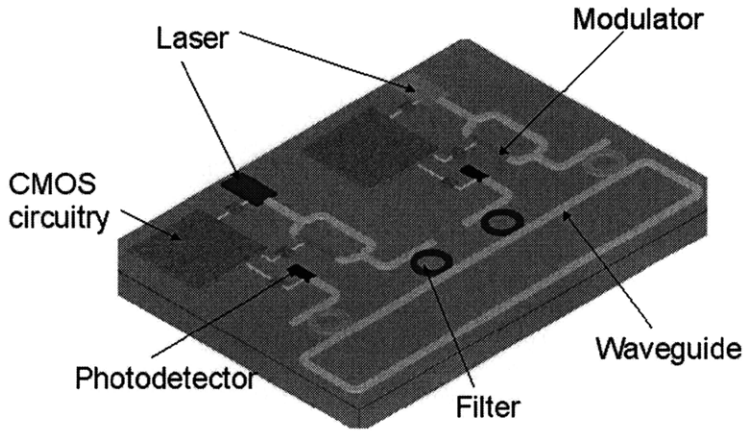

Figure 1.4: Schematic of on-chip optical interconnects integrated with electronic circuits.

Fig. 1.4 shows a simplified schematic of on-chip optical interconnects integrated with electronic circuit. As in optical fiber communication, the photon, used as the information carrier, is generated by a light source (usually a laser) with a specific wavelength λ_1. But

the photon does not propagate in a optical fiber, instead, a waveguide, which confines the light in the high refractive index core region, is used to guide the light. The continuous-wave (CW) light is then modulated by a modulator to translate the electric signal to the optical signal in terms of light intensity or phase. The modulated light is then switched to the main waveguide bus via an optical filter which only allows the wavelength λ_1 through. The main bus waveguide connects all the electronic circuits (e.g. core) and contains all the wavelengths accordingly. When another circuit acquires the information from the above circuit, another filter with the allowable wavelength of λ_1 is used to retrieve the signal from the main bus and switch to the local waveguide. A photodetector detects the light and translate the optical signal back to the electronic signal that can be used by the circuit.

The integration of these optical components on silicon chips is very challenging, because, in general, they cannot be fabricated with the electronic circuits in the mean time. The possible introduction of incompatible materials such as III-V semiconductors and polymeric materials [12] may require many fabrication techniques incompatible with the traditional Si-CMOS processing. The involvement of such materials on silicon is called the hybrid integration, by contrast, the silicon photonics based integration is called monolithic integration. It is obvious that the monolithic integration is favorable in both the material compatibility and fabrication compatibility with electrics, thus how to make all these optical components above with silicon based materials and fabrication techniques has become a hot topic since the mid-1980s.

Silicon is an ideal material for the passive components in the optical interconnects, owing to its transparency in a large wavelength range between 1.1 μm and 7 μm, which is far from being limited to the most commonly used near-infrared (NIR) communication band of 1.3 μm and 1.55 μm. In addition, the high refractive index contrast between silicon ($\sim$3.6), as a core material, and its surrounding medium (air 1.0 or SiO_2 $\sim$1.5) allows the extremely compact waveguide design ($\sim$ 0.1 μm^2) on the same scale of typical dimensional encountered in Si-CMOS fabrication. The small footprint allows the optical device density over $10^6/cm^2$, one of the objectives of optical interconnection. Low optical losses of the silicon waveguides have been achieved in the range of 0.1-3 dB/cm depending on the dimension and processing conditions. The main source of the losses is the scattering at the interfaces (top surface and sidewalls), which can be reduces by thermal oxidation [14] or chemical oxidation [15].

Besides the waveguides, many other passive components have been demonstrated using silicon including arrayed waveguide grating (AWG) [46] and microring/microdisk structures [47, 48] for add/drop filtering in WDM applications.

On the other hand, silicon is not an ideal choice for active applications such as electrooptic modulation, photodetection and photon generation. With the lack of linear electrooptic effect (Pockel effect) due to its centrosymmetric crystal structure, the only viable mechanism to archive fast modulation in silicon is the plasma dispersion effect related to the free carrier concentration. Such silicon modulators have been demonstrated using various structures [49, 50, 51, 52]. A more efficient approach for optical modulation is to use SiGe, whose optical band gap can be engineered for proper wavelength band, based on the Franz-Keldysh (FK) effect. SiGe based optical modulation has been demonstrated by using either the electo-optical (EO) change [53] or the electo-absorption (EA) change [54].

Silicon cannot be used for photodetector due to its transparency at near-infrared wavelength band. Germanium, however, has a strong direct band gap absorption below 1.55 μm, which can be further extended using tensile strain engineering. High speed tensile-strained germanium photodetector has been demonstrated [55, 56] and has been integrated with silicon waveguide with enhanced performance [57].

Germanium and SiGe alloy which are used in above applications are complete Si-CMOS compatible materials and have been used in silicon IC to improve the performance of transistors for years. The use of germanium in Si photonics solves many problems met in the active components and it also motivates this thesis work of using germanium to make a light source for optical interconnects.

1.3 Silicon-Based Light Emitters

A light source which provides photons as the information carriers, is an essential part of the optical interconnects, A simple idea is to supply photons by an external light source through optical fibers, in analogy to the electrical power supply. An immediate problem is the optical loss from the coupling between the optical fibers and the waveguides on-chip, due to the large modal mismatch between them (50 μm^2 v.s. 0.1 μm^2). Efficient fiber-waveguide coupling

has been extensively investigated using various structures, such as inverse taper [58], graded taper [59], evanescent taper [60], surface grating [39, 61], blazed grating [62], and prism [63]. However, high efficiencies achieved by all these approaches require precise alignment between the fiber and the waveguide which is difficult in practice and dramatically increases the packaging cost thus impractical for mass production.

In order to completely achieve the photonic-electronic integration for optical interconnection, a silicon-based light source is required. A silicon-based laser is arguably the most challenging element in silicon photonics because both silicon and SiGe (including pure germanium), though successfully solve many issues in active components, are inefficient light emitters due to their indirect band structure.

Many different approaches have been studied to overcome this issue and provide a silicon-based solution to the light source. Efforts on porous Si [64, 65], Si nanostructures [66] and SiGe nanostructures [67] tried to modify the crystalline silicon or the germanium band structure to achieve efficient optical transition. Silicide [68], erbium doped Si [69], and other potentially compatible materials have also been investigated. However, all above approaches are challenged by the lack of enough gain to surpass materials losses to achieve net gain for laser action.

Erbium-doped silicon dielectric, which suffers less from the energy back transfer than erbium-doped silicon, is another heatedly studied material system. Erbium atoms, as active material emitting at 1.54 μm, are incorporated into silicon oxide [70, 71, 72] or silicon nitride [73, 74] matrix materials containing silicon nanocrystals as sensitizer. But the optical gain from such extrinsic emitting materials is very small [75] due to the limited erbium solubility and energy up-conversion. Therefore the laser action can only occur in extremely low loss resonators such as the toroidal structures [76]. Another severe issue is the difficulty of electrical injection since these materials are all dielectrics, where the carriers can only be injected under very high electric field via tunneling or other effects [77, 78].

The non-linear effect of silicon can also be used as a gain mechanism to achieve laser action. Based on stimulated Raman scattering (SRS) effect, optically pumped pulsed silicon lasers [79, 80] and continuous-wave lasers [81] have been demonstrated respectively. But the inevitable requirement of the optical injection makes them not suitable for integrated

photonics.

Following a hybrid method, researchers successfully integrated III-V semiconductor lasers, which is widely used as light sources in traditional optical applications, on silicon chips. This integration can be accomplished either by growing GaAs/InGaAs lasers on Si with graded Si_xGe_{1-x} buffer layers to match the lattice constant of GaAs [82] or by bonding III-V lasers on silicon surface [83, 84]. These lasers meet the wavelength and the power requirement, but the introduction of III-V materials, which are dopants in Si, complicates processing.

The electronic-photonic integration at chip level prefers the light source with the following features: (1) room temperature operation with electrical injection; (2) Si-CMOS compatible materials and fabrications; (3) preferred emission wavelength at near infrared, especially near 1.55 μm. The third feature comes from the transparent wavelength range of silicon, which is the primary choice of waveguide core material because of the capability of high density photonic integration. Another advantage of the usage of near infrared light is the ability of integrating with various active components (e.g. modulators and detectors) developed for this wavelength range as we discussed in the previous section.

A complete solution of such silicon-based laser remains to be present. In this thesis work, the author attempts to solve this problem by using the engineered germanium, which potentially meets all the features above.

Chapter 2

Tensile-Strained n^+ Ge: A Gain Medium

This chapter is intended to introduce the concept of engineering the band structure of Ge so as to make Ge behave like a direct band gap material. We begin with the explanation of the band structure engineering of Ge aiming for high efficient direct gap light emission and net gain. Then the direct band-to-band optical transition and optical gain of Ge are theoretically analyzed. The calculations show that the efficient direct gap light emission and the net gain can be achieved in the Ge engineered by introducing proper tensile strain and n-type doping.

2.1 Ge Band Structure Engineering

Ge is normally recognized as a poor light emitting material due to its indirect band structure. The radiative recombination through the indirect band-to-band optical transition is inefficient as a result of a phonon-assisted process. The direct band-to-band optical transition in Ge, however, is a very fast process with radiative recombination rate 4-5 orders of magnitude higher than that of the indirect transition [13], thus the direct gap emission of Ge is, in principle, as efficient as that of direct gap III-V materials. The challenge is that the number of the electrons for the direct optical transition is deficient due to an indirect band structure. Fortunately, Ge is a pseudo direct band gap material because of a small energy difference (0.136 eV, refer to Fig. 2.1) between its direct gap and indirect gap. It will be shown that

with a combination of tensile strain and n-type doping Ge can be engineered to be a direct band gap material.

2.1.1 Ge Band Structure at Equilibrium and under Injection

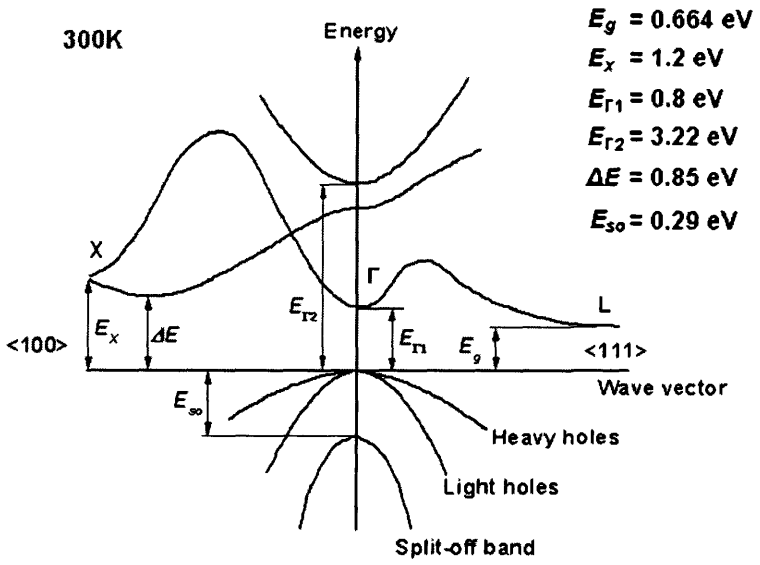

Figure 2.1: Ge band structure at 300K. [3]

The band structure of bulk Ge is shown in Fig. 2.1. The valence band is composed of a light-hole band, a heavy-hole band, and a split-off band from spin-orbit interaction. The light-hole band and the heavy-hole band are degenerate at wave vector $\mathbf{k} = 0$ or Γ point which is the maximum of valence band. The lowest energy point of the conduction band is located at $\mathbf{k} =< 111 >$ or L point. The energy difference between the conduction band at L point and the valence band at Γ point determines the narrowest band gap in Ge: $E_g = 0.664$ eV. This band gap is an indirect band gap since it does not occur at the same $\mathbf{k}$. On the contrary, another two energy gaps ($E_{\Gamma 1}$ and $E_{\Gamma 2}$) between the two local minima of the conduction band and the maximum of the valence band at Γ point are direct energy gaps. Because the direct energy gap $E_{\Gamma 2}$ is much larger than $E_{\Gamma 1}$ and E_g, there is barely any electrons at such high energy levels so that it has negligible effect on the light-matter interaction discussed in this work. Therefore, we refer direct band gap only to $E_{\Gamma 1}$ throughout this thesis and denote $E_{g\Gamma} \equiv E_{\Gamma 1}$ and $E_{gL} \equiv E_g$. The part of the conduction band near Γ point is called direct valley

or Γ valley and the part near L point is called indirect valley or L valley. Since the energy is 4-fold degenerate with regard to the changes of the secondary total angular-momentum quantum number, four L valleys are considered.*

The electron and the hole distributions of Ge at equilibrium are schematically shown in the Fig. 2.2 (a). Most of the thermally activated electrons occupy the lowest energy states in the indirect L valleys following the Fermi distribution

$$f(E) = \frac{1}{1 + (E - E_f)/k_B T}, \tag{2.1}$$

where E_f is the equilibrium Fermi level. On the contrary, most of the electrons stay in the direct Γ valley in a direct band gap material such as InGaAs shown in Fig. 2.2 (b).

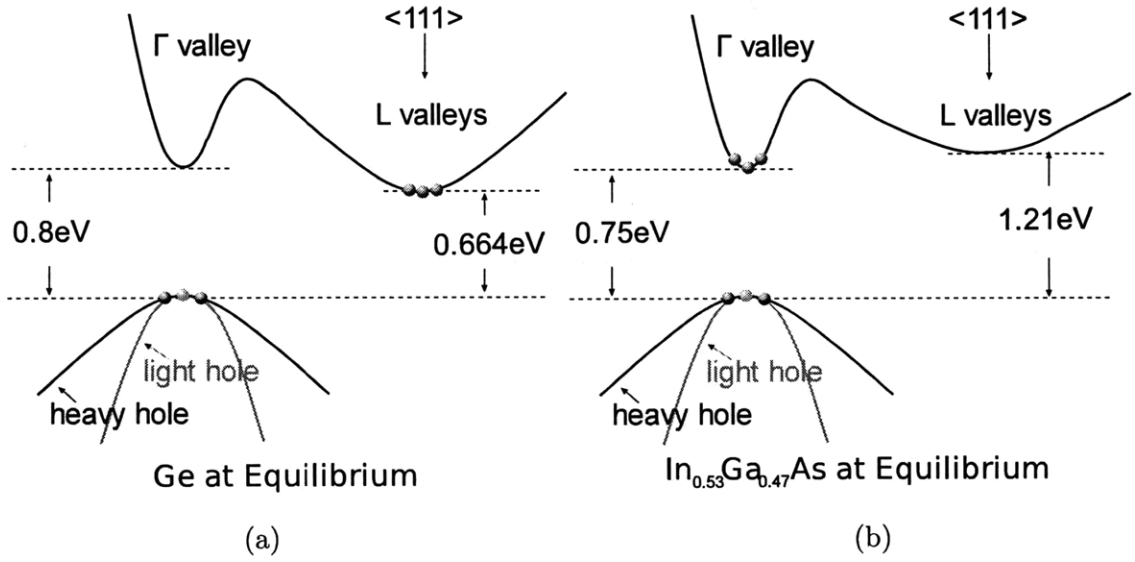

Figure 2.2: Comparison of the electron and the hole distributions between (a) Ge and (b) $In_{0.53}Ga_{0.47}As$ at equilibrium.

The band-to-band optical transition requires excess carriers (electrons and holes) which can be injected by either electrical pumping or optical pumping. At steady state, the electrons and the holes obey the quasi Fermi distributions with respect to the electron quasi Fermi

*Degeneration with regard to the changes of electron spin quantum number is not explicitly accounted here. It is considered in the density of states calculation in Section 2.2.

level and the hole quasi Fermi level respectively:

$$f_c(E) = \frac{1}{1 + (E - E_{fc})/k_B T}, \text{and} \tag{2.2}$$

$$f_v(E) = \frac{1}{1 + (E - E_{fv})/k_B T}, \tag{2.3}$$

where E_{fc} and E_{fv} are the quasi Fermi levels for the electrons in the conduction band and the holes in the valence band respectively. A single quasi Fermi level exists for electrons in both the Γ valley and the L valleys in the optical transition analysis because of a much faster inter-valley scattering ($\sim$1 ps) than any radiative or non-radiative recombination processes. There are a non-negligible amount of electrons in the Γ valley owing to the small energy difference (0.136) between the direct band gap and the indirect band gap of Ge as shown in Fig. 2.3 (a). The excess electrons in the Γ valley lead to recombination with the holes in the valence band, which is a highly efficient light emission process because that the direct band-to-band radiative recombination is generally faster than the non-radiative recombinations such as Auger and defect-assisted processes. But the overall light emission efficiency is very low because most of the injected electrons, staying in the L valleys, recombine non-radiatively due to the slower indirect phonon-assisted radiative recombination than the non-radiative recombinations. On the contrary, the light emission in a direct band gap material such as InGaAs is very efficient because almost all injected electrons are in the Γ valley thus recombine radiatively as shown in Fig. 2.3 (b).

To improve the light emission efficiency in Ge, more injected electrons are required to be pumped into Γ valley at the same carrier injection level. The band structure of Ge can be engineered to accomplish this goal, discussed in the next section.

2.1.2 Effect of Tensile Strain on Ge Band Structure

Efficient direct gap light emission in Ge requires a large amount of electrons in the direct Γ valley. The ratio of the number of the direct Γ valley electrons to the indirect L valleys electrons is determined by the energy difference between the direct band gap and the indirect band gap at quasi-equilibrium. Band structure is associated with crystal lattice which can be

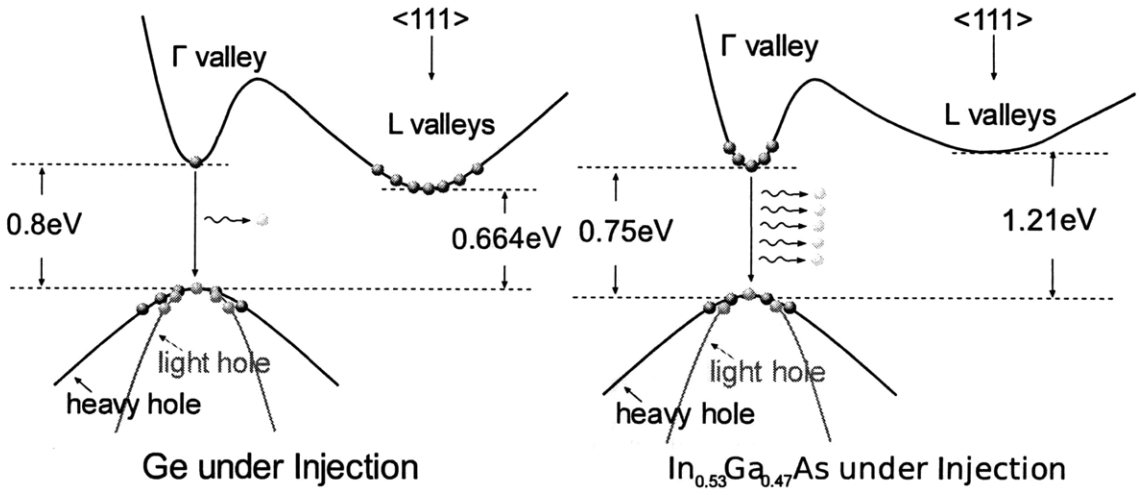

Figure 2.3: Comparison of the electron and the hole distributions and the light emission between (a) Ge and (b) $In_{0.53}Ga_{0.47}As$ under injection.

changed by the existence of strain. This effect can be calculated using a strain-modified $k\dot{p}$ method [85]. Pikus-Bir Hamiltonian and Luttinger-Kohn's model are used in the method to describe the degenerate bands in Ge. This calculation shows that strain changes the energy levels of the direct Γ valley, the indirect L valleys, the light-hole band, and the heavy-hole band relative to vacuum level.[†] Moreover, the light-hole and the heavy-hole band becomes non-degenerate and separates at Γ point as shown in Fig. 2.5 (a). The direct band gap and indirect band gap under strain can be calculated using this method[‡]

$$E_{g\Gamma hh} = a_{c\Gamma}(\epsilon_{xx} + \epsilon_{yy} + \epsilon_{zz}) + P + Q \tag{2.4}$$

$$E_{g\Gamma lh} = a_{c\Gamma}(\epsilon_{xx} + \epsilon_{yy} + \epsilon_{zz}) + P - Q/2 + E_{so}/2 \; - \sqrt{E_{so}^2 + 2E_{so}Q + 9Q^2} \tag{2.5}$$

$$E_{gLhh} = a_{cL}(\epsilon_{xx} + \epsilon_{yy} + \epsilon_{zz}) + P + Q \tag{2.6}$$

$$E_{gLlh} = a_{cL}(\epsilon_{xx} + \epsilon_{yy} + \epsilon_{zz}) + P - Q/2 + E_{so}/2 \; - \sqrt{E_{so}^2 + 2E_{so}Q + 9Q^2} \tag{2.7}$$

[†]The energy levels of other bands such as spin-orbit split-off band are also changed.

[‡]Shear strain $\epsilon_{xy(x\neq y)}$, which is negligible in the thin film material, is not considered here.

where

$$P = -a_v(\epsilon_{xx} + \epsilon_{yy} + \epsilon_{zz}) \tag{2.8}$$

$$Q = -b(\epsilon_{xx}/2 + \epsilon_{yy}/2 - \epsilon_{zz}) \tag{2.9}$$

. $E_{g\Gamma hh}$ and $E_{g\Gamma lh}$ are energy gaps between the Γ valley and the heavy-hole band and the light-hole band respectively. E_{gLhh} and E_{gLlh} are energy gaps between the L valley and the heavy-hole band and the light-hole band respectively. ϵ_{xx}, ϵ_{yy}, and ϵ_{zz} are strain components. E_{so} is the energy difference between valence bands and spin-orbit split-off band at Γ point. $a_{c\Gamma}$, a_{cL}, a_v and b are deformation potentials for Γ valley, L valleys, the average of three valence bands (light-hole, heavy-hole and spin-orbit split-off) and a strain of tetragonal symmetry. They are material properties which can be either calculated from first-principle calculation or determined by experiments. For thin film Ge, the strain is induced by in-plane biaxial stress from the adjacent layers. Therefore

$$\epsilon_{xx} = \epsilon_{yy}, \text{and} \tag{2.10}$$

$$\epsilon_{zz} = -2C_{12}/C_{11}\epsilon_{xx}, \tag{2.11}$$

where C_{11} and C_{12} are the elements of the elastic stiffness tensor.

The direct and the indirect band gaps of Ge under strain can be obtained using Eq. 2.4-2.7 with the experimental results of $a_{c\Gamma} = -8.97$ eV and $b = -1.88$ eV from Ref. [86] $C_{11} = 128.53$ GPa and $C_{12} = 48.26$ GPa from Ref. [86], and the calculated results of a_{cL}=-2.78 eV and a_v=1.24 eV from Ref. [87]. These energy gaps are calculated and shown in Fig. 2.4. We can see both the direct band gap and the indirect band gap shrink with tensile strain (positive ϵ_{xx}) and the direct band gap shrinks faster than the indirect band gap due to $|a_{c\Gamma}| > |a_{cL}|$. The direct band gap becomes equal to the indirect band gap at $\epsilon \approx 1.8\%$ where Ge becomes a direct band gap material. The energy gaps from the conduction band (equal for both direct Γ valley and indirect L valley) to the light-hole and the heavy-hole band are 0.53 eV and 0.66 eV respectively.[§]

[§]There are two energy gaps at both Γ point and L point due to the separation of the light-hole band and the heavy-hole band. The optical band gap is determined by the smaller gap related to the light-hole band. We refer the band gap to this energy gap in the following discussions unless explicitly stated otherwise.

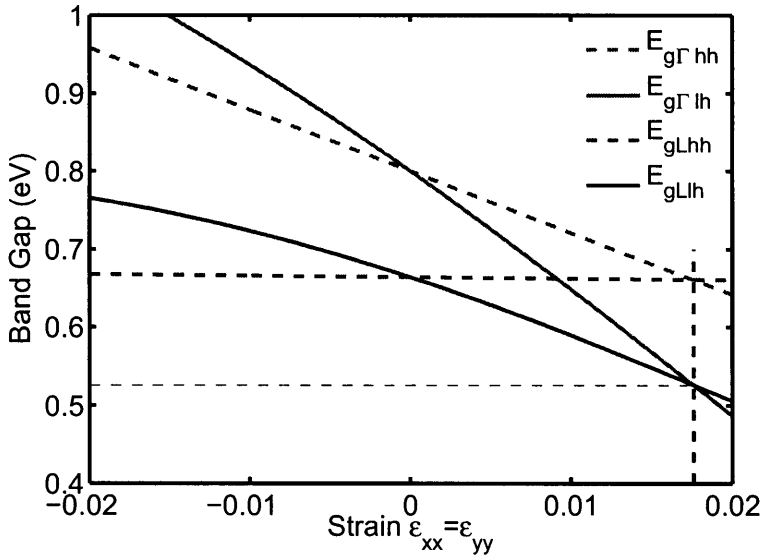

Figure 2.4: The direct and the indirect band gaps of Ge under in-plane strain. $E_{g\Gamma hh}$ and $E_{g\Gamma lh}$ are energy gaps between the Γ valley and the heavy-hole band and the light-hole band respectively. E_{gLhh} and E_{gLlh} are energy gaps between the L valley and the heavy-hole band and the light-hole band respectively.

The carrier distribution and the light emission properties of 1.8% tensile-strained Ge under injection are schematically shown in Fig. 2.5 (a). Since the Ge becomes a direct gap material, a considerable amount of the excess electrons occupying the direct Γ valley capable of radiative recombination leading to efficient direct gap light emission. The overall emission efficiency of the strained Ge is comparable to that of InGaAs (Fig. 2.5).

Biaxial tensile strain is an effective way to transform Ge to a direct band gap material nevertheless two issues exist.

Firstly, highly strained, high quality single crystalline Ge film is difficult to form because the large lattice change causes thermodynamic instability resulting in dislocations, surface roughness, and other lattice defects. Tensile strain can be induced either by lattice mismatch or by thermal mismatch. The former approach requires a substrate material with larger lattice constant than that of Ge. As high as 0.5% tensile strain in Ge has been achieved using $In_xGa_{1-x}As$ compositionally graded layers as a virtual substrate [88]. The latter approach requires different thermal expansion coefficient between Ge and the substrate material, which is adopted in this research. Up to 0.25% tensile strain has been achieved in Ge epitaxially

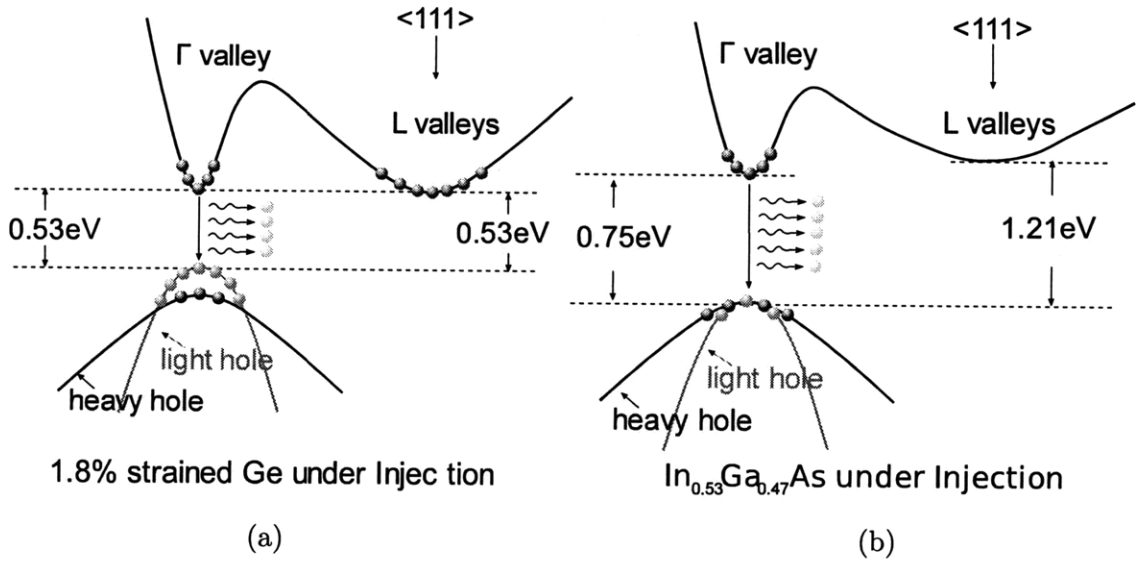

Figure 2.5: Comparison of the electron and the hole distributions and the light emission between (a) 1.8% tensile-strained Ge and (b) $In_{0.53}Ga_{0.47}As$ under injection.

grown on Si substrate [89] which is discussed in Chapter 3. However, higher tensile strain, such as projected 1.8%, is very challenging to obtain using either of these two approaches.

The second issue is the excessive change of the band gap in highly tensile-strained in Ge. Both the direct band gap and the indirect band gap become 0.53 eV at 1.8% tensile strain as shown in Fig. 2.5 (a). This optical band gap is corresponding to an emission wavelength of about 2300 nm which is far away from the 1550 nm telecommunication wavelength band which is also the primary choice for Si photonics.

These two issues suggest that very high tensile strains are not favorable in both material growth and photonics applications. Therefore, a moderate tensile strain is used instead in this work. Thus the increase of the number of the injected excess electrons in the Γ valley owing to strain effect is limited. This problem can be solved by n-type doping in Ge shown in Session 2.1.3.

2.1.3 Tensile Strain and N-Type Doping

The energy difference between the direct band gap and the indirect band gap of Ge is decreased up to 20 meV with a moderate tensile strain of 0.20~0.25%, whereas majority of the injected excess electrons still occupy the lower energy indirect L valleys. N-type doping can

be used in Ge to solve this problem because the quantum states of the indirect L valleys are filled with the extrinsic electrons thermally activated from n-type donors, which is called the indirect valley state filling effect. This effect raises the Fermi level thus raises the effective bottom of the indirect L valleys leading to the increase of the injected electrons in the direct Γ valley. An example of the Fermi level versus active n-type doping concentration of 0.25% tensile-strained Ge is shown in Fig. 2.6. We can see that the Fermi level becomes equal to the direct band gap at about 7×10^{19} cm^{-3} doping concentration, where the effective bottom of the indirect L valleys equates the bottom of the direct Γ valley therefore Ge becomes a direct band gap material.

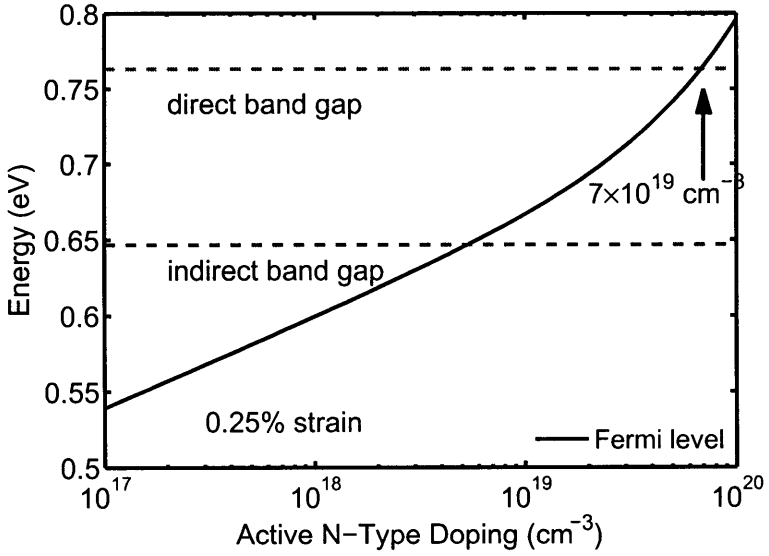

Figure 2.6: Calculations of the Fermi level as a function of active n-type doping concentration in 0.25% tensile-strained Ge is shown in black line. The direct band gap and the indirect band gap at the same strain level is shown in red and in blue respectively. All energies are referred to the top of the valence band.

Using the heavily doped Ge increases the optical gain by making Ge direct band gap but also raises an immediate question of whether the large amount of the extrinsic electrons introduce so much free carrier (electron in this case) optical loss that negatively affects the occurrence of the net material gain. This trade-off can be analyzed theoretically and confirmed by experiments. The theoretical calculations in the next session shows that n-type doping is favorable in achieving lasing in most of the cases.

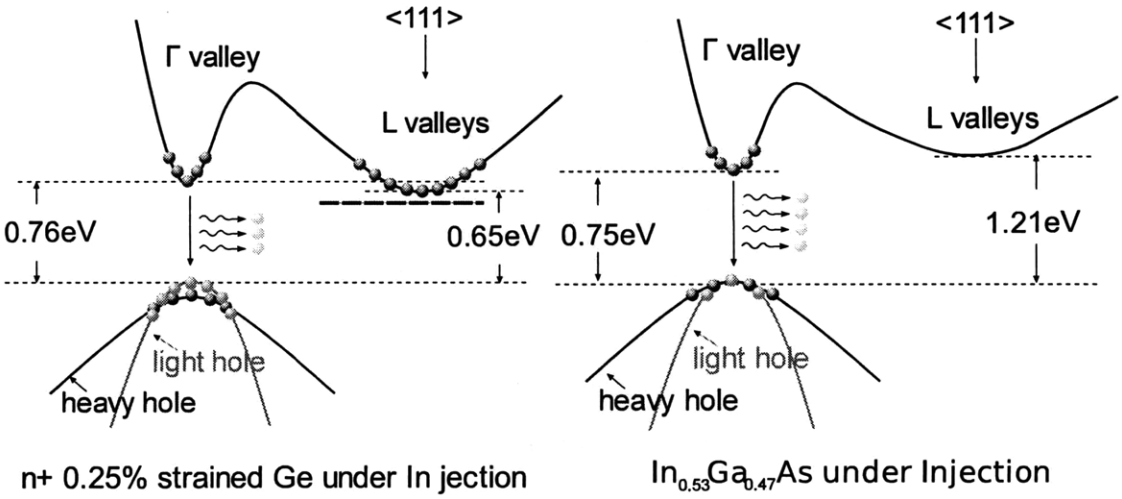

Figure 2.7: Comparison of the electron and the hole distributions and the light emission between (a) n-type doped 0.25% tensile-strained Ge and (b) $In_{0.53}Ga_{0.47}As$ under injection.

The carrier distribution and the light emission of 0.25% tensile-strained Ge under injection are schematically shown in Fig. 2.7 (a). Since the lower quantum states of the indirect L valleys are filled by the extrinsic electrons thermally activated from the n-type donors, the energy levels of the available states in both the direct Γ valley and the indirect L valleys are equal. The excess electrons are injected into both valleys and the electrons in the direct Γ valley contribute to the direct gap light emission. The overall emission efficiency is a little less but to that in direct band gap III-V materials such as InGaAs as shown in Fig. 2.7 (b).

2.2 Optical Gain Modeling

In the previous section, it has been shown that a combination of tensile strain and n-type doping can effectively make Ge a direct band gap material with efficient direct gap light emission owing to the increased number of electrons in the direct Γ valley. This direct band gap behavior, in principle, is capable of optical gain in analogy to direct band gap III-V materials. The difference of tensile-strained n^+Ge from III-V materials is the existence of the large amount of extrinsic electrons which introduce free-carrier-induced optical loss. The following theoretical calculations show that the n-type doping has a positive effect on the net gain in most of the cases and it is essential to a laser action in Ge. [90]

2.2.1 Direct Band-to-Band Transition

Direct band-to-band optical transition includes optical absorption, stimulated emission, and spontaneous emission between the direct Γ valley of the conduction band and the valence band. These electron-photon scattering processes can be described by the product of the strength of the scattering and the occupation probabilities of the electrons and the holes. We denote the scattering strength of absorption, stimulated emission, and spontaneous emission at photon energy $h\nu$ are $\alpha(h\nu)$, $e_{st}(h\nu)$, and $e_{sp}(h\nu)$ respectively. The rate equation of the number of carriers N related to radiative recombinations in the material is

$$\frac{dN}{dt} = \alpha f_v(1-f_c)N_{ph} - e_{st}f_c(1-f_v)N_{ph} - e_{sp}f_c(1-f_v) \tag{2.12}$$

where N_{ph} is the number of photons and f_c and f_v are the occupation probabilities of the electron with respect to the electron quasi Fermi level at E_1 and the hole with respect to the hole quasi Fermi level at E_2, respectively. E_1 and E_2 obtained by

$$E_1 = E_c + \frac{h\nu - E_g}{1 + m_c/m_v} \text{and} \tag{2.13}$$

$$E_2 = E_v - \frac{h\nu - E_g}{1 + m_v/m_c} \tag{2.14}$$

are the energy levels associated with the optical transition at photon energy $h\nu$ and are related by $E_1 - E_2 = h\nu$. Since quasi Fermi levels depends on the injection level, f_c (or f_v) is an implicit function of the total electron (hole) density which is the summation of the equilibrium electron (hole) density and the excess injected electron (hole) density.

The physics meaning of $f_c(1-f_v)$ is the joint probability of the existence of an electron at E_1 in the conduction band and the absence of a hole at E_2 in the valence band, which have to be simultaneously satisfied when an optical transition occurs at photon energy $h\nu$. Therefore, the same term of $f_c(1-f_v)$ exists for both the stimulated emission and the spontaneous emission. Optical absorption is the opposite process of the stimulated emission therefore $f_v(1-f_c)$ is used instead.

Optical gain $g(h\nu)$ is determined by the competition of the stimulated emission and the

absorption:

$$g(h\nu) = e_{st} f_c(1 - f_v) - \alpha f_v(1 - f_c). \tag{2.15}$$

A detail balance analysis proves that all the three scattering strength coefficients, α, e_{st}, and e_{sp}, are equal at any photon energy $h\nu$. Therefore optical gain can be rewritten as

$$g(h\nu) = \alpha(f_c - f_v). \tag{2.16}$$

$(f_c - f_v)$ is called population inversion factor. It is negative at equilibrium or low injection levels representing a net optical loss (absorption). While it becomes positive at higher injection levels, when the population of the electrons inverts (more electrons in the conduction band than in the valence band), underlying a net optical gain.

2.2.2 Direct Gap Absorption

The direct band-to-band absorption is required to calculate the optical gain according to Eq. 2.16. The direct gap absorption can be theoretically calculated by using Fermi's golden rule to solve the electron-photon scattering in crystalline potential:

$$\alpha(h\nu) = \frac{e^2 hc\mu_0}{2{m_e}^2} \frac{|p_{cv}|}{n} \frac{1}{h\nu} \rho_r(h\nu - E_g), \tag{2.17}$$

where $|p_{cv}|$ is related to the transition matrix element and n is the refractive index, both of which are materials properties and can be considered as constants in a small range of photon energy. ρ_r is the joint density of states of the conduction band (direct Γvalley) and the valence band. A quadratic approximation is usually used to describe the density of states near an extremum of an energy band in semiconductor and ρ_r is subsequently calculated

$$\rho_r(h\nu - E_g) = 2\pi \left(\frac{2m_r}{h^2}\right)^{3/2} \sqrt{h\nu - E_g}, \tag{2.18}$$

where $m_r = \frac{m_c m_v}{m_c + m_v}$ is the reduced effective mass of the conduction band and the valence band. Therefore, the absorption near direct band gap can be approximately written as

$$\alpha(h\nu) = A\frac{\sqrt{h\nu - E_g}}{h\nu}, \tag{2.19}$$

where A is a constant usually determined from experiments.

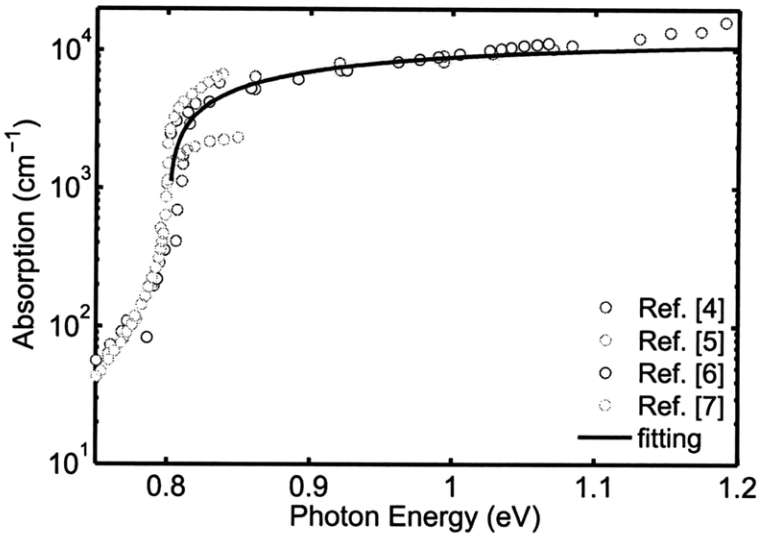

Figure 2.8: Comparison of the absorption of Ge near direct band gap from different literatures. Four experimental absorption data are obtained from Ref. [4, 5, 6, 7] respectively. The theoretical fitting is shown with the black solid line.

The absorption spectra of intrinsic bulk Ge near direct band gap (0.8 eV) from a few experiments [4, 5, 6, 7] are shown in Fig. 2.8. The absorptions from Ref. [4] and Ref. [6] show good agreement above the direct band gap. The theoretical fitting to these data using Eq. 2.19 shown with black solid line gives $A = 2.0 \times 10^4$ eV$^{1/2}$/cm.

The absorption edge of tensile strain Ge moves towards lower energy because of the shrinkage of the direct band gap. Since the light-hole band and the heavy-hole band separate under strain, two optical transitions corresponding to the two energy gaps compose the total absorption. Therefore, the absorption of tensile-strain Ge is

$$\alpha(h\nu) = A\left(k_1\frac{\sqrt{h\nu - E_{g\Gamma lh}}}{h\nu} + k_2\frac{\sqrt{h\nu - E_{g\Gamma hh}}}{h\nu}\right), \tag{2.20}$$

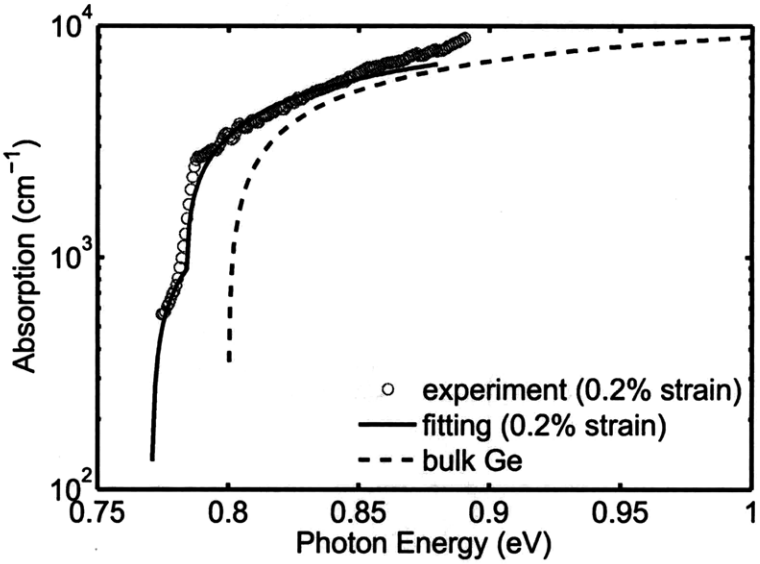

Figure 2.9: The experimental result and the theoretical fitting of the absorption of 0.2% tensile strained Ge. The absorption of bulk Ge is also shown with the black dash line for comparison.

where $k_1 = {m_{rlh}}^{3/2}/({m_{rlh}}^{3/2} + {m_{rhh}}^{3/2})$ and $k_2 = {m_{rhh}}^{3/2}({m_{rlh}}^{3/2} + {m_{rhh}}^{3/2})$ are coefficients attributing to the difference between the two transitions due to the different reduced effective masses. k_1 and k_2 are normalized so that $k_1 + k_2 = 1$. $k_1 = 0.68168$ and $k_2 = 0.31832$ are calculated for Ge. The measured absorption spectrum of 0.2% tensile strained Ge is shown in Fig. 2.9 and $A = 1.9 \times 10^4$ $\text{eV}^{1/2}/\text{cm}$ is calculated by fitting the experimental result using Eq. 2.20. The A of strained Ge is approximately the same as that of bulk Ge underlying that small strain does not affect the optical transition matrix much. In the following two sections, $A = 2.0 \times 10^4$ $\text{eV}^{1/2}/\text{cm}$ is used to calculate optical gain in both the bulk Ge and the strained Ge.

2.2.3 Optical Gain Spectrum

The optical gain spectrum of Ge at a certain injection level can be calculated by using Eq. 2.16 with absorption coefficients obtained from the previous section. The effect of tensile strain and n-type doping on optical gain of Ge is analyzed in this section.

As we calculated in Section 2.1.3, a combination of 0.25% tensile strain and 7×10^{19} cm^{-3} n-type doping results in the raise of the equilibrium Fermi level to the bottom the direct Γ

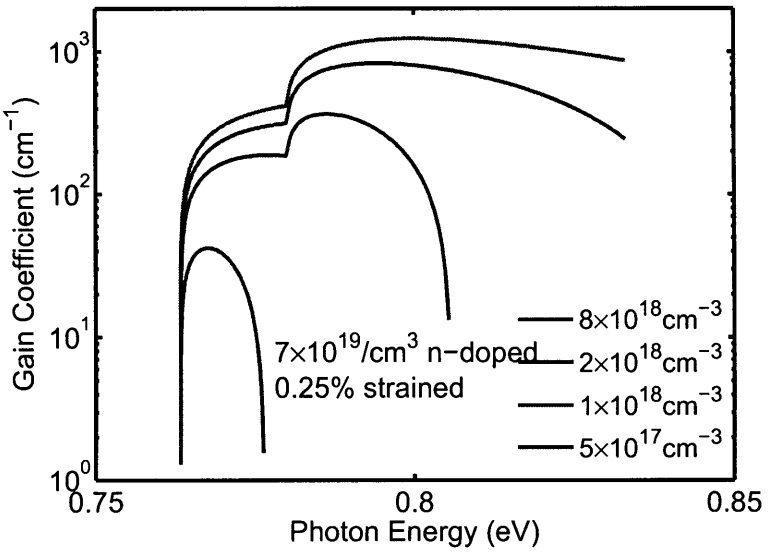

Figure 2.10: Calculated optical gain spectrum of Ge with 0.25% tensile strain and 7 × $10^{19}cm^{-3}$ n-type doping at various injection levels near the direct band gap energy.

valley therefore Ge becomes a direct band gap material. The optical gain spectrum of such Ge is shown in Fig. 2.10. The optical gain starts to occur at 0.76 eV which is the energy gap between direct Γ valley and the light-hold band under 0.25% tensile strain. Since the effective masses of both the electrons in the Γ valley ($0.038m_{e0}$) and the light holes ($0.043m_{e0}$) are very small, considerably population inversion starts to occur at a fairly low injection level of $\sim 10^{17}$ cm^{-3}. As the injection level increases, the separation of the electron and the hole quasi Fermi levels becomes larger than the energy gap between the direct Γ valley and the heavy-hole band. Thus the optical gain contributed from the electron heavy-hole recombination starts to occur, which can be seen from the fast raise of the optical gain at 0.78 eV at injection levels above 10^{18} cm^{-3}. A peak gain over 1000 cm^{-1} around 0.8 eV (1550 nm) is achieved an injection level of 8×10^{18} cm^{-3} which is readily achievable.

The effects of tensile strain and n-type doping on optical gain in Ge are shown in Fig. 2.11. We can see that the high n-type doping dramatically enhances the optical gain by two orders of magnitude for both the strained and the unstrained Ge. Tensile strain also increases the optical gain by a few times and it extends the gain spectrum to lower energy (longer wavelength) thus shifts the peak gain to preferred 0.8 eV (1550 nm) as well as broadens the entire gain spectrum. The optical gain of Ge benefits from both n-type doping and tensile

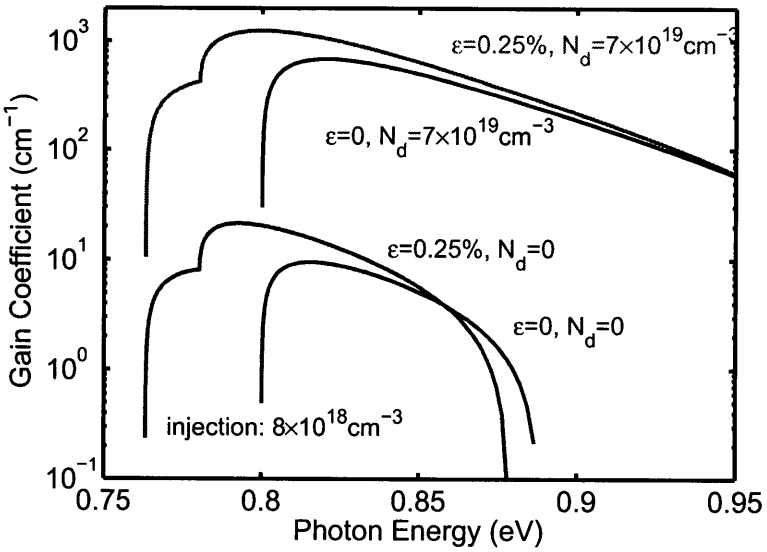

Figure 2.11: Comparison of the calculated optical gain of the Ge with both tensile strain and n-type doping, with either of them, and with neither of them at the injection level of 8×10^{18} cm^{-3} near the direct band gap energy.

strain.

2.2.4 Net Material Gain

The occurrence of optical gain in a material under injection does not necessarily lead to a laser action which requires that the optical gain overcomes all kinds of optical losses. With regard to the material itself, the optical loss is dominated by the free carrier absorption in which an electron in the conduction band absorbs the energy of a photon and moves to an empty state higher in the conduction band (correspondingly for holes in the valence band) without inter-band recombination. The free carrier absorption increases with wavelength and becomes significant at higher carrier densities. When a gain medium is pumped to achieve population inversion, the large amount of injected carriers induce the free carrier absorption to compete against the optical gain. The free carrier absorption is usually the major obstacle for lasing in a gain medium, especially for heavily n-type doped Ge because of the existence of additional extrinsic electrons.

The free carrier absorption $\alpha_{\rm fc}$ can be calculated by using

$$\alpha_{\rm fc}(\lambda) = k_e n_c \lambda^{a_e} + k_h p_v \lambda^{a_h}, \tag{2.21}$$

where n_c and p_v are the electron density in the conduction band and the hole density in the valence band and k_e, k_h, a_e and a_h are constants of the material. a_e and a_h are usually between 1.5 and 3.5. By fitting the free carrier absorption data in n^+Ge [91] and p^+Ge [92] in a carrier density range of $10^{19} - 10^{20}$ cm^{-3} at room temperature, we obtain

$$\alpha_{\rm fc}(\lambda) = -3.4 \times 10^{-25} n_c \lambda^{2.25} - 3.2 \times 10^{-25} p_v \lambda^{2.43}, \tag{2.22}$$

where α_{fc} is in unit of cm^{-1}, n_c and p_v in units of cm^{-3}, and λ in units of nm.

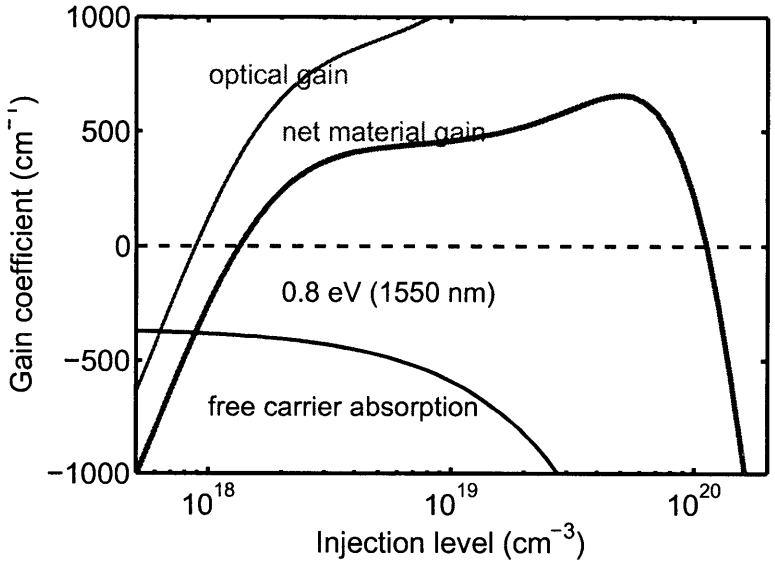

Figure 2.12: The optical gain, the free carrier absorption, and the net material gain of Ge with 0.25% tensile strain and 7×10^{19} cm^{-1} n-type doping at various injection levels at the photon energy of 0.8 eV (1550 nm).

The optical gain, the free carrier absorption, and the net material gain which is the difference between them are calculated versus injection level at the photon energy of 0.8 eV (1550 nm) are calculated for Ge with 0.25% tensile strain and 7×10^{19} cm^{-3} n-type doping as shown in Fig. 2.12. The optical gain starts with negative values (optical loss) at low injection levels. The free carrier absorption is large (negative) even at low injections since the material

is heavily doped. But the optical gain overcomes the free carrier loss above the injection level of 1.2×10^{18} cm^{-3} where Ge becomes a gain medium. We can see that net gain can be achieved in heavily n-typed doped Ge in spite of excess free carrier absorption from extrinsic electrons. At very high carrier injection levels ($> 10^{20}$ cm^{-3}), the free carriers absorption exceeds the optical gain again and causes net loss in the material. Therefore, between a large injection range of 10^{18} cm^{-3} and 10^{20} cm^{-3}, the tensile-strained n$^+$Ge is a gain medium at 0.8 eV photon energy. At photon energies near 0.8 eV, this range changes a little but the same characteristic holds.

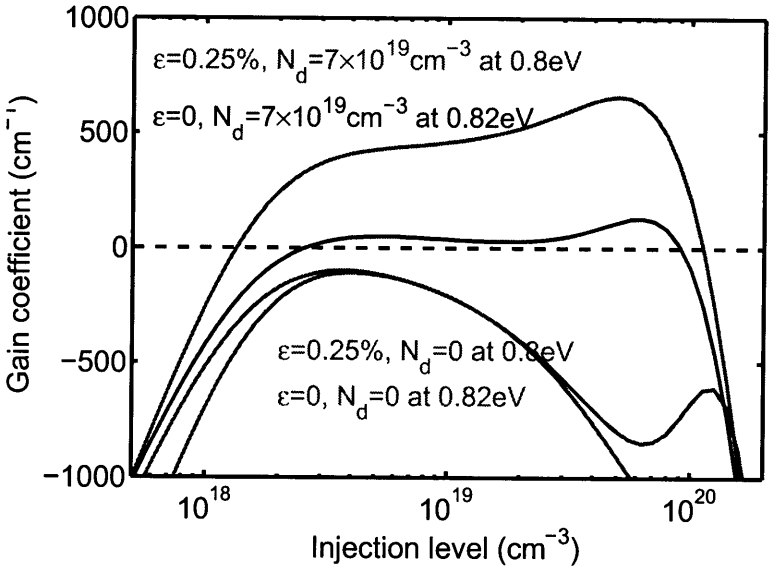

Figure 2.13: Comparison of the calculated net material gain versus injection level of the Ge with both tensile strain and n-type doping, with either of them, and with neither of them at their peak gain photon energies respectively.

The comparison of the net material gain versus injection level of Ge with both tensile strain and n-type doping, with either of the them, and with neither of them are shown in Fig. 2.13. Since the optical gain spectrum varies with strain, the net gains for different conditions are calculated at different photon energies.* The net gain can never occur for intrinsic Ge no matter with or without 0.25% tensile strain because the free carrier absorption always exceeds the optical gain. It is the reason that the net gain has never been observed from Ge. However, with n-type doping, the net gain can be achieved in both tensile-strained and

*The photon energy of the peak gain also depends on the injection level. The photon energies at which the net gain are calculated are corresponding to peak gains at injected carrier density of $\sim 1 \times 10^{19}$ cm^{-3}

unstrained Ge. Tensile strain further increases the population of the injected electrons in the direct Γ valley leading to a lower net gain threshold and higher net gain at given injection levels. At very high injection levels, all the materials show net loss due to the exceedingly high free carrier absorption.

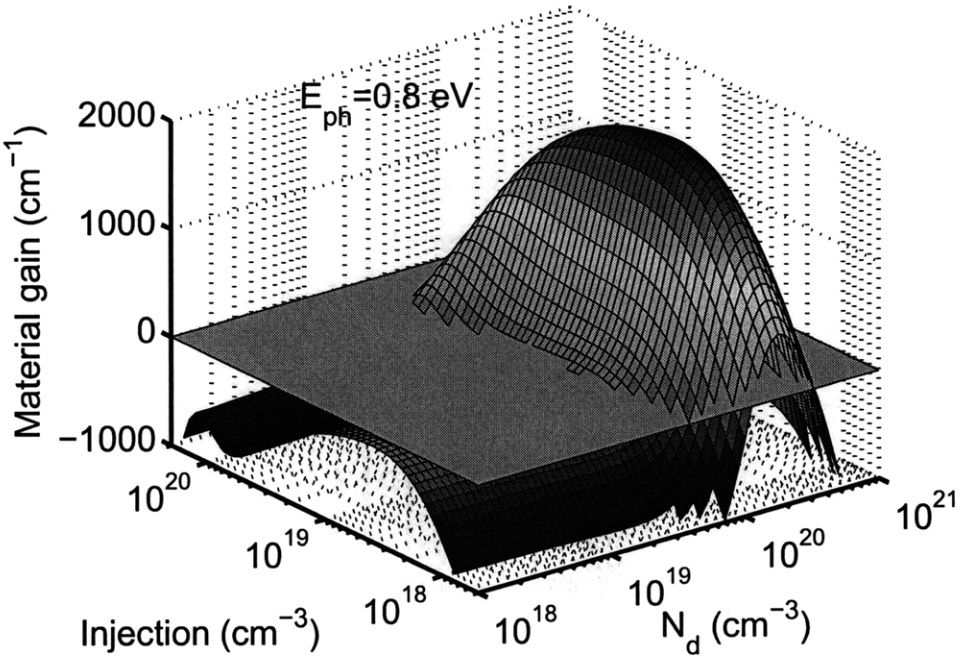

Figure 2.14: Dependence of the calculated net material gain of Ge on the n-type doping level (N_d) as well as the carrier injection level at the photon energy of 0.8 eV.

In order to further understand the effect of the n-type doping, a simulation showing the dependence of the net gain on the n-type doping level at various injection levels is calculated and shown in Fig. 2.14. We can see that there is a certain range of the n-type doping levels and the carrier injection levels, in which the net gain occurs. Doping concentrations higher than $\sim 10^{19}$ cm^{-3} are required for the occurrence of the net gain at the photon energy of 0.8 eV. Below this doping level, optical loss from the free carrier absorption is always larger than the optical gain no matter how hard the material is pumped. On the other hand, net loss occurs at either very high doping levels or very high injection levels because too many free carriers are introduced that the free carrier loss cannot be compensated by the optical gain. The cross-section of the 3-D net gain plot at the zero gain plane is the threshold boundary surrounding the net gain region as shown in the figure. This threshold boundary may vary

at photon energies other than 0.8 eV.

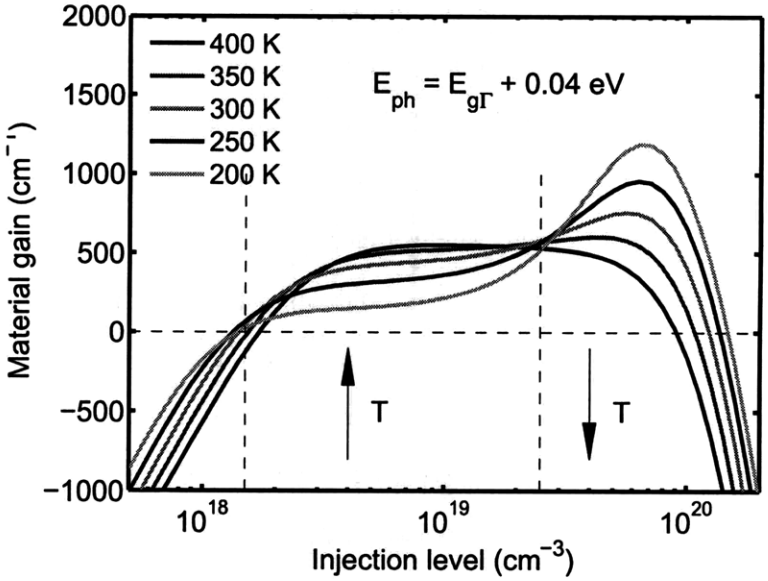

Figure 2.15: The calculated net material gain of tensile-strained n^+Ge versus the carrier injection level at various temperatures. The temperature dependence of the band gap is considered in the calculation and the photon energy is 0.04 eV above the direct band gap at each temperature for a fair comparison.

Temperature is another factor which can affect the optical gain. The dependence of the net gain of 0.25% tensile-strained, 7×10^{19} cm^{-3} n-type doped Ge on temperature is calculated and shown in Fig. 2.15. Since the band gap of Ge also changes with temperature, the photon energy chosen in the calculation is always 0.04 eV lager than the direct band gap at each temperature for a fair comparison. The photon energy used at 300 K is about 0.8 eV while the direct band gap (between the Γ valley and the light-hole band) is about 0.76 eV under of 0.25% tensile strain. The temperature dependence of the direct and the indirect band gap of Ge used in the calculation is found in Ref. [3]:

$$\begin{cases} E_{g\Gamma} = 0.89 - 5.82 \times 10^{-4} \frac{T^2}{T+296} (\text{eV}) \\ E_{gL} = 0.742 - 4.8 \times 10^{-4} \frac{T^2}{T+235} (\text{eV}). \end{cases}$$

Besides the change of the band gap, which we already excluded by using the photon energy $E_{ph} = E_{g\Gamma} + 0.04$ at each temperature, the influence of temperature on optical gain

mainly results from two effects: (1) the relative distribution of the electron between the direct Γ valley and the indirect L valleys and (2) the fraction of the electrons contributing to the light emission at the given photon energy. The competition between these two effects determines the temperature dependence of the optical thereby the net gain of Ge. The net gain versus the injected carrier density at temperatures between 200 K to 400 K is shown Fig. 2.15. The net gain threshold is only slightly changed with temperature while the influence of temperature on the net gain above threshold can be divided into two ranges. The net gain increases with temperature between the threshold and mid-10^{19} cm^{-3} but it decreases with temperature from mid-10^{19} cm^{-3} to 10^{20} cm^{-3}. At etch range, one of the two effects mentioned above dominates the temperature dependence behavior.

The distribution of the electrons changes with temperature because the probability of the electrons (or holes) occupying higher energy states is higher at elevated temperatures. It can also been seen from the Fermi distribution function

$$f(E) = \frac{1}{1 + \frac{E-E_f}{k_B T}}$$

in which the exponential rate is lower at high temperatures leading to more occupation probability at higher energy E. More high energy electrons means more electrons in the direct Γ valley which is responsible for the direct gap stimulated emission. Thus the optical gain increases with temperature if this effect dominates. It explains the temperature dependence of the net gain between the threshold and mid-10^{19} cm^{-3} injection level. This effect is an unique feature of indirect band gap materials with small energy difference between the direct band gap and the direct band gap.

On the contrary, the second effect makes optical gain thereby net gain favorable to lower temperatures. This effective is schematically shown in Fig. 2.16. In the figure, the energy distributions of the injected direct Γ valley electron density and the injected hole density are drawn at high temperature and low temperature, respectively. The carrier density distribution is the multiplication of the (quasi) Fermi distribution and the square root density of states of the band edge. The peak width of the carrier density distribution is proportional to the thermal energy (1.5-2 kT) hence the peak is narrower at lower temperature. The total

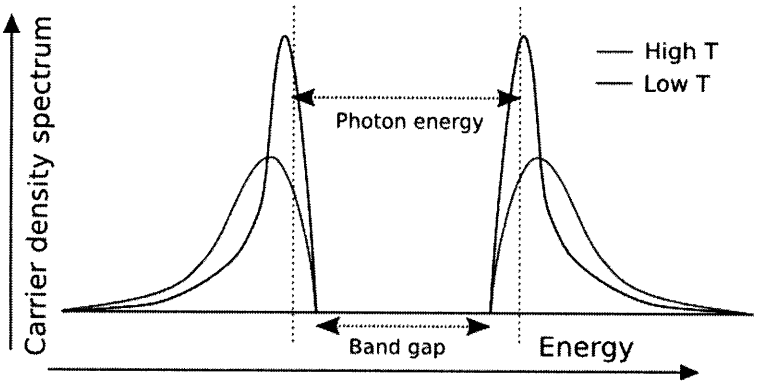

Figure 2.16: Schematic of the injected excess carrier (direct Γ valley electrons and holes) density energy distributions at high temperature and low temperature, respectively.

carrier density represented by the area of the distribution curve is same for both temperatures since we are comparing the carrier behavior at the same given injected carrier density. It requires the peak height of the distribution at low temperature is higher than that at high temperature. The stimulated emission at a certain photon energy is determined by the available electrons and holes at two energy levels corresponding to the photon energy. These two energy levels are shown in two vertical dotted lines in the figure. We can see the carrier density at these two energy levels are higher at lower temperature therefore the optical gain is higher. This effect explains the temperature dependence of the net gain from mid-10^{19} cm^{-3} to 10^{20} cm^{-3}.

In normal pumping conditions, the injected excess carrier density is most likely within the range between the threshold and mid-10^{19} cm^{-3}. Therefore, the increase of the net gain with temperature is possibly observed. It also explains the phenomenon observed from the temperature dependent photoluminescence of tensile-strained n^{+}Ge discussed in Section 4.3.2.

Chapter 3

Tensile-Strained n^+Ge Epitaxial Growth and Fabrication

In Chapter 2, we have proved theoretically that a combination of tensile-strain and n-type doping can effectively change Ge to a direct band gap material and a gain medium. In this chapter, we present how to grow such material directly on Si substrate, which is extremely attractive in practice since such Si-based material growth and fabrication is completely compatible to massively used, mature Si complimentary metal oxide semiconductor (Si-CMOS) technology thus minimize the cost for production. We first introduce the ultra high vacuum chemical vapor deposition (UHVCVD) which is the technique used to epitaxially grow Ge on Si in this work. Then the detail of the growth is exhibited including the procedure to form tensile strain the heavy n-type doping in Ge during the growth. Finally, we discuss two methods, selective growth and dry etching, to fabricate Ge devices such as Ge light emitting diodes shown in Chapter 5.

3.1 Ultrahigh Vacuum Chemical Vapor Deposition (UHVCVD)

Ultrahigh vacuum chemical vapor deposition (UHVCVD) is one type of chemical vapor deposition process, in which the wafer (substrate) is exposed to one or more volatile precursors, which react and/or decompose on the substrate surface to produce the desired deposit. UHVCVD is the CVD process operating at a very low pressure, typically below 10^{-6} Pa

($\sim 10^{-8}$ torr).

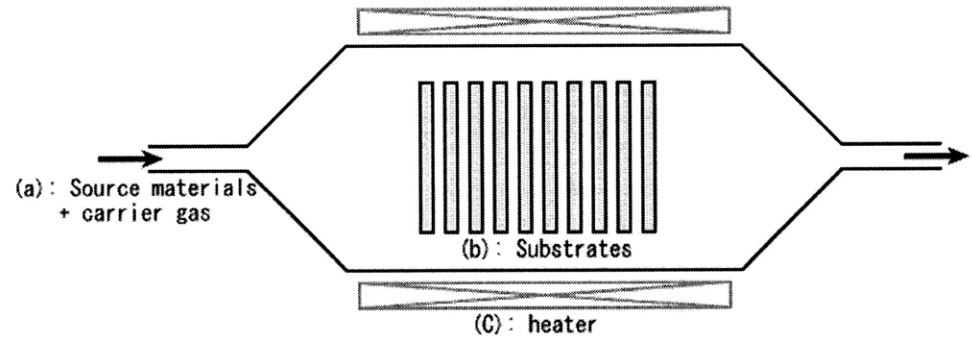

Figure 3.1: Schematic of a typical hot-wall chemical vapor deposition (CVD) system.

A typical hot-wall thermal CVD system is schematically shown in Fig. 3.1. A batch of substrates are placed in the reactor chamber which is kept at atmosphere pressure, low vacuum, or high vacuum depending on the type of the deposition technique. The whole chamber can be evenly heated and kept at high temperatures by the specially designed heating system (e.g. a three-zone heating system). The hot-wall system here means no intentional cooling applied to the chamber wall so that the deposition occurs on both hot substrates and hot walls. The gas precursors (source materials) are flowed into the chamber at high temperature leading to chemical reactions (e.g. pyrolysis) and deposition. The chamber is usually pumped to keep the desired pressure during the growth.

UHVCVD is invented by Bernard. S. Meyerson and co-workers at IBM T. J. Watson Research Center in mid-80s. [93] In UHVCVD system, the chamber is usually pumped at all time using a multiple pump system including turbomolecular pumps. The base pressure of the chamber is usually in the range of 1×10^{-9} torr when idling and 1×10^{-3} torr (1 mtorr) during the growth. At this ultrahigh vacuum environment, the contamination can be well controlled in a very low level. For example, the system induced background partial pressure of contaminants such as water vapor, oxygen, and hydrocarbons is limited to values in the range of 10^{-11} torr. [94] Therefore, the key source of the impurities coming from the gaseous source precursors.

Besides the excellent impurity control in epitaxial growth, UHVCVD is also invented to solve the autodoping problem, a phenomenon where doped regions existent in a substrate

transfer substantial amounts of dopant into the epitaxial layer. In traditional, Si epitaxy, the growth is carried on at high temperature, typical in excess of 1100 °C, to volatilize or dissolve native SiO_2 or carbon on the Si surface before the growth [95, 96]. In UHVCVD, ultrahigh vacuum in additional to hydrogen-assisted surface passivation allows perfectly Si epitaxy at low temperatures (e.g. 500 °C) to prevent autodoping.

Due to these superior properties of UHVCVD, it has also been used to grow a number of different materials including SiGe alloys [97, 98] not long since it was first invented. Since 1990s, Ge, has been widely studied in electronics and photonics applications, has also been successfully grown on Si using UHVCVD [99, 100]. All Ge epitaxial films discussed in this work are grown using a Sirius 300 UHVCVD manufactured by Unaxis. A picture of this UHVCVD reactor is shown in Fig. 3.2.

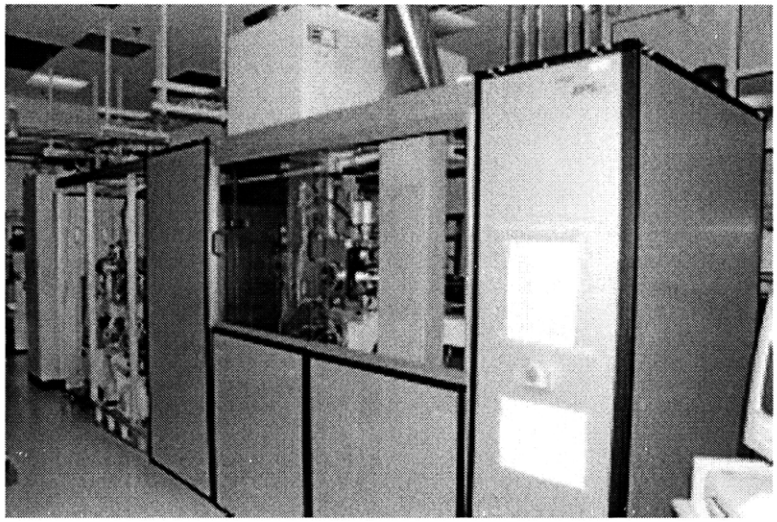

Figure 3.2: Picture of the UHVCVD reactor used in this work.

3.2 Ge Epitaxy on Si

Since the lattice constants of Si (5.431 Å) and Ge (5.658 Å) are different, hetero-epitaxial growth of Ge on Si beyond critical thickness generally results in the formation of misfit and associated threading dislocations even islanding in such 4% lattice-mismatched system. There are a number of ways to grow high quality single crystalline Ge on Si including using a graded Ge_xSi_{1-x} buffer [101, 102] or overgrowing Ge in a Si/SiO_2 template [100]. We use a two-step

growth approach [103, 99] to grow high quality Ge on Si substrate.

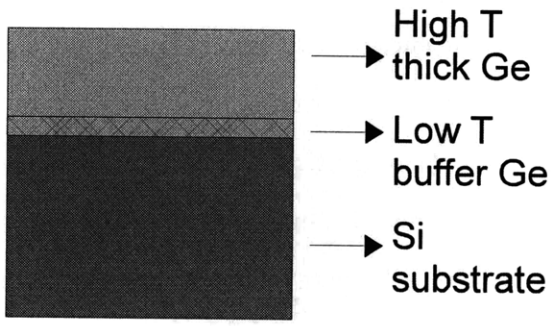

Figure 3.3: Schematic of two-step Ge epitaxial growth on Si.

The Si substrates for Ge epitaxy are first cleaned by standard RCA clean procedure followed by an additional dilute hydrofluoric acid ($HF:H_2O = 1:50$) dip to have the Si surface passivated by hydrogen and completely hydrophobic to the hydrofluoric acid (HF) solution. After the substrates are transferred into the UHVCVD chamber, they are baked at a high temperature in hydrogen (H_2) ambient to further passivate the Si surface with hydrogen atoms preparing for best epitaxy condition. This high temperature H_2 bake is not necessary for blanket film growth since the Si surface is perfectly passivated after the HF dip, while it is essential for Ge selective growth in SiO_2 trench (refer to Section 3.4.1) because the hydrophobic surface condition can no longer be achieved due to the existence of SiO_2.

Germane (GeH_4) is then flowed to the chamber to produce Ge atoms on Si substrate in a pyrolysis reaction:

$$GeH_4(g) = Ge(s) + 2H_2(g). \tag{3.1}$$

The Ge growth is accomplished in two steps. A 40-60 nm thin Ge layer is first grown on Si at 360 ^oC, a relatively low temperature. Then the temperature of the chamber are ramped to high temperatures, usually 600-750 ^oC, for fast growth rate. The as-grown Ge epitaxial film is schematically shown in Fig. 3.3.

The purpose of the low-temperature buffer layer is to prevent the Ge from island growth. From the Stranski-Krastanov (S-K) growth theory, a very thin Ge film can be epitaxially grown in Si lattice free of dislocations below a critical thickness (less than $\sim 10^1$ nm) and the

lattice mismatch induces strain in the film. The Ge film below critical thickness is too thin to be used in any applications we want to investigate, thus further growth is necessary.

Above critical thickness, the energy of the strain stored in the film becomes so much that it has to be released by two ways: the formation of misfit dislocations (a plastic process) or the modification of surface morphology that forms 3-dimensional islands. To prevent such island growth, the temperature must be sufficiently low to kinetically prohibit such process since the atoms need adequate kinetic energy moving around to form islands. Moreover, it has been shown that the hydrogen on the surface acts as surfactant at such a low temperature to dramatically hinder the nucleation of the 3-dimensional islands [104]. In practice, the misfit dislocation may start to form even before the critical thickness due to the large lattice mismatch and low temperature that prevents complete equilibrium.

Once the strain energy is fully relaxed plastically by misfit dislocation, the temperature can be raised the Ge growth on the buffer layer becomes homo-epitaxial case. A high temperature growth not only increases the growth rate to allow a thick Ge film (e.g. > 1 μm) grown in a reasonable time.

Thermal annealling is usually performed after the epitaxial growth to decrease threading dislocations which propagate to the edge of the substrate (or devices for the selective growth) faster at high annealing temperature. It has been shown the threading dislocation density in the Ge epitaxial film can be reduced by 1-2 order of magnitude to 2×10^7 cm^{-2} using a post-growth thermal annealing at 900 ^oC [105]. The threading dislocations acts as both defect centers (non-radiactive recombination centers) which degrade the electrical and optical properties of material. The threading dislocations connecting from the surface to the bottom of the film are also high conductance paths which is the major cause for the leakage current in Ge diode devices (refer to Section 5.4.1).

3.2.1 Tensile-Strain Formation

In thin film epitaxy, strain is usually formed due to the lattice mismatch between two layers. The lattice constants in Ge (5.658 Å) is larger than in Si (5.431 Å), so a Ge epitaxial film less than the critical thickness is compressive-strained. But in the two-step growth explained above, the low temperature buffer layer is beyond the critical thickness and releases the

compress strain by introducing misfit dislocations, thus the following high temperature thick Ge layer fully relaxed at the growth temperature. Once the temperature is cooled down to room temperature, both the Ge film and the Si substrate will shrink. But Ge tends to shrink more due to a larger thermal expansion coefficient than that of Si, so in-plain tensile strain is accumulated in Ge layer upon cooling.

Since Si substrate (600-700 μm) is much thicker than Ge film ($\sim$ 1 μm), the in-plain tensile strain $\epsilon_{//}$ in Ge can be calculated by

$$\epsilon_{//} = \int_{T_0}^{T_1} (\alpha_{\mathrm{Ge}} - \alpha_{\mathrm{Si}}) dT, \tag{3.2}$$

where, T_0 and T_1 are room temperature and growth temperature respectively, and $\alpha_{\mathrm{Ge}} = \alpha_{\mathrm{Ge}}(T)$ and $\alpha_{\mathrm{Si}} = \alpha_{\mathrm{Si}}(T)$ are thermal expansion coefficients of Ge and Si respectively. Thermal expansion coefficients of Si and Ge are generally functions of temperature, which can be found in Ref. [106] and [107]:

$$\alpha_{\mathrm{Ge}}(T) = 6.050 \times 10^{6} + 3.60 \times 10^{9} T - 0.35 \times 10^{-12} T^{2} (^{o}C^{-1}), \tag{3.3}$$

$$\alpha_{\mathrm{Si}}(T) = 3.725 \times 10^{-6} \times [1 - \exp(-5.88 \times 10^{-3} \times (T + 149.15))] + 5.548 \times 10^{-10} T (^{o}C^{-1}). \tag{3.4}$$

If the post-growth thermal annealing is performed, the Ge film is relaxed at the annealing temperature and more tensile-strain formed at room temperature is expected. In practice, the tensile strain Ge doesn't change much at growth temperatures or annealing temperatures above 750 and it is always a little less than the theory predicts ^{o}C [108]. This indicates the existence of a small amount of residual compressive strain that prevent Ge from further relaxing.

Various tensile strains in Ge epitaxial film can be formed at difference growth temperature (below 750 ^{o}C) without post-growth high temperature annealing. A relationship between the direct energy gaps, from the direct Γ valley to the light-hole band and to the heavy-hole band, in Ge and the tensile strain is shown in Fig. 3.4. The direct energy gaps are measured by photoreflectance (PR) and the tensile strain is calculated from the lattice constant determined by X-ray diffraction (XRD) [8]. The deformation potential at direct gap of Ge can be obtained

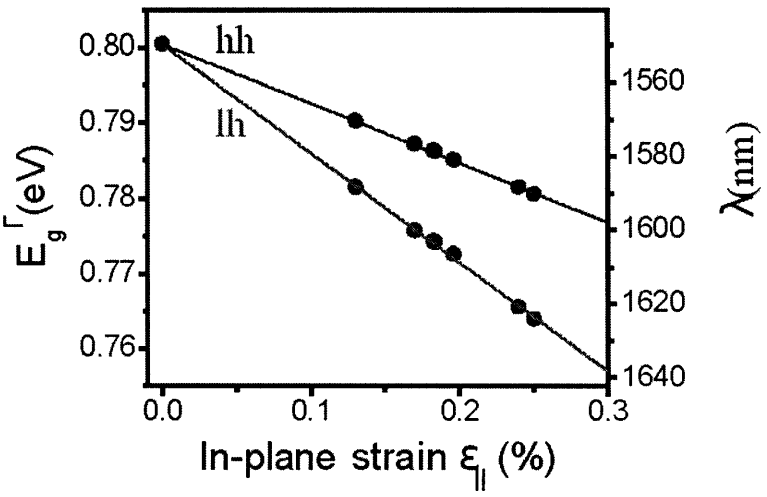

Figure 3.4: Ge direct energy gaps versus tensile strain measured by X-ray diffraction (XRD) and photoreflectance (PR) experiments. [5]

from fitting the experimental data as shown by the solid lines in the figure, and these results are used in the calculation in Section 2.1.2.

3.3 N^+Ge Epitaxy with in situ Doping

Besides tensile strain, n-type doping is essential for the realization of net gain in Ge as shown in Section 2.2, from which, we know at least 10^{19} cm^{-3} n-type doping is required for a decent net gain. There are a couple of different approaches to dope certain impurities as dopants in materials.

Since we grow Ge epitaxially on Si, it is natural to dope the Ge during the epitaxy. This approach is called in situ doping which is adopted and investigated in this work.

Another way to dope materials is ion-implantation, by which accelerated ions of impurities can be implanted into the materials. However, the crystallographic structure of the material is usually badly damaged by the high energy incident ions on impact. Although the damage can be reduced by a post-implantation thermal annealing to recrystallize the lattice, the material quality is generally worse than the case using in situ doping. A comparison of the photoluminescence from both ion-implanted and in situ doped n^+Ge, shown in Section 4.3.1 shows worse optical properties of Ge doped by using ion-implantation.

Phosphorus (P) and arsenic (As) are two commonly used n-type dopants in Si semiconductor applications. But it has been reported that arsenic is tend to segregate at SiGe surface to prevent further incorporation [109, 110]. This is because the arsenic atom has one extra valence electron compared to the silicon atom, its presence on the silicon surface terminates dangling bonds and reduces the surface energy [111]. Therefore, we choose to in situ dope phosphorus in Ge.

To in situ dope Ge with phosphorus, phosphine (PH_3) precursor gas is introduced in the second step of the Ge growth, high temperature growth step, to produce phosphorus atoms through the PH_3 dissociation reaction:

$$2PH_3(g) = 2P(s) + 3H_2(g). \tag{3.5}$$

When the growth is performed at high temperatures (600-750 °C), the epitaxy falls in gas phase mass transport limited regime as explained later. The phosphorus content in the doped Ge is supposed to increase with the PH_3 exposure controlled by the mass flow and the chamber pressure. It has been shown that in situ doping is a complicated process that may be affected by many issues such as surface poisoning effect observed for heavy level phosphorus in situ doping in Si [112]. In this section, some studies on n^+Ge epitaxy and phosphorus in situ doping at different temperatures, gas flow conditions, and pressures are investigated. A in situ doping model is built to explain the temperature dependence of the doping concentration.

3.3.1 Effect of Growth Temperature

The growth rate of both the intrinsic Ge epitaxy and the n^+Ge epitaxy versus growth temperature is shown in Fig. 3.5. At lower temperatures below 450 °C, the epitaxy rate is limited by the surface chemical reactions that produce Ge atoms on the growing surface. Thus the growth rate increases with temperature because the surface reactions are generally thermally activated.

At higher temperatures above 450 °C, the surface reaction rate becomes so high that the growth rate is limited by the number of reactant atoms supplied by the gas flow instead.

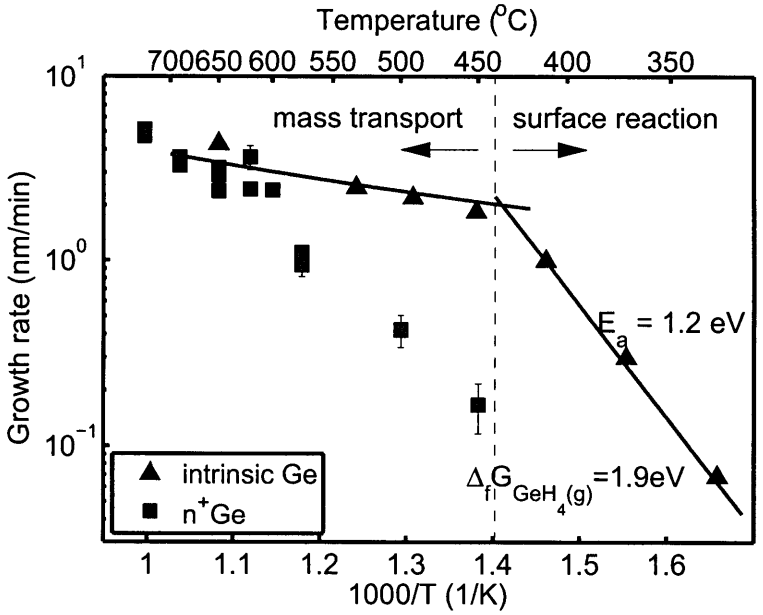

Figure 3.5: Arrhenius plot of n^+Ge epitaxial growth rate and comparison with intrinsic Ge epitaxial growth.

Thus the epitaxial growth enters the mass transport regime which is much weakly dependent on temperature. In CVD epitaxy, the mass transport regime is usually preferable because the growth is not affected by the variant of temperature at different zones of the chamber. But the growth is subsequently influenced by gas flow pattern in the mass transport regime. This issue is much less concerned in low pressure growth technique, such as UHVCVD in this work, in which the molecular flow of the gas at low gas pressure assures a relatively uniform gas flow condition.

The activation energy of the Ge epitaxial growth rate in the surface reaction limited regime can be calculated from the Arrhenius relation. The calculated activation energy of 1.2 eV is corresponding to the Gibbs free energy of dissociation reaction of GeH_4 gas on the growing surface. The Gibbs free energy of formation of GeH_4 is 1.17 eV at standard condition [113]. The free energy at growth temperature other than the $T_0 = 300$ K can be calculated using the formula derived from the definition of Gibbs free energy and the ideal gas approximation:

$$\Delta G_f = \Delta G_f^0 - \Delta C_p T(\log(T) - 1) + \Delta C_p T_0(\log(T_0) - 1), \tag{3.6}$$

where $\Delta G_f^0 = 1.17$ eV for GeH_4 and ΔC_p is the heat capacity difference of the products (Ge and H_2) and the reactant (GeH_4):

$$\Delta C_p = C_p(GeH_4) - C_p(Ge) - 2C_p(H_2).$$

The heat capacities $C_p(GeH_4) = 45.02$ J/K/mol, $C_p(Ge) = 23.3$ J/K/mol, and $C_p(H_2) = 28.84$ J/K/mol can be found in Ref [113]. By substituting these data to the Eq. 3.6, $\Delta G_f = 1.9$ eV is calculated at 350 ^{o}C. A positive ΔG_f indicates the formation reaction is not thermodynamically favorable meaning the opposite reaction, the dissociation reaction is favorable. The formation Gibbs free energy ΔG_f is the activation energy of the dissociation reaction since the reaction constant K_d of this dissociation reaction is

$$K_d = K_{d0}\exp(-\frac{\Delta G_d}{k_B T}) = K_{d0}\exp(-\frac{-\Delta G_f}{k_B T}) = K_{d0}\exp(\frac{\Delta G_f}{k_B T}). \tag{3.7}$$

The calculated activation energy of 1.9 eV is larger than the fitted activated energy from the experimental growth rate data because the dissociation reaction occurring near or on the growth surface changes the reactants and products Gibbs free energies documented for gas phase reaction.

At temperatures above 450 ^{o}C, the growth enters gas phase mass transport limited regime. The growth rate weekly depends on temperature in this regime. The dependence on growth rate can be approximately estimated by

$$g \propto T^{1.5}. \tag{3.8}$$

The blue solid curve in Fig. 3.5 represents this relation which agrees well with the intrinsic growth rate data.

It can be seen that both intrinsic Ge and n^+Ge have a similar growth rate above 600 ^{o}C, but the growth rate of the n^+Ge is much lower than that of the intrinsic Ge between 450 ^{o}C and 600 ^{o}C. The growth rate reduction is a result of the surface poisoning effect that the available epitaxial growth sites on the growth surface are occupied by other molecules. It has been shown, in phosphorus in situ doped Si epitaxy, the dominant cause of the dramatic

reduction of the Si epitaxy rate is the adsorption of PH_3 and phosphorus on the surface [14,9]. This effect has been found so severe that even a very small amount of PH_3 flow extensively slows down Si epitaxy rate.

The adsorption behavior of a certain type of substance is usually analyzed by a sticking coefficient which describes the ratio of the number of adsorbate atoms (or molecules) that adsorb to a surface to the total number of atoms that impinge upon that surface during the same period of time. The sticking coefficient of PH_3 on Si surface is measured to be 40 times larger than that of SiH_4 on Si surface. The sticking coefficient of PH_3 on Ge surface can be estimated by comparing the growth rates of the two kinds of growths. At 450 ^oC, the growth rate is reduced by about 10 times when the PH_3 is introduced, thus the sticking coefficient of PH_3 is about 10 times larger than that of GeH_4 on Ge surface.

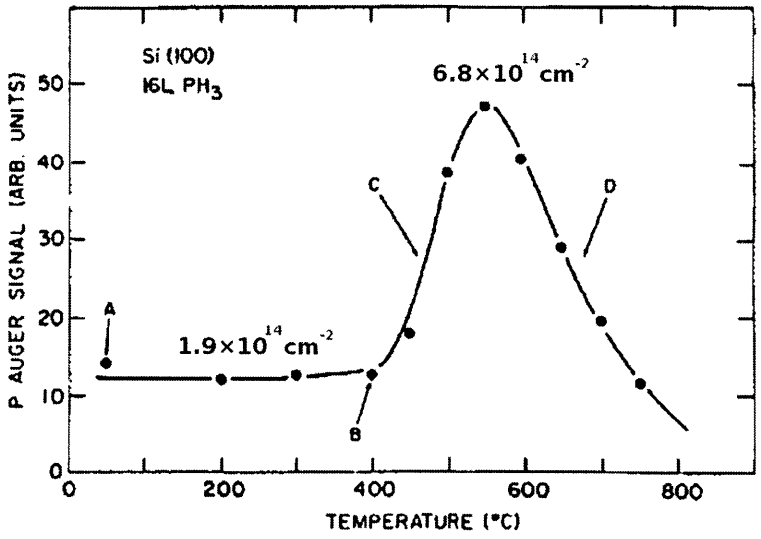

Figure 3.6: The saturated phosphorus coverage on Si (100) surface measured by *LMM* phosphorus Auger line after exposing the Si surface to PH_3 at various temperatures. (After Yu et al. [9])

The difference between the growth rates of n^+Ge and intrinsic Ge becomes less with temperature above 450 ^oC because the adsorbed PH_3 starts to desorb from the surface. After most of the PH_3 (including dissociated PH_3 on the surface) evaporated from the surface above 600 ^oC, the growth rate becomes equal for both cases. This conclusion is based on the study of the adsorption behavior of PH_3 on Si stated below.

This surface poisoning effect of PH_3 on Si (100) surface has been investigated using Auger electron spectroscopy (AES), low energy electron diffraction (LEED), X-ray photoemission (XPS), and mass spectrometer thermal desorption (TDS) equipped in a ultrahigh vacuum (UHV) chamber [9]. Fig. 3.6 shows the saturated phosphorus coverage on Si (100) surface obtained from this work. The phosphorus count is measured by LMM phosphorus Auger line after exposing the Si surface to PH_3 at various temperatures. Combined with some other measured results from XPS and TDS, Yu et al found the adsorbed phosphorus signal between room temperature and 200 °C is from the non-dissociated PH_3. The adsorbed PH_3 becomes dissociated between 200 °C and 400 °C while the coverage of phosphorus does not change. Above 400 °C, hydrogen starts to desorb from the surface and more phosphorus occupies the empty site left by hydrogen subsequently thus the coverage of phosphorus increases. Above 580 °C phosphorus itself starts to thermally desorb from the surface thus the coverage dramatically decreases.

The behavior of the PH_3 (and its dissociated products) adsorption on Si in this study explains the phenomenon in the temperature dependence of n^+Ge growth. Since Si and Ge has similar crystalline structure and chemical properties, we believe it is the same effect that causes the reduction of the n^+Ge growth rate.

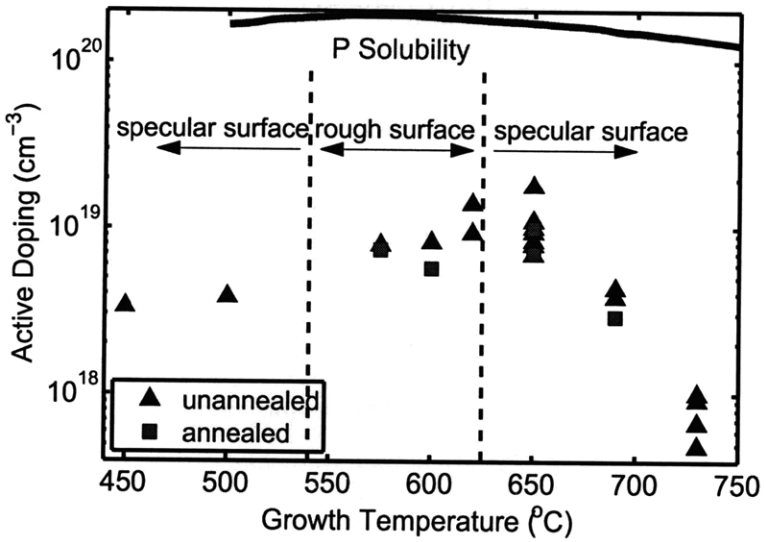

Figure 3.7: The active doping concentrations of the n^+Ge grown at different temperatures. The equilibrium solubility of phosphorus in Ge is also shown in magenta for comparison.

High quality intrinsic Ge can be grown in a wide range of temperatures above 450 ^{o}C as shown in Fig. 3.5. However, in order to obtain high doping concentration of phosphorus, the temperature dependence of the doping concentration is studied. All doping concentrations used in this thesis are active doping concentrations. The free carrier sheet density of the Ge films are measured by Hall effect using the Van der Pauw approach. The free carrier volume density which is equal to the active doping concentration can be calculated from the sheet density and the film thickness. The Ge film thickness is measured by using a selective etch approach. To measure the thickness of a Ge film, part of the film surface was covered by melting wax. After the wax cooled and solidified, the Ge film was submerged in hydrogen peroxide (H_2O_2) solution and the exposed Ge area was etched at a rate about 1 nm/s. H_2O_2 does not react with the Si substrate underneath the Ge film. After etching, the covered wax was heated and wiped away and the residual wax was cleaned by acetone. This selective etch leaves a step from the Ge surface (covered by the wax earlier) to the Si surface (exposed earlier). This step was measured by a Tencor P-10 Surface Profilometer. Since the films are not perfectly uniform, a number of thickness measurements are performed at different locations. The average and the standard deviation is calculated and used in the thesis.

The active doping concentrations of the n^+Ge epitaxial films versus growth temperature is shown in Fig. 3.7. Most of the growths are done with the following recipe parameters: 3.8 sccm GeH_4 flow, 12.0 sccm PH_3 flow, 16% throttle valve opening of the exhaust line which keeps a base pressure of 10 mtorr during the growth. It can be seen that the doping concentrations at all growth temperatures are at least one order of magnitude less than the equilibrium solubility of phosphorus in Ge also shown in the figure. In order to study the activation of the dopants, post thermal annealing is performed after the epitaxy. To prevent the out-diffusion of phosphorus into air, a 1 μm thick SiO_2 cap layer is deposited at 400 ^{o}C by using an Applied Materials Centura 5200 plasma enhanced chemical vapor deposition (PECVD) system. Two types of post annealing are used: thermal annealing in a UHVCVD tube with H_2 ambient at 780 ^{o}C for 30 mins and rapid thermal annealing (RTA) by using a Heatpulse 410 RTA furnace with N_2 ambient at 780 ^{o}C for 30-60s. Both annealing approaches give similar results which are shown in Fig. 3.7 with red square. It can be seen there is no appreciable change in active doping concentration after thermal annealing underlying the

complete activation of the dopants.

The doping level incorporated in the Ge films decreases at both high temperatures and low temperatures. At high temperatures, the thermal desorption of the absorbed phosphorus atoms is faster than that of the absorbed Ge atoms leading to less molar fraction of phosphorus on the growing surface. At low temperatures, the dissociation of adsorbed PH_3 molecules on the surface is slow.

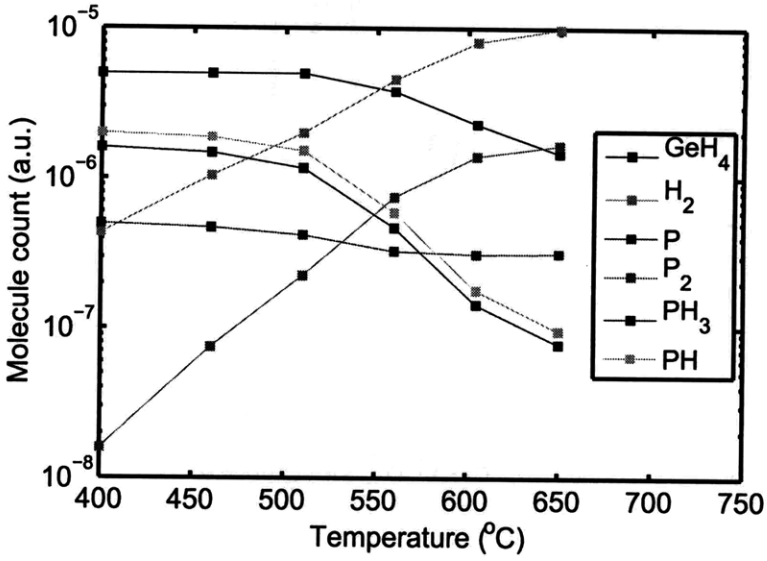

Figure 3.8: The gas chemicals in the UHVCVD reactor chamber at different temperatures under constant GeH_4 and PH_3 gas flows.

The dissociation of the PH_3 in the gas phase can be investigated by the residual gas analyzer (RGA), a small mass spectrometer typically designed for process control and contamination monitoring, equipped with the UHVCVD reactor. The relative count of chemical molecules in the reactor chamber measured by the RGA at different temperatures is shown in Fig. 3.8. The GeH_4 and PH_3 gas flows are 3.8 sccm and 12.0 sccm respectively and are kept constant at each temperature. The PH_3 and the $PH_x(x = 1, 2)$ molecules start to dissociate massively at about 500 °C and the product is mainly P_2 which increases dramatically with temperature. The phosphorus, on the other hand, does not change much at all temperatures. The GeH_4 molecules start to dissociate massively above 550 °C, and as a result of the dissociation of GeH_4 and PH_3, the H_2 molecules increase dramatically at elevated temperatures. The behavior of PH_3 dissociation at different temperature is considered in the in situ doping

modeling work in Section 3.3.3.

3.3.2 Effect of Gas Flow and Pressure

The gas flow and base pressure in the chamber during the growth are two other factors which can influence the epitaxy rate and doping concentrations.

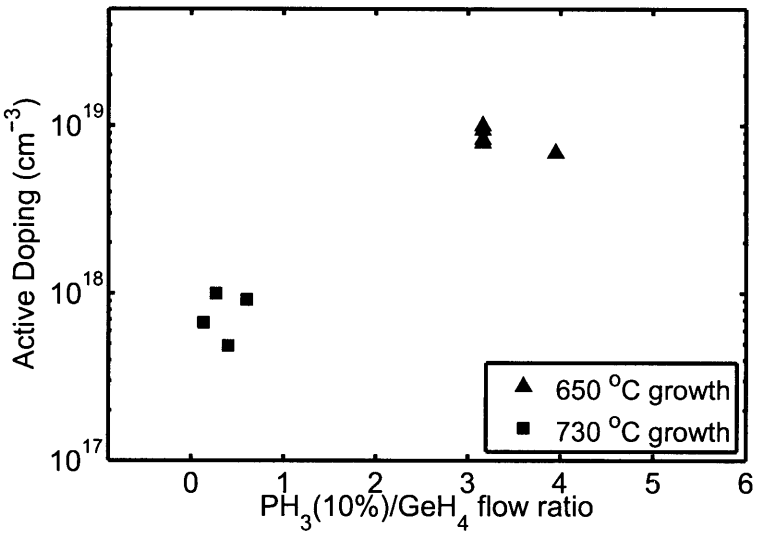

Figure 3.9: The active doping concentrations in n^+Ge grown with different PH_3 to GeH_4 gas flow ratios at growth temperatures of 650 °C and 730 °C respectively.

The ratio of PH_3 gas flow to GeH_4 gas flow is expected to affect the phosphorus doping concentration. Fig. 3.9 shows the active doping concentrations in n^+Ge grown with different PH_3 (15% diluted by He) to GeH_4 gas flow ratios at two growth temperatures: 650 °C and 730 °C, respectively. It can be seen that, at a given temperature, the doping concentration does not change much with the gas flow ratio. This phenomenon indicates that the partial pressure of PH_3 in the chamber is sufficiently high for the saturated doping concentration at the given temperature. Thus the mass flow is not the limiting factor of the doping concentration. The fact that the phosphorus doping concentration achieved is less than the phosphorus solubility in Ge must a result of other reasons such as surface reaction and kinetics.

The chamber pressure is determined by the turbo-molecular pump pumping rate which is controlled by the throttle valve opening at the end of the chamber. The pumping rates of different molecules are different resulting from the different molecular weights. The heavier

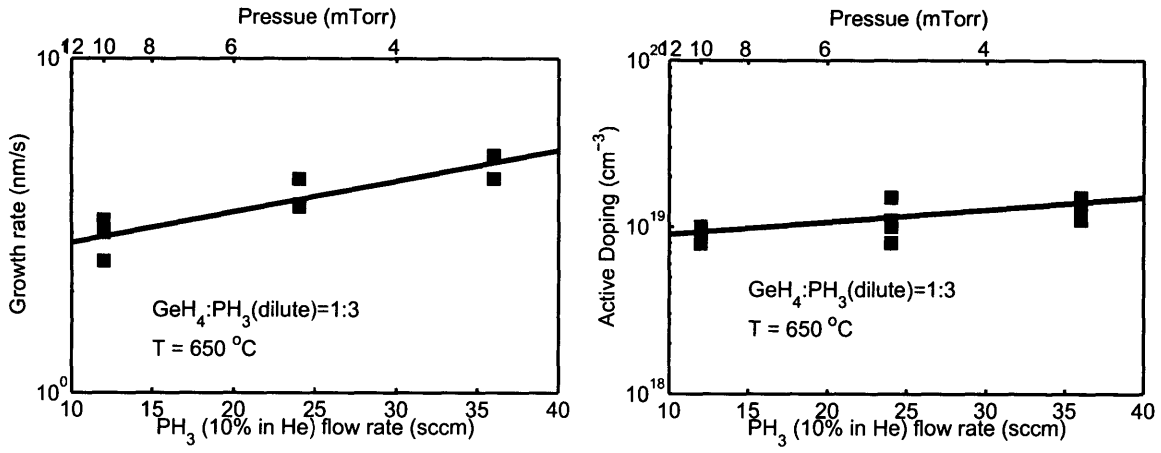

Figure 3.10: The PH_3 gas flow dependence of (a) growth rate and (b) doping concentration. The growth temperature is 650 °C and the PH_3 to GeH_4 gas flow ratio is 3:1 for all these growths.

GeH_4 gas is pumped faster than lighter PH_3 gas. The throttle valve is opened wider in order to pump GeH_4 faster than PH_3 aiming for more phosphorus incorporation in the Ge epitaxial films. As a result, the chamber pressure decreases thus the total flow rates of both gases are increased by the same ratio for compensation in order to maintain the same growth rate following the equation of the deposition rate r_{dep} in the mass flow limited regime:

$$r_{\text{dep}} \propto n \cdot \text{flow} \propto p \cdot \text{flow} \quad \text{(for ideal gas)}, \tag{3.9}$$

where n is the molar density and p is the partial pressure of the gas.

The results are shown in Fig 3.10. The reduction of chamber pressure thereby increasing the extraction rate of the GeH_4 gas compared to that of the PH_3 gas slightly increases the doping concentration in Ge. But this effect is too weak to be used to effectively increase the phosphorus doping.

In mass transport limited regime, Gas flow affects growth characteristics. Gas flow is affected by a number of geometric conditions including substrate size and position. The influence of the substrate size and the substrate position in the chamber on growth rate and doping concentration is shown in Fig. 3.11. These data are from two separate growths with five 6" wafers and seven 1" pieces, respectively. The growth temperature is 650 °C, the PH_3

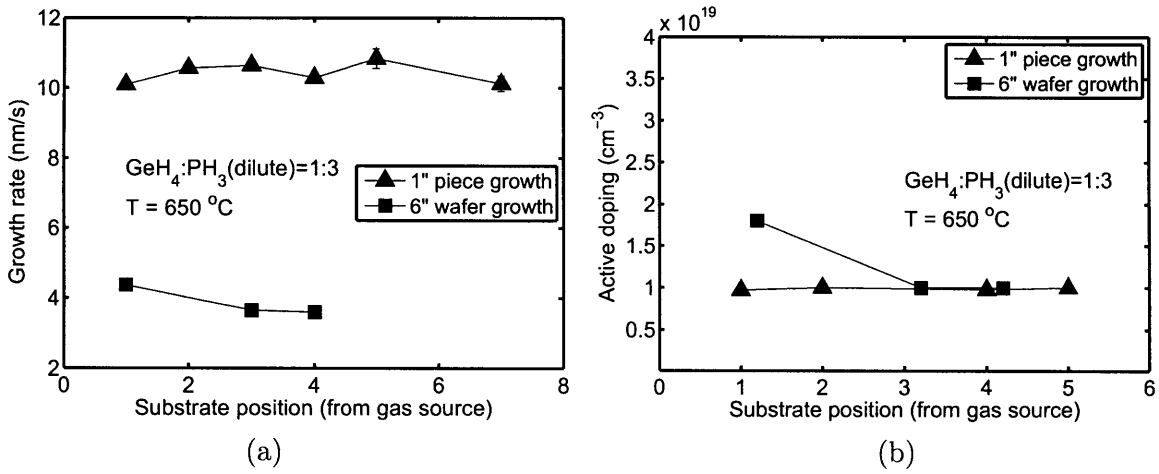

Figure 3.11: The substrate size and position dependence of (a) growth rate and (b) doping concentration. The growth temperature is 650 ^{o}C and the PH_3 to GeH_4 gas flow ratio is 3:1 for all these growths.

to GeH_4 gas flow ratio is 3:1, and the base pressure is 10 mtorr for both growths. It can be seen that the growth rate of the 1" pieces is nearly three times higher underlying a loading effect which states that the geometry of the wafers affects the chemicals exposure thereby the growth rate. On the other hand, no appreciable change has been found for the phosphorus doping concentration in both growths. The small variation of the growth rates and the doping concentrations of the substrates at different positions show the flow uniformity between the substrates.

3.3.3 Modeling of in situ Doping

A theoretical modeling is helpful to understand the in situ doping process and investigate the approach to increase the doping concentrations. In this section, we try to build a model to describe the phosphorus doping process during the Ge epitaxy.

This work is followed the same approach which is used by Reif and co-workers to study the arsenide doping in Si epitaxy [15, 16]. This approach, which is especially appropriate for a relatively small sticking coefficient of the dopant precursor (e.g. AsH_3) on the growth surface (e.g. Si surface) is a good model to study PH_3 assisted in situ doping on Ge surface since we estimate a similar sticking coefficient of PH_3 as that of GeH_4 in Section 3.3.1. On the other hand, phosphorus in situ doping in Si is a more complicated problem since PH_3 has

a much larger (40 times) sticking coefficient than that of SiH_4 as we mention before [114].

Following the same idea in Reif's work, we divide the doping process into 8 steps including mass transport and reaction in the gas stream and on the growing surface. A terrace-ledge-kink model is used for the processes on the growing surface. The description of each step is listed below:

1. Mass transport of dopant precursor gas (PH_3) from the reactor enhance to the deposition region.

2. Boundary layer mass transport of PH_3 from the main gas stream through the boundary layer to the growing surface.

3. Gas phase chemical reaction: PH_3 may dissociate into several different P-containing species at elevated temperatures. From the residual gas analysis (Fig. 3.8) in Section 3.3.1, the production is dominated by PH and H_2 at lower temperatures ($< 550^oC$) and P_2 and H_2 at higher temperatures ($> 550^oC$).

4. Adsorption of P-containing species at an adsorption site on the growing surface.

5. Chemical dissociation into P and H in the adsorbed layer.

6. Surface diffusion and incorporation of the adsorbed P at step and kink sites on the growing surface.

7. "Burying" of the incorporated P by subsequently arriving Ge atoms during the epitaxy.

8. Desorption of H from the surface.

The mass balance equations governing these steps at steady-state are:

1. Mass balance of PH_3 in the main gas stream within the deposition region:

$$0 = N_{300} v (X^i_{PH_3} - \bar{X}_{PH_3}) - k_m (\bar{X}_{PH_3} - X^s_{PH_3}) \tag{3.10}$$

$$= \frac{(X^i_{PH_3} - \bar{X}_{PH_3})}{R_1} - \frac{(\bar{X}_{PH_3} - X^s_{PH_3})}{R_2}, \tag{3.11}$$

where,

$$\frac{1}{R_1} = N_{300}v, \text{and } \frac{1}{R_2} = k_m. \tag{3.12}$$

2. Mass balance of PH_3 just above the gas-solid interface: For the PH reaction dominated at low temperatures:

$$0 = k_m(\bar{X}_{PH_3} - X^s_{PH_3}) - (k_{f3}X^s_{PH_3} - k_{r3}X^s_{PH}P_{H_2}) - (k_{f4}X^s_{PH_3}P\theta - k_{r4}\theta_{PH_3}) \tag{3.13}$$

$$= \frac{(\bar{X}_{PH_3} - X^s_{PH_3})}{R_2} - \frac{X^s_{PH_3} - X^s_{PH}P_{H_2}/K_3}{R_3} - \frac{X^s_{PH_3} - \theta_{PH_3}/(K_4P\theta)}{R_4}, \tag{3.14}$$

where,

$$\frac{1}{R_3} = k_{f3}, \text{and } \frac{1}{R_4} = k_{f4}P\theta. \tag{3.15}$$

For the P_2 reaction dominated at high temperatures:

$$0 = k_m(\bar{X}_{PH_3} - X^s_{PH_3}) - (k_{f3}X^s_{PH_3}P^{1/2} - k_{r3}X^{s\ 1/2}_{P_2}P^{3/2}_{H_2}) - (k_{f4}X^s_{PH_3}P\theta - k_{r4}\theta_{PH_3}) \tag{3.16}$$

$$= \frac{(\bar{X}_{PH_3} - X^s_{PH_3})}{R_2} - \frac{X^s_{PH_3} - X^{s\ 1/2}_{P_2}P^{3/2}_{H_2}/(K_3P^{1/2})}{R_3} - \frac{X^s_{PH_3} - \theta_{PH_3}/(K_4P\theta)}{R_4}, \tag{3.17}$$

where

$$\frac{1}{R_3} = k_{f3}P^{1/2}, \text{and } \frac{1}{R_4} = k_{f4}P\theta. \tag{3.18}$$

3. Mass balance of PH_3 adsorbed on the surface:

$$0 = (k_{f4}X^s_{PH_3}\theta - k_{r4}\theta_{PH_3}) - (k_{f5}\theta_{PH_3}\theta^3 - k_{r5}\theta_P\theta_H{}^3) \tag{3.19}$$

$$= \frac{X^s_{PH_3} - \theta_{PH_3}/(K_4P\theta)}{R_4} - \frac{\theta_{PH_3}/(K_4P\theta) - \theta_P\theta_H{}^3/(K_4K_5P\theta^4)}{R_5}, \tag{3.20}$$

where,

$$\frac{1}{R_5} = K_4k_{f5}P\theta^4. \tag{3.21}$$

4. Mass balance of P adsorbed on the surface:

For PH reaction:

$$0 = (k_{f5}\theta_{\mathrm{PH_3}}\theta^3 - k_{r5}\theta_P{\theta_H}^3) + (k_{f5'}\theta_{\mathrm{PH}}\theta - k_{r5'}\theta_{\mathrm{P}}\theta_{\mathrm{H}}) - (f_{f6}\theta_{\mathrm{P}} - k_{r6}\theta_{\mathrm{P}}^i N_s^i\theta) \quad (3.22)$$

$$= \frac{\frac{\theta_{\mathrm{PH_3}}}{(K_4P\theta)} - \frac{\theta_{\mathrm{P}}{\theta_{\mathrm{H}}}^3}{K_4K_5P\theta^4}}{R_5} + \frac{\frac{K_{5'}{\theta_{\mathrm{H}}}^2\theta_{\mathrm{PH}}}{K_4K_5P\theta^3} - \frac{\theta_{\mathrm{P}}{\theta_{\mathrm{H}}}^3}{K_4K_5P\theta^4}}{R_{5'}} - \frac{\frac{\theta_{\mathrm{P}}{\theta_{\mathrm{H}}}^3}{K_4K_5P\theta^4} - \frac{{\theta_{\mathrm{H}}}^3\theta_{\mathrm{P}}^i N_s^i}{K_4K_5K_6P\theta^3}}{R_6} \quad (3.23)$$

where,

$$\frac{1}{R_{5'}} = \frac{k_{r5'}K_4K_5P\theta^4}{{\theta_{\mathrm{H}}}^2}, \text{and } \frac{1}{R_6} = \frac{k_{f6}K_4K_5P\theta^4}{{\theta_H}^3}. \quad (3.24)$$

For P_2 reaction:

$$0 = (k_{f5}\theta_{\mathrm{PH_3}}\theta^3 - k_{r5}\theta_P{\theta_H}^3) + (k_{f5'}\theta_{\mathrm{P_2}}\theta^2 - k_{r5'}{\theta_{\mathrm{P}}}^2) - (f_{f6}\theta_{\mathrm{P}} - k_{r6}\theta_{\mathrm{P}}^i N_s^i\theta) \quad (3.25)$$

$$= \frac{\frac{\theta_{\mathrm{PH_3}}}{(K_4P\theta)} - \frac{\theta_{\mathrm{P}}{\theta_{\mathrm{H}}}^3}{K_4K_5P\theta^4}}{R_5} + \frac{\frac{K_{5'}{\theta_{\mathrm{H}}}^3\theta_{\mathrm{P_2}}}{K_4K_5P\theta^2\theta_{\mathrm{P}}} - \frac{\theta_{\mathrm{P}}{\theta_{\mathrm{H}}}^3}{K_4K_5P\theta^4}}{R_{5'}} - \frac{\frac{\theta_{\mathrm{P}}{\theta_{\mathrm{H}}}^3}{K_4K_5P\theta^4} - \frac{{\theta_{\mathrm{H}}}^3\theta_{\mathrm{P}}^i N_s^i}{K_4K_5K_6P\theta^3}}{R_6}, \quad (3.26)$$

where,

$$\frac{1}{R_{5'}} = \frac{k_{r5'}K_4K_5P\theta^4\theta_{\mathrm{P}}}{{\theta_{\mathrm{H}}}^3}. \quad (3.27)$$

5. Mass balance of P atoms occupying incorporation sites:

$$0 = (f_{f6}\theta_{\mathrm{P}} - k_{r6}\theta_{\mathrm{P}}^i N_s^i\theta) - (g\theta_{\mathrm{P}}^i N_s^i\frac{K_7}{k_{\mathrm{H}}}) \quad (3.28)$$

$$= \frac{\frac{\theta_{\mathrm{P}}{\theta_{\mathrm{H}}}^3}{K_4K_5P\theta^4} - \frac{{\theta_{\mathrm{H}}}^3\theta_{\mathrm{P}}^i N_s^i}{K_4K_5K_6P\theta^3}}{R_6} - \frac{\frac{{\theta_{\mathrm{H}}}^3\theta_{\mathrm{P}}^i N_s^i}{K_4K_5K_6P\theta^3}}{R_7}, \quad (3.29)$$

where,

$$\frac{1}{R_7} = \frac{gK_4K_5K_6K_7P\theta^3}{k_H\theta_{\mathrm{H}}^3}. \quad (3.30)$$

6. Mass balance of PH (or P_2) just above the gas-solid interface:

$$(k_{f3}X_{\mathrm{PH3}}^s - k_{r3}X_{\mathrm{PH}}P_{\mathrm{H_2}}) - (k_{f4'}^s\theta - k_{r4'}\theta_{PH}) = 0 \quad (3.31)$$

7. Mass balance of PH (or P_2) adsorbed on the surface:

$$(k_{f4'}^s\theta - k_{r4'}\theta_{PH}) - (k_{f5'}\theta_{\mathrm{PH}}\theta - k_{r5'}\theta_{\mathrm{P}}{\theta_{\mathrm{H}}}^2) = 0 \quad (3.32)$$

The reactions used in these processes are:

- Chemical dissociation of PH_3 into PH:

$$PH_3(g) \rightleftharpoons PH(g) + H_2, \qquad K_3 = \frac{k_{f3}}{k_{r3}}. \tag{3.33}$$

- Chemical dissociation of PH_3 into P_2:

$$PH_3(g) \rightleftharpoons \frac{1}{2}P_2(g) + \frac{3}{2}H_2, \qquad K_3 = \frac{k_{f3}}{k_{r3}}. \tag{3.34}$$

- Adsorption of PH_3 on the surface:

$$PH_3(g) + s \rightleftharpoons PH_3\text{-}s, \qquad K_4 = \frac{k_{f4}}{k_{r4}}. \tag{3.35}$$

- Adsorption of PH on the surface:

$$PH(g) + s \rightleftharpoons PH\text{-}s, \qquad K_{4'} = \frac{k_{f4'}}{k_{r4'}}. \tag{3.36}$$

- Adsorption of P_2 on the surface:

$$P_2(g) + 2s \rightleftharpoons P_2\text{-}s, \qquad K_{4'} = \frac{k_{f4'}}{k_{r4'}}. \tag{3.37}$$

- Chemical dissociation of PH_3 in the adsorbed layer:

$$PH_3\text{-}s + 3s \rightleftharpoons P\text{-}s + 3H\text{-}s, \qquad K_5 = \frac{k_{f5}}{k_{r5}} \tag{3.38}$$

- Chemical dissociation of PH in the adsorbed layer:

$$PH\text{-}s + s \rightleftharpoons P\text{-}s + H\text{-}s, \qquad K_{5'} = \frac{k_{f5'}}{k_{r5'}} \tag{3.39}$$

- Chemical dissociation of P_2 in the adsorbed layer:

$$P_2\text{-}s + 2s \rightleftharpoons 2P\text{-}s, \qquad K_{5'} = \frac{k_{f5'}}{k_{r5'}} \tag{3.40}$$

- Incorporation of adsorbed P into step or kink sites on the surface:

$$P\text{-}s + s^i \rightleftharpoons P\text{-}s^i + s + s^i, \qquad K_6 = \frac{k_{f6}}{k_{r6}} \tag{3.41}$$

- Burying of P at incorporation sites:

$$P\text{-}s^i + s^i \rightleftharpoons P(ss) + s^i, \qquad K_7 = \frac{\alpha_P}{\theta_P^i N_s^i} = \frac{k_H N_P}{\theta_P^i N_s^i} \tag{3.42}$$

The math symbols used in all the equations above are:

symbols	descriptions
N_{300}	total gas-phase molecular concentration at 300 K. (cm^{-3})
v	carrier gas velocity at 300 K. (cm/s)
$X^i_{PH_3}$	PH_3 molar fraction in the main gas upstream of the deposition region.
$\bar{X}_{PH_3}$	average molar fraction of PH_3 in the main gas stream within the deposition region.
$X^s_{PH_3}$	PH_3 molar fraction just above the gas-solid interface.
k_m	boundary layer mass transport coefficient of PH_3 in the carrier gas.
P	base pressure in the deposition region.
P_x	partial pressure of x molecule in the gas.
θ	fraction of adsorption sites which are vacant.
θ_x	fraction of adsorption sites occupied by x molecule.
θ^i_P	fraction of incorporation sites occupied by P.
N^i_s	surface density of incorporation sites.
g	epitaxial growth rate.
α_P	activity of P in the solid solution.
k_H	Henry's constant.

By solving these linear equations, we can obtain the expression of phosphorus doping

concentrations. After some mathematical manipulation, the result can be written as:

$$N_{\mathrm{P}} = \frac{R^{-1}}{g + R^{-1}\frac{k_H}{K_p}} X^i_{\mathrm{PH_3}}, \tag{3.43}$$

where,

$$R = R_1 + R_2 + \frac{(R_4 + R_5)(R_3 + R_{4'} + R_{5'})}{R_3 + R_4 + R_{4'} + R_5 + R_{5'}} + R_6, \tag{3.44}$$

$$K_p = K_4 K_5 K_6 K_7 P \frac{\theta^3}{{\theta_{\mathrm{H}}}^3}. \tag{3.45}$$

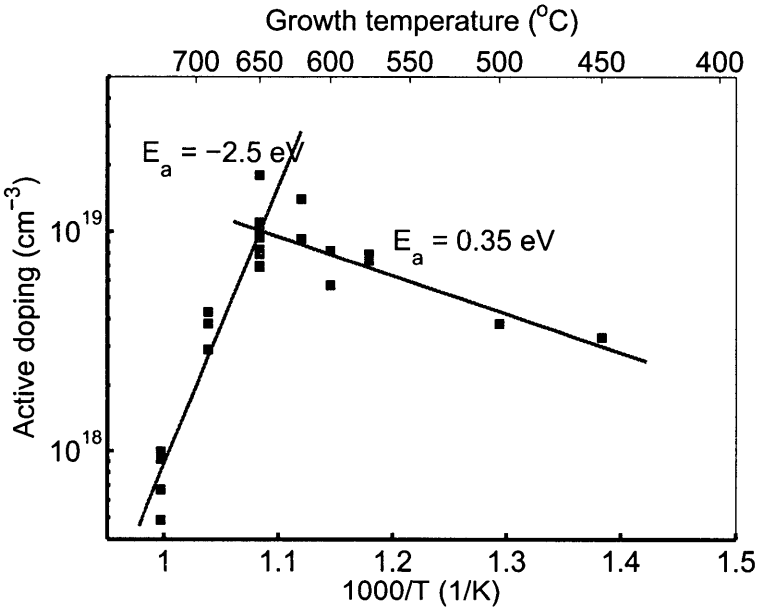

Figure 3.12: Arrhenius plot of in situ phosphorus doping concentration in Ge epitaxial films.

The doping concentrations is a complicated function depending on many variables, to apply Eq. 3.43 for analyzing the experimental results, we need to consider the controlling mechanism at a certain condition that limits the doping process.

At higher growth rate, that doping concentration is limited by the slowest process (controlling mechanism), i.e. one of $R_j (j = 1, 2, \cdots, 7)$ dominates R. At lower temperature, the doping concentration is primarily limited by the gas phase chemical reaction at the gas-solid interface region (R_3), and the PH is the major product at this temperature as shown in the

residual gas study (Fig. 3.8), thus the doping concentration is

$$N_{\mathrm{P}} \simeq \frac{k_{f3}}{g} X^{i}_{\mathrm{PH_3}}. \tag{3.46}$$

k_{f3} causes Arrhenius temperature dependence on the doping concentration shown in Fig. 3.12. The activation energy fitted from the Arrhenius plot is 0.35 eV. This activation energy is related to the formation energy of PH_3 through the reaction

$$\mathrm{PH_3}(g) \rightleftharpoons \mathrm{PH}(g) + \mathrm{H_2}.$$

Due to the lack of data of PH gas, this formation energy is not calculated here. The formation energy of PH_3 through the reaction

$$\mathrm{PH_3}(g) \rightleftharpoons \mathrm{P}(g) + \frac{3}{2}\mathrm{H_2}$$

is 0.14 eV which can be a rough estimation for the order of magnitude of this activation energy.

At higher temperatures, the most likely controlling mechanism limiting the doping concentration is the phosphorus containing species desorption process (R_4 and/or $R_{4'}$). The doping concentration controlled by this mechanism is given by

$$N_{\mathrm{P}} \simeq \frac{k_{f4'} K_3 \theta}{g} X^{i}_{\mathrm{PH_3}}. \tag{3.47}$$

In this process, phosphorus containing species desorb faster at higher temperatures explaining the behavior in high temperature region of Fig. 3.12. The fitted activation energy -2.5 eV is the desorption activation energy.

Besides the influence of growth temperature, the phosphorus doping concentration in Ge also depends on other growth parameters. These dependences are summarized in Table 3.1. It can be seen that the temperature dependence of doping can be well explained by the model. However, the experimental results disagree with the model prediction for other growth condition dependences.

Dependence	Model Prediction	Growth Condition	Experiments
temperature	low T: T ⇑, doping ⇑ High T: T ⇓, doping ⇑	growth T	match prediction
PH_3 pressure	$P(PH_3)$ ⇑, doping ⇑	PH_3/GeH_4 ratio (0.02-0.47)	doping: no change
growth rate	growth ⇓, doping ⇑	total flow (4sccm, 8.5sccm)	doping: no change
H_2 pressure	$P(H_2)$ ⇓, doping ⇑	H_2 flow	doping: no change

Table 3.1: Growth condition dependence of active doping concentration in Ge predicted by the model and investigated by the experiments.

Based on the model, the phosphorus doping concentration is proportional to the molar fraction of partial pressure of the dopant precursor X_P^i. According to the experimental results, there is no appreciable change in the active doping concentration with the PH_3 partial pressure even at a very large PH_3 to GeH_4 gas flow ratio (0.02-0.47), which can be seen in Fig. 3.9.

The model predicts that the phosphorus doping concentration increases with the decrease of epitaxial growth rate as shown in Eq. 3.43, which can be explained by the dopant incorporation and burying processes described the model. The rate at which the incorporated phosphorus atoms are covered by subsequently arriving Ge atoms is given by $r = g \cdot N_P$. This rate is balanced with other rates that cause the change of the surface density of the incorporated phosphorus at steady state, therefore, a faster growth rate results in less doping incorporation as all other conditions remain the same. The growth rate is controlled by the GeH_4 gas flow in the mass flow limited regime. We increased the total gas flow of GeH_4 and PH_3 but keep the their ratio the same to investigate the effect of growth rate. However, the active doping concentration does not change accordingly.

The phosphorus doping concentration is also a function of H_2 partial pressure predicted by the model, whereas a simple study in which the H_2 gas was flowed during the growth disagrees with this prediction again.

Since this in situ doping model has been adopted to successfully explain the doping characteristics in Si epitaxy [116], the deviation of the experimental results from the model predictions indicates the partial activation of dopants in Ge. Since all the as-grown epitaxial Ge films are subjected to post-growth rapid thermal annealing (RTA) at 780 ^oC to activate the dopants, the mechanism of partial activation is a compensation effect at equilibrium. It

has been shown that the vacancy-group-V-impurity atom pairs (E centers) is served as p-type dopants so as to compensate the n-type doping formation in Ge [117]. A secondary ion mass spectrometry (SIMS) experiment which can determine the total doping concentration in Ge helps the future investigation on this compensation mechanism.

3.4 Ge Device Fabrication

Making a light emitter out of Ge requires to fabricate the Ge epitaxial film to some devices. In addition, in order to study some characteristics of the tensile-strained n^+Ge, fabricated devices other than blanket films are necessary. For example, a light emitting diode (LED) is fabricated to study electroluminescence (EL) in Chapter 5 and a mesa structure is fabricated to study optical gain in Chapter 6. Two approaches are used in this work to fabricate a Ge device: selective growth and dry etching which are discussed in the following two sections.

3.4.1 Ge Selective Growth

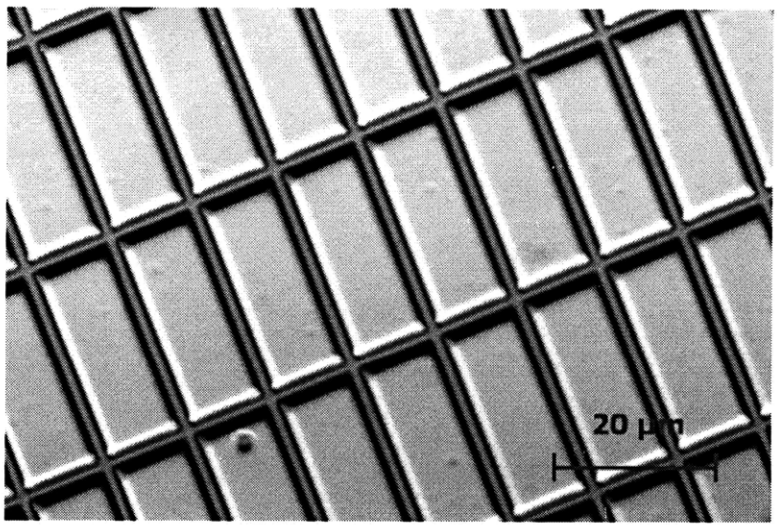

Figure 3.13: Microscopic image of Ge mesas selectively grown on SiO_2 patterned Si.

Since pure Ge is barely deposited on silicon oxide (SiO_2) surface, we can use SiO_2 masked Si substrate to have Ge selectively grown in the exposed Si areas, which is called Ge selective growth. A thin layer (e.g. 200 nm) of thermal SiO_2 is first deposited on Si substrate, followed by a lithography patterning and etching to etch away certain areas of oxide and expose the

underlying Si substrate. The oxide etch can be a wet etching process, e.g. a buffer oxide etching (BOE), or a dry etching process, e.g. reactive ion etching (RIE). Fig. 3.13 shows a microscopic image of rectangle shape (25 μm by 10 μm) Ge mesas grown on SiO_2 patterned Si.

The wet etching usually creates non-vertical sidewalls which is not favorable for the Ge selective growth since a V-shape air gap exists between the SiO_2 sidewall and the Ge mesa. Therefore, RIE is usually used to etch the SiO_2 trench with relatively straight vertical sidewalls. But the by-product polymer depots produced from the RIE etching process partially cover the exposed Si areas sometimes and are extremely difficult to remove by subsequent chemical cleanings. These polymer deposits poison the Si surface and are severely detrimental to the Ge epitaxy. The solution is to use a combination of BOE and RIE. The SiO_2 layer is first etched by RIE to a depth 10-20 nm away from the SiO_2/Si interface, and the rest of the SiO_2 is etched by BOE. Using this approach, a SiO_2 trench with vertical sidewall and clean Si surface is formed and is ready for selective Ge epitaxial growth.

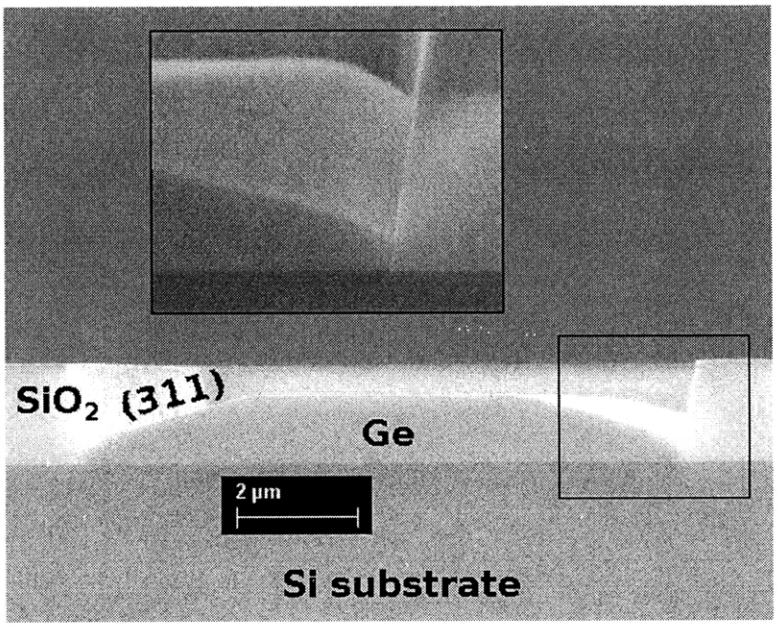

Figure 3.14: Cross-section scanning electron microscope (SEM) image of the Ge selective epitaxial growth in a 10 μm wide SiO_2 trench.

Fig. 3.14 shows a cross-section scanning electron microscope (SEM) image of the Ge selective epitaxial growth in a 10 μm wide SiO_2 trench etched with the RIE+BOE technique

discussed above. We can see that the top surface of Ge is not planar and facets are formed at the edge of the Ge mesa. The facets is a result of the competition of the different Ge growth rate along different crystallographic direction in the trench. The calculation of the angle of the facets indicates it is the (311) plane and (111) plane can be also observed for thicker Ge growth. A detail analysis of the formation of the facet in Ge selective growth can be found in Chapter 5 of Liu's PhD thesis [105].

The facets in Ge mesa is sometimes a problem for further fabrication steps since the non-planar structure distorts the subsequently deposited layers leading to possible flaws in device isolation, metal contact, and other issues. To avoid the facets, a thicker Ge can be grown in the trench thus the overgrown Ge fills the trench and leaves the facets above the SiO_2 layer. Then a chemical mechanical polishing (CMP) is used to planarize the surface to the SiO_2 layer (or a little below the SiO_2 layer due to over polishing).

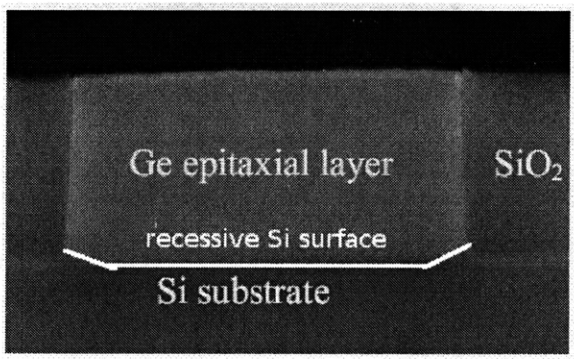

Figure 3.15: The facet free Ge selective growth in the SiO_2 trench with recessively etched Si surface. (after Wang et al. [10])

Another interesting approach addressing this facet issue is the attempts to grow Ge free of facet. Wang et al. reported to use a recessive etched Si area to prevent the facets in Ge selective growth using low pressure chemical vapor deposition (LPCVD) [10] as shown in Fig. 3.15. The recessive shape of Si is etched by hydrogen chloride (HCl) gas and a low growth temperature (400 ^{o}C) is used to suppress the kinetic process of forming the facets during the Ge growth. This approach may be adapted in UHVCVD Ge epitaxial growth with some efforts.

3.4.2 Ge Dry Etching

Dry etching is another useful approach to fabricate Ge devices. Reactive ion etch (RIE) is widely used process in semiconductor microfabrication. It uses chemically reactive plasma to remove material deposited on wafers. The plasma is generated under low pressure (vacuum) by an electromagnetic field. High-energy ions from the plasma attack the wafer surface and react with it.

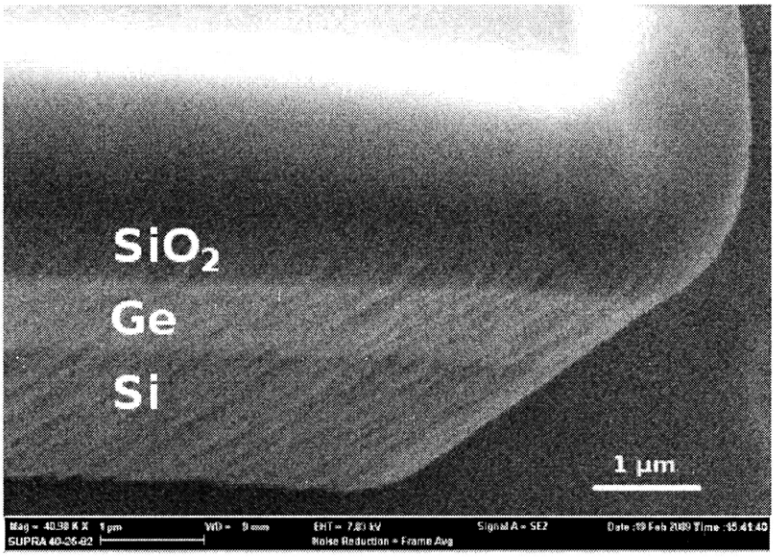

Figure 3.16: Tilted view scanning electron microscope (SEM) image of a SiO_2/Ge/Si mesa etched by reactive ion etching (RIE).

The recipe used for Ge RIE is a little different from the standard Si etching. A recipe of 40 sccm Cl_2, 40 sccm HBr, 400 W coil power and 100 mtorr base pressure is used for Ge/Si etching using an Applied Materials AME 5000 reactive-ion etching (RIE) system in this work. Fig. 3.16 shows a typical SEM image tilted at 45^o of a SiO_2/Ge/Si mesa etched with this recipe. The top SiO_2 layer serves as a hard mask to define a sharper edge than ordinary photoresist. There is strip roughness patterns on the sidewall of the etch stack structure resulting from the vertically introduced etchant gas. The roughness of the sidewall can be alleviated by using a 1:6 de-ionized water diluted hydrogen peroxide (H_2O_2) solution to etch a thin layer of the Ge surface.

Chapter 4

Photoluminescence Studies of Ge

This chapter includes the photoluminescence (PL) studies of both intrinsic Ge and tensile-strained n^+Ge. The calculations in Chapter 2 show the direct band gap light emission from Ge can be enhanced by n-type doping and tensile strain. PL is used to investigate the light emission properties of the Ge films which can be compared with the theory. The fundamentals of PL is first reviewed followed by the PL measurement setup used in this work. Then the PL experiment results of both bulk single crystalline Ge and tensile-strained n^+Ge epitaxial films are discussed. The room temperature direct gap PL is observed from Ge. Its dependences on n-type doping concentration and temperature which are very different from the cases in direct band gap materials confirm the theoretical prediction in Chapter 2.

4.1 PL Basics

Photoluminescence is a process in which a substance absorbs photons (electromagnetic radiation) and then re-radiates photons. Quantum mechanically, this can be described as an excitation to a higher energy state called photo-excitation and then a return to a lower energy equilibrium state. The excess energy is released and may include the emission of light (a radiative process) or may not (a nonradiative process). The energy of the emitted light (PL) relates to the difference in energy levels between the two electron states involved in the transition between the excited state and the equilibrium state. The quantity of the emitted light is related to the relative contribution of the radiative process.

4.1.1 PL Applications

PL spectroscopy is a contactless, nondestructive method of probing the electronic structure of materials. The intensity and spectral content of the luminescence is a direct measure of various important material properties.

The most common radiative transition in semiconductors occurs between the quantum states in the conduction and the valence band, with the energy difference being known as the optical band gap. The emission peak in a PL spectrum from semiconductor is usually broad in the order of thermal energy (kT) therefore it is not an accurate way to directly measure the band gap energy. Nevertheless, a band-to-band optical transition model can be used to evaluate the peak and obtain the information of the band gap. In addition, the photon energy shift of a PL peak usually indicates the band gap change resulting from some factors such as temperature and strain therefore it can be used to study the characteristics of these factors.

Radiative transitions in semiconductors can also involve localized states. The photon energy of the PL associated with these states can be used to identify specific defects, and the amount of PL (PL intensity) can be used to determine their concentration. But accurate determination of the concentration requires precise measurement of all PL emission so that an omnidirectional light collection setup must be used. A simpler way is to compare these defect-related PL to some know PL such as band-to-band optical transition and to calculate the defect concentration accordingly. To study the defect properties, PL measurement is usually performed at low temperatures to separate different peaks which are boarder at room temperature due to a larger thermal energy.

PL is often used to study the electron-hole recombination mechanisms as well. The return to equilibrium, also known as recombination, can involve both radiative and non-radiative processes. Non-radiative recombination is the process that an electron recombines with a hole without emitting photons. Typical non-radiative recombinations includes Auger recombination and defect-assisted recombination. The electron-hole recombination in Auger process transfers the released energy to another carrier which subsequently jumps to a higher energy level and gradually releases its energy to phonons. In defect-assisted recombinations, carriers are captured by some localized defects without crossing the band gap. Generally,

the presence of any of these non-radiative recombinations are detrimental to material quality and subsequent optical device performance.

The amount of PL and its dependence on the level of photo-excitation and temperature are related to the competition of all possible recombination processes (both radiative and non-radiative). Analysis of photoluminescence helps to understand the underlying physics of the recombination mechanism. A time-resolved PL measurement is usually performed for this purpose. The time decay of the light emission characterizes the total carrier lifetime after which the number of non-equilibrium carriers decreases to $1/e$ of the number at the beginning. With a series experiment under different conditions or with different samples, the radiative and the non-radiative lifetimes can be possibly distinguished and determined. This approach is widely used to investigate the material quality.

As can be seen from the discussion above, more than one type of optical transitions (i.e. radiative recombinations) are able to contribute to measured PL. In this work, we only study the direct band-to-band optical transition related PL which is potentially a very efficient light emission and capable of optical gain.

4.1.2 PL Measurement Setup

The schematic of a typical PL setup which is used in this work is shown in Fig. 4.1. It is a free-space PL measurement system built on an optical bench. The excitation source is an Argon ion gas laser. Gas lasers are usually chosen as excitation laser in PL experiment owing to their high output power and low divergence. Solid-state lasers are also common choices as the excitation source. The photon energy of the excitation laser is always larger than that of the aimed PL emission in order to pump the excited carrier to higher energy states. The excitation laser in our experiment is modulated by a mechanical wheel chopper at a given frequency so that a lock-in method can be used to enhance the signal-to-noise ratio. The excitation laser light is focused on the top surface of a sample with a proper incident angle. The reflected light is blocked for eye safety. The PL emission escaping through the top surface of the sample is collected, collimated and then re-focused into a monochromator by a free-space lens system. A long wavelength pass filter is placed in front of the entrance slit of the monochromator to allow PL light to enter but block the excitation laser light randomly

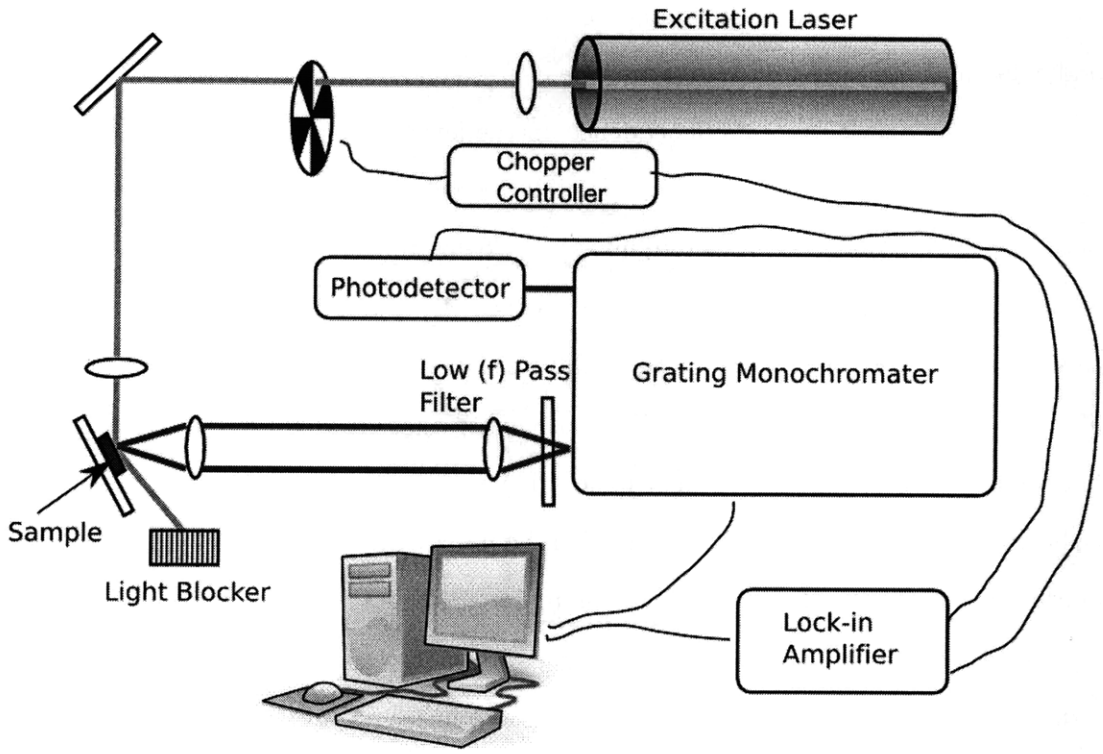

Figure 4.1: Schematic of the PL setup used in this work.

scattered to the slit area. Inside the monochromator, there is an optical grating whose angular position can be adjusted by the controller in order to allow a certain wavelength to form constructive interference at the exit slit region of the monochromator. Thus the spectral intensity of the PL emission can be analyzed. A photodetector is attached to the exit slit to measure the PL light power at a given wavelength. The detected light power is a modulated signal because of the modulation of the excitation laser. The signal is analyzed by a lock-in amplifier synchronized with the chopper frequency so that noises with other frequencies are filtered leading to higher signal-to-noise ratio. A computer program is made to control the angle of the monochromator and to acquire the output from the lock-in amplifier at the chosen wavelength. Therefore, a whole PL spectrum is obtained after a wavelength scan.

For low temperature or temperature dependent PL measurement, samples are contained in a vacuum chamber with a transparent window on one side. The sample can be either cooled by a liquid gas (e.g. nitrogen or helium) or by a cryostat (e.g. helium compressor). The sample can also be heated by some heating elements attached to the sample holder. Therefore

the temperature of the sample can be stabilized at a certain temperature by balancing the heating and cooling though a feedback mechanism automatically controlled by a temperature controller during PL measurement.

Some variants of PL measurement exist to perform other kinds of experiments such as time-resolved studies in which a oscilloscope is needed to capture the time decay of the PL signal.

4.2 PL of Intrinsic Ge

Ge is a multi-valley indirect band gap material therefore both the direct and the indirect band-to-band radiative recombination exist. As discussed in Chapter 2, for intrinsic Ge, the indirect band-to-band transition is a slow process therefore many injected electron-hole pairs recombine non-radiatively before they can recombine radiatively leading to a very low light emission efficiency. Generally, indirect band gap PL can only be observed in very high purity and quality single crystalline Ge at cryogenic temperatures (e.g. below 77K) at which the non-radiative recombinations are greatly suppressed. The direct band-to-band transition in Ge, on the other hand, is a very fast process with radiative recombination rate 4-5 orders of magnitude higher than that of the indirect transition [11]. However, the lack of sufficient numbers of the injected electrons in the direct Γ valley following the quasi Fermi distribution results in weak light emission.

4.2.1 Intrinsic Bulk Ge

Challenges exist for the observation of both the direct gap PL and the indirect gap PL in intrinsic Ge at room temperature. For indirect gap PL, very high purity and material quality are required to reduce the non-radiative recombination rate to the level of the indirect transition rate. The requirement is extremely difficult so that the indirect gap PL in Ge has hardly been observed at room temperature. On the other band, the challenge for the direct gap PL - the lack of the injected electrons in the direct Γ valley - can be overcome by increasing the excitation level. However, the direct gap PL is still difficult to be observed in intrinsic thick Ge bulk samples due to the re-absorption of the emitted photons. In 1964, Haynes et

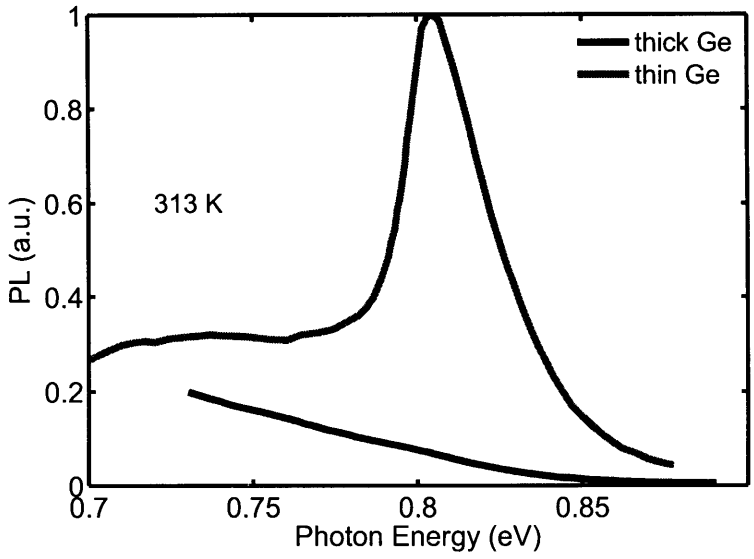

Figure 4.2: PL of a thick Ge sample and a thin Ge sample at room temperature. Direct gap PL at 0.8 eV is shown from the thin Ge sample. (After Haynes et al. [11])

al first observed direct gap PL in Ge by mechanically polishing the Ge bulk (attached to a metal chunk) to a thin film with thickness less than 10 μm. He compared the PL from a thick sample and from a thin sample and concluded that the direct gap PL in Ge could only be observed from a sufficiently thin sample. This comparison can be seen in Fig. 4.2. The peak position of the PL of the thin Ge sample is located at 0.8 eV corresponding to the direct band-to-band optical transition. In late 1970s, Klingenstein et al investigated the dependence of the direct gap PL of mechanically polished Ge thin films on excitation power at low temperature and showed the direct gap PL becomes stronger at higher excitation levels. [118, 119]

4.2.2 Intrinsic Ge-on-Insulator

A study of PL in high quality single crystalline Ge thin films a good starting point before investigating the light emission in Ge epitaxial films. Unlike the mechanically polished Ge thin film described in the previous section, Ge-on-insulator (GeOI) samples prepared by wafer-bonding technique are used in our experiment. The single crystalline Ge lightly doped with gallium was bonded to a silicon wafer covered by 1 μm thermal oxide on top. The Ge was then polished down to 3.5 μm by chemical mechanical polishing (CMP) technique which

enables good surface quality and thickness control.

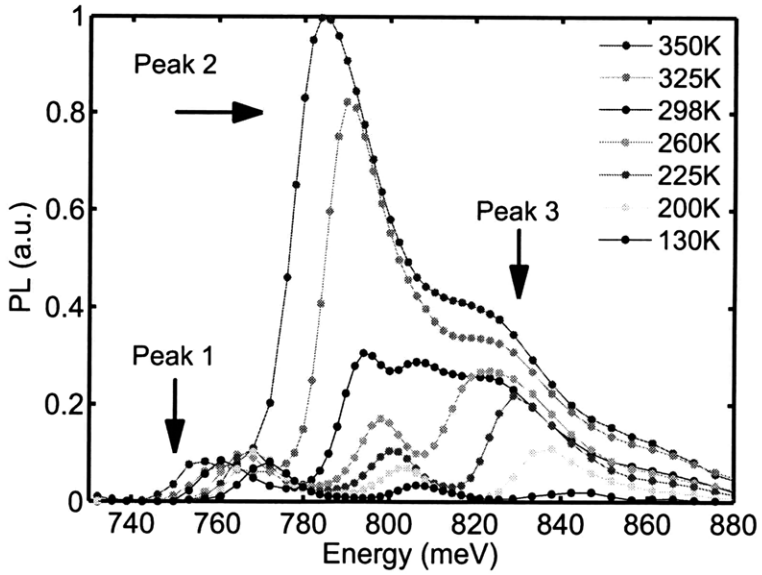

Figure 4.3: PL spectra of GeOI measured at various temperatures. Each spectrum shows three peaks. Peak 2 dominates the PL at higher temperatures and locates at the direct band gap energy in Ge at each temperature. Peak 1 and Peak 3 are clearly observed at lower temperatures due to some other mechanisms. [12]

PL measurements at various temperatures were performed on a GeOI sample using an argon ion laser emitting at 488 nm as the excitation source. The results are shown in Fig. 4.3. All PL spectra clearly show three peaks. The peak in the middle (Peak 2) located at around 0.8 eV (1550nm) corresponds to the direct band-to-band optical transition in Ge. The low photon energy cutoff of the PL peak is slightly less than the direct band gap energy of bulk Ge possibly because the band gap of Ge may be reduced by tensile strain caused by the mismatch of the thermal expansion coefficients between Ge ($5.9 \times 10^{-6}\mathrm{K}^{-1}$) and SiO_2 ($5 \times 10^{-7}\mathrm{K}^{-1}$). Since all layers are relaxed during the wafer bonding process performed at elevated temperatures (200-300 C), Ge, which has a larger thermal expansion coefficient, is stretched by the underlying SiO_2 layer upon cooling to room temperature.

The maximum of this peak versus temperature is shown in Fig 4.4. The slope of this relationship is related to the direct band gap change with respect to temperature. The slope calculated from linearly fitting the data in Fig 4.4 is $dE_{g\Gamma}/dT = -1 \times 10^{-4}\mathrm{K}^{-1}$ which is smaller (in absolute value) than the temperature-dependent band gap change of bulk Ge

($-4\times10^{-4}K^{-1}$) in this temperature range [3]. This difference is due to the increased thermally induced tensile strain in Ge upon cooling, reducing the band gap to partially compensate the temperature-induced energy gap increase.

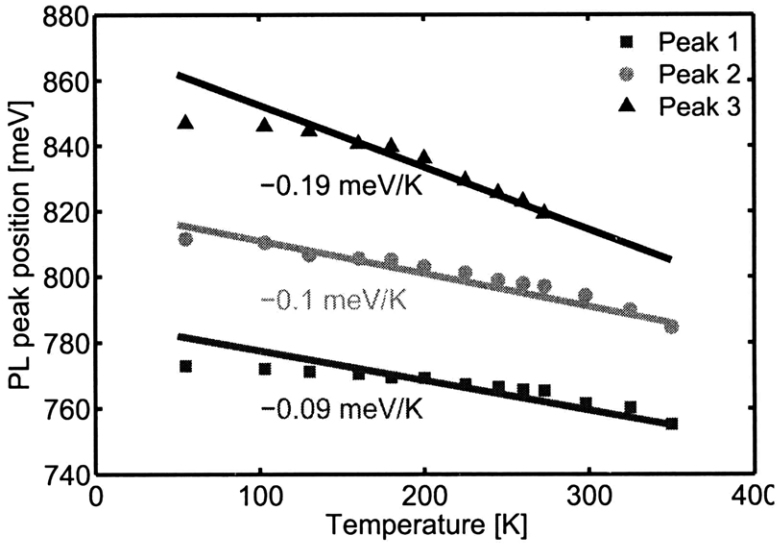

Figure 4.4: Temperature dependence of the three peaks. All three peaks show a red shift with the increase of temperature. [12]

All the spectra contain two other peaks. Combining their characteristics summarized below with future investigation, the origins of these two peaks can be understood.

The temperature dependence of the peak at near 0.76 eV (Peak 1) is the same as that of the direct band-to-band transition underlying the involvement of a energy level with a temperature-independent gap from the direct band edge. This energy level could be a result of exciton with high binding energy of 33 ± 3 meV. The larger-than-usual binding energy results in an excitonic band gap of $\approx$ 0.77eV consistent with Weber's results [120]. An alternative explanation of this energy level is shallow surface defect level near the valence band. The temperature dependence of the peak indicates that the defect level is 33 ± 3 meV above the valence band.

The temperature dependence of the above-band-gap peak near 0.83 eV (Peak 3) is different from that of the direct band-to-band transition indicating a different optical transition mechanism. The PL possibly results from optical transition between other bands since the 488 nm (2.54 eV) pump laser can excite electrons to high states in the conduction bands.

It should also be noticed that the PL intensity increases with temperature. This temperature dependence is a unique feature of the direct PL of an indirect band gap material because of the distribution of injected electrons between the direct valley and the indirect valley. The injected electrons under excitation are scattered to the lower energy states in the indirect L valleys therefore only a very small portion of electrons populated into the direct Γ valley. The distribution of the electrons is described by the quasi Fermi statistics. As the temperature rises, the quasi Fermi distribution allows more electrons in the higher energy states in the direct Γ valley. Therefore more electrons recombine with holes via the fast direct band-to-band transitions and emit photons at elevated temperatures. This phenomenon will be observed again in the n-typed doped Ge in the next section.

4.3 Direct Gap PL of Tensile-Strained n^+Ge

The direct gap PL has been observed from intrinsic bulk Ge films (Ge-on-insulators), however, the calculations in Chapter 2 show that n-type doping is necessary for the occurrence of net material gain. The effect of n-type doping on direct gap light emission is discussed in this section. The n-type impurities in Ge are incorporated using in situ approach during the epitaxial growth other than implantation in order to avoid lattice damage. A comparison of the PL from the n^+Ge films prepared with these two approaches is shown in the section. The use of Ge epitaxial film other than bulk Ge lower the material cost and enable the compatibility with Si IC. In addition, thermally induced tensile strain in the Ge-on-Si epitaxial films reduces the direct band gap hence further enhances the direct gap light emission.

4.3.1 N-Type Doping Dependence

A 515 nm Ar ion laser was used as excitation source in the PL studies. The excitation power density is about 30 W/cm^2. A liquid-nitrogen-cooled InGaAs photodetector and a grating monochromator were used to measure PL spectrum. The spectral response of the PL system ranges from 800 nm (1.55 eV) to 1770 nm (0.70 eV), well covering the entire direct gap emission wavelength range of 0.2% tensile-strained Ge. The doping concentrations mentioned in the following discussion are all active doping concentrations which are measured by Hall

effect at room temperature.

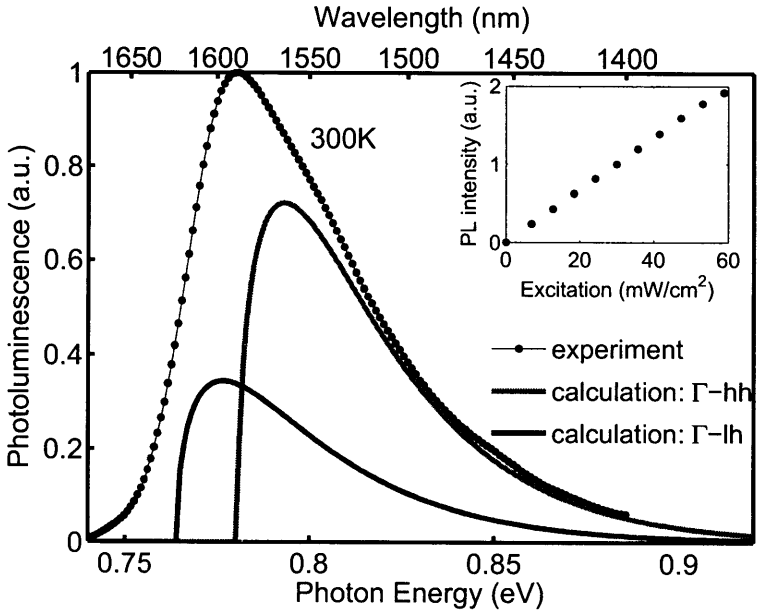

Figure 4.5: Room temperature PL spectrum of an 0.2% tensile-strained epitaxial Ge film with 1×10^{19}cm^{-3} active n-type doping. The PL is peaked at 0.78 eV (1590 nm) corresponding to the direct band-to-band optical transition. Calculated PL spectra of optical transitions from the direct Γ valley to the heavy-hole band and to the light-hole band are represented in the red and the blue solid line, respectively. The inset shows the linear excitation power dependence of the integral PL intensity. [13]

Room temperature direct band gap PL was observed from all n-type tensile-strained Ge epitaxial films. The PL spectrum shown in Fig. 4.5 is measured from an epitaxial Ge film with 1×10^{19} cm^{-3} active n-type doping. The PL band peaks at about 0.78 eV (1590 nm) corresponding to the direct band-to-band optical transition. The full width at half maximum (FWHM) of the peak is 52 meV which is a little larger than the theoretical FWHM of 45 meV for a single band-to-band transition because of the valence band splitting under tensile strain resulting in two closely spaced PL transitions.

Direct gap PL spectrum can be calculated from spontaneous emission model described by

$$P(h\nu) \propto \alpha f_c(1 - f_v) \tag{4.1}$$

where α is the absorption coefficient described by Eq. 2.20 and f_c, f_v are electron occupation probabilities explained in Chapter 2. Two types of optical transitions exist due to the strain-

induced separation of the light-hole and the heavy-hole bands. The PL spectra owing to the optical transitions from the Γ valley to the heavy-hole band and to the light-hole band are both shown in Fig. 4.5 with red and blue respectively. The overlap of these two PL spectra causes the broadening of the overall peak. The PL intensity from the Γ valley to the light-hole band is weaker than that to the heavy-hole band due to a lower joint density of states of the former transition.

The experimental PL spectrum extends slightly more towards long wavelength compared to the calculation from the direct band-to-band transition theory indicating the deviation from the ideal assumption of square root joint density of states. This deviation is a result of an Urbach tail in the band gap which is well documented [121].

The linear excitation power dependence of the integral PL intensity shown in the inset of Fig. 4.5 does not indicate the effect of non-radiative recombination such as Auger recombination. It underlies that higher carrier injection levels can be achieved with increased excitations so that more light emission can be obtained potentially leading to optical gain.

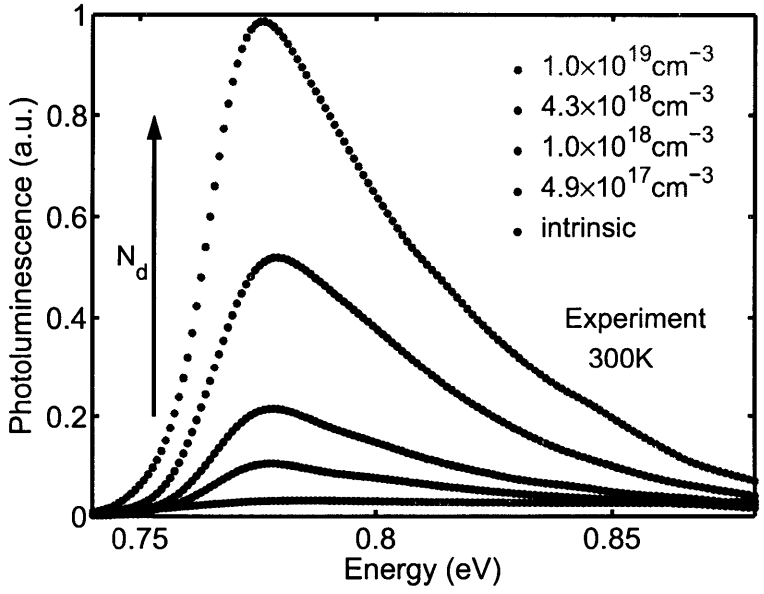

Figure 4.6: PL spectra of tensile-strained Ge film with various n-type doping levels. The PL of a 1×10^{19} cm^{-3} doped Ge film is over 50 times larger than that of the intrinsic Ge film. [13]

The effect of n-type doping concentration on PL is investigated using a series of Ge-on-Si samples with doping concentrations from less than $1 \times 10^{16} cm^{-3}$ (nearly intrinsic) to 2×10^{19}

cm^{-3}. Some example PL spectra are shown in Fig. 4.6. The doping dependence of PL intensities of these samples agree with our analysis in Chapter 2 that the direct gap light emission is enhanced with higher n-type doping due to the indirect valley states filling effect analyzed in Chapter 2. All PL spectra are measured at room temperature. The PL spectrum of a 1×10^{19} cm^{-3} doped Ge film is over 50 times brighter than that of the intrinsic Ge film. All spectra exhibit the same shape and peak position indicating that the doped phosphorous has negligible effect on either direct band gap or tensile strain in Ge.

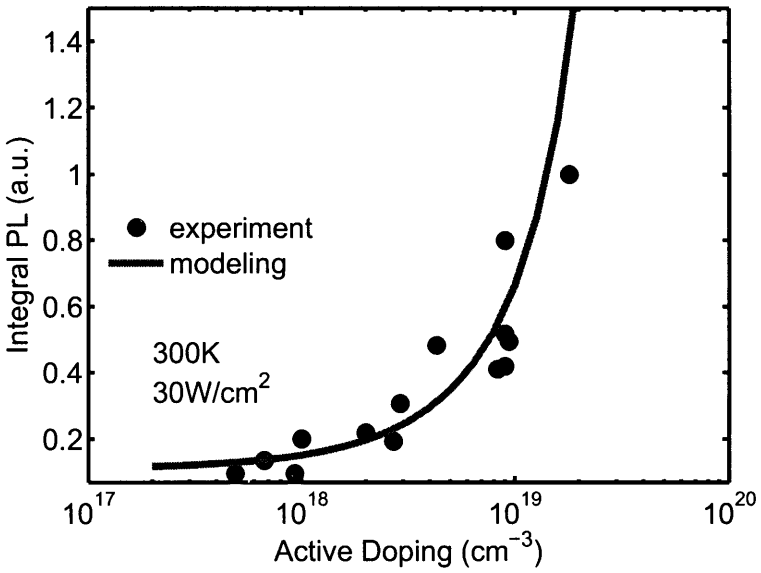

Figure 4.7: A summary of integral PL intensity versus active doping concentration. The theoretical calculation is represented in red solid line and describes the trend of the experimental data. [13]

A plot of the enhancement of integral PL intensity with the increase of active doping concentration is shown in Fig. 4.7. This relationship can be calculated by the following model:

$$I(N_d) \propto n_e^{\Gamma}(N_d) n_h \propto n_e^{\Gamma}(N_d) \tag{4.2}$$

This equation shows the direct gap integral PL intensity is proportional to the product of the electron concentration in the Γ valley and the hole concentration at quasi-equilibrium under excitation. The hole concentration remains the same for each sample at the same excitation level therefore the PL intensity is only determined by the electron concentration

in the direct Γ valley which is a function of n-type doping concentration. According to the analysis in Chapter 2, higher n-type doping results in more injected electrons in the direct Γ valley. A theoretical calculation based on this analysis was performed, and Fermi statistics instead of Boltzman statistics was used in the calculation for a more accurate description of the heavily doped Ge. The calculated results are shown in Fig. 4.7 with red line, exhibiting good agreement with the experimental data.

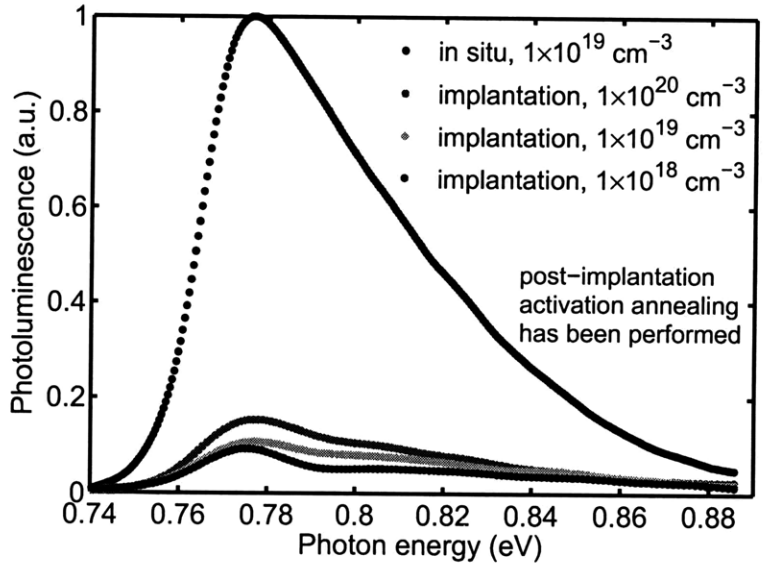

Figure 4.8: PL Comparison of in situ doped Ge and phosphorus implanted Ge. Post-implantation annealing has been performed for implanted Ge films to activate the dopants.

Ion-implantation is an effective way to achieve high doping concentration in materials at the cost of the damage in crystalline lattice. The lattice damages introduce point defects as non-radiative recombination centers thus reduce lifetime in the materials, which can be confirmed by the PL experiment results. Fig. 4.8 shows the PL from the epitaxial Ge films implanted with three different phosphorus doses aiming for doping concentrations of 1×10^{18} cm^{-3}, 1×10^{19} cm^{-3}, and 1×10^{20} cm^{-3}, respectively. All samples are annealed at 800 ^{o}C after implantation for dopant activation and the subsequent Hall effect measurement shows over 80% dopants are activated. It can be seen that the PL increases with the doping level of implanted Ge films but all the implanted films show much weaker PL than the in situ doped one, underlying the fact the lattice damage plays a detrimental role in Ge lifetime thereby light emission. Therefore, in situ doping is a superior approach adopted in this work

to achieve n-type doping in epitaxial Ge films.

4.3.2 Temperature Dependence

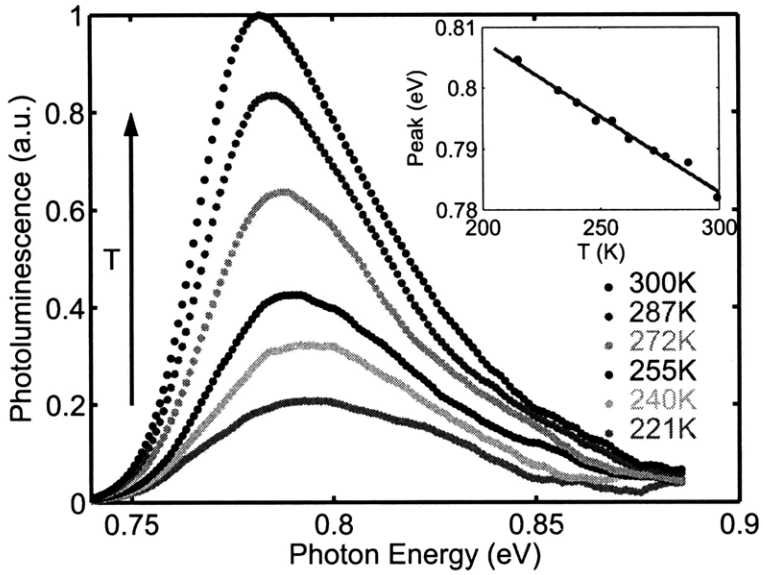

Figure 4.9: PL spectra at temperatures from 220 K to 300 K for a Ge film with 0.2% tensile-strain and 1×10^{19} cm^{-3} n-type doping. The linear relationship between the peak position and temperature with a slope of -2.2×10^{-4} eV/K is shown in the inset. [13]

A temperature dependent PL study is performed on a Ge film with 0.2% tensile-strained and 1×10^{19} cm^{-3} n-type doping. Fig. 4.9 shows a series of PL spectra at temperatures between 220 K and 300 K. The direct gap PL emission from Ge increases with temperature because the number of injected electrons in the direct Γ valley increases at elevated temperature following the Fermi distribution at quasi-equilibrium. This temperature dependence is a unique feature of the direct gap emission from an indirect gap material. The direct gap PL could hardly be observed below 200K due to the deficiency of the direct Γ valley electrons. The enhancement of PL emission at elevated temperatures is favorable for light emission applications since inevitable heating effects during operations, usually detrimental to semiconductor light emission, enhances the light emission of the Ge instead.

A linear relationship between the positions of the maxima of the PL spectra and temperature is shown in the Fig. 4.9 inset. The calculated $dE_{g\Gamma}/dT = -2.2 \times 10^{-4}$ eV/K is a little smaller (in absolute value) than the direct band gap change with temperature of

about -4×10^{-4} eV/K in this temperature range [3]. This difference is due to the increased thermally induced tensile strain in Ge upon cooling, reducing the band gap to partially compensate the temperature-induced energy gap increase. Indirect gap PL was not observed at any temperature above 20 K because non-radiative recombination (0.1-1 μs for the epitaxial film) are much faster than the indirect transition (~ms). The direct transition, on the other hand, is much faster (~10 ns) than the non-radiative recombination so that the direct gap PL can be observed at room temperature.

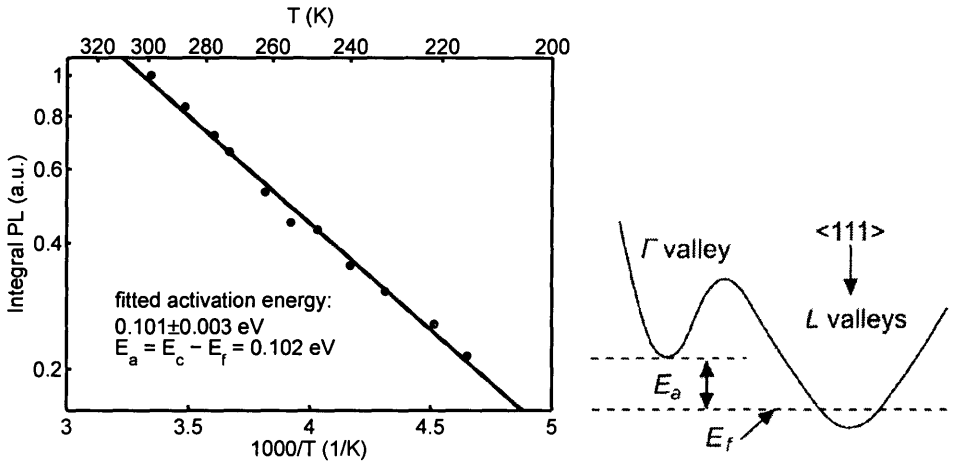

Figure 4.10: Integral PL intensity versus temperature. An activation energy of 0.101±0.003 eV is fitted from Arrhenius relation. The activation energy is equal to the energy difference between the bottom of the conduction band (E_c) and the Fermi level (E_f). [13]

An Arrhenius plot of integral PL intensity versus temperature shown in Fig. 4.10 exhibits a thermally activated behavior. An activation energy of 0.101 ± 0.003 eV is fitted from linear regression. The activation energy is equal to the energy difference between the bottom of the conduction band (E_c) and the Fermi level (E_f). This activation energy is the energy barrier that the injected electrons overcome to go to the direct Γ valley resulting in direct gap emission. Since the Ge is heavily n-type doped, the equilibrium Fermi level is above the bottom of the indirect L valleys as shown in the schematic in Fig. 4.10. The use of "energy difference" in the above analysis is actually not very accurate since it is a conclusion from the Boltzman statistics. The Fermi statistics is used for the heavily doped degenerate Ge instead. The integral PL intensity can be obtained using Eq. 4.2 in the previous section whereas the doping concentration N_d is constant in this case and the injected electron density

in the direct Γ valley as a function of temperature is calculated. The calculation gives an activation energy of 0.102 eV which agrees with the experimental results very well.

From all these PL experiments, we can see the characteristics of the direct gap light emission in Ge, and indirect band gap material, are very different from that of direct gap materials such as many III-V semiconductors. The increase of the direct gap PL emission with either n-type doping concentration or temperature is an unusual phenomenon in semiconductors. But all these behaviors are well predicted by the theory. The emission spectrum, the doping concentration dependence, and the temperature dependence are all accurately consistent with the theoretical calculations. The great agreement between the experimental results and the theory validates the concept of using n-type doping and tensile-strain to increase the direct gap light emission. Therefore, the engineered Ge can be used to fabricate light emitters at 1550 nm wavelength band. In addition, the theory also predicts the engineered Ge is a gain medium. These two subjects are discussed in the following two chapters.

Chapter 5

Electroluminescence from Ge-on-Si Light Emitting Diodes

An important advantage of direct gap light emission in Ge over many other Si-based light emitting materials, such as Er-doped Si dielectrics, is the ability of the electrical injection of the excess carriers. In this chapter, the electrical injected light emission, or electroluminescence (EL), from Ge is discussed. The basics of EL and the EL experiment setup used in this work are first presented. Then, we introduce the fabrication processes of Ge-on-Si heterojunction light emitting diodes (LEDs). Finally, the characteristics of the room temperature direct gap EL from Ge LEDs are discussed. We also perform numerical simulations to study the I-V and direct gap light emission characteristics of the Ge LEDs. The modeling work agrees with the experimental findings and is used to optimize the performance of the n^+Ge heterojunction devices.

5.1 EL Basics

Electroluminescence (EL) from semiconductors is a result of radiative recombination of electrons and holes via optical transition processes. Compared to PL, EL emission is excited electrically other than optically. EL is usually described as an electrical-optical phenomenon in which a material emits light in response to an electric current passed through it, or to a strong electric field. Due to the difference injection process, the optical transitions observed

in EL are not necessary observable in PL and vice versa. This section explains the basics of electrical carrier excitation (injection) and the EL experiment setup used in this work.

5.1.1 Electrical Carrier Injection

Radiative recombination in semiconductors requires both free electrons and free holes and excess non-equilibrium electrons and holes must co-exist for net light emission under carrier injection. Therefore a single-carrier electronic device (e.g. MOSFET) is normally not a good choice for EL emission. The excess electrons and holes are excited either as a result of doping of the material to form a p-n junction, or through excitation by impact of high-energy electrons accelerated by a strong electric field (as with the phosphors in electroluminescent displays). A p-n junction is the most common semiconductor light emitting device. In this work, the latter type of EL device using high-energy electrons is not discussed in this work.

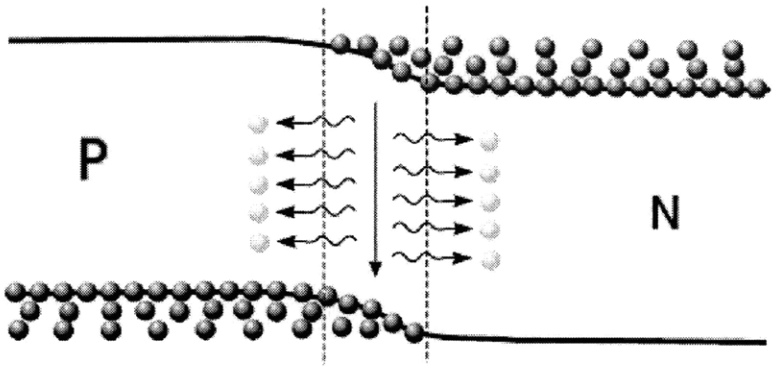

Figure 5.1: Band diagram schematic of a p-n junction under forward bias and the occurrence of the light emission in the active region.

The band diagram of a p-n junction under forwarding bias is schematically shown in Fig. 5.1. The built-in potential resulting from different type of doping in the p-type side and the n-type side is reduced by forward bias so that more electrons and holes injected into the depletion region from the n-type side and the p-type side respectively. This carrier injection process is balanced with carrier recombinations leading to the mutual existence of the excess non-equilibrium electrons and holes in the depletion region *. The excess carriers recombine

*The majority carriers in one side of the junction can diffuse further into the other side and become a minority carrier in a range of a diffusion length and co-exist with the majority carriers in the other side. Therefore, strictly speaking, the light emission region of the p-n junction is the depletion region plus two adjacent diffusion lengths in both sides.

either radiatively or non-radiatively. The radiative recombination is responsible for the light emission from the device. The ratio of radiative recombination rate over total recombination rate (radiative and non-radiative) gives the internal quantum efficiency of the light emitting device.

There are some variations of such p-n junction devices aiming for more light emission. A p-i-n junction other than a p-n junction can be used to broaden the active region where the light emission occurs while the operating voltage is increased to compensate the reduced current due to the additional intrinsic region. A larger band gap material can used for the p-type and n-type regions and forms a type I band alignment with the intrinsic light emitting material. The band discontinuity at the region interface produces a diffusion barrier to prevent the carrier diffuse out of the depletion region hence increases light emission. Such heterojunction diode is often used in laser devices for higher injected carrier confinement.

5.1.2 EL Measurement Setup

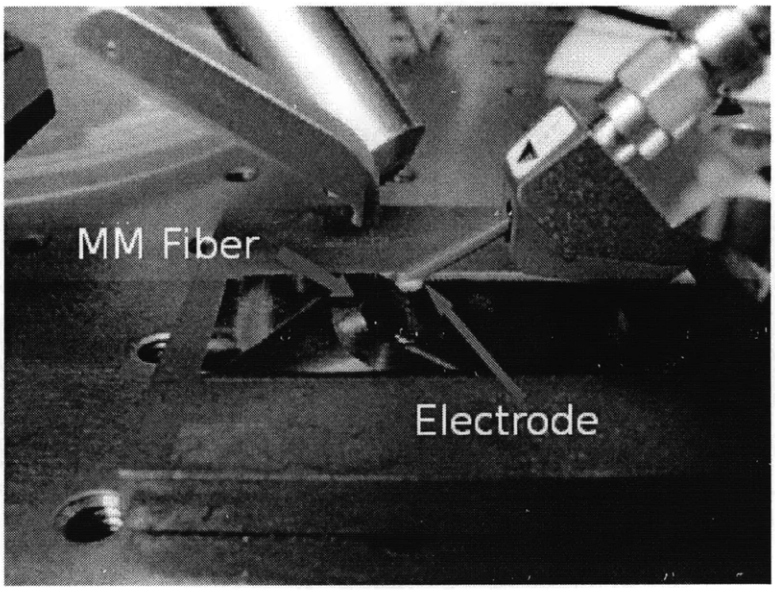

Figure 5.2: Picture of the EL measurement setup used in this work.

The EL measurement setup is similar to a PL experiment setup shown in Chapter 4 Fig. 4.1 expect that the excitation laser is replaced by the electrical power source which supply voltage to devices under test. A 3-dimensional XYZ manipulator is usually needed

to precisely position the attached electrodes to the metal contacts of the devices to form the electrical connection.

The electrode on the manipulator is positioned to contact the metal pads of Si/Ge/Si diodes from above. A free-space lens system as we do in the PL setup is difficult to be deployed here to collect light emission from the compact region above the device. A multi-mode (MM) fiber is used instead as shown in Fig. 5.2. The end of the fiber is placed above and very closed to the top surface of the diode for better light emission collection. While part of the light emission cannot be collected by the fiber due to its relatively small core diameter (50 μm) and the large divergence of the luminescence light emitting from the device surface. The other end of the multi-mode fiber is connected to an Ando AQ6315E optical spectrum analyzer which has a measurement wavelength range between 350 nm to 1750 nm with a dynamic range of 110 dBm (-90 dBm to +20 dBm). Two manipulators holding the multi-mode fiber and the electrode respectively are shown in Fig. 5.2. Both the fiber and the electrodes are too tiny to see and are pointed by two arrows in the picture. The electrode and the fiber are aligned to the diode surface under a microscope.

5.2 Si/Ge/Si Diode Simulation

In order to have a wider Ge active region, we choose to design a p-i-n light emitting diode. Si is a good choice as p-type and n-type region to form a p-i-n diode since Ge can be directly grown on Si. In addition, the larger band gap of Si can possibly form carrier confinement which is beneficial to the device performance. Although the electron affinity of Si ($\chi_{Si} = 4.05$ eV) is slightly larger than that of Ge ($\chi_{Ge} = 4.0eV$) so that the Si/Ge is a type II band alignment. Since the band gap of Si (1.12 eV)is much larger than Ge (0.8 eV), the hole injection still benefit from the Si/Ge heterojunction.

5.2.1 Band Diagram and I-V Characteristic

The calculations of the band diagram and the Fermi level (or quasi Fermi levels under forward bias) of a Si/Ge/Si p-i-n diode are shown in Fig. 5.3. The diode used in the simulation is composed of two 1 μm Si layers (only 0.5 μm is drawn) as p-type and n-type materials (both

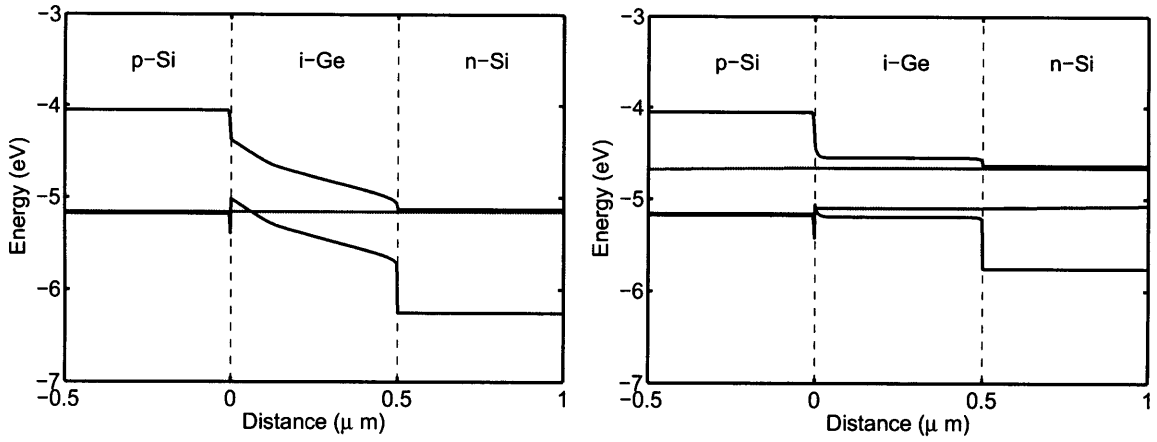

Figure 5.3: (a) Simulated band diagram and Fermi level of a Si/Ge/Si p-i-n diode at equilibrium. (b) Calculated band diagram and quasi Fermi levels of a Si/Ge/Si p-i-n diode under 0.5 V forward bias.

with doping level of 1×10^{19} cm^{-3}) with a 0.5 μm Ge layer in between. At equilibrium, the majority carrier in the middle Ge layer changes from p-type to n-type because of the carrier diffusion from the heavily doped p-type and n-type Si regions, respectively. Under forward bias, the electron Fermi level and the hole Fermi level become separated and approach the edge of the conduction band and the valence band of the Ge, respectively. Therefore, a large amount of excess electrons and holes exist in the Ge layer, so called active region, leading to recombination events including radiative recombinations (light emission).

The I-V characteristic of this Si/Ge/Si p-i-n diode can be numerically simulated and is shown in Fig. 5.3. The fitted ideality factor $n = 1.5$ at small forward biases deviates from an ideal diode with $n = 1$ indicating the occurrence of the carrier recombinations. The physical model of carrier recombination in the depletion region gives an ideality factor of 2. The total current of the device includes the diffusion-drift current and the recombination current leading to an ideality factor of 1.5. This effect can be also seen from the experimental I-V characteristic results discussed in Section 5.4.1.

5.2.2 Internal Quantum Efficiency

Efficiency which evaluates the conversion of the electrical energy to optical energy is a very important figure of merit of a light emitting device. The efficiency of a light emitting device

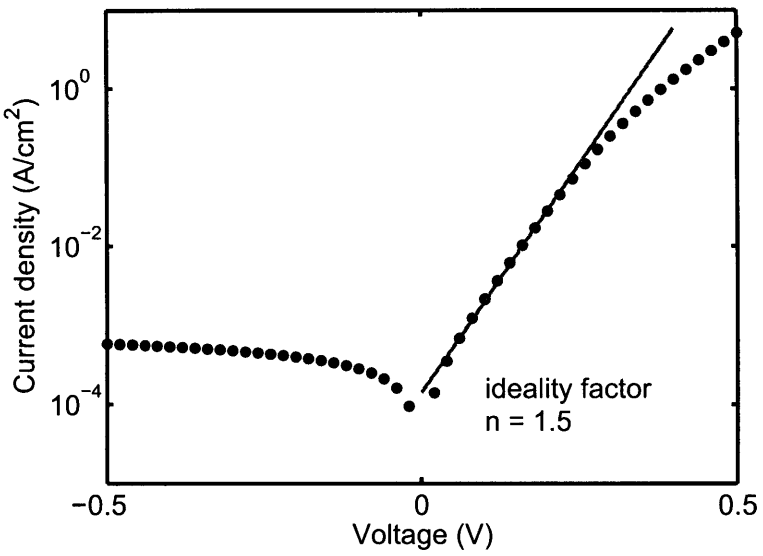

Figure 5.4: Simulated I-V characteristic of the Si/Ge/Si p-i-n diode.

is total result of a number of factors including the injection efficiency, the light extraction efficiency, and the internal quantum efficiency. The first two can be optimized by the device design while the internal quantum efficiency is a properties of the active material describing the fraction of the excess electron-hole pairs contributing to the photon generation. It is very challenging to achieve high internal quantum efficiency in Ge since only the injected electrons in the direct Γ valley contribute to the direct gap light emission. Tensile-strain and n-type doping can be used to have more injected electrons pumped to the direct Γ valley then enhance the direct gap light emission. These effects have been observed and are shown in the PL studies in Chapter 4.

The internal quantum efficiency of the direct gap EL can be estimated from the simulation results shown earlier. As we have seen in Chapter 4, the direct gap light emission is determined by the electron concentration at the direct Γ valley n_Γ which can be calculated from the electron quasi Fermi level shown in Fig. 5.3 (b) by using

$$n_\Gamma = N_{c\Gamma} F_{1/2}(-\frac{E_{c\Gamma} - E_{fc}}{k_B T}), \tag{5.1}$$

where

$$F_{1/2}(x) = \frac{2}{\sqrt{\pi}} \int_0^\infty \frac{t^{1/2}}{\exp(t-x)+1} dt \tag{5.2}$$

is complete Fermi-Dirac integral with an index of 1/2. $n_\Gamma = 3 \times 10^{13}$ cm^{-3} is obtained by using this equation considering the change of band structure due to 0.2 % tensile strain. The recombination rate of the direct Γ valley electrons and holes is obtained from the rate equation:

$$\frac{dn_\Gamma}{dt} = \frac{n_\Gamma}{\tau_\Gamma} - R_\Gamma \tag{5.3}$$

at steady state where $\frac{dn_\Gamma}{dt} = 0$, we have

$$R_\Gamma = \frac{n_\Gamma}{\tau_\Gamma}, \tag{5.4}$$

where τ_Γ is the total life time of the direct Γ valley electrons. This life time is dominated by the radiative life time since the direct band-to-band optical transition is generally a faster process than non-radiative transitions in single crystalline Ge. We conservatively let this carrier direct transition radiative life time 10 ns which leads to a radiative recombination rate of 3×10^{21} cm^{-3}s^{-1}. The light emission power P can be obtained by

$$P = \frac{hc}{\lambda} R_\Gamma V, \tag{5.5}$$

where hc/λ is the energy of a single photon. We assume the volume of the Ge region V is 20 μm by 100 μm by 0.5 μm, and the light emission is at the band gap energy ($\sim$ 0.8 eV), so we have $P \sim 0.1$ μW. Although not all the light emission escapes from the device due to the total reflection and interface scattering, it is adequate to be observed.

The internal quantum efficiency of the light emission, which is defined as the percentage of the injected carriers that radiatively recombine hence emit photons, can be calculated by

$$\eta_i = \frac{R_\Gamma V}{JA/e}, \tag{5.6}$$

where J is the current density at 0.5 V simulated and shown in Fig. 5.4 and A is the device area (20 μm by 100 μm). Using Eq. 5.6, we obtain $\eta_i = 10^{-2}$ which is a quite good number for light emission in Ge. The internal quantum efficiency can be further improved by larger tensile-strain and/or heavy n-type doping.

5.3 Ge-on-Si LED Fabrication

A hot-wall UHVCVD reactor is used grow epitaxial Ge on boron-doped p+ Si (100) substrates with a resistivity of 0.005 Ω cm. But Unlike the blanket epitaxial growth, a SiO_2 layer first deposited on the Si substrate was patterned to expose certain regions of Si and Ge was selectively grown in these opened trenches with high selectivity [55]. More details of this Ge selective epitaxial growth are covered in Chapter 3.

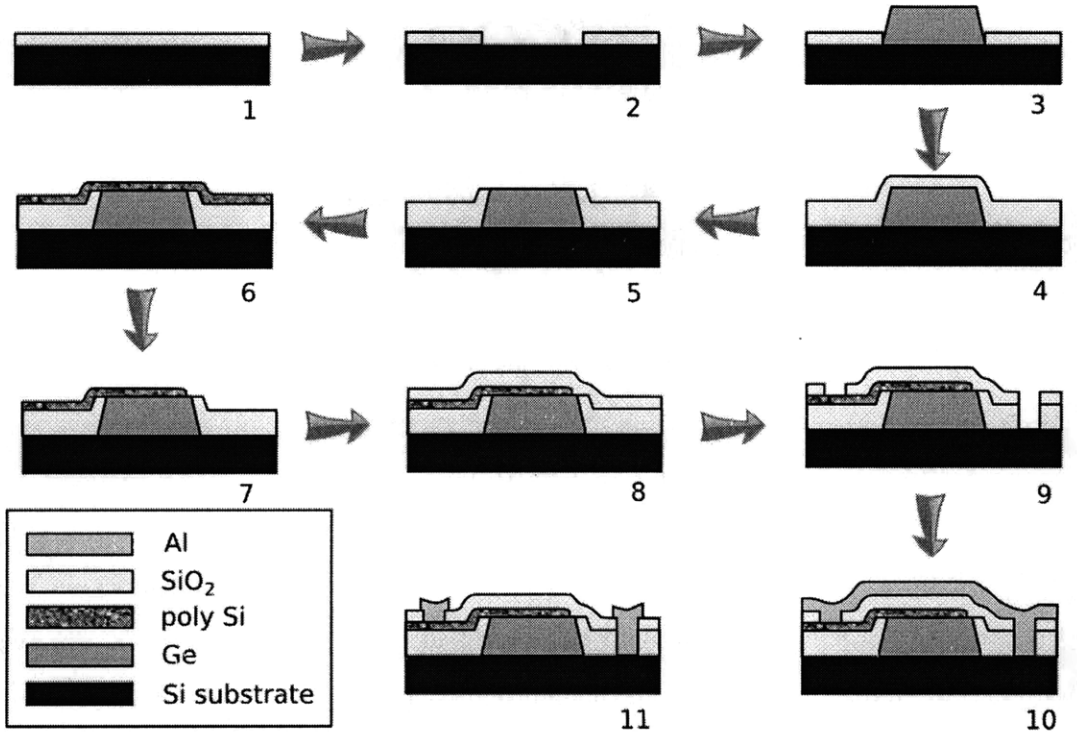

Figure 5.5: The fabrication flow of the Si/Ge/Si light emitting diodes.

The fabrication flow of the Si/Ge/Si diodes are shown in Fig. 5.5. A 200nm thick thermal SiO_2 was first grown on a 6 inch Si substrate (Step 1). The SiO_2 was then patterned by using an Electronic Visions EV620 mask aligner lithography system with a contact mask and 10 mW/cm^2s high-pressure mercury lamp exposure (all lithography processes in some following steps were deployed with the same system and parameters). The patterned SiO_2 film was etched by using an Applied Materials AME 5000 reactive-ion etching (RIE) system with Halocarbon 14 (CF_4) plasma to expose Si substrate underneath in patterned device areas

(Step 2).

A 50 nm Ge buffer layer was selectively grown in these devices areas defined by SiO_2 windows at 335 ^oC to kinetically suppress island formation. A 1.7 μm thick Ge layer then grown on the buffer layer at an elevated temperature of 700 ^oC (Step 3). The root-mean-square surface roughness of as-grown Ge is less than 1 nm measured by atomic force microscopy (AFM). Details about this two-step growth method can be found in Chapter 3. Post-growth thermal annealing at 900 ^oC was performed to reduce the threading dislocation density to 1.7×10^7 cm^{-2} measured from etch pit density studies [122]. The Ge film was fully relaxed at this high annealing temperature, and tensile strain was introduced by cooling to room temperature due to the large thermal expansion coefficient difference between Ge and Si as we discussed in Chapter 3. As a result, an in-plane tensile strain of 0.2% was introduced into the Ge film, causing a reduction of the direct band gap between the minimum of the direct Γ valley and the maximum of light-hole band to 0.76 eV according to both our calculation and experiment results.

A SiO_2 layer was deposited by using a low temperature oxide (LTO) technique (Step 4). The SiO_2 layer was patterned and etched to expose the Ge device area and some adjacent SiO_2 to isolate the edge the device (Step 5). A poly-crystalline Si film with a thickness of 200 nm was then deposited on top, implanted with $5 \times 10^{15}/cm^2$ dose of phosphorus at 100 keV with 7-degree tilting aiming at 10^{20} cm^{-3} doping concentration (Step 6). After ion-implantation, a H_2 ambient thermal annealing was performed at 650 ^oC for 30 minutes to activate the dopants to form the n-type electrode of the heterojunction diode. The poly-crystalline Si was subjected to photolithography and etched by the RIE system with Chlorine (Cl_2) and Hydrogen Bromide (HBr) plasma to expose some SiO_2 areas near the device areas (Step 7).

Another SiO_2 layer with a thickness of 800 nm was deposited at 400 ^oC by using an Applied Materials Centura 5200 plasma enhanced chemical vapor deposition (PECVD) system (Step 8). Reactive-ion etching was performed to etch SiO_2 to expose some areas of the n+ polycrystalline Si and the p+ Si substrate (Step 9).

Aluminum was deposited by using Applied Materials Endura 5500 physical vapor deposition (PVD) system served as the electrical contact material. The aluminum layer was

patterned and then etched by using Lam Rainbow 9600 Metal Etch System with boron trichloride (BCl_3) gas to isolate the p-side and n-side contacts and to expose the diode area. The aluminium was subsequently sintered at 400 °C in forming gas (N_2/H_2) for 20 minutes to obtain Ohmic contact with n^+ and p^+ Si respectively.

The entire device was fabricated using materials and processing that can be implemented in a standard Si complementary metal oxide semiconductor (CMOS) process flow.

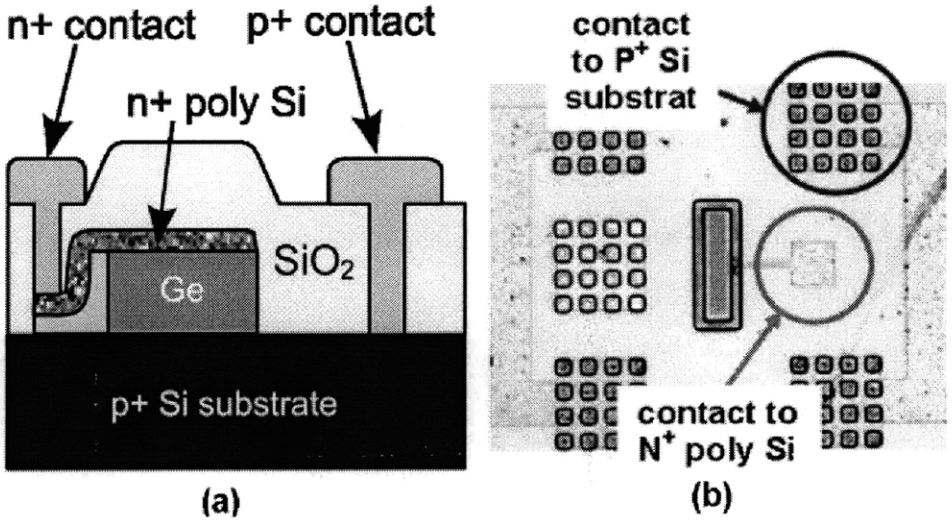

Figure 5.6: (a) Schematic cross-section of a tensile-strained Ge/Si heterojection p-i-n light emitting diode. (b) The microscopic image of the top view of a 20 μm by 100 μm Ge/Si p-i-n diode.

The cross-section of the p-i-n heterojunction diode is schematically shown again in Fig. 5.6 (a) with an example of the microscopic image of the fabricated device. The device shown in Fig. 5.6 (b) is a rectangle shape diode with dimension of 20 μm by 100 μm surrounded by a few metal contact pads, one of which is connected to the p+ Si substrate and the other is connected to the n+ polycrystalline Si layer on top of Ge. In the EL measurement, a micro-electrode is probed to these metal pads. Two tiny leads on the electrode are connected to one of the p-type side metal pads and the n-type side metal pad to complete the circuit. The electrical power source connected to the micro-electrode supplies the voltage to Si/Ge/Si diode.

5.4 EL from Ge-on-Si LEDs

Electrical characterization and electroluminescence measurement were performed on the as-fabricated Si/Ge/Si heterojunction light emitting diode.

5.4.1 Electrical Characterizations

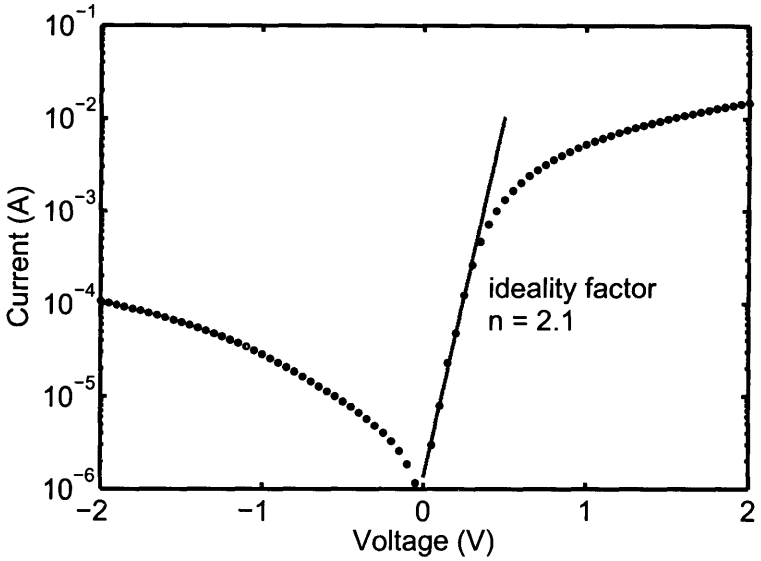

Figure 5.7: The I-V characteristics of a 20 μm by 100 μm Si/Ge/Si diode with ideality factor of 2.1. [14]

The current-voltage (I-V) characteristic, shown in Fig. 5.7, was measured by using a HP 4145A semiconductor parameter analyzer on a 20 μm by 100 μm diode. The I-V curve exhibits a good rectifying behavior with a dark current of 5×10^{-5} A at 1 V reverse bias. The ideality factor $n = 2.1$ is calculated at small positive biases using linear regression of the simple diode IV model:

$$I = I_0(\exp(\frac{eV}{nk_BT}) - 1). \tag{5.7}$$

As we explained in the simulation section earlier, the deviation from ideal diode with an ideality factor of 1 indicates the occurrence of carrier recombinations in the depletion region of the diode. The carrier recombination contributed current gives an ideality factor of 2. The fitted ideality factor of 2.1 underlies that the carrier recombination is dominant the total electrical current. The carrier recombination includes both the non-radiative recombination

and the radiative recombination. The former one which can be a result of defects in Ge is detrimental to the internal quantum efficiency since the injected carriers do not emit photons. While the latter one is responsible for the EL emission. The internal quantum efficiency is determined by the competition of these two types of recombinations.

The deviation of I-V from ideal diode model at large forward biases and reverse biases is due to the effects of series resistance and shut resistance respectively. These two resistances can be calculated from fitting the experimental data at forward and reverse bias region respectively.

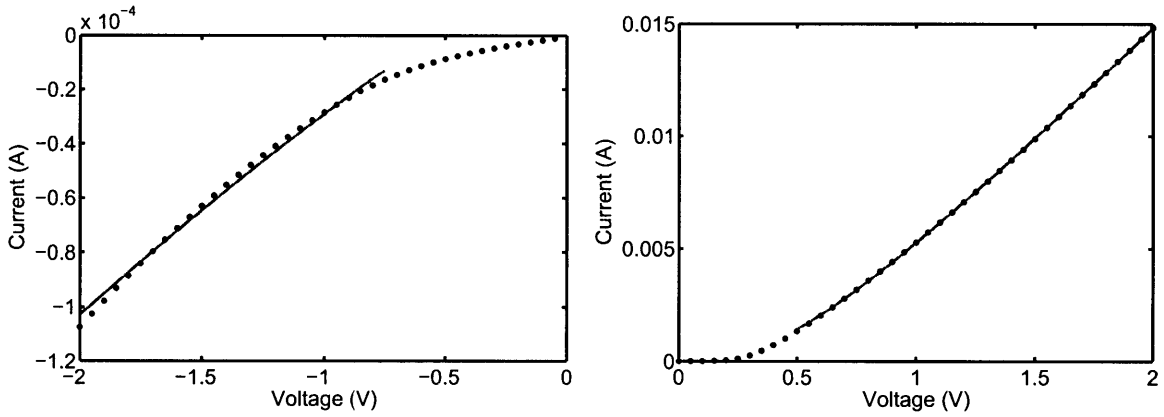

Figure 5.8: (a) Reverse I-V fitting considering the effect of shunt resistance. (b) Forward I-V fitting considering the effect of series resistance.

By fitting the forward I-V shown in Fig. 5.8 (b), a series resistance of $R_s = 93\Omega$ is calculated. This series resistance probably results from the electrode contact resistance, cable resistance, and the Al/Si interface resistance due to fabrication imperfection.

By fitting the reserve I-V shown in Fig. 5.8 (a), a shunt resistance of $R_{sh} = 9.4 \times 10^3\Omega$ (or a conductance of $G_{sh} = 1.1 \times 10^{-4}$ S) is calculated. We know that two origins of the reverse current in a diode are usually concerned: the ideal drift-diffusion current and depletion region defect-related generation current. The drift-diffusion current saturates above a few k_BT reverse bias and the carrier generation current is proportional to the depletion width thus increases with the square root of the reverse bias. But neither of them can explain the linear increasing of the reverse current. In addition, the generation current saturates at large reverse biases due to the saturation of the carrier drift velocity at high electric field as shown

in Fig. 5.9.

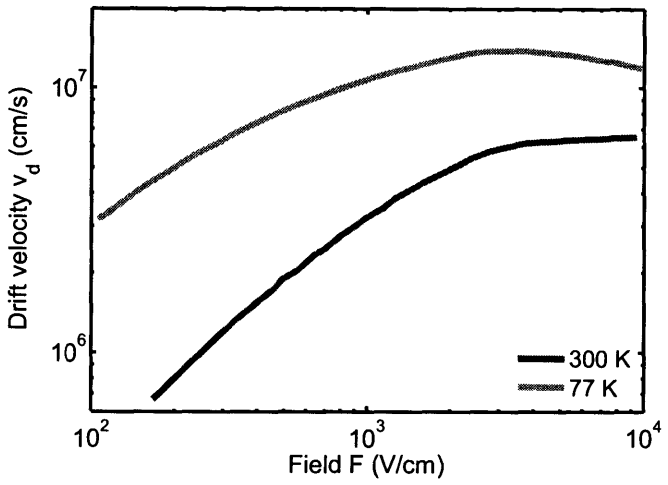

Figure 5.9: Electron drift velocity of Ge versus electric field. (After Jacoboni et al. [15])

The I-V measurement was performed on the Si/Ge/Si diode with reverse bias up to -5 V which correspond to an electric field of 2×10^4 V/cm beyond the saturation electric field shown in Fig. 5.9. However, no saturation phenomenon in the electrical current was observed at such high electric field. Therefore this large reverse current cannot be explained by carrier generation current alone. The existence of this conductor parallel to the diode indicates other conduction mechanisms.

We know that the threading dislocations in epitaxial Ge film act as defect centers which contribute to the carrier recombination/generation current. In fact, it has been shown that the threading dislocations can also be conduction paths due to the continuous overlapping of the dangling bonds along the dislocation lines [123, 124, 125, 126, 127]. A model of one-dimensional, quasi-metallic conduction along 60° dislocations in Ge has been established based on the I-V measurements along the dislocations in Ge thin plates and electron beam induced current (EBIC) measurements [123, 127]. A positive relationship of the reverse bias conductivity of Ge diode to the threading dislocation density has been demonstrated in Ref. [105] by using the author's own experimental data along with the data from other studies [128, 129].

5.4.2 EL Spectroscopy

In the EL spectrum experiment, the onset of EL from Si/Ge/Si diodes at forward bias has been observed. The onset of the EL was observed at 0.5 V forward bias or 1.3 mA injection current from a 20 μm by 100 μm diode.

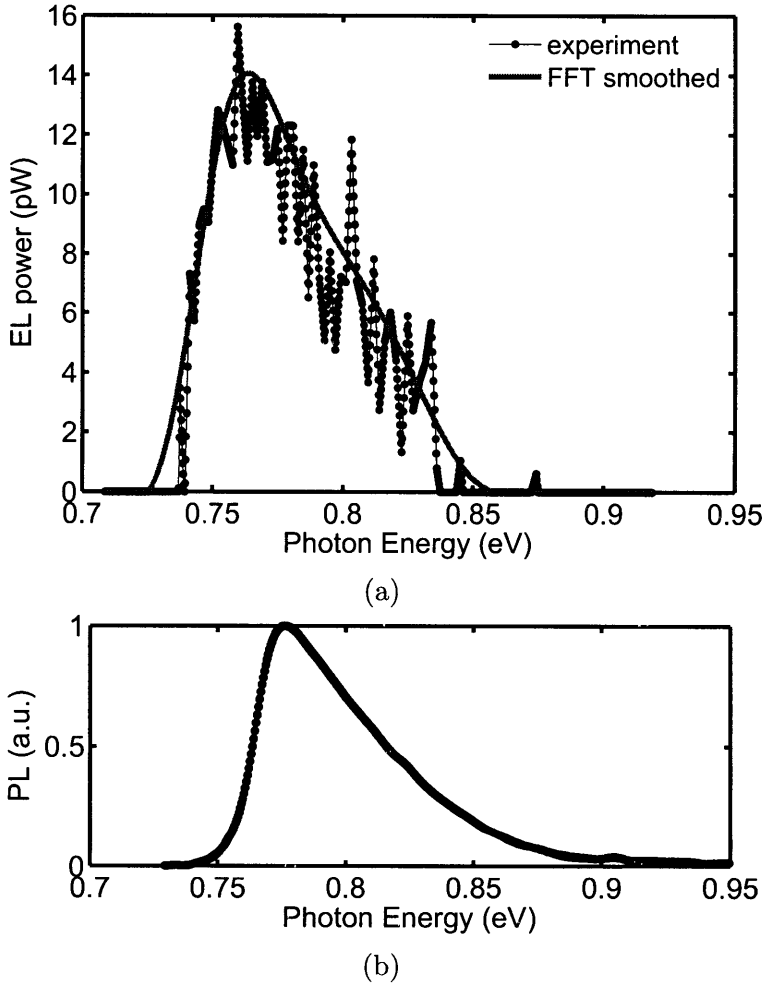

Figure 5.10: (a) Direct gap EL spectrum of a 20 μm by 100μm 0.2% tensile-strained Si/Ge/Si p-i-n light emitting diode measured at room temperature. The multiple sharp peaks in the spectrum are highly periodic due to Fabry-Perot resonances. (b) Room temperature direct gap photoluminescence of a 0.2% tensile-strained Ge film epitaxially grown on Si. [14]

The EL spectrum measured at room temperature from the 20 μ by 100 μ diode at 50 mA forward electrical current is shown in Fig. 5.10 (a). The EL peak is located 0.76 eV corresponding to the direct band-to-band optical transition in 0.2% tensile-strained Ge. The full width at half maximum (FWHM) of the peak is about 60 meV (~2 kT) consistent with

the direct band-to-band transition model as well as the PL result. The sharp peaks which are explained later are from the Fabry-Perot resonance thus can be filtered by fast Fourier transformation (FFT). After the FFT filtering, the smoothed curve represents the "real" EL characteristics is shown with read solid line in the figure.

The EL spectrum is consistent with the room temperature photoluminescence (PL) spectrum measured from a 0.2% tensile-strained epitaxial Ge film on Si shown in Fig. 5.10 (b). A 488nm Ar ion laser was used in the PL measurement and the spectral response was measured by a Hamamatsu R5509-72 photomultiplier tube (PMT) through a grating monochromator. The steeper drop of the intensity in the PL spectrum than in the EL spectrum near 0.75eV is due to the dramatic decline in responsivity of the PMT. The small red shift in the EL peak position compared to PL peak position is a result of the heating effect under electrical current injection that slightly reduces the band gap. To our knowledge, this is the first observation of direct gap EL from any Ge devices.

The same characteristic of the EL and the PL confirms the same direct gap optical transition mechanism for both low energy (slightly above band gap) electrical injection and high energy photon (488nm, 2.5eV) optical injection. This is an important conclusion since all investigation and optimization results obtained from optical characterizations (e.g. PL measurement) can be directly applied to the design of the electrically pumped light emitting devices. This fact is the same as what we observed in direct gap III-V compound semiconductors but is not always true in other Si-based light emitting systems such as Er-doped dielectric materials which is easily pumped optically but very difficult pumped electrically.

The multiple sharp peaks in the EL spectrum are reproducible and not due to noise. The linear relationship between the energy position of these peaks and the peak number shown in the Fig. 5.11 indicates the occurrence of the Fabry-Perot resonance corresponding to an air gap between the end of the optical fiber and the device surface. The distance of this gap can be calculated from the periodicity (5.3 meV) of the resonance. The m^{th} order peak wavelength λ_m satisfies the resonance condition:

$$m\lambda_m = 2nt, \tag{5.8}$$

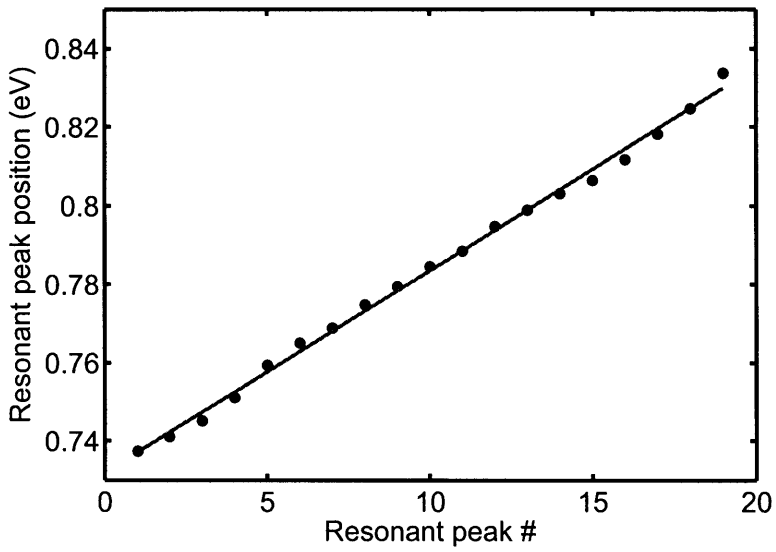

Figure 5.11: The linear behavior of the peak position versus peak number demonstrates a periodicity of 5.3 meV due to Fabry-Perot resonances between the device surface and the end of the coupling fiber. [ ]

where n the refractive index which is 1 for air and t is the distance of the air gap. By applying Eq. 5.8 to two adjacent peaks, we can have

$$\frac{1}{2nt} = \frac{1}{\lambda_{m+1}} - \frac{1}{\lambda_m} = \frac{E_{m+1}}{hc} - \frac{E_m}{hc} = \frac{\Delta E}{hc}, \tag{5.9}$$

where the wavelength λ is replaced by photon energy E using $E = hc/\lambda$. Then

$$t = \frac{hc}{2n\Delta E}. \tag{5.10}$$

By substituting $\Delta E = 0.53$ meV, we have $t = 120$ μm.

5.4.3 Internal Quantum Efficiency

Using this air gap distance obtained above, other geometry information, and the material properties of the collection fiber and the device, the total light emission thus the internal quantum efficiency can be calculated. The schematic of the light emission collection using the multi-mode fiber is drawn in Fig. 5.12. The area of the fiber core subtends a given point

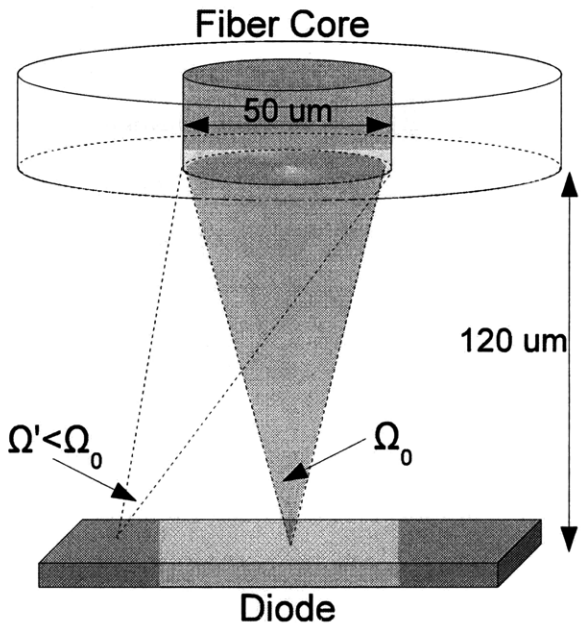

Figure 5.12: Schematic of the light emission collection using a multi-mode fiber above the Si/Ge/Si diode.

on the diode surface with a solid angle Ω^*. We assume, for simplicity, this solid angle is the same for any point on the device surface and is equal to the solid angle Ω_0 of the point right under the center of the fiber core[†]:

$$\Omega_0 = 2\pi(1 - \cos(\sin^{-1}\frac{d}{2t})), \tag{5.11}$$

where $d = 50$ μm is the diameter of the fiber core and $t = 120$ μm is the air gap distance. Since the EL is a spontaneous emission process, the direction of the light emission (the momentum of the emitted photons) is totally random. Therefore we can assume the light emission escaped from every point on the surface is omnidirectional and angularly uniform above the surface, and the percentage of the light hitting the core area of the fiber is

$$\eta_\Omega = \frac{\Omega_0}{2\pi} = 1 - \cos(\sin^{-1}\frac{d}{2t}). \tag{5.12}$$

*The solid angle is the angle in three-dimensional space that an object subtends at a point.

[†]This assumption is conservative since any point on the diode surface other than the center point has a smaller solid angle than Ω_0 therefore less light from this point is collected by the fiber. Therefore the actual light emission escaped from the diode surface is more than we calculate with Ω_0.

$\eta_\Omega = 0.087$ is calculated for the geometry shown in Fig. 5.12.

A fraction of the light is reflected from each interface when it travels from the Ge region into the core of the fiber. A single pass of light through each interface is considered for simplicity (the interference effect is ignored in this analysis) and the transmittance of the light from medium 1 to medium 2 can be calculated by

$$T_{1,2} = \frac{2n_1 n_2}{{n_1}^2 + {n_2}^2}, \tag{5.13}$$

where n_1 and n_2 are refractive indices for medium 1 and medium 2 respectively. There are three interfaces in total: Ge/Si interface, Si/air interface, and air/silica interface. The total transmittance is the product of transmittances of all these three interfaces:

$$T_{\text{tot}} = T_{\text{Ge/Si}} \cdot T_{\text{Si/air}} \cdot T_{\text{air/silica}}. \tag{5.14}$$

By substituting the refractive index data of each material near 1550 nm ($n_{\text{Ge}} = 4.2$, $n_{\text{Si}} = 3.5$, and $n_{\text{silica}} = 1.5$), $T_{\text{tot}} = 0.082$ is calculated.

The angle of the light emission from each emission center (an electron-hole pair associated with radiative recombination) in Ge is generally random. Only the light emission with an incident angle (to both the Ge/Si interface and the Si/air interface) less than the total internal reflection (TIR) angle can escape out of the device. This can be also calculated by the solid angle defined by the total internal reflection angle and gives another efficiency reduction represented by

$$\eta_{\text{TIR}} = \frac{\Omega}{4\pi} = \frac{1}{2}(1 - \cos(\sin^{-1}\frac{n_{\text{Si}}}{n_{\text{Ge}}}\frac{1}{n_{\text{Si}}})) = \frac{1}{2}(1 - \cos(\sin^{-1}\frac{n_1}{n_{\text{Ge}}})), \tag{5.15}$$

where n_{Si} and n_{Ge} are refractive indices of Si and Ge respectively, and the use of 4π instead of 2π in the fiber collection calculation above is due to the fact that the internal light emission can be in any direction other than just top half plane. $\eta_{\text{TIR}} = 0.014$ is calculated using this equation with $n_{\text{Ge}} = 4.2$ at the emission wavelength range.

Another source of optical loss is from the connection between the fiber and the optical spectrum analyzer on which the fiber input interface is not specifically designed for multi-

mode fiber only. A simple measurement was performed to determine this optical loss. A 1550 nm laser with fixed output power was used as the light source which the multi-mode fiber used in the EL measurement is connected to. The output light power from the other end of the fiber was measured by an optical power meter with an integral optical head which detects nearly 100% light. The fiber was then connected to the optical spectrum analyzer to measure the output light power and the ratio of this light power to the previous one gives the fraction of the light η_{osa} transmits into the analyzer while the rest of the light is lost. $\eta_{\text{osa}} = 30\%$ was obtained using this approach.

Therefore, the total fraction of the light measured by the optical spectrum analyzer to the light emitted from Ge material is

$$\eta_{\text{tot}} = \eta_{\text{osa}} \cdot \eta_{\Omega} \cdot \eta_{\text{TIR}} \cdot T_{tot}, \tag{5.16}$$

By substituting η_{osa}, η_{Ω}, η_{TIR} and T_{tot} calculated above, we obtain $\eta_{\text{tot}} = 3.0 \times 10^{-5}$.

The total light power detected by the optical spectrum analyzer can be calculated by integrating the EL spectrum which can be estimated by the product of the EL intensity at the maximum and the full width at half maximum divided by the resolution at which the light intensity is integrated by the optical spectrum analyzer:

$$P_{\text{osa}} = \frac{EL_{\text{max}} \cdot \Delta E_{\text{fwhm}}}{\Delta E_{\text{res}}}. \tag{5.17}$$

From Fig. 5.10, we have $EL_{\text{max}} = 15$ pW and $\Delta E_{\text{fwhm}} = 65$ meV. The EL spectrum was measured at a resolution (from the slit width of the monochromator) of $\Delta\lambda_{\text{res}} = 5$ nm hence $\Delta E_{\text{res}} = 2$ meV calculated by

$$\Delta E_{\text{res}} = \frac{\Delta\lambda_{\text{res}}}{\lambda} E. \tag{5.18}$$

By substituting all these data into Eq. 5.17, we obtain $P_{\text{osa}} = 0.5$ nW.

Finally total light emission from Ge $P_{\text{tot}} = 20$ μW is calculated using

$$P_{\text{tot}} = \frac{P_{\text{osa}}}{\eta_{\text{tot}}}. \tag{5.19}$$

This EL emission from the Si/Ge/Si diode was injected at a forward current of 50 mA, therefore the quantum efficiency is

$$\eta = \frac{20 \times 10^{-6}}{50 \times 10^{-3}} \frac{e}{h\nu} \sim 10^{-3}, \tag{5.20}$$

which is a little less than what we simulated in Section 5.2.2 mainly due to a few reasons.

A most likely reason is the modal mismatch between the free-space light and the propagated light in the fiber. We assume the light collected by the fiber is any light hitting the fiber core area. In fact, optical fiber can only support a certain number of optical modes so that only a portion of the electric field of incident light (projected to axes with some certain angles) can be coupled into the fiber core. A large coupling loss from free-space to guided fiber core can decrease the amount of the light into the optical spectrum analyzer.

Another reason stems from the fact that the Ge film may be more defective than that used in the simulation. The increased number of defects states increases the non-radiative recombination events therefore decreases the internal quantum efficiency. An ideality factor of 2.1 fitted from the experimental result larger than 1.5 fitted from the simulation also indicates the possible increased defects states.

We have proved the n-type doping is beneficial to the direct gap light emission. On the contrary, p-type doping is detrimental to the light emission efficiency since it reduces the injected electron numbers as well as increases the electrical current in the p-i-n diode. It has been shown the as-grown "intrinsic" Ge shows p-type behavior which is believed to be a result of the threading dislocation in Ge. Therefore, this dislocation-induced p-type doping may be part of the reason of efficiency reduction.

In addition, the top Si layer is heavily n-typed doped which results in free carrier absorption at the emission wavelength range. This absorption results in additional photon loss.

5.4.4 Injection Dependence

The injection dependence of the direct gap EL emission was measured to provide information about the direct gap light emission characteristic of Ge which is different from that of a direct

gap semiconductor.

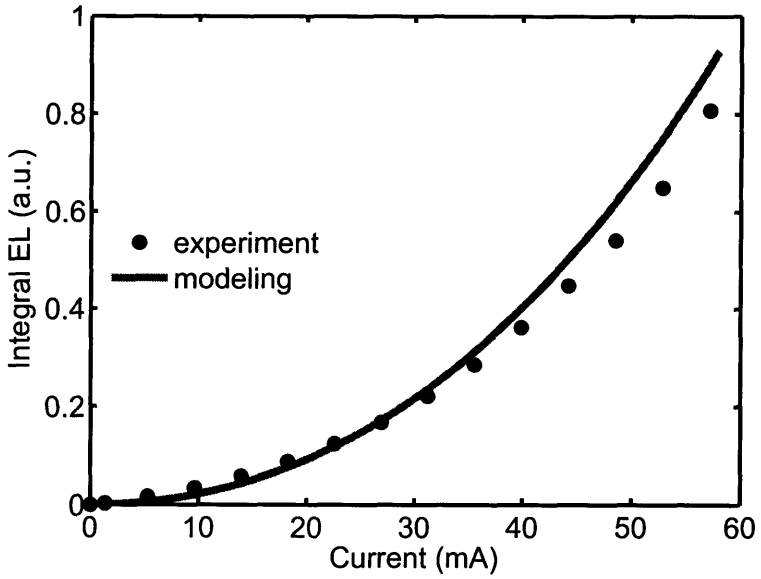

Figure 5.13: Integral direct gap EL intensity of a 20 μm by 100 μm 0.2% tensile-strained Si/Ge/Si p-i-n light emitting diode. The EL intensity increases superlinearly with electrical current. The theoretical calculation (solid line) agrees well with the experimental result.

A superlinear relationship of the integral direct gap EL intensity with the injected electrical current is shown in Fig. 5.13. In a direct band gap semiconductor, this relationship is expected to be linear at lower injection level and becomes sublinear at higher injecion level due to the occurrence of some non-radiative recombination processess that prevent injected carrier density from further increasing. This superlinear dependence on injection is a unique feature of direct gap light emission in the indirect band gap Ge. As we discussed in Section 4.3.1, the direct light emission intensity is determined by the number of the injected electrons in the direct Γ valley $n_{e\Gamma}$ and can be further expressed as

$$P_\Gamma \propto n_{e\Gamma} = n_{\text{tot}} \cdot f_\Gamma, \tag{5.21}$$

where n_{tot} is the total injected electron density and f_Γ is the fraction of the electrons injected into the direct Γ valley. The total injected electron scales linearly with the injected electrical current. The fraction term also increases with the injection level due to the increase of the electron quasi Fermi level leading to more electrons scattered into the direct Γ valley. The

multiplication of these two terms results in a superlinear behavior of the integral direct gap EL with electrical current.

The theoretical calculation based on the analysis above is performed as shown by the solid curve in Fig. 5.13 and it agrees well with the experimental data. The small difference between the theoretical and the experimental result is due to the small deviation from the square-root density of states near the band edge. This result again supports the theory that the efficiency of the direct gap luminescence in Ge benefits from high carrier injection as we analyzed in Chapter 2. But net gain can not be achieved by solely increasing the carrier injection due to the increased free carrier absorption. The introduction of n-type doping in Ge is necessary to overcome this issue and lead to laser action.

In this section, we demonstrate the first observation of the direct band gap EL from a Si/Ge/Si heterojunction light emitting diode at room temperature. The room temperature direct gap EL spectrum is consistent with the PL spectrum. The integral EL intensity increases superlinearly with electrical current because the direct gap luminescence efficiency benefits from an indirect valley filling effect to scatter more electrons to the direct valley under injection, which agrees with our theoretical calculation.

5.5 n^+Ge-on-Si Diode Design

To increase the direct gap light emission intensity as well as light emission efficiency in Si/Ge/Si diode, Ge has to be doped with n-type impurities to increase the number of the electrons injected into the direct Γ valley. In this section, some design issues of such a n+Ge light emitting diode is discussed.

5.5.1 Electrical Injection in a Si/Ge/Si p-n-n Diode

By replacing the intrinsic Ge with n^+Ge, the Si/Ge/Si p-i-n diode becomes p-n-n diode which is unusual for a light emitting diode. One immediate doubt of such a diode may be that the junction and the active region occurs only near the n^+Ge/p^+Si interface. This is not true since the p+Si and n+Si regions are also heavily doped and create a built-in voltage to inject the whole Ge region with both electrons and holes from the two adjacent Si layers

respectively.

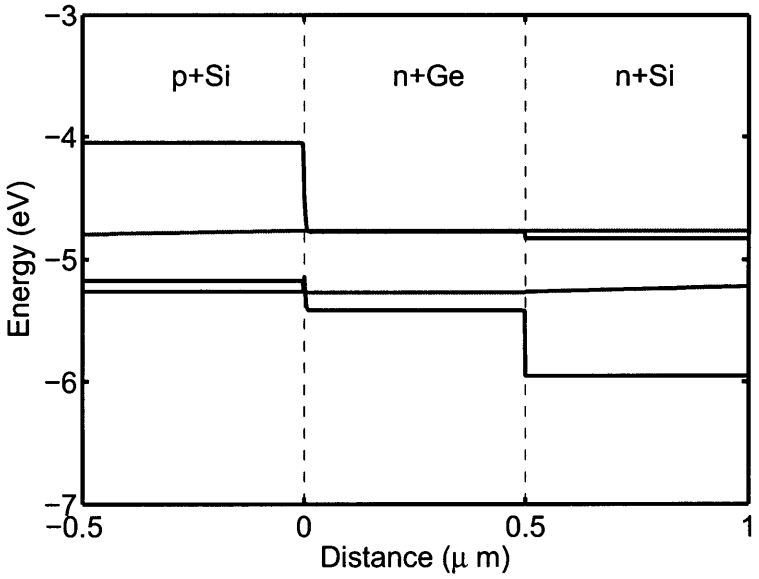

Figure 5.14: Band diagram of a $p^+Si/n^+Ge/n^+Si$ diode at 0.5 V forward bias. The doping concentrations in $p^+Si/n^+Ge/n^+Si$ are 1×10^{20} cm^{-3}, 1×10^{19} cm^{-3}, and 1×10^{20} cm^{-3}, respectively

The simulated band diagram of a $p^+Si/n^+Ge/n^+Si$ diode at 0.5 V forward bias shown in Fig. 5.14 underlies the fact that both electron and hole quasi Fermi levels shift from their equilibrium position to band edge leading both types of carriers injected into Ge.

The simulated I-V characteristic of this $p^+Si/n^+Ge/n^+Si$ diode shown in Fig. 5.15 exhibits the same rectifying behavior as that of the Si/Ge/Si p-i-n diode indicating the same injection process in both cases. An ideality factor of 1.5 obtained at small forward biases is equal to that in the simulation of a p-i-n diode.

By using the approach discussed in Section 5.2.2, the direct gap light emission intensity and the internal quantum efficiency can be calculated with the simulated quasi Fermi level and electrical current. The direct gap light emission intensity versus forward bias is calculated for both Si/Ge/Si p-i-n diode and p-n-n diode shown in Fig. 5.16. We can see that the light emission from the $p^+Si/n^+Ge/n^+Si$ diode is one order of magnitude larger than that of the $p^+Si/i\text{-}Ge/n^+Si$ diode above 0.4 V forward bias due to the increased number of the injected electrons in the direct Γ valley resulting from the filling of the indirect L valleys states in n-type doped Ge. Less light emission from the $p^+Si/n^+Ge/n^+Si$ diode below 0.4 V is because

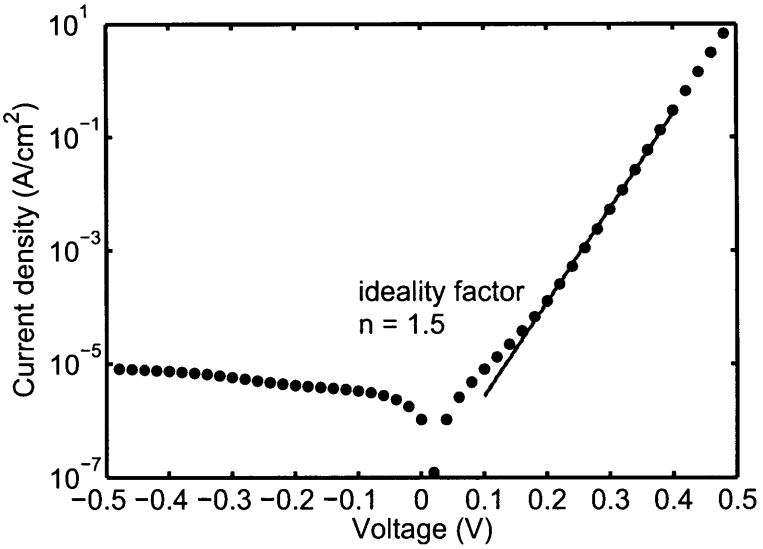

Figure 5.15: Simulated I-V characteristic of the $p^+Si/n^+Ge/n^+Si$ diode.

that the deficiency of injected holes in n-type doped Ge at small forward bias limits the radiative recombination. At higher injection level, the direct gap radiative recombination becomes limited by the number of the electrons in the direct Γ valley and the n-type doped Ge prevails the intrinsic Ge.

The light emission quantum efficiency is improved by over a order of magnitude in $p^+Si/n^+Ge/n^+Si$ diode as shown in Fig. 5.17. An internal quantum efficiency of $\sim 10^{-1}$, though still a few times smaller than III-V direct gap material based light emitters, makes Ge light emitting diode a very good choice for integrated light emitters at 1550 nm band. Compared to III-V devices, the Ge LEDs benefits from their lower material cost and fabrication complexity.

The internal quantum efficiencies of both type of diodes decrease beyond 0.6 forward bias because the carrier injection approaches saturation because the non-radiative recombination processes (e.g. Auger recombination) become sufficiently significant at high carrier concentration. This can be seen from the light emission intensity simulation in Fig. 5.16 that the light emission starts to saturate beyond 0.6 V forward bias. Since the current still increases rapidly[‡], the internal quantum efficiency decreases at higher injection current.

[‡]The current increases a little less than exponential due to the non-negligible series resistance at high current flow.

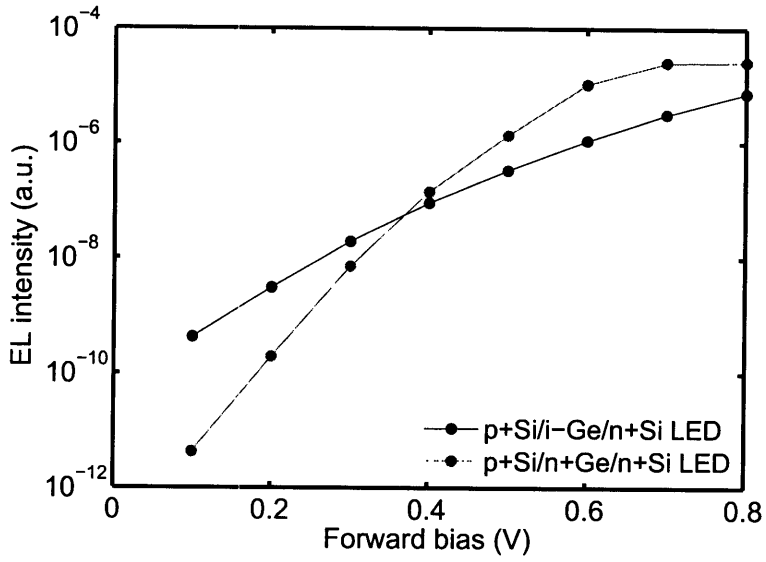

Figure 5.16: Calculated direct gap light emission intensities at various forward biases for both Si/Ge/Si p-i-n diode and p-n-n diode.

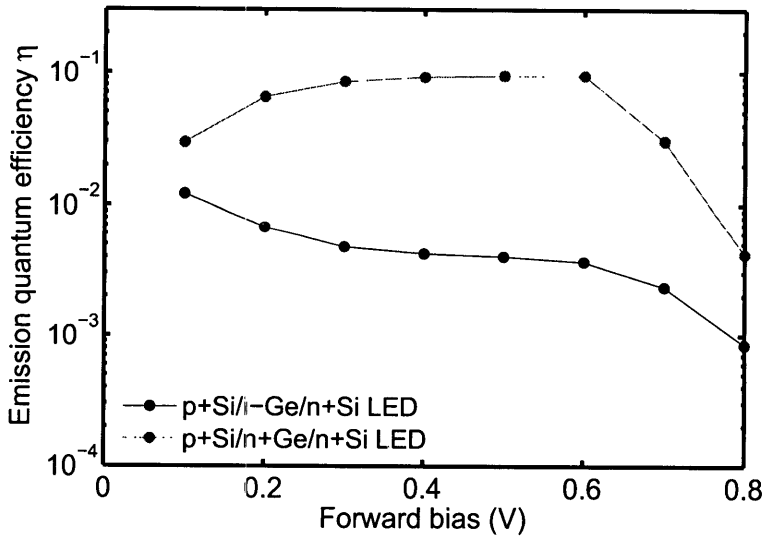

Figure 5.17: Calculated direct gap light emission quantum efficiency at various forward biases for both Si/Ge/Si p-i-n diode and p-n-n diode.

5.5.2 Si Doping Optimization

We have proved that $p^+Si/n^+Ge/n^+Si$ p-n-n diode is a better light emitter compared to its p-i-n counterpart in terms of both the emission intensity and quantum efficiency. In the previous simulations, the p^+Si and n^+Si regions are both doped at 1×10^{20} cm^{-3}. In this section, the dependence of these doping levels on the light emitter is investigated in details.

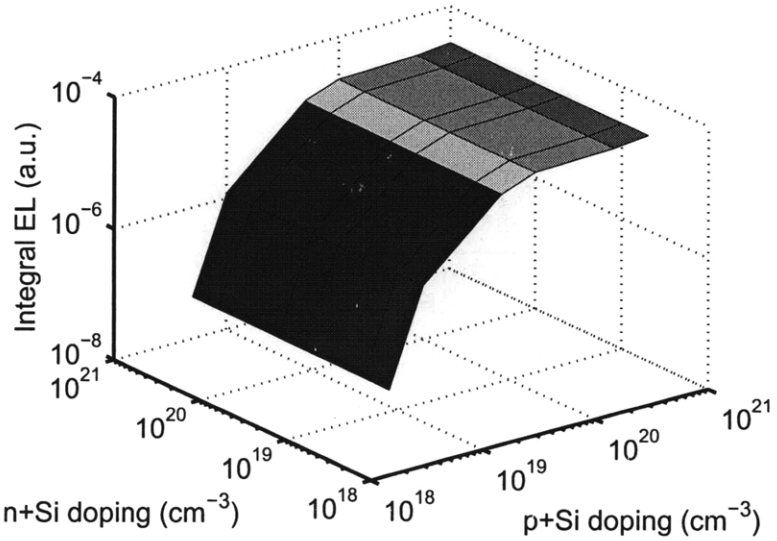

Figure 5.18: The calculated light emission intensity from the $p^+Si/n^+Ge/n^+Si$ p-n-n diode versus the doping concentrations in both p-type and n-typ Si regions at 0.5 V forward bias.

The light emission intensity from the $p^+Si/n^+Ge/n^+Si$ p-n-n diode versus the doping concentrations in both p-type and n-type Si regions at 0.5 forward bias is calculated and shown in Fig. 5.18. We can see the light emission is more sensitive to the doping level in p-type Si region below 1×10^{20} cm^{-3} because the concentration of the injected holes is less than that of the injection electrons in the direct Γ valley at 0.5V forward bias therefore limiting the light emission. The increase of the doping in p-type Si promotes the hole injection level leading to more direct gap radiative recombination. This effect diminishes above 1×10^{20} cm^{-3} doping in p-type Si since the injected holes becomes more than the direct Γ valley electrons which begin to limit the direct gap light emission instead. On the other hand, Ge is already heavily n-type doped thus the injected electrons in the direct Γ valley does not strongly depend on the doping level of n-type Si.

The internal quantum efficiency of the direct gap light emission also follows the similar

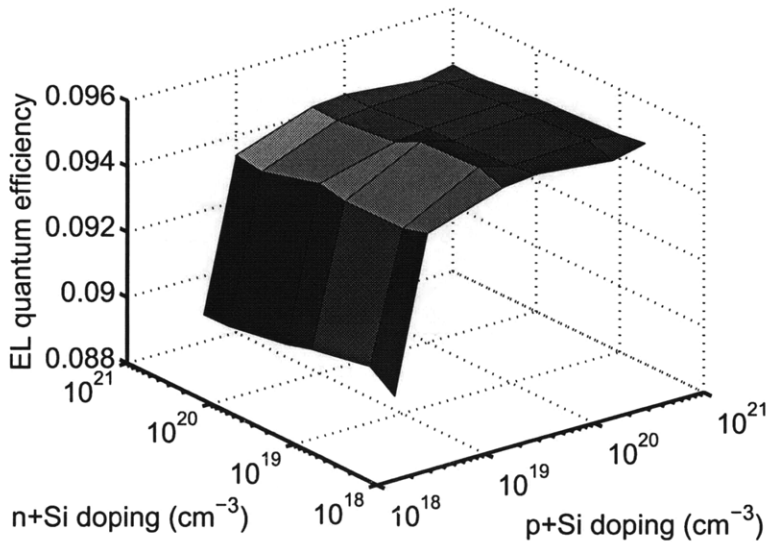

Figure 5.19: The calculated light emission quantum efficiency from the $p^+Si/n^+Ge/n^+Si$ p-n-n diode versus the doping concentrations in both p-type and n-typ Si regions at 0.5 V forward bias.

dependence on doping concentrations in both p-type and n-type Si region as shown in Fig. 5.19. This dependence can be explained similarly. The change of quantum efficiency is not as dramatical (orders of magnitude) as the light emission intensity does because the electrical current also decreases with the decrease of the doping concentration in p-type Si region, compensating the reduced light emission.

In order to design a $p^+Si/n^+Ge/n^+Si$ p-n-n diode with high light emission and quantum efficiency, the p-type Si region has to be doped above 1×10^{20} cm^{-3} while the n-type Si region can be doped relatively less (e.g. 1×10^{19} cm^{-3}). Since heavily-doped material absorbs light with photon energy even below its band gap (free carrier absorption), the doping in Si region is designed to be as low as possible. Therefore, 1×10^{20} cm^{-3} p^+Si and 1×10^{19} cm^{-3} n^+ Si is an appropriate combination for designing this $p^+Si/n^+Ge/n^+Si$ p-n-n light emitting diode.

5.5.3 Ge/Si Band Alignment

Since A $p^+Si/n^+Ge/n^+Si$ p-n-n device is a heterojunction diode, the band alignment between Si and Ge affects the current injection behavior hence the light emission properties. In this section, this effect is analyzed.

In III-V material based laser design, a material with larger band gap is usually used to

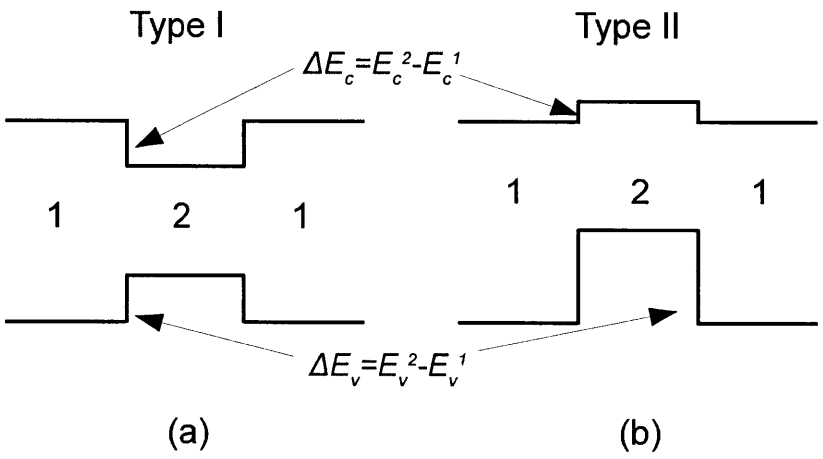

Figure 5.20: Schematics of type I and type II band alignment at Material 1/2 interface.

form a type I band alignment with the active (light emitting) material to inject electrons and holes more efficiently (carrier confinement). A type I band alignment, as drawn in Fig. 5.20 (a), is the conduction band edge of Material 2 is lower than that of Material 1 and the valence band edge of Material 2 is higher than that of Material 1. Therefore, when a p-i-n junction is formed, both electrons and holes injected in the Material II region have to overcome a potential barrier due to the band offset in order to leave the region, so that more carriers are confined leading to more radiative recombination events. On the other band, Ge/Si interface is usually believed to be a type II band alignment, as shown in Fig. 5.20 (b), which can only confine the injected holes.

The band offset of Ge/Si interface we used in all previous simulations is calculated from the difference of the electron affinity data of Ge (4.05 eV) and Si (4.0 eV) in Ref. [96]. So the band offset $\Delta E_c = -0.05$ eV for conduction band and $\Delta E_v = 0.51$ eV for valence band. However, the band offset calculated from the difference between the affinity data of the materials is not accurate since the interface condition can possibly change the band offset. $\Delta E_c = -0.01$ eV, hence $\Delta E_v = 0.47$ eV, was reported in a work on strained $Si_{1-x}Ge_x$ alloys on $Si_{1-y}Ge_y$ substrates [130]. Another work claimed $\Delta E_v = 0.36 \pm 0.02$ eV, hence $\Delta E_c = 0.1$ eV, measured for relaxed Ge on Si grown by ultra-high vacuum chemical vapor deposition (UHV-CVD) [131]. In that case, the band alignment between Ge and Si becomes type I providing both electron and hole confinement.

Moreover, there are some techniques that can be used to engineer the band offset of the Si/Ge interface. It has been shown that SiGe alloy with some proper compositions can provide type I band alignment with Ge. For example, the conduction and valence bands of $Si_{0.17}Ge_{0.83}$ are 0.15 eV higher and 0.1 eV lower than those of pure Ge, respectively [130]. Therefore, SiGe can also be used as a barrier layer in this heterojunction structure. A nano-crystalline Si film is another alternative to replace the Si layers in the $p^+Si/n^+Ge/n^+Si$ p-n-n diode design since it has larger band gap than single crystalline to provide more band offset to form type I band alignment.

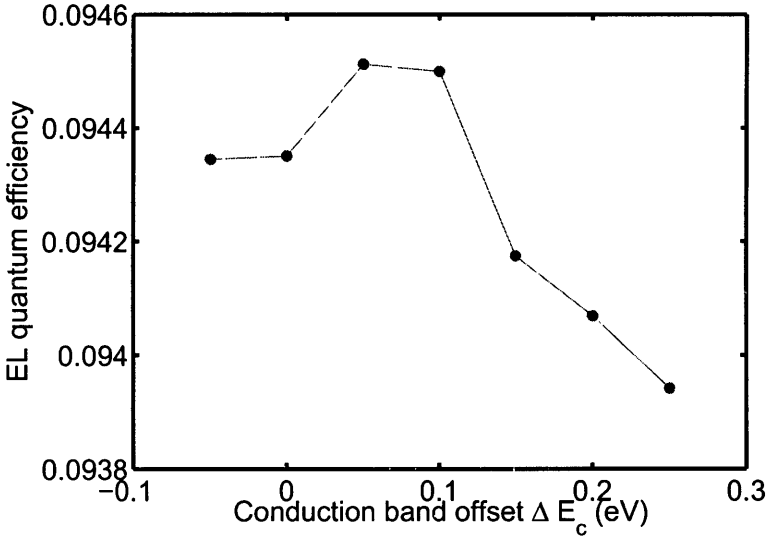

Figure 5.21: The internal quantum efficiency of the direct gap light emission from $p^+Si/n^+Ge/n^+Si$ diode versus the conduction band offset of Si/Ge interface.

The effect of the band alignment of Si/Ge on the internal quantum efficiency of the direct gap light emission is shown in Fig. 5.21. We can see the internal quantum efficiency does benefit from the type I band alignment ($\Delta E_c > 0$) below a certain conduction band offset of Si/Ge interface (0.1 eV). The efficiency decreases at larger band offset due to the reduction of the hole confinement since the number of the injected holes is small in the heavily n-typed doped Ge thereby limiting the light emission as well. We can also see that the band alignment does not strongly affect the internal quantum efficiency like the case in a common heterojunction diode because the heavy n-type doping in Ge diminishes the injected electron confinement effect.

In order to design a laser device with higher slope efficiency, a strained-Ge/Si quantum well structure can be considered. The use of the strained Ge quantum well can be benefit from the enhanced electrical current injection efficiency. But the energy of the direct Γ valley of the conduction band raises more than the indirect L valleys under the quantum confinement effect. This energy level shift decreases the number of the injected electrons in the direct Γ valley. The net effect of the quantum well structure is determined by the competition of these two effects. This subject is worth further investigation.

Chapter 6

Optical Gain from Ge

We have demonstrated that Ge, though an indirect band gap material, can be engineered for direct gap light emission at room temperature. The direct gap light emission can be either excited optically (Chapter 4) or electrically (Chapter 5). All experimental results support our theory about using n-type doping and tensile strain to engineer Ge for more efficient direct gap light emission. The theory also predicts that Ge, with sufficient n-type doping level, can be a gain medium. In this chapter, the study of the optical gain from Ge is discussed. First, the pump-probed approach used to study optical bleaching and optical gain is introduced. Then we discuss the phenomenon of the optical bleaching effect at direct band gap energy from both Ge-on-insulator and tensile-strained n^+Ge epitaxial films. Finally, the observation of net gain from a Ge mesa is demonstrated followed by a comparison of optical gain and inversion factor between the Ge films with different doping levels.

6.1 Pump-Probe Spectroscopy Measurement

Pump-probe spectroscopy, different from a PL spectroscopy which studies the spontaneous emission, is a approach to study the stimulated optical transition process in an active material under carrier injection. In pump-probe measurement, a probe light is introduced along with the pump (excitation) light therefore the characteristic of the optical transition (absorption and stimulated emission) at the photon energy (or wavelength) of this probe light is investigated.

There are a number of different types of pump-probe experiments. The pump source can either be a pulsed laser or be a continuous-wave (CW) laser. The pulsed laser is usually used to obtain information of ultrafast phenomena in materials by monitoring the time decay of the probe signal. The pump source used in this work is a continuous-wave laser since we want to study the gain characteristics of Ge under as close as the operating condition in real applications. In both the optical interconnects and optical telecommunication applications, a continuous-wave light source is preferred. Then an electro-optical modulator is used to modulate the light to carry information instead of direct modulation of the laser since it allows independent optimization of the laser and the modulator for better system performance.

The probe laser in a pump-probe measurement can be the pump laser itself (usually with a certain time delay) or a different laser. The former approach is called degenerate pump-probe measurement while the latter one is called non-degenerate pump-probe measurement. The non-degenerate approach with a wavelength tunable laser as the probe laser is used in this work in order to study spectral information of the optical bleaching and optical gain near the direct band gap energy of tensile-strained Ge.

6.1.1 Measurement Setup

The pump-probe experiment setup is schematically drawn in Fig. 6.1. A Sumitomo SLA5633-XC/JD1 1480 nm semiconductor laser is used as the pump light. The laser has a maximum output power of 100 mW. The probe source is a HP (Agilent) 81640A tunable laser module embedded in a HP 8164A lightwave measurement system. It is an external cavity laser whose wavelength can be tuned from 1515 nm to 1640 nm. The maximum of output light power is 800 μ W at 1550 nm and decreases at both shorter and longer wavelengths. Both the pump laser and the probe laser are fiber coupled output. These single-mode fibers of the two lasers are combined to another single-mode fiber through a wavelength division multiplexing (WDM) coupler. The end of coupler output fiber is placed on top of a sample. The light traveling through the fiber arrives perpendicularly on the front side of the sample. The transmitted light is collected by the integral optical head of an optical power meter placed at the backside of the sample. There is widely opened hole on the optical head for incident light coming through and a empty cavity connecting to the hole to trap almost all the incoming

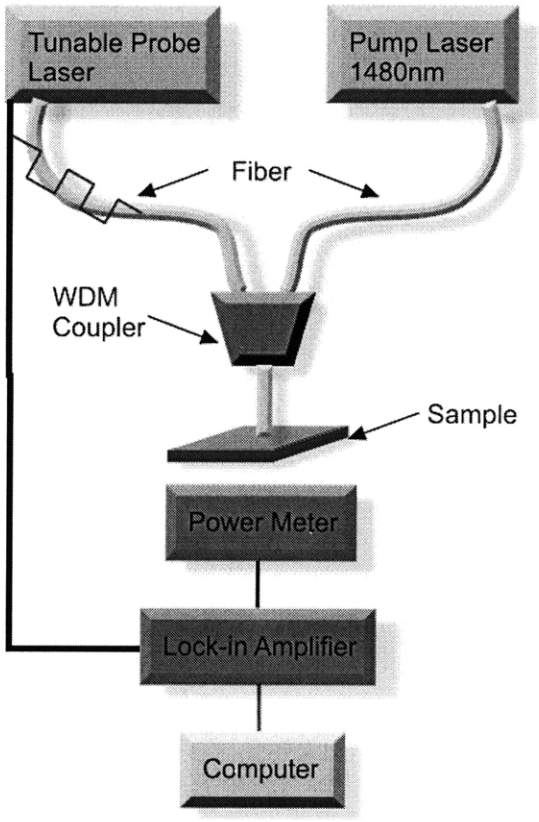

Figure 6.1: Schematic of the pump-probe measurement.

light. The light power is measured by an InGaAs photodetector in the cavity.

To be distinguished from the pump light, the probe light is internally modulated at 500 Hz. A lock-in amplifier synchronized at the same 500 Hz frequency is used to analyze the photodetector signal. This lock-in approach effectively blocks DC pump signal and noises with frequencies other than 500 Hz therefore increases the signal-to-noise ratio. The continuous wave operation of pump laser assures a steady-state injection level while the probe light transmittance is monitored.

A close-up picture of the experiment setup is shown in Fig. 6.2. The fiber is fixed in a vertical track on a stage capable of X-Y-Z manipulation. The end of the fiber is either a pigtail shown in the figure or packaged with a standard connector (e.g. a FC-PC connector). One issue we met in the measurement is the air gap between the flat fiber head and the top surface of the sample results in Fabry-Perot interference superimposed with the real signal. This interference effect makes the precise determination of the absorption in the materials

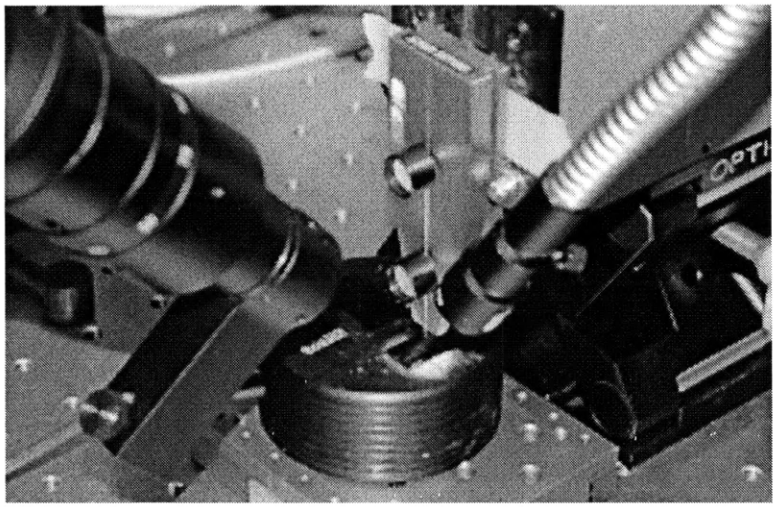

Figure 6.2: Picture of the pump-probe measurement setup.

difficult. This problem can be solved by using some index matching fluid (refractive index equal to that of the silica composing the fiber core) between the fiber and sample.

The cylindrical object under the sample is the optical head. The cavity and photodetector used for light trapping and detection are located in the optical head. The lens system in the picture is connected to a CCD camera used for fiber alignment.

6.1.2 Measurement Procedures

The pump-probe measurement on a Ge-on-Si sample is accomplished with the following steps:

Firstly, the incident light power of the modulated probe laser coming out of the fiber is measured by positioning the fiber head in the cavity of the optical head through the top opening. The light is measured by the photodetector in the cavity. The reproducibility of the light trapping in the cavity was tested by moving the fiber end around in the cavity. No appreciable change of optical power meter reading indicates the insensitive dependence of the fiber position. A LABVIEW program is used to perform a wavelength scan of the probe laser. The reading of the lock-in amplifier at each probe laser wavelength is recorded in the program to obtain a reference incident light power spectrum. This reference spectrum is calibrated each time before a pump-probe measurement.

Then a sample is placed on top of the optical head (covering the opening on the surface).

The end of the fiber is positioned as close as possible on the sample surface with the help of the CCD camera image. The index matching fluid is used if necessary. The tunable probe laser is turned on and a wavelength scan is performed. The recorded signal from the lock-in amplifier represents the transmitted light power at each wavelength. The ratio of the transmitted light power to the incident light power at each wavelength gives the transmittance spectrum of the Ge/Si stack.

Finally, the power laser is turned on and the transmitted light power of the modulated probe laser is measured again. Now, the ratio of the transmitted light power to the incident light power is the transmittance spectrum of the Ge/Si stack under pumping (carrier injection). The difference between the two transmittance spectra (without pumping or under pumping) gives information of the stimulated optical transition in Ge.

6.1.3 Data Analysis

The optical absorption measured at a certain wavelength is a net result of the stimulated emission and stimulated absorption. A negative optical absorption means net gain and a positive optical absorption means net loss. In order to study the net gain/loss, the optical absorption must be calculated from the transmittance spectrum measured from the pump-probe experiment.

We re-write Eq. 2.16 in Chapter 2 here:

$$g(h\nu) = \alpha(f_c - f_v), \tag{6.1}$$

where the inversion factor $(f_c - f_v)$ describes the differential occupation probability of the electron in the conduction band and in the valence band. This inversion factor ranges from -1 to 1. In the case of zero pumping (carrier injection), $(f_c - f_v) = -1$. Thus the absorption of the materials is just $-\alpha$ (negative value means net loss). This can be called the small-signal absorption. As the carrier injection level increases, $(f_c - f_v)$ increases from -1 towards 0. Thus the measured optical absorption becomes less (in absolute value). This phenomenon is called optical bleaching effect. At a sufficiently high injection level making $(f_c - f_v) = 0$, the material becomes transparent. The corresponding injected carrier density is called the

transparent carrier density Δn_{trans}. When the injection level further increases resulting in $(f_c - f_v) > 0$, the optical absorption becomes positive meaning the occurrence of net gain.

Another optical absorption mechanism, free carrier absorption, must be considered at high injection levels. Free carrier absorption is an electron in the conduction band absorbs the energy of a photon and moves to an empty state higher in the conduction band (correspondingly for holes in the valence band) without inter-band recombination. Free carrier absorption is considered in Chapter 2 in order to calculate the net material gain. For n^+ Ge, the free electron absorption dominates the free carrier optical loss unless the injected carrier density is as high as or higher than the extrinsic electron density. The net gain/loss measured or calculated in the experiment includes both the optical gain/loss and the free carrier absorption. Therefore,

$$g_{\text{tot}}(h\nu) = -\alpha_{\text{tot}}(h\nu) = \alpha(f_c - f_v) - \alpha_{\text{fc}}, \tag{6.2}$$

where α_{fc} is the free carrier absorption. The existence of the free carrier absorption increases the injection level required for the transparency or net gain.

In the transmittance measurement, the absorption of the material measured without pumping is the small-signal absorption $-\alpha$ while it becomes $g_{\text{tot}} = -\alpha_{\text{tot}}$ under carrier injection. A positive g_{tot} or a negative α_{tot} means the occurrence of net gain.

The ratio of these two absorptions can be used to calculate the inversion factor:

$$(f_c - f_v) - \frac{\alpha_{\text{fc}}}{\alpha} = -\frac{\alpha_{\text{tot}}}{\alpha}. \tag{6.3}$$

Because of the existence of the free carrier absorption, this ratio is smaller than the inversion factor $(f_c - f_v)$. The deviation from the inversion factor increases with injection level and wavelength since the free carrier absorption increases with both carrier density and wavelength. In the analysis of the inversion factor in Section 6.3.2, the "inversion factor" denotes to the value calculated by using $-\frac{\alpha_{\text{tot}}}{\alpha}$. Therefore, the calculated "inversion factor" could be smaller than -1 which can be seen in the comparison of the inversion factor between different samples in that section.

It can be seen that it is very important to accurately obtain the absorption of Ge in order to study the carrier inversion phenomenon. Since the samples used in the pump-probe experiment are Ge/Si double layer or Ge/Si/Ge multi-layer (Ge epitaxy on both side of Si substrates) structures, the absorption of Ge can not be simply calculated because of the interference effect. Transfer matrix method (TMM) is a useful tool to calculate the transmittance from a multi-layer stack with known refractive index and absorption data of each layer. Similarly, the refractive index and the absorption data can also be solved from the transmittance using TMM. But two unknowns, the refractive index and the absorption, can not be solved simultaneously from one equation (TMM). However, the refractive index and the absorption of any material is correlated by the Kramers-Kronig (K-K) relations which are mathematical properties of any analytic complex function (the polarization $\mathbf{P}$ of the material in this case). Therefore, two unknowns, the refractive index and the absorption, can be solved from these two equations (TMM and K-K). Since both equations are non-linear functions of the refractive index and the absorption, the absorption is calculated using an iterative self-consistent regression approach. The details about this approach is explained in Appendix C.

A particular issue needs to be addressed in the TMM calculation. Because the thickness of the Si substrate in any Ge epitaxial film sample is much thicker (>600 μm) than the coherence length of the light source used in the experiment, no interference exists in the Si layer which is confirmed by no observation of the dense interference peaks in the measured transmittance spectrum*. Thus, a modified TMM approach considering the non-coherency of the Si substrate layer is used in the data analysis instead, which is explained in details in Appendix B.

The accuracy of the absorption data obtained from the pump-probe measurement is very important to evaluate the optical bleaching and the net gain. The error of the pump-probe experiment is carefully examined in order to be confident about the conclusion we made based on these data. With the lock-in approach described in the Section 6.1.1 we can clearly resolve 0.5% relative difference in the transmittance of the probe laser, so an accuracy of ± 0.25

*The free spectral range, the spectral distance of two successive interference maxima or minima, is inversely proportional to the thickness of the layer. Therefore, if the interference exists in the Si layer, there would be very dense interference peaks observed ($\approx$ 0.5 nm at the wavelength range).

% in transmittance measurement is guaranteed. To be even more conservative, a ±0.4% transmittance error bar is adopted to estimate the error in the absorption/gain coefficient data.

In fact, the transmittance is more likely to be underestimated than overestimated in the experiment because the input optical power from the fiber-pigtailed laser, P_{in}, can be easily measured accurately by placing the tip of the optical fiber in close proximity to the photodetector. While the transmitted optical power through the sample, P_{out}, could be underestimated in the measurement since the laser beam diverges after passing through the sample and may not be completely collected by the photodetector. Considering that an underestimated transmittance leads to an overestimated absorption coefficient, subsequently an underestimated gain coefficient. Therefore the transmissive pump-probe measurement used in this work is actually a conservative approach to determine optical gain. It is also to be noted that the system error of the photodetector and the read-out circuits are cancelled out in the transmittance measurement since P_{in} and P_{out} are measured with exactly the same system and condition.

To estimate the upper and lower limits of the gain coefficient data, we vary the measured transmittance by the largest possible measurement error of +0.4% and -0.4%, respectively, and derive the corresponding absorption/gain coefficient using the iterative self-consistent regression approach mentioned earlier.

6.1.4 Comparison with Variable Stripe Length Method

Variable stripe length (VSL) measurement is usually used to study the optical gain in a material. However, there are at least two drawbacks of VSL that advises me to use a pump-probe spectroscopy measurement instead.

The most important reason is the pump power density consideration. We need a relatively higher pump power to inject tensile-strained n+Ge for optical gain since it supports less gain than direct band gap semiconductors does (refer to Chapter 2), especially the n-type doping concentration we can doped in Ge is not as high as we want as discussed in Chapter 3. Therefore, a high pump power density is required to inject sufficient high carrier concentrations. Since the maximum power of the pump laser is fixed, the requirement means a smaller pump

area is preferred.

As we showed in the above, the pump light coming out the fiber has a circular spot area of $\sim 10^{-2}$ μm^2. In VSL measurement, the pump light is required to be shaped to narrow stripe with a cylindrical lens and the length of the stripe is usually in the order of mm. To archive the same injection level as we have in the pump-probe measurement, the width of the strip need to be $\sim 10^{-1}$ μm which is almost impossible to be achieved by a free-space lens system. Moreover, even this submicron width focusing can be done, in order to observe net gain, as we will show in Section 6.3, the Ge has to be fabricated to confine the carriers. To have a high quality Ge stripe (waveguide) with width less than μm is very challenging.

Another reason that let us choose pump-probe measurement over VSL measurement is the error control. Both VSL and pump-probe measurements have multiply sources of errors, but the errors in pump-probe measurement can be reasonably analyzed and corrected as we in the last section. On the other hand, VSL measurement suffers from a number of errors, such as edge effect and artifacts due to the quality of the blade, which are not easy to eliminate.

6.2 Direct Gap Optical Bleaching

In this section, the results of the pump-probe measurement on both Ge-on-insulator and tensile-strained n^+ Ge are discussed. Room temperature optical bleaching is observed for both cases. The optical bleaching effect is the reduction of the absorption because of the electron occupation in the empty higher energy states required in the absorption process. This phenomenon is important since it is the prelude of the net gain. Further occupation of the electrons in the higher energy states leads to population inversion. The net gain occurs if the positive optical gain overcomes the optical loss dominated by free carrier absorption.

6.2.1 Ge-on-Insulator

Similarly as we did in Chapter 4, a thin film of bulk single crystalline Ge is a good starting point to study the optical properties. The results of the crystalline Ge can be used to compare the results of tensile-strained n^+ Ge. The same Ge-on-insulator (GeOI) sample used in the PL studies in Section 4.2.2 is used in the pump-probe measurement.

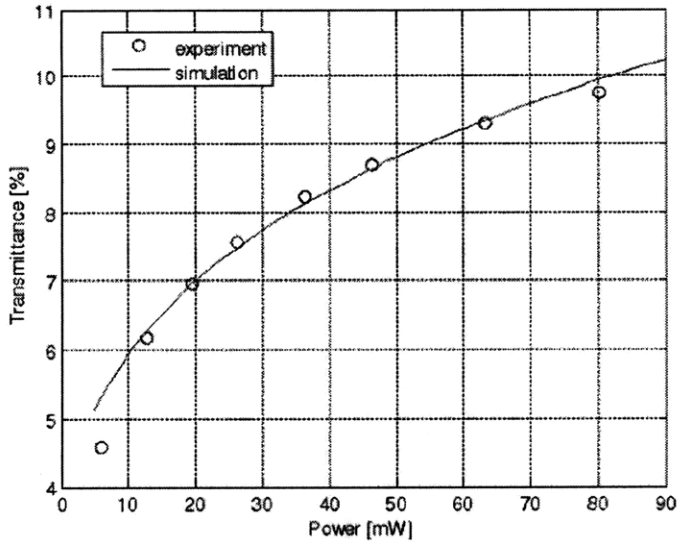

Figure 6.3: The measured and the calculated transmittance of the pump laser light as a function of laser output power of the Ge-on-insulator.

Before turning on the probe laser, the transmittance of the pump laser light versus laser output power is measured and the result is shown in Fig. 6.3. This measurement is a degenerate pump-probe measurement in which the pump light and the probe light are the from the same laser. The enhancement of the transmittance with pump power underlies the occurrence of the optical bleaching effect at the pump wavelength.

The transmittance enhancement thus the optical bleaching starts to saturate at high injection levels due to non-radiative recombinations usually dominated by Auger recombination. The non-radiative recombination becomes significant at higher injected carrier densities limiting the number of the injected carriers in radiative recombination. This effect can be modeled using a rate equation approach. The injected excess carrier density is solved from a equation system composed of the carrier rate equation in steady-state:

$$0 = \frac{j}{V} - K(f_c - f_v)n_{ph} - \frac{1}{V}Kf_c(1 - f_v) - R_{nr} \tag{6.4}$$

and the photon rate equation in steady-state:

$$0 = K(f_c - f_v)n_{ph} + \frac{1}{V}Kf_c(1 - f_v) - v_g\alpha_{\mathrm{fc}}n_{ph}, \tag{6.5}$$

where n is the excess carrier density, n_{ph} is the photon density. f_c and f_v are electron occupation probabilities at the optical transition energy levels at a given photon energy. The formula of these two terms can be found in Chapter 2. R_{nr} is the non-radiative recombination rate including Auger recombination and defect-assisted recombination. α_{fc} is the free carrier absorption proportional to n. v_g is the group velocity of light in the material. V is either the active region volume or the photon volume which are the approximately same for the Ge films without any modal confinement. K is the optical transition rate coefficient of spontaneous emission, stimulated emission and absorption which can be proven to be equal for a specific optical transition such as direct band-to-band optical transition in this case. The relations between K, the small signal absorption coefficient $\alpha = \alpha(n)$ and the gain coefficient $g = g(n)$ are given by:

$$K = \frac{v_g}{f_v(1 - f_c)}\alpha = \frac{v_g}{f_c - f_v}g. \tag{6.6}$$

f_c, f_v, R_{nr}, α_{fc}, K, α and g are all a function of excess carrier density n. j is the optical injection rate is determined by the incident light power and the absorption in the Ge layer.

Using Eq. 6.4 and Eq. 6.5, we can calculate the injected excess carrier density n at a given optical injection rate j and the absorption coefficient at n. Because both the direct Γ valley and the indirect L valleys are considered in Ge, multiply K, f_c and f_v are required to taken into account for the four transitions between the direct Γ valley or the indirect L valley and the light hole band or the heavy hole band. The transition matrix element of the Γ valley to the light hole or the heavy hole band is calculated from the absorption spectrum of Ge sample as discussed in Ref. [90]. For the indirect transitions, a transition coefficient of 5.1×10^{-15} cm^3/s is obtained from Ref. [132].

The modified transfer matrix method (TMM), as we mentioned earlier, is used to calculate the transmittance at a given injection level calculated from the pump power. The calculation result which well agrees with the experimental result is shown in Fig. 6.3 with solid line.

The modulated probe light combined with the continuous-wave pump light is then launched into the GeOI samples. The measured transmittance spectra at various pump powers is shown in Fig. 6.4. The increase of the transmittance below a wavelength of 1550 nm or above a photon energy of 0.8 eV, corresponding to the direct band gap energy in bulk Ge, underlies

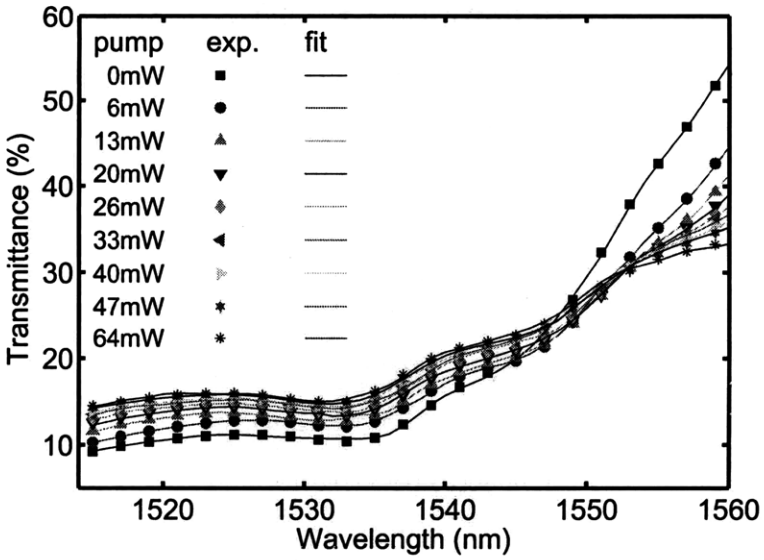

Figure 6.4: The transmittance spectra of the probe light at various pump powers measured from the Ge-on-insulator. The transmittance spectra is fitted using modified TMM to extract the refractive index and absorption data.

the occurrence of the optical bleaching effect. The decrease of the transmittance above 1550 nm is a result of the lack of gain mechanism and the existence of the free carrier absorption at high injection levels.

Using the iterative self-consistent regression approach mentioned earlier in Section 6.1.3, the absorption coefficient data is calculated from the measured transmittance and shown in Fig. 6.5. The optical bleaching effect can be clearly seen from the decrease of absorption coefficient at wavelengths below 1550 nm (i.e. photon energies above 0.8 eV). The optical bleaching effect begins to saturate at about 60 mW corresponding to the saturation of injected carrier density exhibited in Fig. 6.3.

The increase of absorption coefficient at wavelengths above 1550 nm is a result of the free carrier absorption. But the increase of the absorption is more than the free carrier absorption calculated using the data from Ref. [91, 92]. The more-than-expected absorption may be a result of the optical transition at longer wavelength observed in the PL study of the GeOI in Section 4.2.2. This optical transition or absorption phenomenon is not observed in Ge epitaxial films. The physical origin of the unique feature of GeOI samples is speculated in Section 4.2.2.

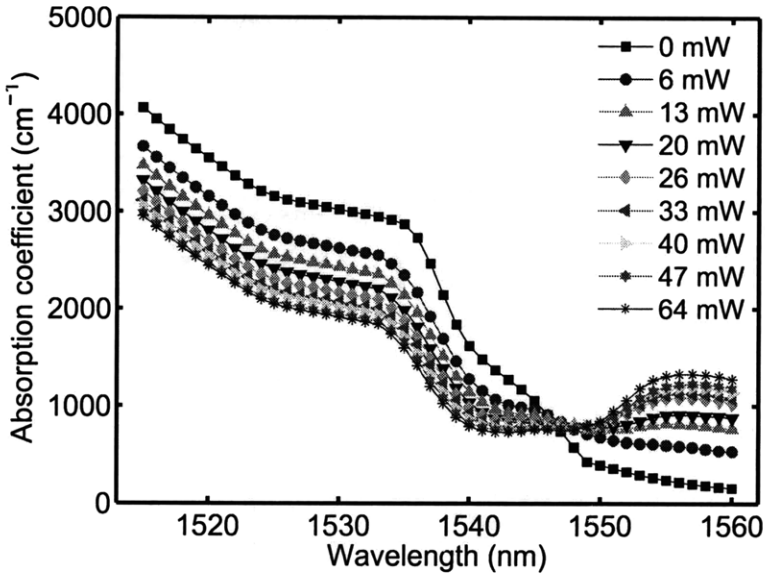

Figure 6.5: The absorption coefficient spectra of Ge-on-insulator calculated from the transmittance spectra at various pump powers. The reduction of absorption below 1550 nm (above 0.8 eV) is a result of the optical bleaching effect.

6.2.2 Tensile-Strained n^+ Ge

A pump-probe measurement is performed on a Ge epitaxial film with 2×10^{18} cm^{-3} n-type doping and 0.2% tensile strain. The thickness of the film is about 1.3 μm. The probe light transmittance spectra of the sample at 0 and 100 mW pump power are shown in Fig. 6.6. The injected carrier density is estimated to be mid 10^{18} cm^{-3} at 100 mW pump power. The transmittance starts to decrease dramatically at wavelengths below 1610 nm as a result of the direct band gap absorption. Under optical pumping, the transmittance of the Ge film is expected to change because of to two reasons. On one hand, the direct gap absorption is decreased due to the band filling by optically injected carriers, i.e the optical bleaching effect. On the other hand, the optically injected free carriers in the conduction and valence bands increase the free carrier absorption thereby decreasing the transmittance. Overall, the change in transmittance upon optical pumping reflects the competition between the decrease in the direct band gap absorption and the increase in the free carrier absorption.

Experimentally, we observe that the transmittance at wavelengths below 1592 nm increases while the transmittance at wavelengths more than 1592 nm decreases under optical

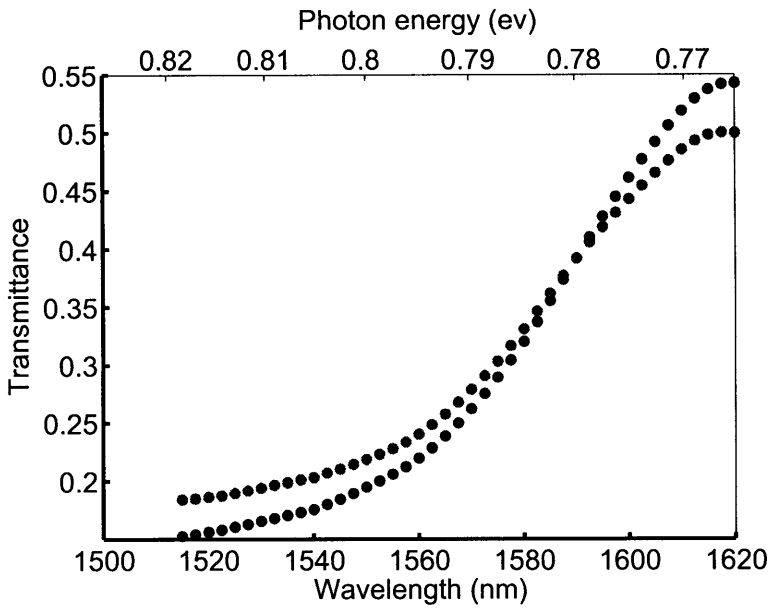

Figure 6.6: The transmittance spectra of the Ge epitaxial film with 2×10^{18} cm^{-3} n-type doping and 0.2% tensile strain at 0 and 100 mW pump power, respectively.

pumping (see Fig. 6.6). Since 1592 nm corresponds to the onset of the optical transition between the heavy hole valence band and the conduction band at the direct Γ valley, the experimental results indicate that the reduction in the absorption due to band filling is large enough to overcome the increase in free carrier absorption.

In the wavelength range of 1590-1620 nm, on the other hand, the transmittance decreases under optical pumping although the photon energy is still above optical gap between the direct Γ valley and the light-hole band. This observation indicates that the reduction in the absorption of the optical transition (from the direct valley to the light hole band) is not large enough to overcome the increase in the free carrier absorption because a much lower density of states of the light hole band compared to the heavy hole band results in a much lower optical gain.

We can define T_{pump}/T_0 as the transmittance enhancement factor under optical pumping, where T_{pump} is the transmittance at a given optical pumping level and T_0 is the transmittance without optical pumping. Fig. 6.7 shows a notable 1.2 fold transmittance enhancement at 1520 nm under 100 mW optical pumping. This result is the first observation of enhanced transmittance in epitaxial Ge-on-Si under stead-state optical pumping.

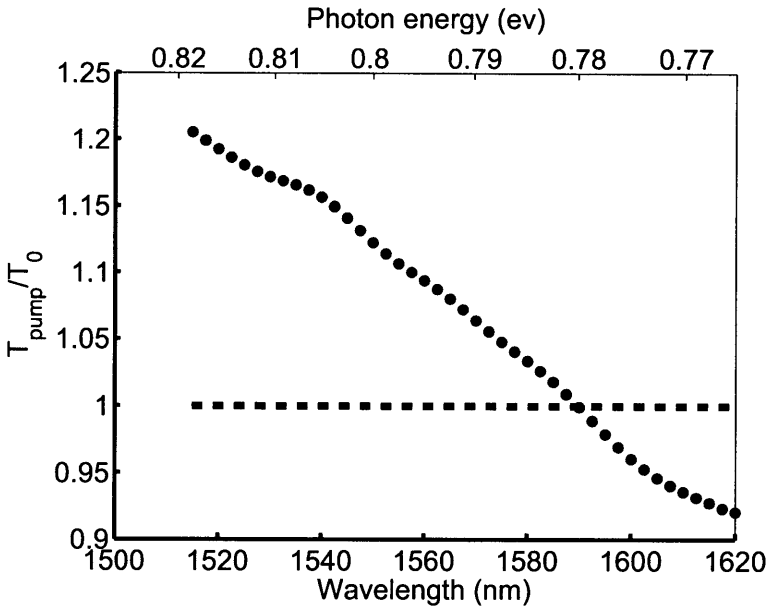

Figure 6.7: The transmittance enhancement factor (T_{100}/T_0) between 100 mW optical pumping and no pumping as a function of wavelength.

Fig. 6.8 shows the absorption spectra of Ge under 0 mW and 100 mW optical pumping calculated from the transmittance data in Fig. 6.6. As we analyzed earlier for the transmittance spectra, the optical bleaching effect reduces the absorption below 1592 nm. The absorption coefficient is reduced by as high as 500 /cm at 1520 nm under 100 mW optical pumping. The increase of absorption above 1592 nm is a result of increased free carrier absorption overwhelming the optical bleaching at this wavelength range.

It can be seen from Fig. 6.9 that the transmittance at 1520 nm increases linearly with pump power underlying that there is no sign of non-radiative recombinations such as Auger recombination. This result is quite different from the result of Ge-on-insulator shown in Fig. 6.4 in which a saturation of optical bleaching occurs. The result is very encouraging since it shows further optical bleaching effect can be achieved with higher injection levels. At sufficiently high injection levels, the optical bleaching effect may become the net gain. The comparison between tensile-strained n^+Ge and the intrinsic bulk Ge (GeOI) supports the calculation in Chapter 2 which states tensile-strained n^+Ge can be a gain medium while the intrinsic Ge can not. The injection level in the experiment is limited by the maximum output power of the pump laser. But the injection level or the injected carrier density can be further

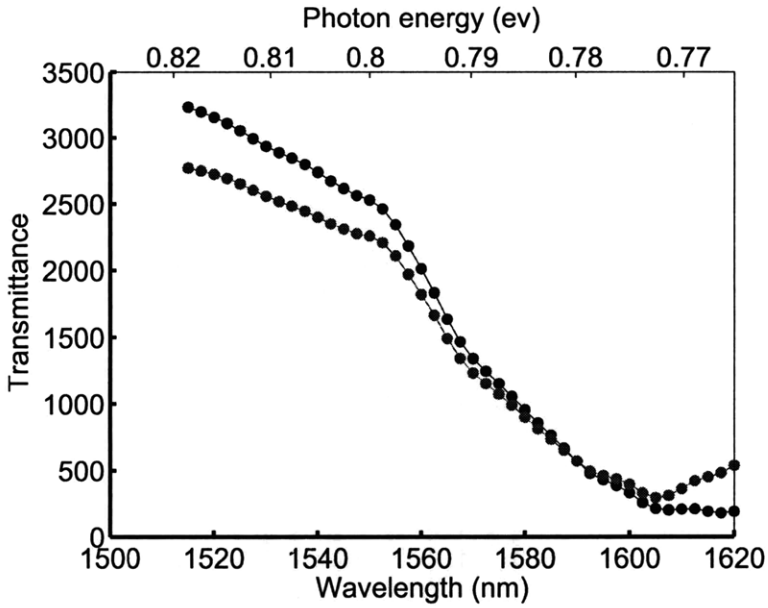

Figure 6.8: Absorption spectra under 0 and 100 mW optical pumping derived from transmittance data Fig. 6.6.

improved by using some carrier confinement structures. The reason of using these structures is that the injected carriers in Ge can diffuse laterally to a larger area and vertically into the bulk Si substrate. And the carrier diffusion increases the effective active volume leading to a lower injection level thus the injection level can be increased by confining these carriers in a small region. The effect of such structures are demonstrated in Section 6.3.1.

6.3 Net Gain

The optical bleaching effect is observed from both the Ge-on-insulators (intrinsic bulk Ge films) and the tensile-strained n^+Ge epitaxial films. It has been shown in the previous section that the optical bleaching of the intrinsic bulk Ge starts to saturate at pump powers above 60 mW while the optical bleaching of the tensile-strained n^+Ge increases linearly with the pump power even at as high as 100 mW. This linear behavior encourages us to further increase the injection level to achieve greater optical bleaching and net gain. As we discussed earlier, the injected carrier diffusion increases the effective active volume leading to a lower injection level. Therefore, the injection level can be increased by confining these carriers in

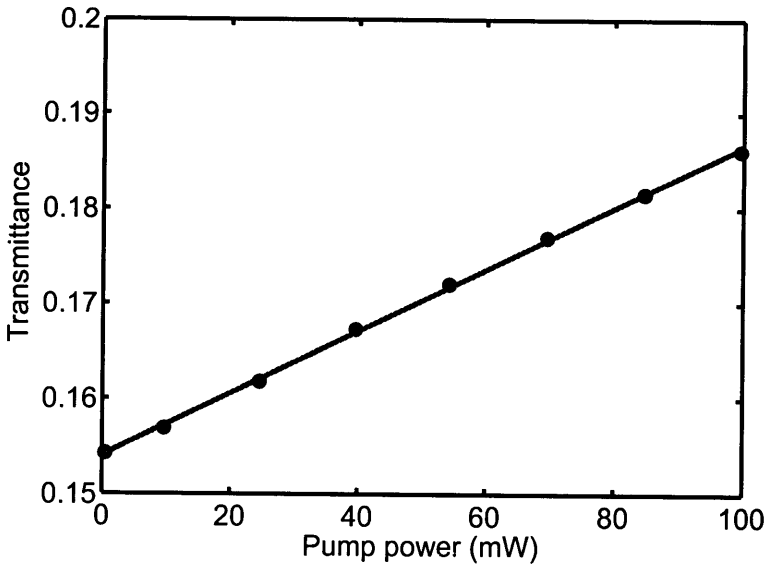

Figure 6.9: The linear relation of the transmittance of the probe light at 1520 nm to the pump laser power measured from the Ge epitaxial film with 2×10^{18} cm^{-3} n-type doping and 0.2% tensile strain.

a small region. In this section, we use mesa structures of Ge to confine the injected excess carriers in order to achieve high injection level. The net gain is observed subsequently from such mesa structures.

6.3.1 Onset of Net Gain from Ge Mesa

The pump power is limited up to 100 mW for the 1480 nm pump laser used in the experiment, so the only way to increase the injection level is to decrease the effective pumped volume where a large number of injected excess carriers (both electrons and holes) exist. This area is not necessary the incident light spot from the fiber output because the injected carriers diffuse from the high carrier concentration region to adjacent region thus increasing the effective pumped volume. The injected carriers can diffuse vertically into Si substrate or laterally into adjacent Ge region. A Ge mesa structure with a small dimension can be used to prevent the carrier lateral diffusion thereby increasing the injection level.

Such tensile-strained n^+Ge mesa structures were fabricated by selectively growing Ge in patterned Si regions defined by oxide trenches as discussed in Section 3.4.1. The scanning electron microscopy (SEM) image of a Ge circular mesa structure with a diameter of 25 μm

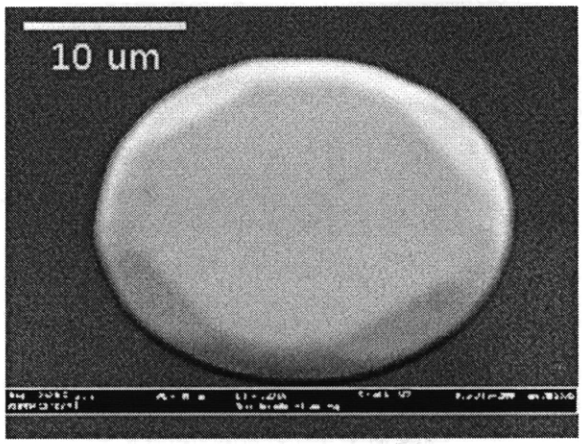

Figure 6.10: The scanning electron microscopy (SEM) image of a Ge mesa structure with a diameter of 25 μm.

is shown in Fig. 6.10. The existence of the facets on the edges of the mesa is a result of the competition of the epitaxial growth along different crystallographic directions.

A Ge mesa with a thickness of 1.0 μm and a size of about 500 μm^2 is used to perform the pump-probe measurement. The Ge mesa is 1.0×10^{19} cm^{-3} n-type doped and 0.2% tensile-strained. The transmittance spectra of the Ge mesa under 0 and 100 mW optical pumping are shown in Fig. 6.11. If we assume the effective pumped area is the whole mesa area, the effective pump power density at 100 mW is estimated to be $\sim$ 7.0 kW/cm^2 calculated from the optical absorption of the pump light considering interference effect.

The direct band gap absorption edge can be clearly seen from the decrease of the transmittance above 0.765 eV in the figure. Under optical pumping, the net change of the transmittance of the Ge film depends on the competition of the direct band gap absorption reduction, or the optical bleaching, and the increased free carrier absorption. Similarly as we have seen the pump-probe results of the blanket n^+Ge epitaxial film, the optical bleaching occurs at wavelengths below a certain wavelength ($\approx$1615 nm) and the free carrier absorption causes transmittance decrease above that wavelength.

The calculated absorption spectrum and refractive index spectrum of the n^+ Ge mesa without optical pumping are compared with those of bulk Ge in Fig. 6.12. The absorption edge is significantly red shifted due to the band gap shrinkage induced by the tensile strain (0.2%). As a result, the refractive index is also notably modified compared to bulk Ge due to

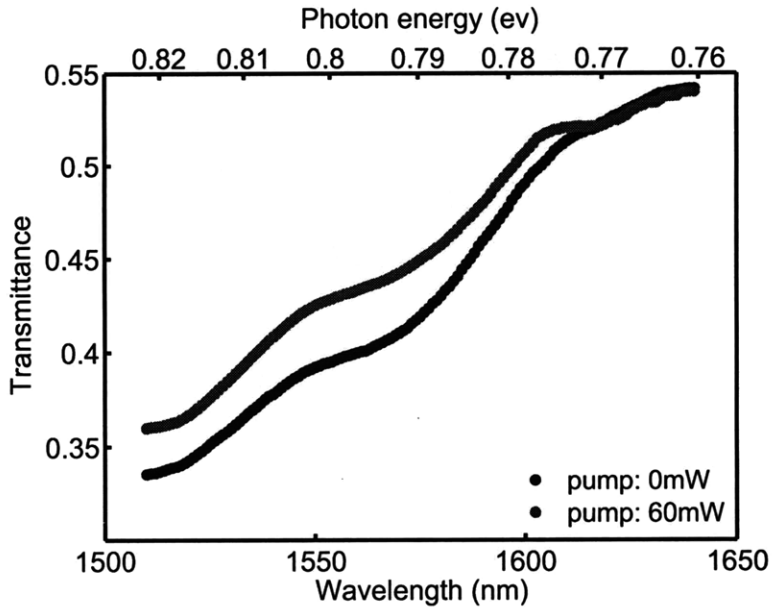

Figure 6.11: The transmittance spectra of a 1.0 μm^2 thick, 500 μm^2 Ge mesa with 1.0×10^{19} cm^{-3} n-type doping concentration under 0 and 100 mW optical pumping. [16]

the Kramer-Kronig relations. Such a self-consistency approach guarantees a more accurate solution to the absorption coefficients than simply assuming bulk Ge refractive index for tensile strained Ge in the transfer matrix calculation. More details about this calculation are explained in Appendix C.

Fig. 6.13 shows the calculated absorption spectra of the n^+Ge mesa sample under 0 and 100 mW optical pumping. The absorption coefficients at photon energies above 0.77 eV (at wavelengths below 1610 nm) decreases significantly upon optical pumping. Especially, negative absorption coefficients corresponding to the onset of optical gain are observed in the wavelength range of 1600-1608 nm, as shown in the inset of Fig. 6.13. The maximum gain coefficient observed is $g_{tot} = -\alpha_{tot} = 50 \pm 25$ cm^{-1} at 1605 nm. The error bars take into account the accuracy of both the transmittance measurement and the film thickness measurement.

The shape of the gain spectrum near the direct band edge of Ge resembles those of III-V semiconductor materials [133]. To our knowledge, this is the first time that optical gain has been observed from the direct gap transition of Ge. This result indicates that band-engineered Ge can be applied as an optical gain medium for monolithically integrated lasers

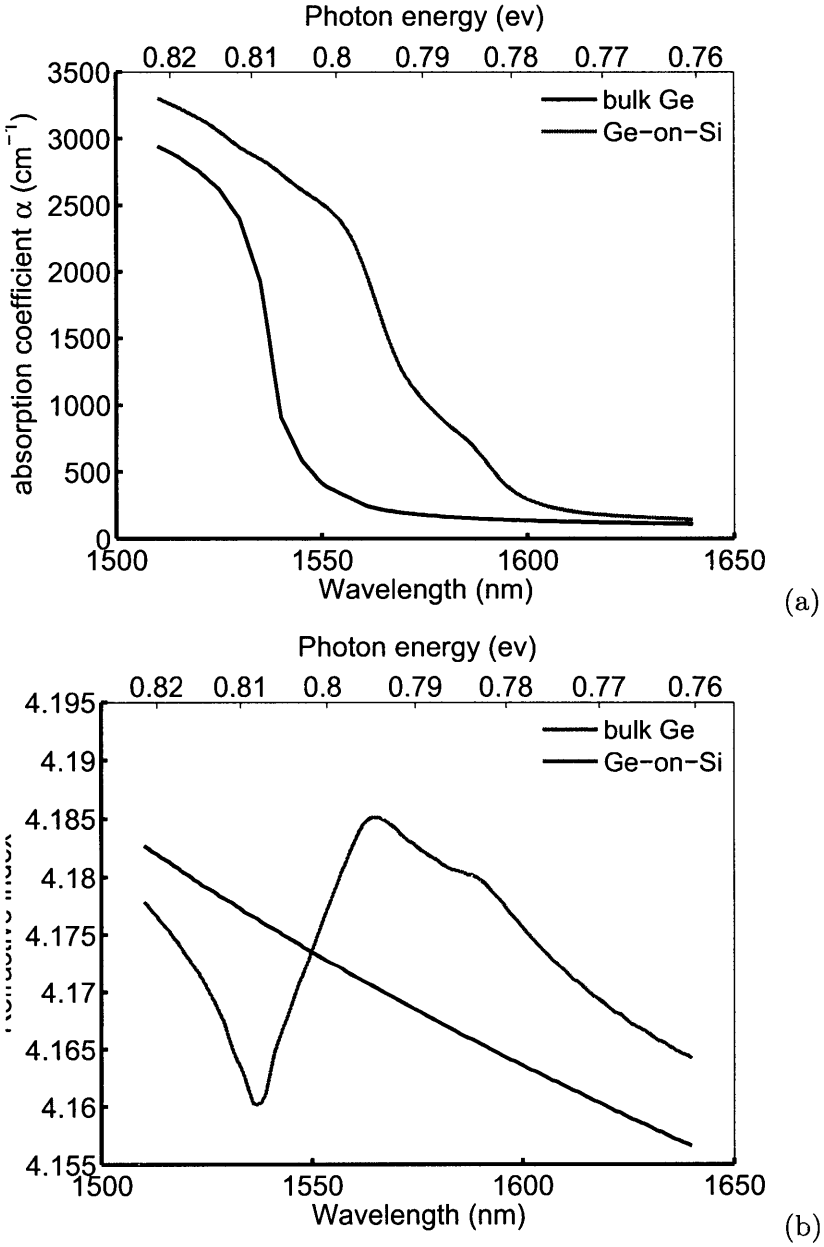

Figure 6.12: Comparison of (a) the absorption spectra, and (b) the refractive index spectra of bulk Ge with the n^+ Ge mesa sample. The absorption and refractive index spectra of the n^+Ge mesa is calculated from the transmittance data by using transfer matrix method (TMM) and self consistency solution of the real refractive index and the extinction coefficient considering the Kramer-Kronig relations. [106]

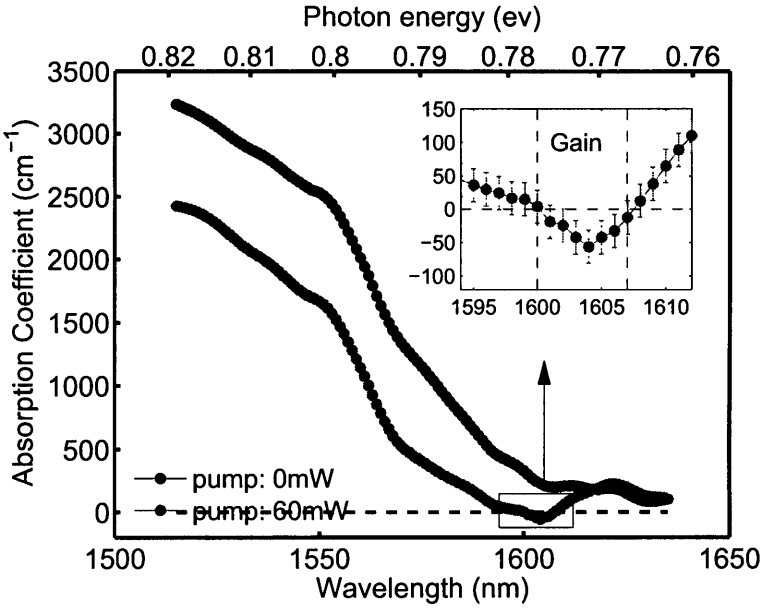

Figure 6.13: The absorption spectra of the n+ Ge mesa sample under 0 and 100 mW optical pumping. Negative absorption coefficients corresponding to the onset of net gain are observed in the wavelength range of 1600-1608 nm, as shown in the inset. The error bars in the inset take into account the accuracy of both the transmittance measurement and the film thickness measurement. [16].

on Si. Further improvement in gain coefficients is expected with higher n^+ Ge doping levels and is supported by the trend of PL intensity enhancement in Chapter 4.

6.3.2 Comparison of Inversion Factor

Like the increase of the integral PL intensity with the doping concentration in tensile-strained n^+Ge shown in Section 4.3.1, the optical bleaching effect also increases with the increase of n-type doping. The optical bleaching effect of Ge epitaxial films with various doping levels is compared in this section.

To avoid the variation of the Ge layer thickness which changes the absolute value of absorption thus optical bleaching, the inversion factor is used instead. As we explained in Section 6.1.3, this "inversion factor" is not the inversion factor $(f_c - f_v)$ of the stimulated optical transition. It also inclusion the influence of the free carrier absorption using Eq: 6.3. It is a real measure of the material gain. The net gain occurs when this "inversion factor" is greater than zero. In the following discussion, we call it the inversion factor for convenience.

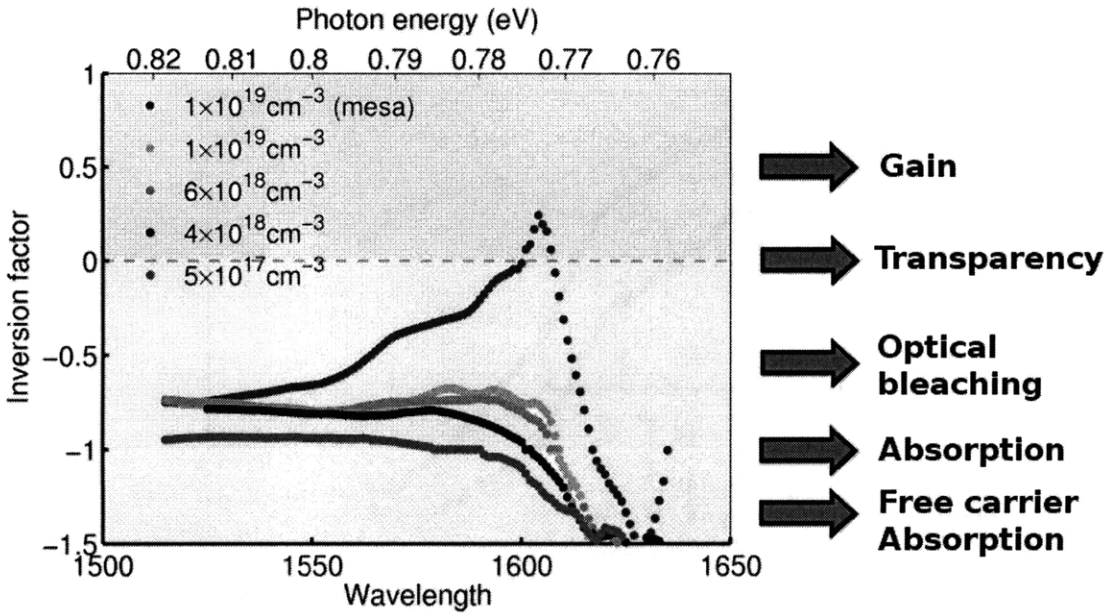

Figure 6.14: Comparison of inversion factor spectra of tensile-strained Ge (film and mesa) with various n-type doping concentrations. The optical bleaching effect increases with n-type doping concentration. The inversion factor of the Ge mesa sample is greater than zero at the direct band edge (1600-1608 nm) indicating the occurrence of the net gain.

The comparison of the inversion factor spectra of tensile-strained Ge for both blanket film and mesa samples with various n-type doping concentrations is shown in Fig. 6.14. The optical bleaching effect (inversion factor more than -1) can be seen from all samples. The bleaching increases with n-type doping concentration confirming the theory of the effect of n-type doping on optical gain discussed in Chapter 2. The Ge mesa sample exhibits a positive inversion factor at the direct band edge (1600-1608 nm) underlying the occurrence of the net gain. The inversion factors at longer wavelengths are less than -1 for all samples because the free carrier absorption overcomes the optical bleaching resulting in more absorption than small-signal optical absorption without pumping.

It is to be noted that the optical bleaching in the Ge mesa sample is much more than any Ge film samples including the one with the same n-type doping concentration. This confirms our speculation of the injected carrier diffusion which increases the volume of the effective pumped active region thereby decreasing the injection level. The phenomenon also suggests that the injected electrons holes must have a sufficiently long carrier lifetime leading

to such long distance diffusion. The carrier lifetime can be then estimated from the following procedure.

We know the Ge mesa measured for optical gain is an approximately cylindrical structure with a diameter of 25 μm. The increase of optical bleaching of the mesa compared to the film samples underlies an efficient carrier confinement hence the diffusion length L of the injected excess carriers is at least 25 μm. We assume the diffusion length is in the order of 10^2 μm. The carrier lifetime can be calculated from the definition of the diffusion length

$$\tau = \frac{L^2}{D}, \tag{6.7}$$

where D is the diffusivity which can be expressed in terms of carrier mobility by Einstein relation:

$$D = \mu k_B T. \tag{6.8}$$

In single crystalline bulk Ge, the electron mobility and the hole mobility are ~ 4000 $cm^2V^{-1}s^{-1}$ and ~ 2000 $cm^2V^{-1}s^{-1}$ respectively. In our epitaxial Ge-on-Si, the mobilities for both electrons and holes decrease due to the introduction of n-type impurities. The electron mobility of the tensile-strained n^+Ge measured from Hall effect is ~ 1000 $cm^2V^{-1}s^{-1}$, about 1/4 of that of bulk Ge. The hole mobility is hard to measure since the material is heavily n-type doped. We can estimate it to be ~ 500 $cm^2V^{-1}s^{-1}$ by assuming it is also decreased to 1/4 of the bulk value. By substituting these numbers into Einstein relation in Eq. 6.8, we can obtain electron diffusivity is about 12 cm^2/s and hole diffusivity is about 6 cm^2/s. Therefore the lifetimes for the excess electrons and holes in tensile-strain n^+Ge can be calculated from Eq. 6.7. The calculated lifetime is in the order of ~ 1 μs. This lifetime addresses the excess electrons in the indirect L valleys and excess holes in the valence band. Such relatively long excess carrier lifetime underlies good material quality control in the Ge epitaxial films.

From all these experiment results, we can see tensile-strained n^+Ge is a much better choice of gain medium than the intrinsic bulk Ge. The net gain cannot be achieved in intrinsic Ge though the optical bleaching effective can be observed. While in tensile-strained n^+Ge epitaxial film, no saturation has been seen in the relation of the optical bleaching

to the pump power. All these results validates the concept and the theory we explained and simulated in Chapter 2. The linear relation of the optical bleaching with pump power encourages us to further increase the injection level by using the carrier confinement mesa structure. Net gain has been observed, for the first time, from such Ge mesa samples. A peak gain of 50 ± 25 cm^{-1} suggests possible laser action with properly designed resonance cavities. The calculation which has been proven by all PL, EL, and gain measurement results shows more net gain can be achieved with higher n-type doping concentrations.

Chapter 7

Summary and Future Work

7.1 Summary

Silicon photonics is capable of being a platform for the optical communication and interconnects applications which aim for the low cost and high capacity data transmission yet constrained by the electrical interconnection currently. Many optical components in silicon photonics have been extensively studied, among which a silicon-based laser is arguably the most challenging element. This thesis mainly focuses on using engineered germanium as the optically active material for silicon-based light emitters with many potential benefits: Si-CMOS compatibility (both material and processing), electrical injection capability, and direct gap emission at preferred 1.55 μm telecommunication band. In Chapter 1, the background of silicon photonics and the progress of silicon-based laser research are briefly reviewed.

In Chapter 2, we explain the concept of using the combination of tensile-strain and n-type doping to effectively make germanium behave like a direct band gap material under carrier injection, because of the direct band gap shrinkage upon the strain and the state-filling in the indirect L valleys with the extrinsic electrons. A direct band-to-band transition model is used to calculate the optical transition (absorption and simulated emission) in this n^+ tensile-strained germanium and shows the occurrence of direct gap optical gain under carrier injection. By considering the free carrier absorption, which dominates the optical loss, the calculation shows the net gain can be achieved with n-type doping concentration in a range of 10^{19} to mid-10^{20} cm^{-3}. The injection threshold of the net gain is about 10^{18} cm^{-3} which

is quite viable using either optical pumping or electrical pumping. The net gain is in favor of the raise of temperature in a large range of injection (threshold to mid-10^{19} cm^{-3}) due to the elevated number of high energy electrons in the direct Γ valley contributing to the radiative recombination at higher temperatures.

In Chapter 3, the fabrication of the tensile-strained n^+ germanium is discussed. Single crystalline germanium is epitaxially grown on silicon substrates using a two-step approach to avoid islanding by releasing the strain energy from the lattice mismatch of the two materials. The 0.2-0.25% tensile strain in germanium is formed during the cooling from the high growth temperature (or post annealing temperature) to room temperature, because of the larger thermal expansion coefficient of germanium compared that of silicon and the fact that germanium epitaxial film is fully relaxed at the high growth temperature. Phosphorus are doped in germanium as n-type dopants during the epitaxial growth and as high as 2×10^{19} cm^{-3} doping concentration is achieved. Higher doping concentrations is favorable according to the calculation in Chapter 2, so the influences of temperature, flow, and base pressure on doping concentration is studied. An in situ doping model, considering both thermodynamics and kinetics in reaction and diffusion processes of phosphorus-containing species, is built to explain the experimental results and optimize the growth condition. The model suggests less epitaxial growth rate and lower hydrogen adsorption on the growing surface can lead to higher doping concentration.

In Chapter 4, photoluminescence (PL) experiments on both bulk crystalline germanium and n^+ tensile-strained germanium are discussed. Direct gap PL from intrinsic bulk germanium is observed when the germanium is polished to thin films, which, in this case, is bonded to a SiO_2 capped silicon substrate forming germanium-on-insulator (GeOI). Room temperature direct gap PL is also observed from the germanium epitaxial films at 1600 nm, corresponding to the direct band gap under the tensile strain, and the spectrum matches the theoretical calculation considering the strain-induced valence band splitting. The intensity of the emission increases with the increase of n-type doping concentration, which confirms the predicted indirect valley filling effect according to the calculation in Chapter 2. The temperature dependence of the PL shows that the emission intensity increases with temperature due to the elevated number of high energy electrons in the direct valley contributing to the

spontaneous emission at higher temperatures. This effect make germanium light emission robust to inevitable heating effect during operation.

In Chapter 5, the fabrication of Si/Ge/Si heterojunction light emitting diodes (LEDs) and the observation of room temperature direct gap electroluminescence (EL) from these diodes are discussed. This is the first observation of EL from germanium in any optical devices. The heterojunction LEDs are fabricated using completely Si-CMOS compatible processes. The room temperature direct gap EL at 1600 nm matches the PL characteristics in Chapter 4, underlying the same injection mechanism in both electrical pumping and optical pumping. The emission intensity increases superlinearly with the injection current resulting from the raised quasi Fermi level allowing larger fraction of the injected electron in the direct Γ valley. The quantum efficiency of the EL is on the order of 10^{-3}, calculated from the measured emission and the collection efficiency of the measurement setup, consistent with the finite-element simulation result. The emission efficiency can be improved to 10^{-1} if the germanium is n-typed doped. The design of n^+Ge based heterojuction diodes is analyzed theoretically and an optimal design with appropriate doping levels in adjacent silicon layers is proposed.

In Chapter 6, pump-probe measurement is used to study the optical gain characteristics in n^+ tensile-strained germanium. Optical bleaching effect, the reduction of absorption under carrier injection due to the raise of the population inversion factor (> -1), is observed at direct band gap energy in n-type doped germanium films and the degree of bleaching increases with the increase of doping concentration, confirming the theory of the doping dependence on the optical gain shown in Chapter 2. To confine the injected carriers for further increase of the injection level, a micro-mesa structure of germanium with 1×10^{19} cm^{-3} doping concentration is fabricated. Net gain, population inversion with inversion factor > 0, is observed from this germanium mesa. A peak gain of 50 ± 25 cm^{-1} at 1605 nm is calculated from the experimental data, which is the first report of observing net gain from direct band-to-band transition in germanium.

In Appendix D, a multi-resonance photonic crystal design is explained. Two approaches, the different order of resonance from one resonator and the resonance splitting from two strong coupled resonators, are analyzed to accomplish the enhanced photon detection at multiple wavelengths using one photonic crystal device. Following this second approach, an

amorphous silicon based photoconductor pixel, with the ability to detect enhanced signals from two wavelengths of 630 nm and 730 nm respectively, is fabricated and characterized. The design is optimized for high detectivity and low cross-talk between two wavelengths, and the detectivities as high as $\sim 10^{10}$ cm·Hz$^{1/2}$W^{-1} are measured for both resonance wavelengths.

7.2 Future Work

All the experimental findings on the optical properties (PL, EL, and optical gain) of tensile-strained n^+ Ge in this thesis work precisely follow the theoretical predictions in Chapter 2. The agreement between the experiments and our model encourages the next step of making a germanium laser. In order to achieve such integrated silicon-based laser, the "holy grail" of silicon photonics, we need to work on the following tasks.

According to our theoretical modeling in Chapter 2, in order to achieve over 10^2 cm^{-1} net material gain from Ge, mid-10^{19} cm^{-3} n-type doping concentration is required. In Chapter 3, we have shown the active phosphorus doping concentration reaches a limit of $1-2\times10^{19}$ cm^{-3} well below the solubility limit of over 1×10^{20} cm^{-3}. Further study is needed to investigate the mechanism of such limit. Two possible aspects are worth looking into in the future: the activation of dopants and the in situ doping process. For the first reason, since post-thermal annealing is always preformed to activate the dopants, and the in situ doping at slow growth rates in our case tends to form substitutional doping, the partial activation of dopants is very possibly a compensation effect at equilibrium. A secondary ion mass spectrometry (SIMS) study can be used to measure the total dopant concentration and examine the existence of partial activation. On the other hand, if the current doping is limited by the in situ doping approach, other doping methods can be considered. Since we have proven that the n^+ Ge prepared by ion-implantation has worse optical properties due to lattice damage, solid diffusion is a likely a better alternative approach. For example, spin-on-dopant is a promising candidate which has been widely used in doping Si. How to further increase the n-type doping concentration is a very important issue for making a Ge laser with desired performance. The limit of doping found in this work is also an interesting subject in material science.

With the current doping limit of $1 - 2 \times 10^{19}$ cm^{-3}, we have demonstrated the net gain

of 50 ± 25 cm^{-1} from a Ge mesa structure. Therefore, we can begin to design resonators for lasing demonstration in the next step. I shall first estimate the cavity Q factor required for such resonators using

$$Q = \frac{\lambda_0}{\Delta\lambda_{\text{FWHM}}} = \frac{2\pi n}{\alpha\lambda}, \tag{7.1}$$

where n is the refractive index and α is the resonance cavity loss. If we assume a cavity loss less than 20 cm^{-1}, the cavity Q factor is calculated to be larger than 7000.

Such high Q factor is difficult to achieve for a micro-resonator such as microdisk or microring due to high optical scattering loss result from the high refractive index contrast between Ge and its surrounding materials (e.g. air or SiO_2). In addition, the faceting effect of small Ge devices discussed in Section 3.4.1 introduces further optical loss that reduces Q factor. If the active n-type doping concentration can be further increased in the future, the requirement of the resonator Q factor can be much relaxed and a micro-resonator will be the preferable choice owing to its small footprint.

However, higher Q factor can be achieved in a larger resonance cavity. In order to demonstrate laser, we can design a long waveguide edge emitting resonator. The Ge/air interface at both ends of the waveguide resonator forms the mirrors which will be prepared by die cleaving and mechanical polishing. If the mirrors are perfectly polished and perpendicular to the waveguide propagation direction, the mirror optical loss is the transmittance of Ge/air interface which can be easily calculated to be 0.45 for each mirror. Then the minimum length required for such resonator is about 500 μm. This type of waveguide resonator can be either optically pumped or electrically pumped. For optical injection, the pump laser light is focused on top of the entire waveguide region using some cylindrical lens system, and the Ge lasing light will be measured laterally from one of the ends of the waveguide. For electrical injection, a Si/Ge/Si heterojunction structure can be used to inject electrons and holes into Ge following the design rules in Section 5.5.

A vertical cavity resonator may also be a feasible design. The high reflectivity dielectric Bragg mirror (DBR) can be deposited on top of Ge to form top mirror. The bottom mirror may be deposited on the backside of a double-side polished (DSP) Si substrate. In order to confine photons in the thick Si substrate layer, a deep etching may have to be used to isolate

the device region. Some advanced resonator designs like those discussed in Appendix D may also be applied in this vertical cavity case for some applications.

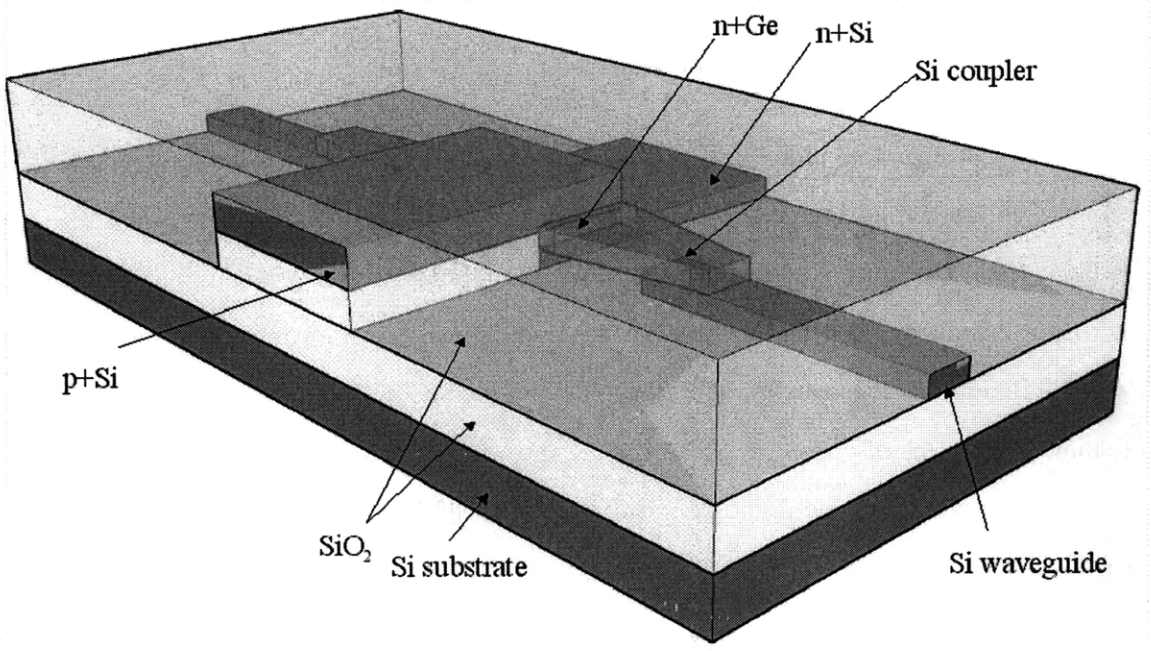

Figure 7.1: Schematic of the integration of a Ge laser and a Si waveguide.

If a discrete Ge laser is demonstrated successfully, the next step will be integrating Ge lasers with Si waveguides on chip for electronic-photonic integration applications. One of the possible integration scheme is shown in Fig. 7.1, similar to the approach used in the integration of Ge photodetector with waveguides [57]. It can be seen the edge emitting Ge laser is butt coupled to a Si taper which transmits light evanescently to a silicon waveguide below. The entire system is fabricated on a silicon-on-insulator (SOI) substrate. Other integration schemes also exist such as a top-down coupling between an amorphous Si waveguide and a Ge microdisk laser. It will take a lot of efforts to accomplish such integrated devices, but the effort will be paid off by huge demands for a on-chip silicon laser in silicon photonics applications.

Appendix A

Fermi Level and Carrier Concentration Calculation

The Fermi level at equilibrium and the quasi-Fermi levels at quasi-equilibrium (e.g. steady state) are important parameters for semiconductors. The carrier (electron or hole) concentration in a semiconductor is a function of the Fermi level, thus the process of solving the Fermi level in a semiconductor or a semiconductor device is the process of solving the electronic states in the whole system. In Chapter 2, such calculations are used to calculate the optical gain characterisitics of tensile-strain n^+Ge under carrier injection. In this appendix, the process of calculating the Fermi level and carrier concentration for both non-degenerate and degenerate semiconductors is explained. All symbols used in the following equations are listed in Section A.3.

The Fermi level at equilibrium is calculated based on the electric neutrality of the semiconductor:

$$n_0 + N_a^- = p_0 + N_d^+, \tag{A.1}$$

where n_0, p_0, N_d^+, and N_a^- are generally functions of the Fermi level E_f, thus the Fermi level can be solved numerically and n_0, p_0 can be calculated subsequently.

At quasi-equilibrium, two quasi-Fermi levels exist upon excess carrier injection. Therefore,

two equations are used to solve the electron quasi-Fermi level and the hole quasi-Fermi level:

$$\begin{cases} n = n_0 + \Delta n \\ p = p_0 + \Delta p \end{cases}, \tag{A.2}$$

where, n_0, p_0 are calculated from Eq. A.1, and Δ_n and Δ_p are usually calculated using the carrier (and photon) rate equations of the system* and are assumed known variables in this discussion.

To solve (quasi-) Fermi level, the expressions of the carrier concentrations as a function of (quasi-) Fermi level are substituted into the equations above. These expressions are different for non-degenerate semiconductors (Boltzman statistics, approximation for low carrier concentration) or degenerate semiconductors (Fermi statistics).

Since the equilibrium condition can be seen as a special case of quasi-equilibrium condition with $\Delta_n = \Delta_p = 0$ and $n = n_0$, $p = p_0$, we only give the expression of n (p) as a function of E_{fc} (E_{fv}). At equilibrium, $E_f = E_{fc} = E_{fv}$.

A.1 Carrier Concentration

A.1.1 Electron Concentration

The square root density of states (DOS) for the quadratic conduction band is

$$\rho_c(E) = 4\pi M_c \left(\frac{2m_c^*}{h^2}\right)^{3/2} \sqrt{E - E_c}, \tag{A.3}$$

where, the double degeneracy of spin is considered. Thus the electron concentration in the conduction band is

$$n = \begin{cases} \int_{E_c}^{+\infty} \rho_c(E) \frac{1}{1+\exp(\frac{E-E_{fc}}{k_B T})}\, dE & \text{degenerate case} \\ \int_{E_c}^{+\infty} \rho_c(E) \exp(-\frac{E-E_{fc}}{k_B T})\, dE & \text{non-degenerate case} \end{cases}. \tag{A.4}$$

*The rate equations also implicitly contains quasi-Fermi levels, thus Δ_n, Δ_p, E_{fc}, E_{fv} are solved from the equation systems composed of rate equations and the carrier equations.

By substituting the expression for DOS, we have

$$n = N_c \begin{cases} F_{1/2}\left(-\frac{E_c - E_{fc}}{k_B T}\right) & \text{degenerate case} \\ \exp\left(-\frac{E_c - E_{fc}}{k_B T}\right) & \text{non-degenerate case} \end{cases} \tag{A.5}$$

where,

$$N_c = 2M_c \left(\frac{2\pi m_c^* k_B T}{h^2}\right)^{3/2} \tag{A.6}$$

and,

$$F_j(x) = \frac{1}{\Gamma(j+1)} \int_0^{+\infty} \frac{t^j}{\exp(t-x)+1}\, dt \tag{A.7}$$

is the Complete Fermi-Dirac Integral.

A.1.2 Hole Concentration

Similarly, the DOS for the quadratic valence band is

$$\rho_v(E) = 4\pi M_v \left(\frac{2m_v^*}{h^2}\right)^{3/2} \sqrt{E_v - E}. \tag{A.8}$$

Therefore the hole density in the conduction band is

$$p = N_v \begin{cases} F_{1/2}\left(-\frac{E_{fv} - E_v}{k_B T}\right) & \text{degenerate case} \\ \exp\left(-\frac{E_{fv} - E_v}{k_B T}\right) & \text{non-degenerate case} \end{cases}, \tag{A.9}$$

where,

$$N_v = 2M_v \left(\frac{2\pi m_v^* k_B T}{h^2}\right)^{3/2} \tag{A.10}$$

If multiply non-degenerate valleys, e.g. the direct Γ valley and the indirect L valleys in Ge, are considered, multiply square root DOSs and band edge energies are used in the equations above.

A.2 Ionized Doping Concentration

The simplest model for the ionization of the dopant levels is the assumption of complete ionization meaning

$$\begin{cases} N_d^+ = N_d \\ N_a^- = N_a \end{cases} . \tag{A.11}$$

This is the most commonly used assumption and is valid in most of the cases in the calculations. But only part of the dopants is ionized if the Fermi level approaches the band edge with high carrier concentrations.

For a simply Δ function donor level, we have

$$N_d^+ = \frac{N_d}{1 + D_d \exp\left(\frac{E_f - E_d}{k_B T}\right)}. \tag{A.12}$$

For high concentration of dopant, an impurity band may form in the band gap. If the impurity band is assumed to be a Gaussian shape function, we can calculate N_d^+ using

$$N_d^+ = \int \frac{\rho_d(E - E_d)}{1 + D_d \exp\left(\frac{E_f - E}{k_B T}\right)} dE \tag{A.13}$$

where,

$$\rho_d(E - E_d) = \frac{N_d}{E_{dh}} \sqrt{\frac{\ln 2}{\pi}} \exp\left(-\ln 2 \frac{(E - E_d)^2}{{E_{dh}}^2}\right) \tag{A.14}$$

and, E_{dh} is the half width at high maximum (HWHM) of the Gaussian shape donor band.

Similarly, for a Δ function acceptor level, we have

$$N_a^- = \frac{N_d}{1 + D_a \exp\left(\frac{E_a - E_f}{k_B T}\right)} \tag{A.15}$$

For a Gaussian shape acceptor band, we have

$$N_a^- = \int \frac{\rho_a(E - E_a)}{1 + D_a \exp\left(\frac{E - E_f}{k_B T}\right)} dE \tag{A.16}$$

where,

$$\rho_a(E - E_a) = \frac{N_a}{E_{ah}}\sqrt{\frac{\ln 2}{\pi}}\exp\left(-\ln 2\frac{(E - E_a)^2}{{E_{ah}}^2}\right) \tag{A.17}$$

and, E_{ah} is the HWHM of the Gaussian shape acceptor band.

A.3 Symbols

symbols	descriptions
n_0	electron concentration at equilibrium (cm^{-3})
Δn	injected excess electron concentration (cm^{-3})
n	total electron concentration (cm^{-3})
p_0	hole concentration at equilibrium (cm^{-3})
Δp injected excess hole concentration (cm^{-3})	
p	total hole concentration (cm^{-3})
m_c^*	effective electron mass of density of states (g)
m_v^*	effective hole mass of density of states (g)
m_0	rest mass of electron (g)
$\rho_c(E)$	density of states for conduction band (cm^{-3}/eV)
$\rho_v(E)$	density of states for valence band (cm^{-3}/eV)
E_c	conduction band edge (eV)
E_v	valence band edge (eV)
E_f	Fermi level at equilibrium (eV)
E_{fc}	electron quasi-Fermi level (eV)
E_{fv}	hole quasi-Fermi level (eV)
M_c	number of equivalent valleys in the conduction band
M_v	number of equivalent valleys in the valence band
N_c	effective density of states of the conduction band
N_v	effective density of states of the valence band
N_d	active donor concentration (cm^{-3})
N_a	active acceptor concentration (cm^{-3})
N_d^+	ionized active donor concentration (cm^{-3})

N_a^-	ionized active acceptor concentration (cm^{-3})
D_d	Degeneracy of the donor level
D_a	Degeneracy of the acceptor level

Appendix B

Modified Transfer Matrix Method (TMM)

The transmittance and reflectance calculation of a stack of thin film layers are used in a number of cases in this work, the method of the calculation is discussed in this appendix.

The transmittance/reflectance of such thin film stack is not simply calculated by the multiplication of that of each interface, because the interference of light influence the light intensity in the stack when the wavelength of the light is comparable to the thicknesses of the layers. Thus the transmittance/reflectance strongly depends on the wavelength due to the interference condition and very different light intensity distribution exists for different wavelength (i.e. photon energy). Since the behavior the of photon in the stack structure is analogical to that of electron in a crystal lattice, the multiply thin film structure is also called one-dimensional (1-D) photonic crystal sometimes.

B.1 TMM for Multilayer Transmittance/Reflectance Calculation

Transfer Matrix Method (TMM) is a commonly used approach to calculate the transmittance and reflectance of the multi-layer stack. It is widely used in optical filters and other optical devices design [134]. The method is obtained from the boundary conditions of the

electromagnetic wave (light) at each interface.

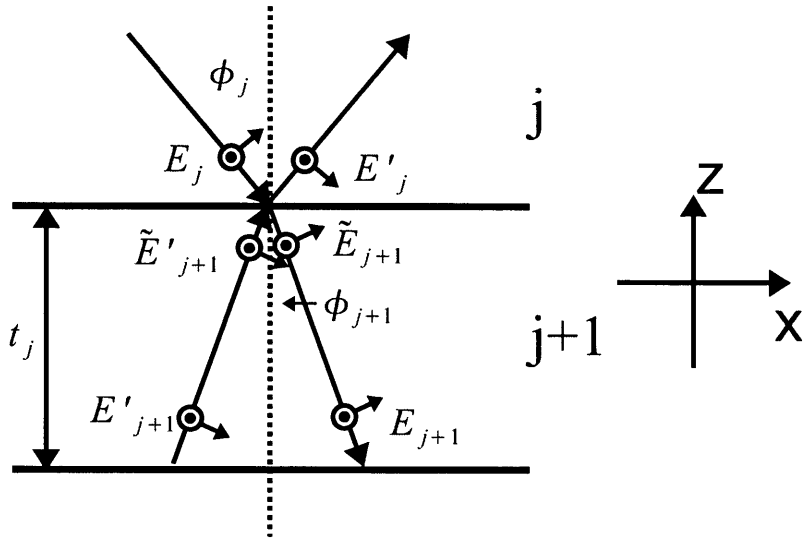

Figure B.1: Schematic of the electric field of the incident light at $j/(j+1)$ interface of a multi-layer stack.

Let us consider the interface of the jth and the $(j+1)$th layers as shown schematically in Fig. B.1. The electric fields for transmitted light (propagating downwards) and reflective light (propagating upwards) at the $j/(j+1)$ interface (in Layer j and in Layer $(j+1)$ respectively) and at the $(j+1)/(j+2)$ interface (in Layer $(j+1)$ respectively) are shown in the figure and denoted by the symbols used in the following equations. For a plane wave light, the electric (and magnetic) field is perpendicular to the propagation direction, thus the electric field can be described by two components: s-wave (electric field perpendicular to the incident plane) and p-wave (electric field parallel to the incident plane). These two components are denoted with a subscript s or p in the following equations.

The boundary conditions at the interface determined from the Maxwell's equations are

$$\begin{cases} (E_j - \tilde{E}_{j+1}) \times e_z = 0 \\ (D_j - \tilde{D}_{j+1}) \cdot e_z = 0 \\ (B_j - \tilde{B}_{j+1}) \cdot e_z = 0 \\ (H_j - \tilde{H}_{j+1}) \times e_z = 0 \end{cases} . \tag{B.1}$$

For the case of a linear material and the plane wave incidence, which is valid for the cases in this work, D, B, H can all be expressed in terms of E:

$$\begin{cases} D = \epsilon E = \epsilon_0 n^2 E \\ B = \frac{k}{\omega} E = \frac{1}{c} n E \\ H = \frac{1}{\mu} B = \frac{c\epsilon_0}{\mu} n E \end{cases} , \tag{B.2}$$

where $n = n_r + ik$ is the complex refractive index of the material, and n_r and k are the refractive index and the extinction ratio which is related to the absorption coefficient by $\alpha = 4\pi/\lambda k$.

Substituting these relations to the boundary condition, we obtain

$$\begin{cases} M_{j,s} \begin{pmatrix} E_{j,s} \\ E'_{j,s} \end{pmatrix} = M_{j+1,s} \begin{pmatrix} E_{j+1,s} \\ E'_{j+1,s} \end{pmatrix} \\ M_{j,p} \begin{pmatrix} E_{j,p} \\ E'_{j,p} \end{pmatrix} = M_{j+1,p} \begin{pmatrix} E_{j+1,p} \\ E'_{j+1,p} \end{pmatrix} \end{cases} , \tag{B.3}$$

where,

$$\begin{cases} M_{j,s} = \begin{pmatrix} 1 & 1 \\ \frac{n_j}{\mu_j} \cos\phi_j & -\frac{n_j}{\mu_j} \cos\phi_j \end{pmatrix} \\ M_{j,p} = \begin{pmatrix} \cos\phi_j & \cos\phi_j \\ \frac{n_j}{\mu_j} & -\frac{n_j}{\mu_j} \end{pmatrix} \end{cases} , \tag{B.4}$$

and ϕ satisfies Snell's law

$$n_{rj} \sin \phi_j = n_{r(j+1)} \sin \phi_{j+1}. \tag{B.5}$$

For non-magnetic materials, relative permeability $\mu = 1$, which is used in the following discussion.

The propagation the light (transmitted and reflective) within the $(j+1)$th layer relates the electric field of at the $j/j+1$ interface and $j+1/j+2$ interface in layer $j+1$ side:

$$\begin{pmatrix} E_{j+1} \\ E'_{j+1} \end{pmatrix} = Lj + 1 \begin{pmatrix} \tilde{E}_{j+1} \\ \tilde{E}'_{j+1} \end{pmatrix}, \tag{B.6}$$

where,

$$L_j = \begin{pmatrix} \exp(i\delta_j) & 0 \\ 0 & \exp(-i\delta_j) \end{pmatrix}, \tag{B.7}$$

and

$$\delta_j = \frac{2\pi}{\lambda} n_j t_j \cos \phi_j$$

, which is same for both s-wave and p-wave.

We define T_j as the transfer matrix of the jth layer as

$$T_j = M_j L_j {M_j}^{-1} = \begin{pmatrix} \cos \delta_j & i/u_j \sin \delta_j \\ i u_j \sin \delta_j & \cos \delta_j \end{pmatrix}, \tag{B.8}$$

where,

$$u_j = \begin{cases} n_{rj} \cos \phi_j & \text{for s-wave} \\ n_{rj} / \cos \phi_j & \text{for p-wave} \end{cases}. \tag{B.9}$$

Combining Eq. B.3 and Eq. B.6 and substituting T_j, we can obtain

$$E_{j+1} = {M_{j+1}}^{-1} T_{j+1} M_j E_j. \tag{B.10}$$

We denote the 1st layer is the incidence medium and the mst layer is the finally transmitted

medium, by multiplying the above expression of each layer, we have

$$\begin{pmatrix} \tilde{E}_m \\ \tilde{E'}_m \end{pmatrix} = {M_m}^{-1} \left(\prod_{j=m-1}^{2} T_j \right) M_1 \begin{pmatrix} E_1 \\ {E'}_1 \end{pmatrix}. \tag{B.11}$$

We denote ${E'}_1 = rE_1$, $\tilde{E}_m = tE_1$, where r and t is the complex reflectivity and transmissivity of the electric field, and $\tilde{E'}_m = 0$ since there is no reflective light in the transmitted medium. Thus the equation can be re-written as

$$\begin{pmatrix} tE_1 \\ 0 \end{pmatrix} = {M_m}^{-1} \left(\prod_{j=m-1}^{2} T_j \right) M_1 \begin{pmatrix} E_1 \\ rE_1 \end{pmatrix}, \tag{B.12}$$

and r, t can be calculated from this equation.

We denote

$$T_f = {M_m}^{-1} \prod_{j=m-1}^{2} T_j M_1$$

therefore,

$$r = -\frac{T_{f21}}{T_f 22}, \tag{B.13}$$

and

$$t = \frac{T_{f11}T_{f22} - T_{f12}T_{f21}}{T_{f22}} = \frac{|T_f|}{T_{f22}} \tag{B.14}$$

The reflectance and transmittance of the light intensity R and T, which are the quantities measured in the experiment, can be calculated from r and t:

$$R = |r|^2 \tag{B.15}$$

$$T = \frac{n_{rm}}{n_{r1}}|t|^2, \tag{B.16}$$

where, n_{rm} and n_{r1} are real refractive indices for the mth layer and the 1st layer respectively.

If the incident light is perpendicular to the stack surface, the reflectance and transmittance for both s-wave and p-wave are the same. While if the incidence angle is not 90^o from the surface, results for s-wave and p-wave are generally different and the final results are linear

combination of the two.

B.2 Modification for an Noncoherent Thick Layer

Transfer matrix method (TMM) considers that the light is completely interfered in each layer of a stack, which is not always true in some cases. A typical exception is the involvement of a very thick layer, the thickness of which is much larger than the wavelength and greater than the coherence length of the incident light, thus the reflective light doesn't interfere with the transmitted light in the layer.

A very common example, met in this work a number of times, is the multi-layer materials on Si substrate. Si substrate is very thick (600-700 μm) compared to the wavelength of the light we used and is also generally thicker than the coherence length of the light source we used to measure the reflectance and the transmittance spectrum. The wavelength-tunable light source for these applications is usually either a halogen lamp with a monochromator or a semiconductor tunable laser. The halogen lamp is very close to a black body, therefore the coherence length is very short (typically a few μm). The tunable laser generally has longer coherency, but in order to achieve a considerable wavelength range of tunability, an external cavity is usually used, which dramatically decrease the coherency. Therefore, the thickness of Si substrate is generally larger than the coherence length of the light source, and a modification to the TMM is required to deal with Si substrate based stack.

If the Si is highly absorbed in the interested wavelength range, the TMM model can still be used with some considerations. The transmittance in such wavelength range is zero since the thick Si substrate absorbs all the light, thus the Si can be used as the last layer in the TMM calculation and the reflectance of the stack can be accurately calculated using the TMM.

However, Si does not has an appreciable absorption in a wide range of 1.2-5 μm, thus the non-coherency of the Si has to be considered for reflectance/transmittance studies of the Si substrate based multi-layer stack. A lot of research in this work is investigated within this wavelength range, i.e. the wavelengths near Ge direct band edge (1400-1700 nm), therefore a modified TMM approach has been studied and is presented in this section.

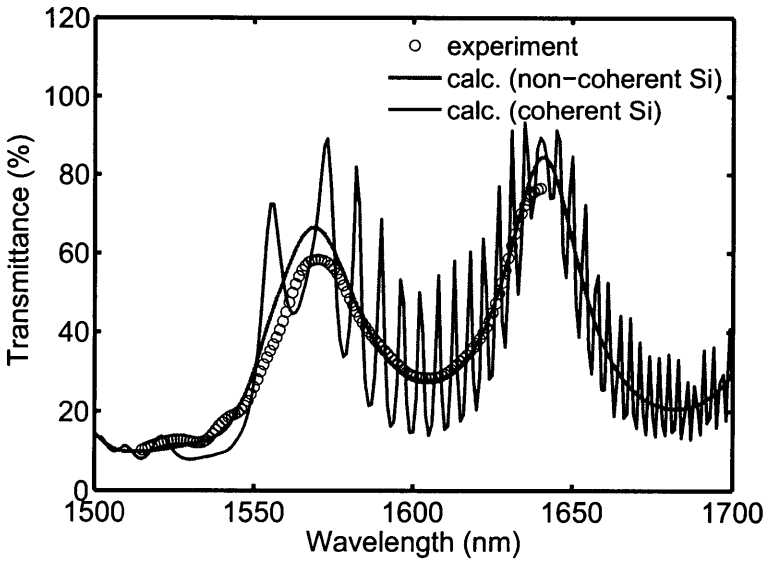

Figure B.2: Comparison of the transmittance calculations with coherent and non-coherent Si substrate consideration and the experimental data for a Ge-on-insulator stack.

A comparison of the transmittance calculations with coherent and non-coherent Si substrate consideration is shown in Fig. B.2. This is a Ge-on-insulator sample with $Ge/SiO_2/Si$ (substrate)$/SiO_2$ layer structure and the experimental transmittance is measured with a HP (Agilent) 81640A semiconductor tunable laser and an optical power meter. We can see, without the consideration of the non-coherency in Si substrate, the calculated transmittance spectrum has many sharp peaks due to the dense interference in the thick Si substrate layer, which is completely unobserved in the measured data confirming our above discussion on coherency. On the other hand, by considering the non-coherency in Si substrate layer, the calculated result matches the measured data very well, underlying the importance of this modification to standard TMM model. The details of this approach are presented as follows.

We denote the kth layer is the thick layer with non-coherency property, thus from the TMM discussion above, we know the relation between the 1st layer (incidence medium) and the kth layer without considering any layers below the kth layer is

$$\begin{pmatrix} t_k^{(0)} \\ 0 \end{pmatrix} = {M_k}^{-1} \left(\prod_{j=k-1}^{2} T_j \right) M_1 \begin{pmatrix} 1 \\ r^{(0)} \end{pmatrix} = T_a \begin{pmatrix} 1 \\ r^{(0)} \end{pmatrix}. \tag{B.17}$$

Here, the electric field of the incident light is assumed to be 1 since only the ratios (reflectance/transmittance) of the electric field are concerned. The superscript number in the parenthesis denotes the number of propagation of the light in the kth layer along the same (reflective or transmitted) direction. Similarly, we have

$$r^{(0)} = -\frac{T_{a21}}{T_{a22}}, \text{and} \tag{B.18}$$

$$t_k^{(0)} = \frac{|T_a|}{T_{a22}}. \tag{B.19}$$

Thus the light intensity in the kth layer right below the $k-1/k$ interface is

$$\frac{n_k}{n_1}\left(t_k^{(0)}\right)^2.$$

When light propagates to the interface $k/k+1$ the intensity changes to

$$\frac{n_k}{n_1}\left(t_k^{(0)}\right)^2\left(e^{-\gamma_k}\right)^2,$$

where, $\gamma_k = (2\pi/\lambda)k_k t_k \cos(\phi_k)$. Thus the electric field at this point $t_k^{(0)}e^{-\gamma_k}$ is served as the incident light for the stack below kth layer.

The relation between the kth layer and the mth layer (transmitted medium) is

$$\begin{pmatrix} t^{(1)} \\ 0 \end{pmatrix} = {M_m}^{-1}\left(\prod_{j=m-1}^{k+1} T_j\right) M_k \begin{pmatrix} t_k^{(0)}e^{-\gamma_k} \\ r_k^{(1)} \end{pmatrix} = T_b \begin{pmatrix} t_k^{(0)}e^{-\gamma_k} \\ r_k^{(1)} \end{pmatrix}, \tag{B.20}$$

and we have

$$r_k^{(1)} = -\frac{T_{b21}}{T_{b22}} t_k^{(0)} e^{-\gamma_k}, \text{and} \tag{B.21}$$

$$t^{(1)} = \frac{|T_b|}{T_{b22}} t_k^{(0)} e^{-\gamma_k} = \alpha_t t_k^{(0)}, \tag{B.22}$$

where,

$$\alpha_t = \frac{|T_b|}{T_{b22}} e^{-\gamma_k}. \tag{B.23}$$

The reflective light at $k/k+1$ interface in the kth layer propagates to the $k-1/k$ interface

and the electric field becomes to be

$$-\frac{T_{b21}}{T_{b22}}t_k^{(0)}e^{-2\gamma_k} \tag{B.24}$$

and served as the incident light to the layers above the kth layer. But this light does not interfere with any previous light in the layers since it is no long coherent. Thus the transmitted light to the 1st layer can be expressed by

$$\begin{pmatrix} t_k^{(1)} \\ -\frac{T_{b21}}{T_{b22}}t_k^{(0)}e^{-2\gamma_k} \end{pmatrix} = T_a \begin{pmatrix} 0 \\ r^{(1)} \end{pmatrix}. \tag{B.25}$$

Thus we have

$$r^{(1)} = -\frac{1}{T_{a22}}\frac{T_{b21}}{T_{b22}}t_k^{(0)}e^{-2\gamma_k} = \alpha_r t_k^{(0)}, \text{and} \tag{B.26}$$

$$t_k^{(1)} = -\frac{T_{a12}}{T_{a22}}\frac{T_{b21}}{T_{b22}}t_k^{(0)}e^{-2\gamma_k} = \beta t_k^{(0)}, \tag{B.27}$$

where,

$$\alpha_r = -\frac{1}{T_{a22}}\frac{T_{b21}}{T_{b22}}e^{-2\gamma_k}, \text{and} \tag{B.28}$$

$$\beta = -\frac{T_{a12}}{T_{a22}}\frac{T_{b21}}{T_{b22}}e^{-2\gamma_k}. \tag{B.29}$$

Combining Eq. B.22, B.26, and B.27, we have the expression for any order the reflectance and transmittance

$$r^{(j)} = \alpha_r t_k^{(j-1)} = \alpha_r \beta^{j-1} t_k^{(0)}, \text{and} \tag{B.30}$$

$$t^{(j)} = \alpha_t t_k^{(j-1)} = \alpha_t \beta^{j-1} t_k^{(0)}. \tag{B.31}$$

The total reflected or transmitted electric field is not the summation of all these electric fields at different orders since they are not coherent. But the reflected and transmitted light intensity is the summation of all these intensities, thus we have

$$R = \left|r^{(0)}\right|^2 + \sum_{j=1}^{\infty}\left|r^{(j)}\right|^2 = \left|r^{(0)}\right|^2 + \alpha_r^2 t_k^{(0)2}\sum_{j=1}^{\infty}\beta^{2(j-1)} = \left|\frac{T_{a21}}{T_{a22}}\right|^2 + \frac{\alpha_r^2}{1-\beta^2}\left|\frac{|T_a|}{T_{a22}}\right|^2, \tag{B.32}$$

and

$$T = \frac{n_{rm}}{n_{r1}} \sum_{j=1}^{\infty} |t^{(j)}|^2 = \frac{n_{rm}}{n_{r1}} \alpha_t^2 {t_k^{(0)}}^2 \sum_{j=1}^{\infty} \beta^{2(j-1)} = \frac{n_{rm}}{n_{r1}} \frac{\alpha_t^2}{1-\beta^2} \left| \frac{|T_a|}{T_{a22}} \right|^2, \tag{B.33}$$

where Eq. B.18 and B.19 are used in the above expression and n_{rm} and n_{r1} are the same as in Eq. B.16.

B.3 Light Intensity Distribution and Absorption in Layers

The light intensity distribution and the light absorption in a layer are also important subjects which are required to design some complex stack structure such as the dual resonance photonic crystal stack in Chapter D. The calculation of these two quantities are discussed in the section.

When we finished transfer matrix calculation as described in the previous sections, we obtain the reflected electric field of the first layer E_1'. Therefore, the electric field of any specific layer k can calculated by

$$\begin{pmatrix} \tilde{E}_k \\ \tilde{E'}_k \end{pmatrix} = {M_k}^{-1} \left(\prod_{j=k-1}^{2} T_j \right) M_1 \begin{pmatrix} E_1 \\ {E'}_1 \end{pmatrix}, \tag{B.34}$$

where M_k are defined in Section $B.1$. And we denote the $\tilde{E}_k = E_k$ and $\tilde{E'}_k = E_k'$ for the following discussion.

We let the z-axis perpendicular to the layers pointing from incidence medium to the transmitted medium. For an arbitrary position z in the kth layer, the electric field can be calculated by

$$E_k(z) = E_k \exp(\frac{2\pi}{\lambda} n_k (z - d_k)) + E_k' \exp(-\frac{2\pi}{\lambda} n_k (z - d_k)), \tag{B.35}$$

where, d_k is the z-axis coordinate of the kth interface, and z point satisfies $d_k \leq z \leq d_{k+1}$.

The power flux (Poynting vector) is used to described the light intensity since it is directly related to the absorption process. The power flux at z is

$$S(z) = n_{rk} |E(z)|^2 \cos \phi_k. \tag{B.36}$$

The absorption in a certain layer can be calculated using energy conservation: the absorbed energy is equal to the net energy flux (Poynting vector) into the layer. Thus the absorption in the kth layer can be expressed by

$$I_{\text{abs}} = n_{rk}(|E_k|^2 - |E'_k|^2)\cos\phi_k - n_{rk}(|E_k \exp(\frac{2\pi}{\lambda} n_k t_k)| - |E'_k \exp(-\frac{2\pi}{\lambda} n_k t_k)|)\cos\phi_k \tag{B.37}$$

$$= (1 - \exp(-\alpha_k t_k))n_{rk}|E_k|^2 \cos\phi_k + (\exp(\alpha_k t_k) - 1)n_{rk}|E'_k|^2 \cos\phi_k, \tag{B.38}$$

where $\alpha_k = \frac{4\pi}{\lambda} n_{ik}$ is the absorption coefficient of the material of the kth layer.

Appendix C

Absorption Coefficient Calculation from Transmittance

In Chapter 6, the optical bleaching and the net gain observed from the epitaxial germanium are represented by the reduction of optical absorption and negative absorption respectively, which are calculated from the transmittance spectrum in the pump-probe measurement. Therefore, to precisely determine the absorption spectrum from the transmittance spectrum is important and the approach is discussed in this appendix.

The optical absorption of tensile-strained Ge is unknown, since the band structure is modified by the tensile strain, but it is related to the absorption of intrinsic bulk Ge through the Kramers-Kronig (K-K) relations. The absorption of bulk Ge is well documented thus contributing to precise determination of absorption of strained Ge. In the following two sections, the numerical K-K relation calculation and the determination of the absorption from the transmittance are discussed respectively.

C.1 Numerical Calculation of Kramers-Kronig Relations

The Kramers-Kronig relations are not physical laws, but mathematical properties, connecting the real and imaginary parts of any complex function which is analytic in the upper half plane. By applying the properties to permittivity $\epsilon = \epsilon_r + i\epsilon_i$ of a material, the relations can be

rewritten as:

$$\begin{cases} \epsilon_r - 1 = \frac{1}{\pi} P \int_{-\infty}^{\infty} \frac{\epsilon_i(\omega')}{\omega' - \omega} d\omega' \\ \epsilon_i = -\frac{1}{\pi} P \int_{-\infty}^{\infty} \frac{\epsilon_r(\omega')}{\omega' - \omega} d\omega' \end{cases} . \tag{C.1}$$

The refractive index n and absorption coefficient α of the material can be expressed by the permittivity:

$$\begin{cases} n^2 = \frac{|\epsilon| + \epsilon_r}{2} \\ \alpha^2 = \left(\frac{4\pi}{\lambda}\right)^2 \frac{|\epsilon| - \epsilon_r}{2} \end{cases} . \tag{C.2}$$

The K-K relationship is applied for the whole frequency domain ($-\infty$ to ∞) which makes the direct calculation of the integral difficult, since, usually, only a portion of the permittivity spectrum known for a given material. However, the $\omega' - \omega$ term in the integrated function imposes the function is only significant in a small range near ω, therefore allowing us to consider the integral in a finite region and calculated by the discrete Fourier transform (DFT) method.

The approach described below follows the work in Ref. [135].

The Fourier transform of a given function $x(t)$ is

$$X(\omega) = F(x(t)) = \int_{-\infty}^{\infty} x(t) e^{-i\omega t} dt, \tag{C.3}$$

and the reverse transform is

$$x(t) = F^{-1}(X(\omega)) = \frac{1}{2\pi} \int_{-\infty}^{\infty} X(\omega) e^{i\omega t} . d\omega \tag{C.4}$$

For numerical calculations, the discrete Fourier transform is used:

$$X_k = \sum_{n=0}^{N-1} x_n e^{-2\pi i \frac{n}{N} k}, \tag{C.5}$$

and

$$x_n = \frac{1}{N} \sum_{k=0}^{N-1} X_k e^{2\pi i \frac{k}{N} n}, \tag{C.6}$$

where, $n, k = 0, \ldots, N-1$.

To prepare of the DFT on K-K relations, we first let

$$\epsilon(t) - \delta(t) = p(t) + q(t) = F^{-1}(\epsilon(\omega) - 1), \tag{C.7}$$

where, $p(t)$ and $q(t)$ is the even and the odd contribution, respectively.

It is easy to prove

$$\epsilon(-\omega) = \epsilon^*(\omega). \tag{C.8}$$

Therefor, $p(t)$ and $q(t)$ are real functions and it can be proved

$$p(t) = sgn(t)q(t) \tag{C.9}$$

Since $\epsilon_r - 1$ and ϵ_i are band-limited, i.e. significantly nonzero only within the frequency range $[-\omega_1, \omega_1]$, they can be expressed by the Fourier series:

$$\epsilon(\omega) - 1 = \sum_{n=-\infty}^{\infty} r_n e^{-\imath \frac{2\pi n}{\omega_1}\omega} \tag{C.10}$$

and r_n will be determined by:

$$\begin{aligned}
r_n &= \frac{1}{2\omega_1}\int_{-\omega_1}^{\omega_1} (\epsilon(\omega) - 1)e^{2\pi\imath\frac{\omega}{\omega_1}n} d\omega && \text{(C.11)}\\
&= \frac{1}{2\omega_1}\int_{-\omega_1}^{\omega_1} d\omega e^{-i\frac{2\pi n}{\omega_1}\omega}\int_{-\infty}^{\infty}(p(t)+q(t))e^{-i\omega t}dt && \text{(C.12)}\\
&= \frac{1}{2\omega_1}\int_{-\infty}^{\infty} dt(p(t)+q(t))\int_{-\omega_1}^{\omega_1} e^{-\imath\omega(t-\frac{2\pi}{\omega_1}n)}d\omega && \text{(C.13)}\\
&= \frac{1}{2\omega_1}\int_{-\infty}^{\infty} dt(p(t)+q(t))2\pi\delta(t-\frac{2\pi}{\omega_1}n) && \text{(C.14)}\\
&= \frac{\pi}{\omega_1}(p(\frac{2\pi}{\omega_1}n) + q(\frac{2\pi}{\omega_1}n)) && \text{(C.15)}
\end{aligned}$$

We let

$$p_n = \frac{\pi}{\omega_1}p(\frac{2\pi}{\omega_1}n), \tag{C.16}$$

and

$$q_n = \frac{\pi}{\omega_1}q(\frac{2\pi}{\omega_1}n). \tag{C.17}$$

From Eq. C.9, we have

$$p_n = sgn(k)q_n \tag{C.18}$$

Thus Eq. C.10 can be re-written as:

$$\epsilon(\omega) - 1 = \sum_{-\infty}^{\infty} (p_n e^{-i\frac{2\pi n}{\omega_1}\omega} + iq_n e^{-i\frac{2\pi n}{\omega_1}\omega}). \tag{C.19}$$

Therefore,

$$\epsilon_r(\omega) - 1 = \sum_{n=-\infty}^{\infty} p_n e^{-2\pi i\frac{\omega}{\omega_1}n} = 2\sum_{n=1}^{\infty} p_n cos(2\pi\frac{\omega}{\omega_1}n) \tag{C.20}$$

$$\epsilon_i(\omega) = \sum_{n=-\infty}^{\infty} -iq_n e^{-2\pi i\frac{\omega}{\omega_1}n} = 2\sum_{n=1}^{\infty} p_n sin(2\pi\frac{\omega}{\omega_1}n) \tag{C.21}$$

Thus by knowing p_n or q_n, we can calculate the permittivity. In practice, they are calculated from the discrete, measured real part or imaginary part of the permittivity or the complex refractive index. We can apply equation (C.20) and (C.21) for discrete ϵ_r or ϵ_i data. Let's say we measure $N/2$ (assuming N is an even number) evenly distributed data in the frequency range $[0, \omega_1]$. We can safely let

$$\epsilon_r(0) = \epsilon_i(0) = 0 \tag{C.22}$$

Thus we have the discrete Fourier series:

$$\epsilon_r(\omega_k) - 1 = \sum_{n=-N/2}^{N/2} p_n e^{-i\frac{k\pi\omega}{\omega_1}}, \tag{C.23}$$

where $\omega_k = \frac{k}{N}\omega_1$, $k \in [-N/2, +N/2)$. The Eq. C.23 can be re-written as

$$\epsilon_{rk} - 1 = \sum_{n=-N/2}^{N/2} p_n e^{-2\pi i\frac{n}{N}k} = \sum_{N/2}^{N-1} p_{n-N} e^{-2\pi i\frac{n-N}{N}k} + \sum_{n=0}^{N/2-1} p_n e^{-2\pi i\frac{n}{N}k} = \sum_{n=0}^{N-1} p_n e^{-2\pi i\frac{n}{N}k} \tag{C.24}$$

Similarly,

$$\epsilon_i(\omega_k) = \sum_{n=-N/2}^{N/2-1} -iq_n e^{-i\frac{k\pi\omega}{\omega_1}}, \tag{C.25}$$

and

$$\epsilon_{ik} = \sum_{n=-N/2}^{N/2-1} -iq_n e^{-2\pi\imath\frac{n}{2M}k} = \sum_{n=0}^{N-1} -iq_n e^{-2\pi i\frac{n}{N}k} \tag{C.26}$$

Using Eq. C.6, we obtain

$$p_n = \frac{1}{N}\sum_{k=0}^{N-1} \epsilon_{rk} e^{2\pi i\frac{k}{N}n}, \tag{C.27}$$

and

$$-iq_n = \frac{1}{N}\sum_{k=0}^{N-1} \epsilon_{\imath k} e^{2\pi\imath\frac{k}{N}n}. \tag{C.28}$$

The K-K relation is usually applied to the difference between the modified and the original permittivity:

$$\Delta p_n = \frac{1}{N}\sum_{k=0}^{N-1} \Delta\epsilon_{rk} e^{2\pi\imath\frac{k}{N}n} \tag{C.29}$$

$$-i\Delta q_n = \frac{1}{N}\sum_{k=0}^{N-1} \Delta\epsilon_{\imath k} e^{2\pi\imath\frac{k}{N}n} \tag{C.30}$$

$$\Delta\epsilon_{rk} = \sum_{n=0}^{N-1} \Delta p_n e^{-2\pi i\frac{n}{N}k} \tag{C.31}$$

$$\Delta\epsilon_{ik} = \sum_{n=0}^{N-1} -i\Delta q_n e^{-2\pi i\frac{n}{N}k} \tag{C.32}$$

Using the above equations and Eq. C.2, we can obtain the relations between Δn and $\Delta\alpha$. Therefore, the change of n can be calculated from the change of α, and vice versa.

C.2 Absorption Calculation

The epitaxial Ge-on-Si samples discussed in Chapter 6 are double-layered structures. The incident light passes the Ge film many times instead of one time due to the reflection from the air/Ge, the Ge/Si, and the Si/air interfaces, which causes interference in the Ge thin film. Therefore, the transmittance can not be calculated from the product of the transmittances of the air/Ge, the Ge/Si, and the Si/air interfaces. A modified transfer matrix method (TMM) with consideration of the non-coherency of the thick Si substrate layer, which is discussed in Appendix B, is adopted in the transmittance calculation.

The refractive index $n(\lambda)$ and the absorption coefficient $\alpha(\lambda)$ of the tensile-strained n^+ Ge films are related by the following equation system composed of two equations (We call them TMM equation and K-K equation respectively in the following text):

$$\begin{cases} \mathrm{A_{indicent}} = \mathrm{T_{TMM}}(n, \alpha)\mathrm{A_{trans}} \\ n = f_{\mathrm{K-K}}(\alpha) \end{cases} \tag{C.33}$$

where $\mathrm{A_{incident}}$ and $\mathrm{A_{trans}}$ are matrices containing the incident and the transmitted electric field intensities, $\mathrm{T_{TMM}}$ is the transfer matrix connection the incident and transmitted fields, and $f_{\mathrm{K-K}}$ is K-K relations connecting n and α.

Therefore, the two unknown variables n and α can be solved from the two equations. Since the two equations are both non-linear equations, an iterative approach is used.

The iterative self-consistent solution of the absorption coefficients from the transmittance data is achieved in the following way. We denote the absorption coefficient and refractive index of bulk Ge at wavelength λ as $\alpha_0(\lambda)$ and $n_0(\lambda)$, respectively. In the first iteration, we substitute the refractive index of bulk Ge $n_0(\lambda)$ into the TMM equation as an initial trial solution to solve $\alpha_1(\lambda)$, then we use the newly derived first order $\alpha_1(\lambda)$ to calculate the first order $n_1(\lambda)$ using the K-K equation described in the previous section.

Since the refractive index is changed to $n_1(\lambda)$ from $n_0(\lambda)$, the TMM equation is no longer satisfied. Therefore, $n_1(\lambda)$ is substituted back into the TMM equation to solve the second order $\alpha_2(\lambda)$, and the same step repeats to obtain higher orders of n and α. This process is iterated back and forth until $n(\lambda)$ and $\alpha(\lambda)$ satisfy both equations with appropriate precision.

The iteration process is illustrated in Fig. C.1. The transmittance calculated by the TMM equation using initial $\alpha_0(\lambda)$ and $n_0(\lambda)$ of bulk Ge clearly deviate significantly from the measured transmittance data, as shown in Fig. C.1 (c). As the iterative regression goes on the calculated transmittance spectrum moves closer to the experimental transmittance data, as indicated by the data at an intermediate step of the iterations in the figure. After final convergence, the transmittance calculated from the final $\alpha(\lambda)$ and $n(\lambda)$ matches the experimentally measured transmittance data.

A C++ program with graphical user interface (GUI) is developed to numerically imple-

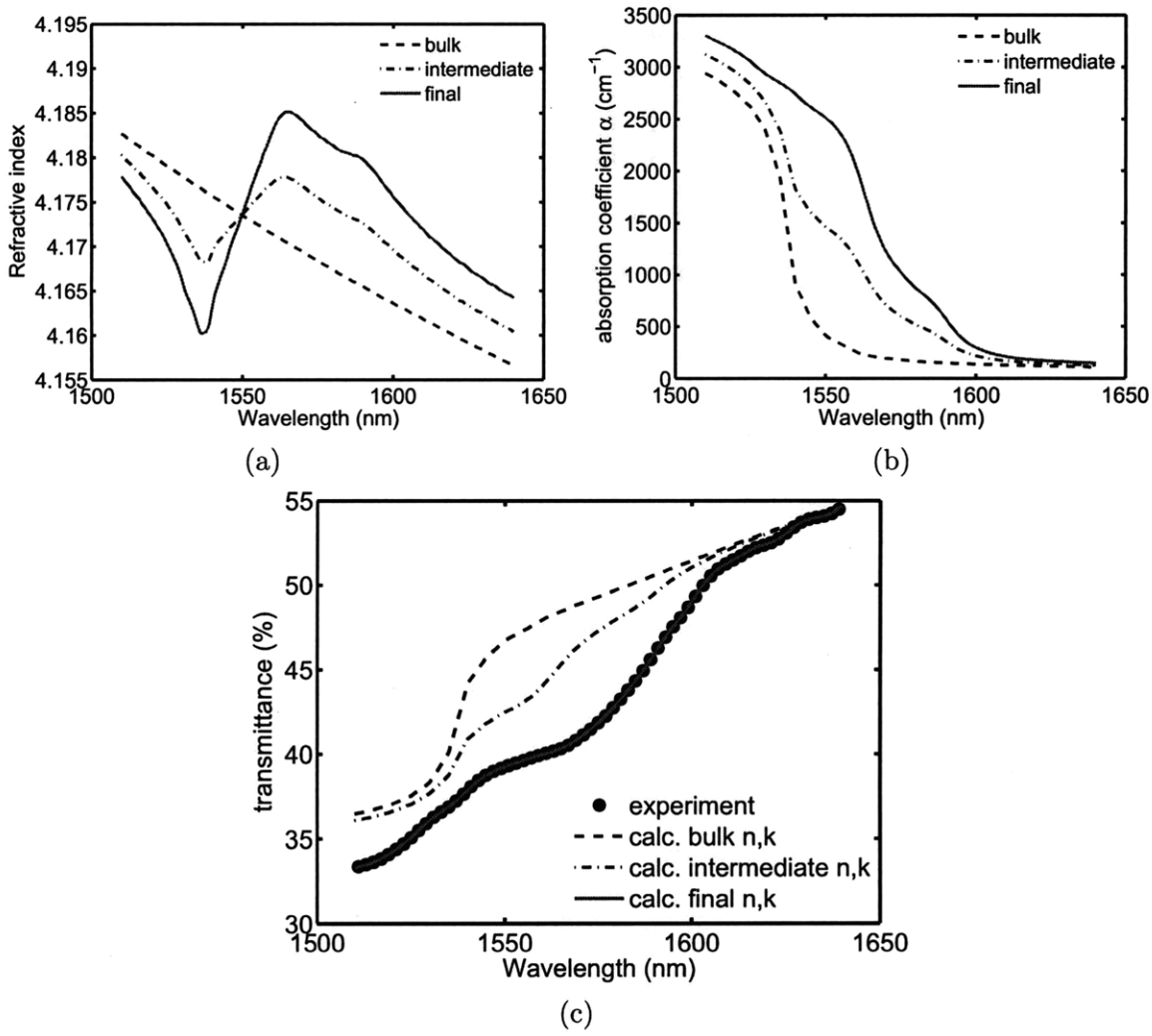

Figure C.1: Initial (using the optical parameters of bulk Ge), intermediate, and final iterative regression results for (a) absorption coefficienct, (b) refractive index, and (c) transmittance. The final absorption coefficients and refractive index completely matches the experimental transmittance data, and they also satisfy Kramers-Kronig relation.

ment this iteration process, as shown in Fig. C.2.

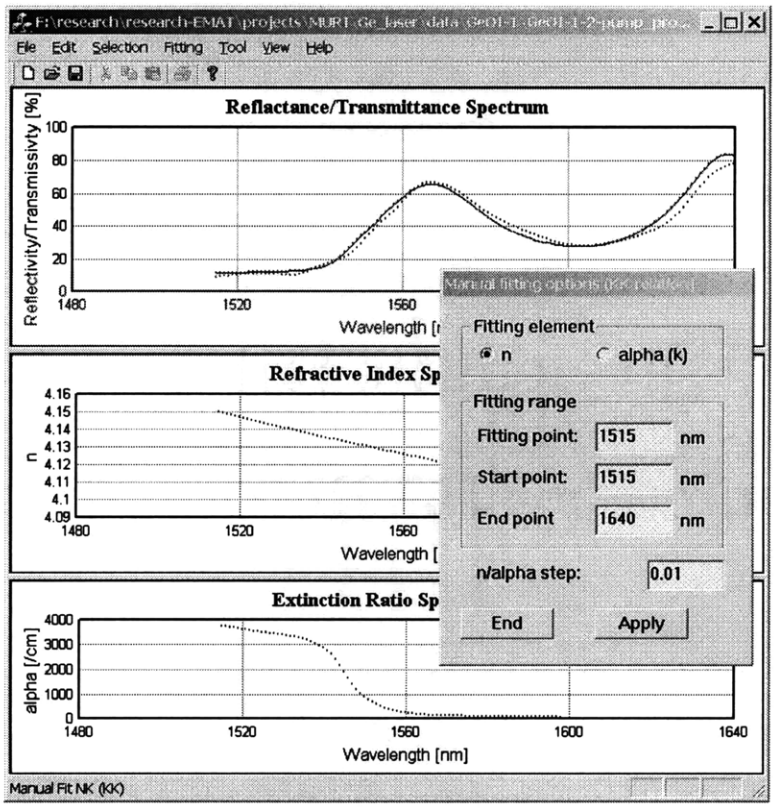

Figure C.2: Screenshot of the C++ program used to solve the absorption from the measured transmittance spectrum.

Appendix D

Multi-Wavelength Enhancement in Photonic Crystal Resonator

This appendix includes my work on some advanced resonator designs which can be used in both light emission and photo sensing applications. The designs involve one-dimensional (1-D) photonic crystal (PhC) made of multi-layer structures capable of multiply wavelength resonance enhancement capability. The concept of the multiply resonance is first explained both qualitatively and quantitatively based on simulations. To verify the concept, an amorphous silicon based, dual-wavelength (630 nm and 730 nm) resonance enhanced photoconductor has been fabricated. Design, fabrication, and characterization of this photoconductor are discussed.

D.1 Multi-Resonance Photonic Crystal Cavity Design

The motivation of this multiply resonance enhancement design stems from the needs for simultaneous detection of multiply wavelengths in the same device. A lot of applications fit this category such as multi-chemical detection, temperature determination, multi-spectral imaging, spectroscopy, and so on.

Fig. D.1 shows some examples of these applications that multiply resonance design can be applied to. Different chemicals have different characteristic light emission wavelengths under excitation, as shown in Fig. D.1(a), thus a device resonantly sensing light at multiply

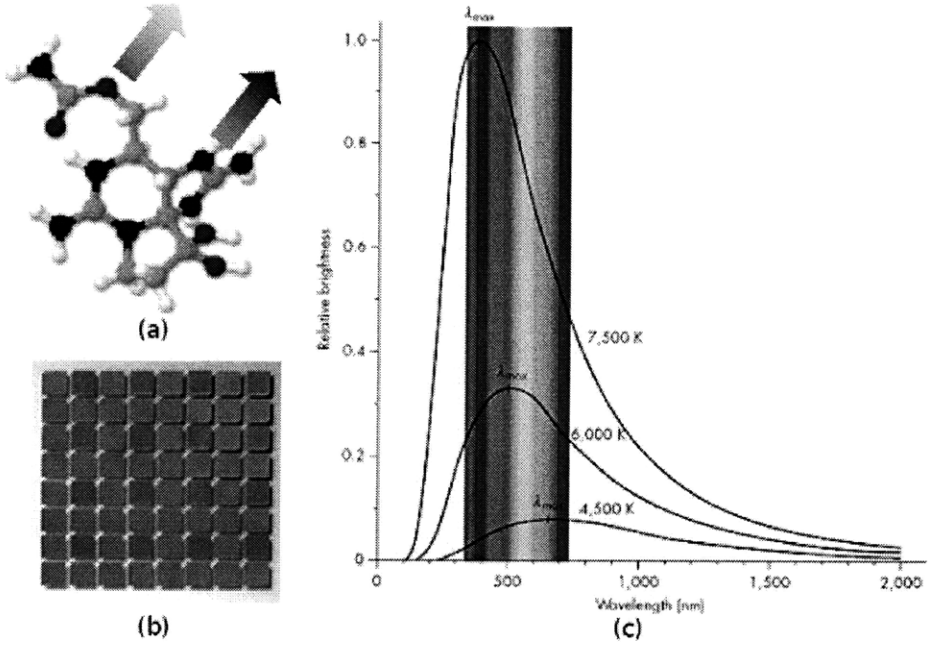

Figure D.1: Illustrations of the possible applications of multiply resonance design in (a) chemical sensing, (b) imaging, and (c) temperature determination.

wavelengths can be used to identify a certain type of chemical. Imaging applications need photodetection at three primary colors: red, green, and blue (RGB), as shown in Fig. D.1(b). The determination of the temperature of a hot object also requires detection at several different wavelengths so as to calculate temperature using the black body emission model, as shown in Fig. D.1(c).

Traditionally, multispectral detection capability has been achieved by several methods, including spatial registration, i.e. color filter array [136, 137], temporal registration (mechanical filter wheel) [138], tandem structure [139], and quantum well photodetectors [140, 141]. The first two methods complicate the pixel design and raise the issue of system reliability. In a tandem detector, the top detector serves as a passband filter for the bottom detector. The problem associated with this design is that only certain spectral bands are accessible due to limited material choices. Despite their high leakage current, quantum well detectors are capable of multispectral detection by varying applied bias. However, the time multiplexing involved prohibits simultaneous detection of different wavelength within a single pixel [142]. The multi-resonance design discussed in this chapter does not have these drawbacks and is a

promising alternative in these applications.

Besides, the same concept of the resonator design discussed here can be readily applied to light emission applications such as a multi-wavelength laser cavity design.

There are a couple of approaches to achieve multiply resonance using 1-D photonic crystal design. We discuss two approaches here: using different resonance orders of one resonator and using multiply strong coupled resonators. Although the simulation is performed for two resonance wavelengths, the same concept can be used for more wavelengths.

The resonator discussed in the following section is designed at visible wavelength range in order to compare the results from the amorphous silicon based photoconductor discussed in the next section. However, the design is not constrained to specific wavelength, so it can also be useful in infrared applications.

D.1.1 Multi-Resonance using Different Resonance Orders

The simplest, most commonly used 1-D photonic crystal is a thin film stack composed of two alternating materials. Both materials are dielectrics and transparent in the working wavelength range. The thicknesses of the two materials are designed to be a quarter of the resonance wavelength in the material, i.e. vacuum wavelength λ_0 divided by the refractive index of the material.

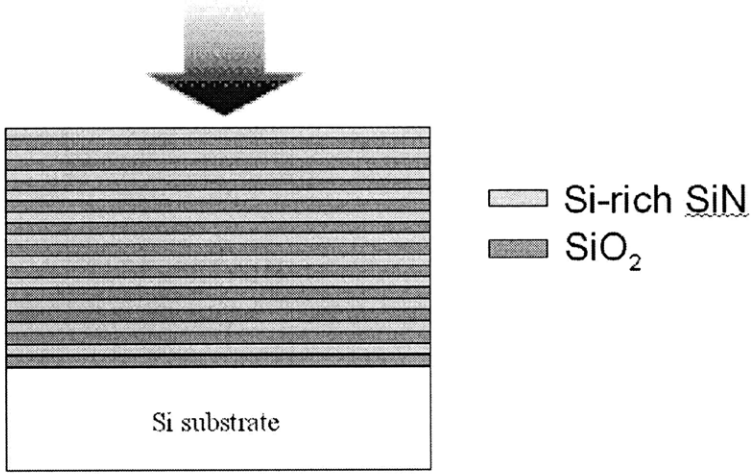

Figure D.2: A simple 1-D photonic crystal, or dielectric Bragg reflector (DBR) design with Si-rich Si nitride (SRN) and SiO_2.

Fig. D.2 shows an example of such stack composed of alternating Si-rich Si nitride (SRN) and SiO_2 layers. When the incident light is illuminated from the top of the stack, the reflected light intensity can be calculated using a transfer matrix method (TMM) explained in Appendix B.

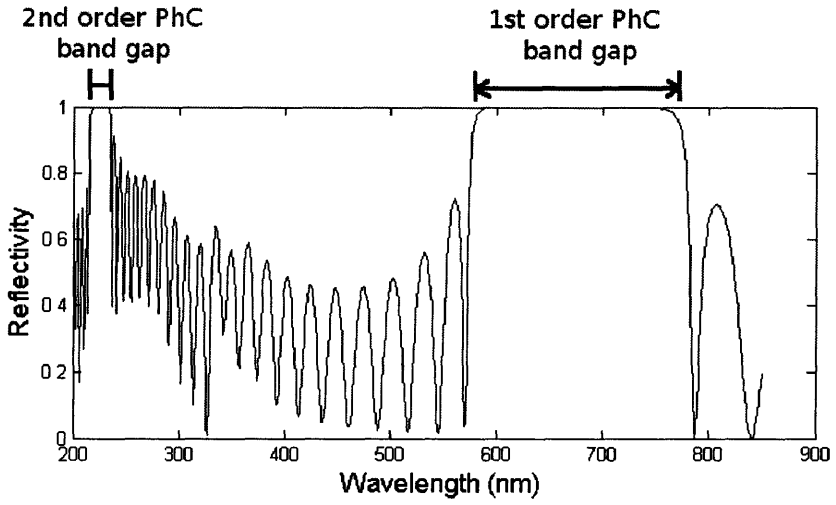

Figure D.3: Calculated reflectance spectrum of the SRN/SiO_2 DBR.

The calculated reflectance spectrum is shown in Fig. D.3. We can see that there is a broad wavelength range of high reflectivity (close to 100%) centered at λ_0. This wavelength range is called photonic bandgap of 1-D photonic crystal in analogy to electronic band gap in semiconductor crystals. Photonic bandgap is a result of the interference of light in DBR layers. Since such film stack serves as a high reflectivity mirror within the photonic bandgap, it is also called a dielectric Bragg reflector (DBR).

In Fig. D.3, we can see another narrower photonic bandgap at a shorter wavelength which is one third of λ_0, because the phase interference condition is the same at this wavelength compared to λ_0. This photonic bandgap is called the second order photonic band gap while the one centered at λ_0 is then called first order photonic bandgap for distinction. Theoretically, there are infinite number of photonic bandgaps with center wavelength satisfying

$$\frac{1}{2}\lambda_0 = (\frac{1}{2}+1)\lambda_1 = \cdots = (\frac{1}{2}+n)\lambda_n. \tag{D.1}$$

In practice, only a couple of low orders can be observed because the wavelength for high

orders is so short that the materials become no longer transparent.

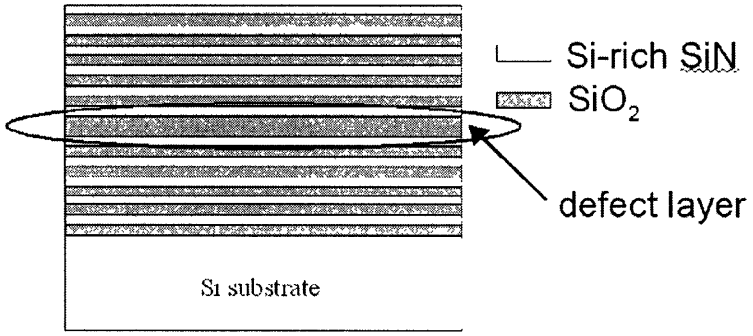

Figure D.4: A 1-D photonic crystal composed of Si-rich Si nitride (SRN) and SiO_2 mirror layers and a SiO_2 defect layer.

What makes 1-D photonic crystal more interesting is the introduction a so-called defect layer which has a different thickness. Fig. D.4 shows such a structure modified from the previous DBR structure by increasing the thickness of one SiO_2 layer by twice. The rest of the layers are called mirror layers sometimes to distinguish themselves from the defect layer.

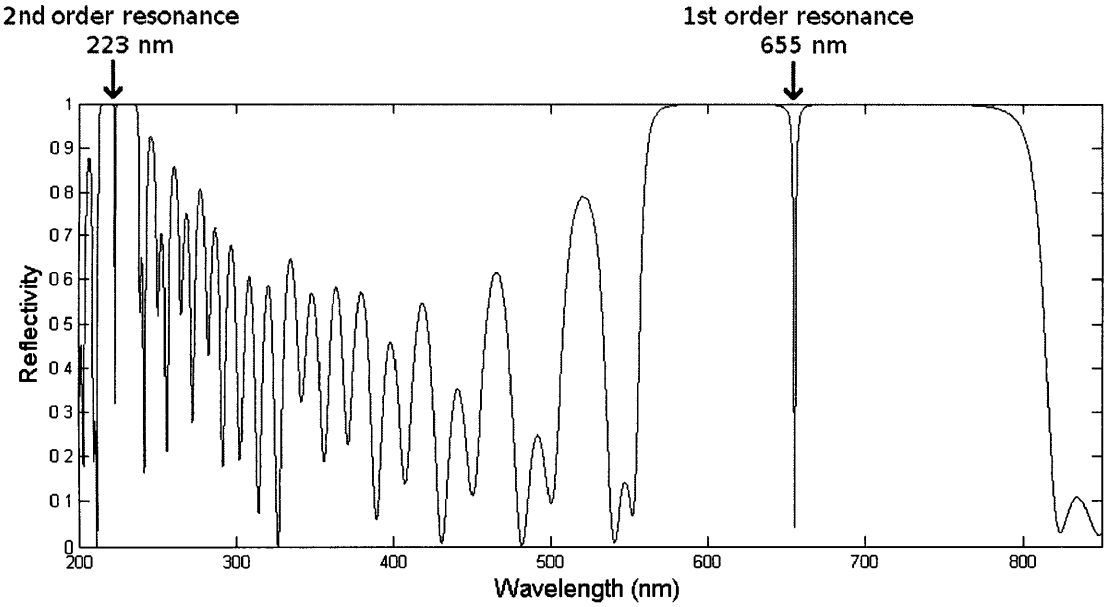

Figure D.5: Calculated reflectance spectrum of the SRN/SiO_2 photonic crystal with one SiO_2 defect layer.

The reflectance spectrum for this photonic crystal is calculated again and shown in Fig.

D.5. Unlike the spectrum without the defect layer, a sharp low reflectivity resonance peak exists at the center of each photonic bandgap as a result of the interference condition change in the defect layer. The first order resonance wavelength is equal to λ_0, the second order resonance wavelength is one third of λ_0, and so on.

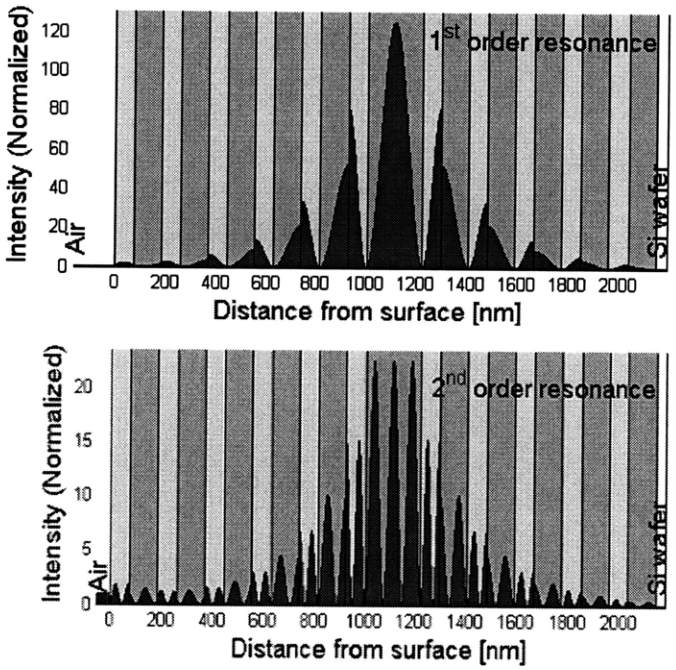

Figure D.6: Calculated light intensity distribution in the SRN/SiO_2 photonic crystal with one SiO_2 defect layer.

The light intensity distribution at the resonance wavelength is calculated for this photonic crystal following the approach in Appendix B. From the distribution, we can see a strong enhancement of light in the defect layer, e.g. over 100 times for the 1st order resonance in this case. Therefore, this defect layer is usually replaced by an photo sensitive material which absorbs the light at this wavelength and generates photocarriers. A photoconductor using this approach is much more sensitive than using the same material and thickness without DBR.

The difference in light intensity distribution between the first order and the second order resonance is the number of the wavelength period in the defect layer. The first order resonance only has one peak while the second order resonance has three, which is schematically drawn in Fig. D.7 again. Therefore, we can insert two thin active layers into the positions shown

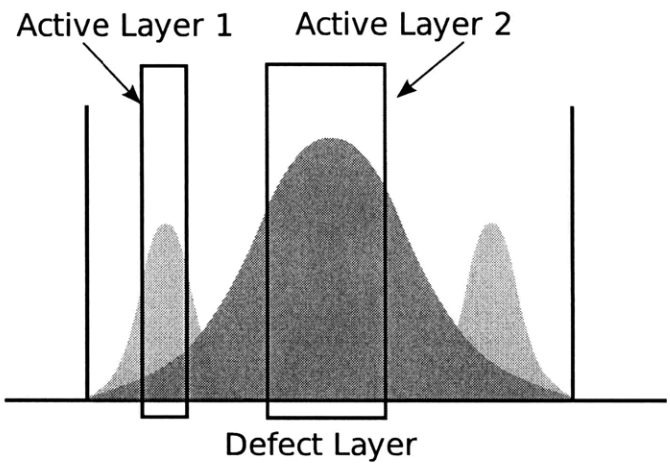

Figure D.7: Schematic light intensity distribution of the first and second order resonance in the SiO_2 defect layer.

in the figure to detect two resonance wavelengths, i.e. active layer 1 absorbs $\lambda_1 = \lambda_0/3$ and active layer 2 absorbs λ_0.

In spectroscopy applications, the wavelength composition of the incident light is unknown. The spectral analysis requires the minimization of the cross-talk between the sensing at λ_0 and λ_1. One solution is to choose the material in active layer 2 with little absorption at λ_0 since both resonance has a maximum at the position of active layer 2. Another way is to use algorithm to differentiate the absorption at two wavelengths after carefully calibrating the absorption at two wavelengths for each layer.

D.1.2 Multi-Resonance using Strong Coupled Resonators

In the previous section, an dual-wavelength resonance photonic crystal using different resonance orders is presented. There are two issues in this design: the large cross-talk between the two resonance mode and the large separation of the two resonance wavelengths (λ_0 and $\lambda_0/3$). We show another design in this section with less cross-talk and closer resonance wavelengths.

Fig. D.8 shows a photonic crystal design with two defect layers instead of one. The two SiO_2 defect layers are separated by a normal quarter-wavelength SRN mirror layer. These two defect layers are strongly coupled in an analogy to two closely placed quantum wells as shown schematically in Fig. D.9.

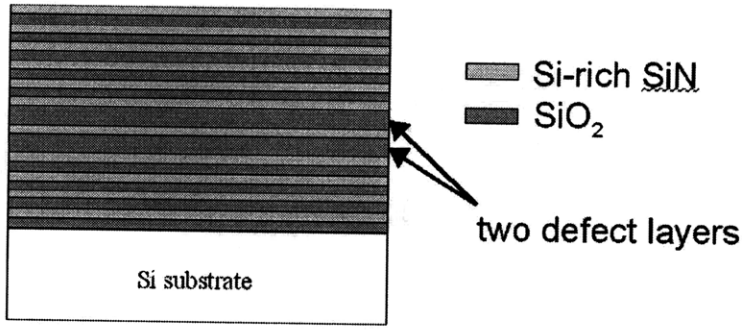

Figure D.8: A 1-D photonic crystal composed of Si-rich Si nitride (SRN) and SiO_2 mirror layers and two SiO_2 defect layers.

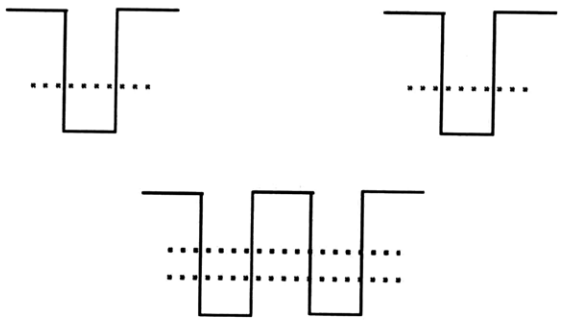

Figure D.9: Schematic quantum well analogy for a photonic crystal with two defect layers.

In analogy to quantum well, the resonance wavelength (or photon energy) is like the electron energy level allowed in the quantum well *. When the two identical quantum wells are separated far away from each other, the energy levels of both quantum well are equal as shown in the above part of the figure. When the two quantum wells are located closed enough, i.e. strongly coupled, the electronic wave function is affected by both quantum well potentials and the one energy level becomes two separated ones, one of which is higher than the original energy and the other is lower. The two electrons in the two quantum well system occupy these two separated states respectively, also a reflection of the Pauli exclusion principle that no two identical fermions may occupy the same quantum state simultaneously. These two quantum states (energy levels) are called bonding state (energy) and anti-bonding

*First order resonance can be thought as fundamental energy level and higher orders resonances are higher energy levels. Only first order resonance of the photonic crystal is considered in this section.

state (energy) respectively.

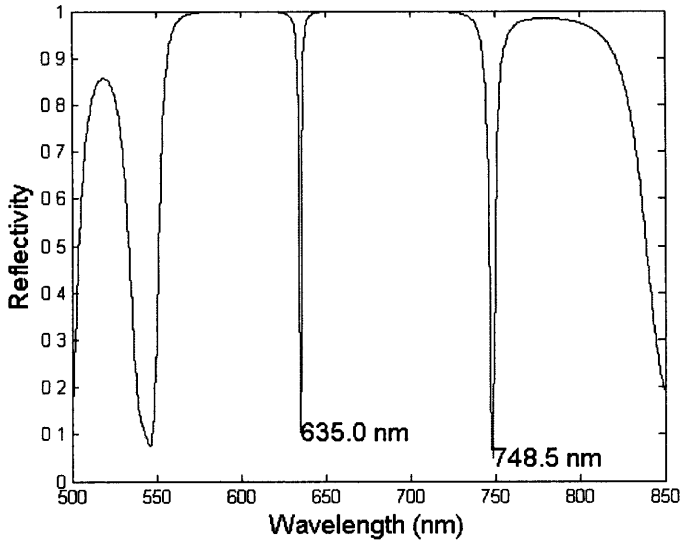

Figure D.10: The calculated reflectance spectrum of the SRN/SiO_2 photonic crystal with two SiO_2 defect layers.

Similarly, in the strongly coupled two defect layers of the photonic crystal, one resonance wavelength becomes two wavelengths, one of which is longer than λ_0 while the other is shorter.

However, the position of the active layers can not be chosen as the defect layers (or within the defect layers), because both resonance wavelengths have maxima in the defect layers, which can be seen from the calculated light intensity distribution at two resonance wavelengths (748 nm and 635 nm) in Fig. D.11. Instead, we should replace the layers adjacent to the two defect layers with active materials. In Fig. D.11, we can see that Layer 1, left to the first defect layer from the left, has an intensity maximum at 748 nm but minimum at 635 nm, on the other hand, Layer 2 sandwiched by the two defect layers has an intensity maximum at 635 nm but minimum at 748 nm. Therefore, by replacing these two layers with active materials, we can enable enhanced absorption at two wavelengths in two different layers with little cross-talk .

It is to be noticed that the quarter-wavelength mirror layers and half-wavelength defect layers are not the optimal design of this strong coupled photonic crystal. In order to minimize the cross-talk, we have adjusted the layer thicknesses in the design discussed in the next

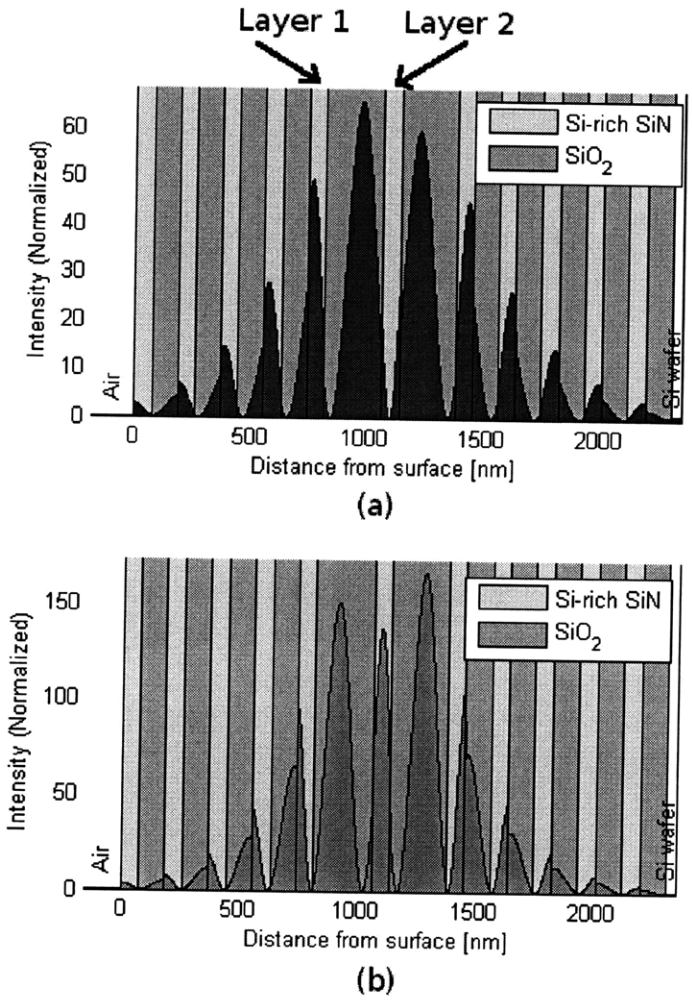

Figure D.11: The calculated light intensity distribution in the SRN/SiO_2 photonic crystal with two SiO_2 defect layers at two resonance wavelengths (a) 748 nm and (b) 635 nm.

section.

D.2 Amorphous-Si Photonic Crystal Photoconductor

Based on the bonding/anti-bonding dual resonance photonic crystal design, an photoconductor has been designed by using amorphous Si layers as active materials. The photoconductor has been fabricated, and it is capable of dual wavelength enhanced detection at 630 nm and 730 nm.

As we mention earlier, multispectral detection capability has been achieved by several

methods, including spatial registration, i.e. color filter array [136, 137], temporal registration (mechanical filter wheel) [138], tandem structure [139], and quantum well photodetectors [140, 141]. In addition to all the drawbacks for these designs mentioned in the previous section, all the aforementioned methods necessitate the engineering of lattice-matched single-crystalline materials in order to reduce dark current, which requires high-cost and complicated material growth facilities such as Molecular Beam Epitaxy (MBE) or Metal-Organic Chemical Vapor Deposition (MOCVD). Therefore the use of amorphous Si in this photoconductor design dramatically reduces the cost for frication as well.

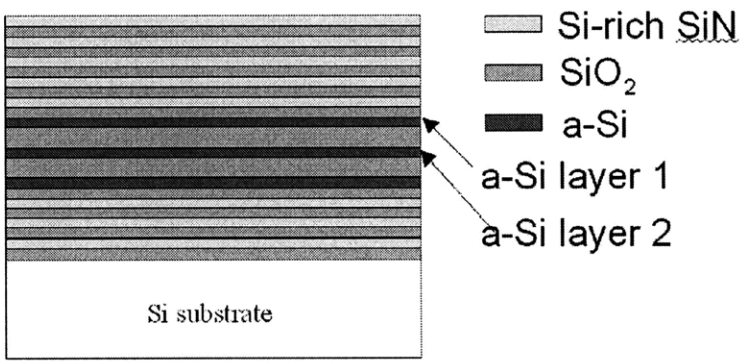

Figure D.12: Schematic of amorphous Si based 1-D photonic crystal photoconductor with dual-wavelength detection with resonant cavity enhancement (RCE).

Fig. D.12 shows the photonic crystal design of the amorphous Si based photoconductor, which is very similar to the design in Fig. D.8 except for the replacement of amorphous Si layers. Three amorphous Si layers are used, while only two of them, denoted as a-Si layer 1 and a-Si layer 2, are electrically contacted for detecting photocurrent at two resonance wavelengths respectively.

The refractive indices for SiO_2 and Si rich Si nitride (SRN) used in the simulation are 1.45 and 2.26, which are nearly constant in the interested wavelength range. SRN instead of stoichiometric Si_3N_4 is used in the stack design in order to maximize the stack refractive index contrast and thus large photonic bandgap is obtained. The use of amorphous Si reduces fabrication cost and simplifies device processing by eliminating the complicated single crystal growth process. Meanwhile, amorphous Si exhibits higher absorption compared to their crystalline counterpart in the wavelength range we investigated.

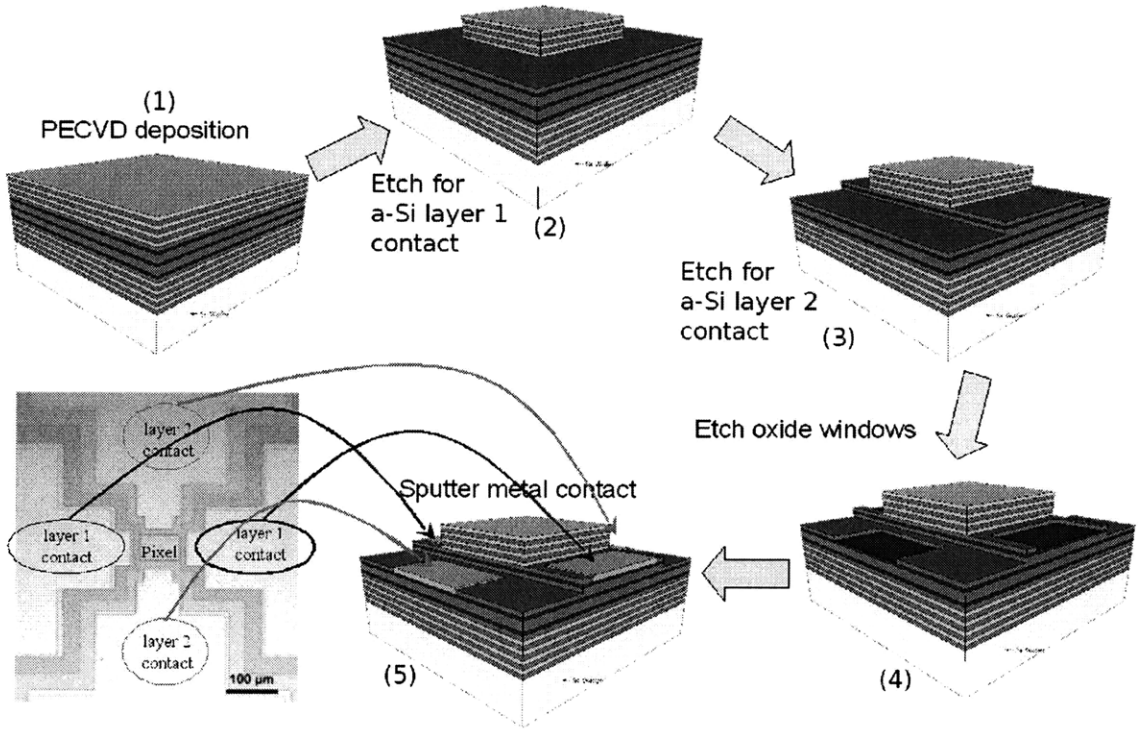

Figure D.13: Fabrication flow of the amorphous Si based 1-D photonic crystal photoconductor and the top view microscopic image of a fabricated device.

The photonic crystal photoconductor pixels were fabricated through the procedure in Fig. D.13. The whole photonic crystal stack was deposited on a 6" Si (100) substrate using Applied Materials Centura 5200 Plasma Enhanced Chemical Vapor Deposition (PECVD) with the deposition temperature of 400 ^oC for SiO_2 and Si-rich Si nitride and 350 ^oC for amorphous Si.

Then the stack is patterned using an Electronic Visions EV620 mask aligner lithography system with a contact mask and 10 mW/cm^2s high-pressure mercury lamp exposure (all lithography processes in some following steps were deployed with the same system and parameters). The whole area except for the device region was etched using an Applied Materials AME 5000 reactive-ion etching (RIE) system with Halocarbon 14 (CF_4) plasma to expose the mirror layer right above the amorphous Si layer 1. Another patterning and plasma etching was performed to expose the mirror layer right above the amorphous Si layer 2 in part of the area as shown in the Step (3) in Fig. D.13. Then the etched area was patterned again for the contact regions and a buffer oxide etching (BOE) was used, for high etching selectivity

between SiO_2 and Si, to etch the mirror layer in the contact regions (Step (4)).

Finally, Al(0.2%Si) pads were sputtered on the surface followed by a patterning and an etching using Lam Rainbow 9600 Metal Etch System to form ohmic contacts through SiO_2 windows. The top view microscopic image of a fabricated device is shown in the figure. We can see the two pairs of contact pads are connected to amorphous Si layer 1 and 2 respectively to form two independent photocurrent measurement circuits.

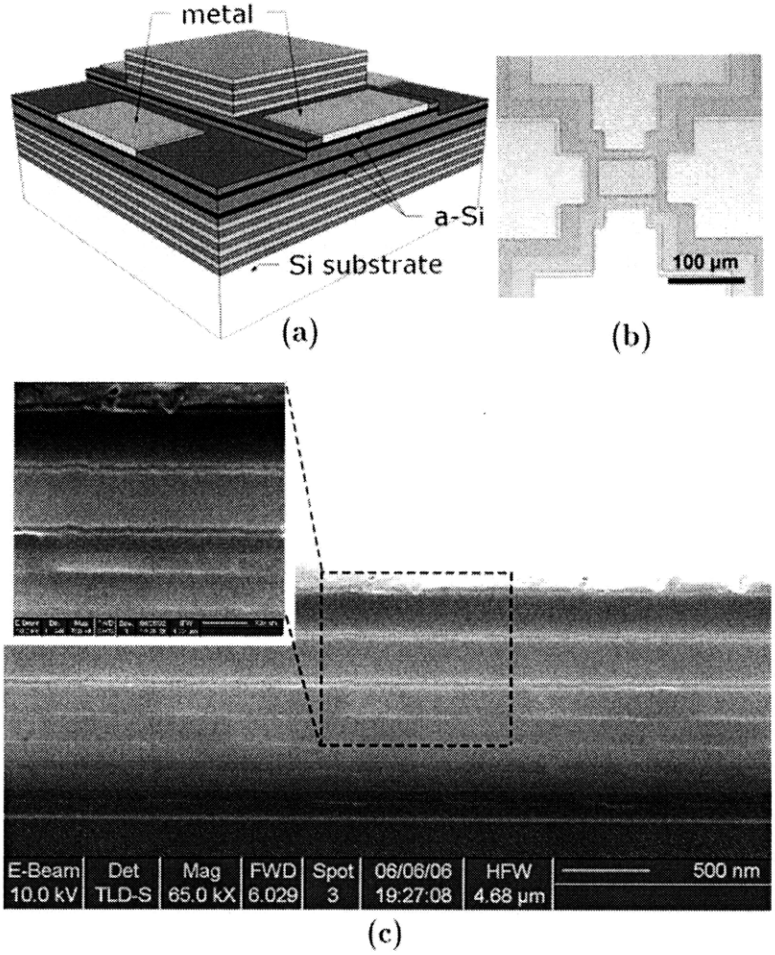

Figure D.14: (a) Design schematic of the dual-wavelength amorphous Si photonic crystal photoconductor. (b) the top view microscopic image of a fabricated photoconductor pixel. (c) High resolution cross-section TEM image of a photonic crystal pixel showing the excellent thickness uniformity and smooth interfaces of the photonic crystal stack. [17]

The entire fabrication process is compatible with standard Si complimentary metal oxide semiconductor (Si-CMOS) technology, which projects significant cost reduction for mass

production. In order to verify the quality of the stack layers, a high resolution cross-section Transmission Electron Microscope (TEM) image of pre-processed structure was taken and is shown in Fig. D.14 (c), in which bottom SiO_2/SRN mirror stack layers as well as three thin amorphous Si layers with uniform thicknesses and smooth interfaces can be seen clearly.

Based on the concept of the dual-resonance due to two strongly coupled defect layers, we optimized the stack design so as to maximize the detectivity (D*) of the photoconductor as well as to minimize the cross-talk of the absorption between the two resonance wavelengths in the two amorphous Si layers.

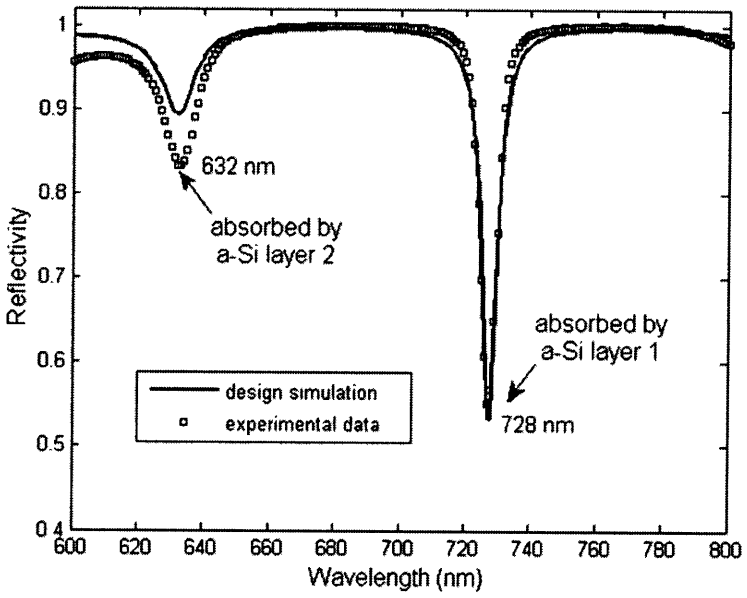

Figure D.15: Experimental data and transfer matrix simulation result of the reflectance of the photonic crystal stack, showing two resonant peaks at 632 nm and 728 nm, which are selectively absorbed by the amorphous Si layer 1 and 2, respectively. [17]

The two resonance wavelengths of the optimized design were 632 nm and 728 nm respectively which can be seen from the two resonant peaks in the reflectance spectrum in Fig. D.15. The experimental reflectance spectrum of the photonic crystal stack measured using a Cary 5E UV-Vis-NIR dual-beam spectrophotometer shows a very good match to the simulation result, which verifies the model and implies the excellent thickness and the refractive index control during the film deposition process. The quality factors of the two peaks shown in this dual-resonance spectrum is relatively less than that in the spectrum of the dielectrics-

only stack shown in Fig. D.10, because the introduction of the amorphous Si layers changes the refractive index periodicity of the original photonic crystal and the absorption of the amorphous Si affects the light interference.

The fabricated device was electrically characterized using a HP 4145A semiconductor parameter analyzer. A fixed voltage (10 V) was applied to the photoconductor and the output current was monitored. A halogen lamp coupled with a Jobin Yvon (Division D Instruments SA) grating monochromator controlled by Optical Science Prop-11 wavelength scanner was used as the light source. Selective multispectral response was observed at resonance wavelength where only one photoconductive layer exhibited photocurrent. Detectivities were calculated using equation

$$D^* = \frac{\sqrt{A \times B}}{\text{NEP}}, \tag{D.2}$$

where, A is the photoconductor pixel area, B is the signal bandwidth, NEP is noise equivalent power. Both shot noise and Johnson noise are considered to calculate the NEP, while the Johnson noise is relatively less due to the high resistance ($> 10^{10}\Omega$) of the thin amorphous Si layers.

As can be seen in Fig. D.16, the detectivities as high as 2.6×10^{10} cm·Hz$^{1/2}$W^{-1} at 632 nm and 2.0×10^{10} cm·Hz$^{1/2}$W^{-1} at 728 nm are obtained for the amorphous Si layer 2 and layer 1, respectively. The measured resonance absorption peaks are significantly broadened due to two major effects. The various incidence angles of non-collimated light through optical lens shift resonant peaks so as to increase the absorption peak bandwidth. The other effect is the fairly broad bandwidth of the incident light when we tuned the grating monochromator slit wider to enhance incident optical flux. Given the amorphous nature of the photoconductor and the unoptimized electrode pad spacing, these detectivity figures compare favorably to state-of-the-art commercial photodiodes made of single-crystalline Si, which feature a detectivity of $\sim 10^{11}$ cm·Hz$^{1/2}$W^{-1}.

In conclusion, we demonstrate an amorphous Si based photoconductive pixel that utilizes photonic crystal structure for dual-wavelength resonance enhancement. Wavelength-selective absorption based on mode discrimination from the strongly coupled two defect layers is achieved, and excellent agreement on reflectance spectrum between theory and experiment

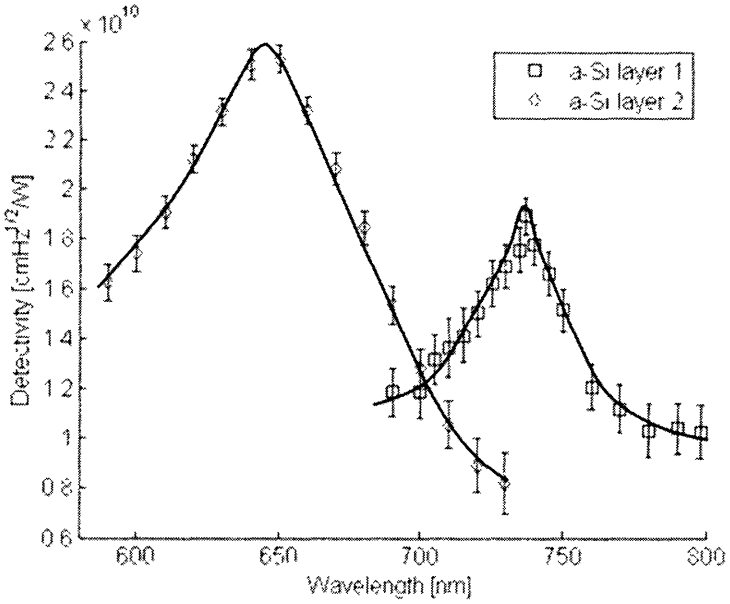

Figure D.16: Detectivity spectra at 10V of the first two amorphous Si photoconductive layers showing wavelength selectivity. Detectivities are calculated from data measured using a tungsten halogen lamp monochromator. The various incidence angles of non-collimated light through optical lens corresponding to various resonant peaks and the fairly broad bandwidth of the monochromator light and account for the measured absorption peak broadening. [17]

is presented. The detector shows detectivities as high as 2.6×10^{10} cm·Hz$^{1/2}$W^{-1} at 632 nm and 2.0×10^{10} cm·Hz$^{1/2}$W^{-1} at 728 nm, corresponding to two resonant modes in the photonic crystal structure.

Bibliography

[1] R. Kirchain and L. C. Kimerling, "A roadmap for nanophotonics," Nature Photonics **1**, 303–305 (2007).

[2] H. S. L. K. Wada, K. K. Lee, S. Akiyama, J. Michel, L. C. Kimerling, M. Popovic, and H. A. Haus, "Silicon and Silica Platform for On-chip Optical Interconnection," in *Proceedings of Lasers and Electro-Optics Society* (2002).

[3] M.Levinstein, S. Rumyantsev, and M. Shur, eds., *Handbook Series on Semiconductor Parameters* (World Scientific, 1996).

[4] W. C. Dash and R. Newman, "Intrinsic Optical Absorption in Single-Crystal Germanium and Silicon at 77K and 300K," Phy. Rev. **99**(4), 1151–1155 (1955).

[5] R. Braunstein, A. R. Moore, and F. Herman, "Intrinsic Optical Absorption in Germanium-Silicon Alloys," Phy. Rev. **109**(3), 695–710 (1958).

[6] M. V. Hobden, "Direct optical transitions from the split-off valence band to the conduction band in germanium," J. Phys. Chem. Solids **23**(6), 821–822 (1962).

[7] A. Frova and P. Handler, "Franz-Keldysh Effect in the Space-Charge Region of a Germanium p-n Junction," Phy. Rev. **137**(6A), A1857–A1861 (1965).

[8] J. Liu, D. D. Cannon, Y. Ishikawa, K. Wada, D. T. Danielson, S. Jongthammanurak, J. Michel, and L. C. Kimerling, "Deformation potential constants of biaxially tensile stressed Ge epitaxial films on Si(100)," Phys. Rev. B **70**(15), 155,309 (2004).

[9] M. L. Yu, D. J. Vitkavage, and B. S. Meyerson, "Doping reaction of PH_3 and B_2H_6 with Si(100)," J. Appl. Phys. **59**, 4032–4037 (1986).

[10] G. Wang, F. E. Leys, L. Souriau, R. Loo, M. Caymax, D. P. Brunco, J. Geypen, H. Bender, M. Meuris, W. Vandervorst, and M. M. Heyns, "Selective epitaxial growth of germanium on Si wafers with shallow trench isolation: an approach for Ge virtual substrates," ECS Trans. **16**(10), 829–836 (2008).

[11] J. R. Haynes and N. G. Nilsson, "The direct radiative transitions in germanium and their use in the analysis of lifetime," in *Proceedings of VIIth International Conference on Physics of Semiconductors*, p. 21 (Paris, 1964).

[12] X. Sun, J. Liu, L. C. Kimerling, and J. Michel, "Optical Bleaching of Thin Film Ge on Si," ECS Trans. **16**(10), 881–883 (2008).

[13] X. Sun, J. Liu, L. C. Kimerling, and J. Michel, "Direct gap photoluminescence of n-type tensile-strained Ge-on-Si," Appl. Phys. Lett. (2009). In review.

[14] X. Sun, J. Liu, L. C. Kimerling, and J. Michel, "Room Temperature Direct Band Gap Electroluminesence from Ge-on-Si Light Emitting Diodes," Optics Lett. **34**(8), 1198–1200 (2009).

[15] C. Jacoboni, F. Nava, C. Canali, and G. Ottaviani, "Electron drift velocity and diffusivity in germanium," Phys. Rev. B **24**(2), 1014–1026 (1981).

[16] J. Liu, X. Sun, L. C. Kimerling, and J. Michel, "Direct band gap photoluminescence and onset of optical gain of band-engineered Ge-on-Si at room temperature," Optics Lett. (2009). Accepted.

[17] X. Sun, J. Hu, C.-Y. Hong, J. F. Viens, X. Duan, R. Das, A. M. Agarwal, and L. C. Kimerling, "Multispectral pixel performance using a one-dimensional photonic crystal design," Appl. Phys. Lett. **89**, 223,522 (2006).

[18] G. Moore, "Cramming more components onto integrated circuits," Electronics **38**, 144–117 (1965).

[19] W. Haensch, E. J. Nowak, R. H. Dennard, P. M. Solomon, A. Bryant, O. H. Dokumaci, A. Kumar, X. Wang, J. B. Johnson, and M. V. Fischetti, "Silicon CMOS devices beyond scaling," IBM J. Res. & Dev. **50**, 339–361 (2006).

[20] R. H. Dennard, F. H. Gaensslen, H.-N. Yu, V. L. Rideout, E. Bassous, and A. LeBlanc, "Design of ion-implanted MOSFETs with very small physical dimensions," IEEE J. Solid-State Circuits **SC-9**, 256–268 (1974).

[21] D. A. Muller, "A sound barrier for silicon?" Nature Mater. **4**, 645–647 (2005).

[22] P. Miller, "Pentium 4 overclocked to 8GHz," `http://www.engadget.com/2007/01/24/pentium-4-overclocked-to-8ghz-lets-see-your-fancy-core-2-try-t` (2007).

[23] S. B. Wijeratne, N. Siddaiah, S. K. Mathew, M. A. Anders, R. K. Krishnamurthy, J. Anderson, M. Ernest, and M. Nardin, "A 9-GHz 65-nm Intel Pentium 4 Processor Integer Execution Unit," IEEE J. Solid-State Circuit **42**, 26–37 (2007).

[24] "International Technology Roadmap for Semiconductors," `http://www.itrs.net/home.html` (2008).

[25] R. Krithivasan, Y. Lu, J. D. Cressler, J.-S. Rieh, M. Khater, D. Ahlgren, and G. Freeman, "Half-TeraHertz Operation of SiGe HBTs," IEEE Electron Dev. Lett. **27**, 567–569 (2006).

[26] R. Beach, "Northrop Grumman develops worlds fastest transistor," `http://compoundsemiconductor.net/blog/2007/12/northrop_grumman_develops_worl.html` (2007).

[27] B. Jalali and S. Fathpour, "Silicon Photonics," IEEE J Lightwave Technol. **24**(12), 4600–4615 (2006).

[28] M. Lipson, "Overcoming the limitations of microelectronics using Si nanophotonics: solving the coupling, modulation and switching challenges," Nanotechnology **15**(10), S622–S627 (2004).

[29] M. Haurylau, G. Chen, H. Chen, J. Zhang, N. A. Nelson, D. H. Albonesi, E. G. Friedman, and P. M. Fauchet, "On-Chip Optical Interconnect Roadmap: Challenges and Critical Directions," IEEE J. Sel. Topic Quantum Electron. **12**(6), 1699–1705 (2006).

[30] "MIT Microphotonics Center," `http://mphotonics.mit.edu/index.php`.

[31] L. Pavesi and D. J. Lockwood, eds., *Si Photonics*, chap. 2, pp. 51–99 (Springer, 2003).

[32] D. H. Sze, T. Landin, A. Lytel, and R. D. H.L., "Optical interconnects: out of the box forever?" IEEE J. Sel. Top. Quant. **9**, 614–623 (2003).

[33] I. Roudas, B. Hemenway, and R. R. Grzybowski, "Optimization of a supercomputer optical interconnect architecture," (2007).

[34] R. Hemenway, R. Grzybowski, C. Minkenberg, and R. Luijten, "Optical-packet-switched interconnect for supercomputer applications," J. Opt. Net. **3**, 900–913 (2004).

[35] L. Kleinrock, M. Gerla, N. Bambos, J. Gong, E. Gafni, L. Bergman, J. Bannister, S. Monacos, T. Bujewski, P. I-In, B. Kannan, B. Kwan, E. Leonardi, J. Peck, and P. Palnati, "The Supercomputer Supernet testbed: a WDM-based supercomputer interconnect," J. Light. Technol. **14**, 1388–1399 (1996).

[36] J. Wallace, "20 petaflop IBM supercomputer will rely on optical interconnects," `http://www.optoiq.com/articles/display/352500/s-articles/s-laser-focus-world/s-technology-news/s-20-petaflop-ibm-supercomputer-will-rely-on-optical-interconnects.html` (2009).

[37] B. E. Floren, T. A. Lane, D. S. Dunning, J. D. Kessinger, S. F. Nugent, and R. L. Traylor, "Optical interconnects in the Touchstone supercomputer program," vol. 1582, p. 46 (1992).

[38] "Kotura Inc. products," `http://www.kotura.com`.

[39] C. Gunn, "CMOS photonics for high-speed interconnects," IEEE Micro **26**, 58–66 (2006).

[40] I. O'Connor, F. Tissafi-Drissi, D. Navarro, F. Mieyeville, F. Gaffiot, J. Dambre, M. D. Wilde, D. Stroobandt, and M. Briere, "Integrated optical interconnect for on-chip data transport," in *Circuits and Systems, 2006 IEEE North-East Workshop on*, p. 209 (Gatineau, Que., 2006).

[41] W. Aicher and K. Haberger, "Influence of optical interconnects at the chip and board levels," Opt. Eng. **38**, 313–322 (1999).

[42] I. OĆonnor, F. Tissafi-Drissi, F. Gaffiot, J. Dambre, M. D. Wilde, J. V. Campenhout, D. V. Thourhout, J. V. Campenhout, and D. Stroobandt, "Systematic Simulation-Based Predictive Synthesis of Integrated Optical Interconnect," IEEE Trans. VLSI Sys. **15**, 927–940 (2007).

[43] R. Chen, L. Lin, C. Choi, Y. Liu, B. Bihari, L. Wu, S. Tang, R. Wickman, B. Picor, M. Hibb-Brenner, J. Bristow, and Y. Liu, "Fully embedded board-level guided-wave optoelectronic interconnects," Proc. IEEE **88**, 780–793 (2000).

[44] J. Takahashi, T. Tsuchizawa, T. Watanabe, and S. Itabashi, "Oxidaion induced improvement in the sidewall morphology and cross-sectional profile of silicon wire waveguides," J. Vac. Sci. Technol. B **22**, 2522–2525 (2004).

[45] D. K. Sparacin, S. J. Spector, and L. C. Kimerling, " Silicon waveguide sidewall smoothing by wet chemical oxidation," J. Lightwave Technol. **23**(8), 2455–2461 (2005).

[46] P. Trinh, S. Yegnanarayanan, F. Coppinger, and B. Jalali, "Silicon-on-insulator (SOI) phased-array wavelength multi/demultiplexer with extremely low-polarization sensitivity," IEEE Photon. Technol. Lett. **9**(7), 940–942 (1997).

[47] T. Tsuchizawa, K. Yamada, H. Fukuda, T. Watanabe, J. ichi Takahashi, M. Takahashi, T. Shoji, E. Tamechika, S. Itabashi, and H. Morita, "Microphotonics devices based on silicon microfabrication technology," IEEE J. Sel. Topics Quantum Electron. **11**(1), 232–240 (2005).

[48] P. Koonath, T. Indukuri, and B. Jalali, "Add-drop filters utilizing vertically coupled microdisk resonators in silicon," Appl. Phys. Lett. **86**, 091,102 (2005).

[49] L. Friedman, R. A. Soref, and J. P. Lorenzo, "Silicon double-injection electro-optic modulator with junction gate control," J. Appl. Phys. **63**, 1831 (1988).

[50] C. K. Tang and G. T. Reed, "Highly efficient optical phase modulator in SOI waveguides," IEEE Electron. Lett. **31**(6), 451–452 (1995).

[51] V. R. Almeida, C. A. Barrios, R. R. Panepucci, and M. Lipson, "All-optical control of light on a silicon chip," Nature **431**, 1081–1084 (2004).

[52] Q. Xu, B. Schmidt, S. Pradhan, and M. Lipson, "Micrometre-scale silicon electro-optic modulator," Nature **435**, 325–327 (2005).

[53] S. Jongthammanurak, J. Liu, K. Wada, D. D. Cannon, D. T. Danielson, D. Pan, L. C. Kimerling, and J. Michel, "Large electro-optic effect in tensile strained Ge-on-Si films," Appl. Phys. Lett. **89**, 161,115 (2006).

[54] J. Liu, D. Pan, S. Jongthammanurak, K. Wada, L. C. Kimerling, and J. Michel, "Design of monolithically integrated GeSi electro-absorption modulators and photodetectors on an SOI platform," Opt. Express **15**, 623–628 (2007).

[55] J. Liu, D. D. Cannon, K. Wada, Y. Ishikawa, S. Jongthammanurak, D. T. Danielson, J. Michel, and L. C. Kimerling, "Tensile strained Ge p-i-n photodetectors on Si platform for C and L band telecommunications," Appl. Phys. Lett. **87**(1), 011,110 (2005).

[56] J. Liu, J. Michel, W. Giziewicz, D. Pan, K. Wada, D. D. Cannon, S. Jongthammanurak, D. T. Danielson, L. C. Kimerling, J. Chen, F. O. Ilday, F. X. Kartner, and J. Yasaitis, "High-performance, tensile-strained Ge p-i-n photodetectors on a Si platform," Appl. Phys. Lett **87**(10), 103,501 (2005).

[57] D. Ahn, C. yin Hong, J. Liu, W. Giziewicz, M. Beals, L. C. Kimerling, and J. Michel, "High performance, waveguide integrated Ge photodetectors," Opt. Express **15**(7), 3916–3921 (2007).

[58] V. R. Almeida, R. R. Panepucci, , and M. Lipson, "Nanotaper for compact mode conversion," Opt. Lett. **28**(15), 1302–1304 (2003).

[59] V. Nguyen, T. Montalbo, C. Manolatou, A. Agarwal, C.-Y. Hong, J. Yasaitis, L. Kimerling, and J. Michel, "Silicon-based highly-efficient fiber-to-waveguide coupler for high index contrast system," Appl. Phys. Lett. **88**, 081,112 (2006).

[60] P. E. Barclay, K. Srinivasan, and O. Painter, "Design of photonic crystal waveguides for evanescent coupling to optical fiber tapers and integration with high-Q cavities," J. Opt. Soc. Am. B **20**(11), 2274–2284 (2003).

[61] D. Taillaert, W. Bogaerts, P. Bienstman, T. Krauss, P. Van Daele, I. Moerman, S. Verstuyft, K. De Mesel, and R. Baets, "An out-of-plane grating coupler for efficient butt-coupling between compact planar waveguides and single-mode fibers," IEEE J. Quantum Electron. **38**(7), 949–955 (2002).

[62] T. W. Ang, G. T. Reed, A. Vonsovici, A. G. R. Evans, P. R. Routley, and M. R. Josey, "Highly efficient unibond silicon-on-insulator blazed grating couplers," Appl. Phys. Lett. **77**, 4214–4216 (2000).

[63] W. Pasmooij, P. Mandersloot, and M. Smit, "Prism-coupling of light into narrow planar optical waveguides," IEEE J. Lightwave Technol. **7**(1), 175–180 (1989).

[64] N. Koshida and H. Koyama, "Visible electroluminescence from porous Si," Appl. Phys. Lett. **60**(3), 347–349 (1992).

[65] B. Gelloz and N. Koshida, "Electroluminescence with high and stable quantum efficiency and low threshold voltage from anodically oxidized thin porous silicon diode," J. Appl. Phys. **88**(7), 4319–4324 (2000).

[66] A. Irrera, D. Pacifici, M. Miritello, G. Franzo, F. Priolo, F. Iacona, D. Sanfilippo, G. D. Stefano, and P. G. Fallica, "Electroluminescence properties of light emitting devices based on silicon nanocrystals," Physica E **16**(3-4), 395–399 (2003).

[67] C. S. Peng, Q. Huang, W. Q. Cheng, J. M. Zhou, Y. H. Zhang, T. T. Sheng, and C. H. Tung, "Optical properties of Ge self-organized quantum dots in Si," Phys. Rev. B **57**, 8805–8808 (1998).

[68] D. Leong, M. Harry, K. J. Reeson, and K. P. Homewood, "A silicon/iron-disilicide light-emitting diode operating at a wavelength of 1.5 μm," Nature **387**(6634), 686–688 (1997).

[69] B. Zhang, J. Michel, F. Y. G. Ren, L. C. Kimerling, D. C. Jacobson, and J. M. Poate, "Room-temperature sharp line electroluminescence at λ=1.54 μm from an erbiqm-doped, silicon light-emitting diode," Appl. Phys. Lett. **64**(21), 2842–2844 (1994).

[70] M. Fujii, M. Yoshida, Y. Kanzawa, S. Hayashi, and K. Yamamoto, "1.54mum photoluminescence of Er^{3+} doped into SiO_2 films containing Si nanocrystals: Evidence for energy tranfer from Si nanocrystals to Er^{3+}," Appl. Phys. Lett. **71**(9), 1198–1200 (1997).

[71] P. G. Kik, M. L. Brongersma, and A. Polman, "Strong exciton-erbium coupling in Si nanocrystal-doped SiO_2," Appl. Phys. Lett. **76**(17), 2325–2327 (2000).

[72] G. W. Adeola, O. Jambois, P. Miska, H. Rinnert, and M. Vergnat, "Luminescence efficiency at 1.5 μm of Er-doped thick SiO layers and Er-doped SiO / SiO2 multilayers," Appl. Phys. Lett. **89**, 101,920 (2006).

[73] L. D. Negro, R. Li, J. Warga, and S. N. Basu, "Sensitized erbium emission from silicon-rich nitride/silicon superlattice structures," Appl. Phys. Lett. **92**(18), 181,105 (2008).

[74] M. Makarova, V. Sih, J. Warga, R. Li, L. D. Negro, and J. Vuckovic, "Enhanced light emission in photonic crystal nanocavities with Erbium-doped silicon nanocrystals," Appl. Phys. Lett. **92**(16), 161,107 (2008).

[75] H.-S. Han, S.-Y. Seo, and J. H. Shin, "Optical gain at 1.54 *mu*m erbium-doped silicon nanocluster sensitized waveguide," Appl. Phys. Lett. **79**(27), 4568–4570 (2001).

[76] A. Polman, B. Min, J. Kalkman, T. J. Kippenberg, and K. J. Vahala, "Ultralow-threshold erbium-implanted toroidal microlaser on silicon," Appl. Phys. Lett. **84**(7), 1037–1039 (2004).

[77] F. Iacona, D. Pacifici, A. Irrera, M. Miritello, G. Franzo, and F. Priolo, "Electroluminescence at 1.54 μm in Er-doped Si nanocluster-based devices," Appl. Phys. Lett. **81**(17), 3242–3244 (2002).

[78] A. Nazarov, J. M. Sun, W. Skorupa, R. A. Yankov, I. N. Osiyuk, I. P. Tjagulskii, V. S. Lysenko, and T. Gebel, "Light emission and charge trapping in Er-doped silicon dioxide films containing silicon nanocrystals," Appl. Phys. Lett. **86**, 151,914 (2005).

[79] O. Boyraz and B. Jalali, "Demonstration of a silicon Raman laser," Opt. Express **12**(21), 5269–5273 (2004).

[80] H. Rong, A. Liu, R. Jones, O. Cohen, D. Hak, R. Nicolaescu, A. Fang, and M. Paniccia, "An all-silicon Raman laser," Nature **433**(1), 292–294 (2004).

[81] H. Rong, R. Jones, A. Liu, O. Cohen, D. Hak, A. Fang, and M. Paniccia, "A continuous-wave Raman silicon laser," Nature **433**, 725–728 (2005).

[82] M. E. Groenert, C. W. Leitz, A. J. Pitera, V. Yang, H. Lee, R. Ram, and E. A. Fitzerald, "Monolithic integration of room-temperature cw GaAs/AlGaAs lasers on Si substrates via relaxed graded GeSi buffer layers," J. Appl. Phys. **93**(1), 362–367 (2003).

[83] H. Park, A. W. Fang, S. Kodamaa, and J. E. Bowers, "Hybrid silicon evanescent laser fabricated with a silicon waveguide and III-V offset quantum wells," Opt. Express **13**(23), 9460–9464 (2005).

[84] A. W. Fang, H. Park, O. Cohen, R. Jones, M. J. Paniccia, and J. E. Bowers, "Electrically pumped hybrid AlGaInAs-silicon evanescent laser," Opt. Express **14**(20), 9203–9210 (2006).

[85] S. L. Chuang, *Physics of Optoelectronic Devices*, chap. 4, p. 144 (John Wiley & Sons. Inc, 1995).

[86] O. Madelung and et al, eds., *Properties of Group IV Elements and III-V, II-VI, and I-VII Compounds*, vol. 17a (Springer, Berlin, 1982).

[87] C. G. V. de Walle, "Band lineups and deformation potentials in the model-solid theory," Phys. Rev. B **39**(3), 1871–1883 (1989).

[88] Y. Bai, K. E. Lee, C. Cheng, M. L. Lee, and E. A. Fitzgerald, "Growth of highly tensile-strained Ge on relaxed InxGa1xAs by metal-organic chemical vapor deposition," J. Appl. Phys. **104**, 084,518 (2008).

[89] J. Liu, D. D. Cannon, K. Wada, Y. Ishikawa, S. Jongthammanurak, D. T. Danielson, J. Michel, and L. C. Kimerling, "Silicidation-induced band gap shrinkage in Ge epitaxial films on Si," Appl. Phys. Lett. **84**(5), 660–662 (2004).

[90] J. Liu, X. Sun, D. Pan, X. Wang, L. C. Kimerling, T. L. Koch, , and J. Michel, "Tensile-strained, n-type Ge as a gain medium for monolithic laser integration on Si," Opt. Express **15**(18), 11,272–11,277 (2007).

[91] W. G. Spitzer, F. A. Trumbore, and R. A. Logan, "Properties of heavily doped n-type germanium," J. Appl. Phys. **32**, 1822–1830 (1961).

[92] R. Newman and W. W. Tyler, "Effect of impurities on free-hole infrared absorption in p-type germanium," Phys. Rev. **105**, 885–886 (1957).

[93] B. S. Meyerson, "Low-temperature silicon epitaxy by ultrahigh vacuum chemical vapor deposition," Appl. Phys. Lett. **48**, 797–799 (1986).

[94] B. S. Meyerson, "UHVCVD growth of Si and SiGe alloys: chmical, physics, and device applications," Proc. IEEE **80**(10), 1592–1608 (1992).

[95] S. I. Raider, R. Flitsch, and M. J. Palmer, "Oxide growth on etched silicon in air at room temperature," J. Electrochem. Soc. **12**, 413 (1975).

[96] J. L. Vossen, J. H. Thomas, J. S. Maa, and J. J. ONeill, "Preparation of surfaces for high quality interface formation," J. Vac. Sci. Technol. A **2**, 212–215 (1984).

[97] B. S. Meyerson, K. J. Uram, and F. K. LeGoues, "Cooperative growth phenomena in siliconigermanium low temperature epitaxy," Appl. Phys. Lett. **53**, 2555–2557 (1988).

[98] B. S. Meyerson, "Low-temperature Si and SiGe epitaxy by ultrahigh-vacuum chemical deposition: process fundamentals," IBM J. Res. Develop **34**(6), 806–815 (1990).

[99] H.-C. Luan, D. R. Lim, K. K. Lee, K. M. Chen, J. G. Sandland, K. Wada, and L. C. Kimerling, "High-quality Ge epilayers on Si with low threading-dislocation densities," Appl. Phys. Lett **75**(19), 2909–2911 (1999).

[100] T. A. Langdo, C. W. Leitz, M. T. Currie, E. A. Fitzgerald, A. Lochtefeld, and D. A. Antoniadis, "High quality Ge on Si by epitaxial necking," Appl. Phys. Lett. **75**(25), 3700–3702 (2000).

[101] E. A. Fitzgerald, Y.-H. Xie, M. L. Green, D. Brasen, A. R. Kortan, J. Michel, Y.-J. Mii, and B. E. Weir, "Totally relaxed Ge_xSi_{1-x} layers with low threading dislocation densities grown on Si substrates," Appl. Phys. Lett. **59**(7), 811–813 (1991).

[102] S. B. Samavedam and E. A. Fitzgerald, "Novel dislocation structure and surface morphology effects in relaxed Ge/Si-Ge(graded)/Si structures," J. Appl. Phys. **81**(7), 3108–3116 (1997).

[103] L. Colace, G. Masini, F. Galluzzi, G. Assanto, G. Capellini, L. D. Gaspare, E. Palange, and F. Evangelisti, "Metal-semiconductor-metal near-infrared light detector based on eptixial Ge/Si," Appl. Phys. Lett. **72**(24), 3175–3177 (1998).

[104] D. J. Eaglesham, F. C. Unterwald, and D. C. Jacobson, "Growth morphology and the equilibrium shape: the role of surfactants in Ge/Si island formation," Phys. Rev. Lett. **70**(7), 966–969 (1993).

[105] J. Liu, "GeSi photodetectors and electro-absorption modulators for Si electronic-photonic integrated circuits," Ph.D. thesis, Massachusetts Institute of Technology (2007).

[106] H. P. Singh, "Determination of thermal expansion of germanium, rhodium, and iridium by x-rays," Acta Crystallogr., Sect. A: Cryst. Phys., Diffr., Theor. Gen. Crystallogr. **24**, 469–471 (1968).

[107] Y. Okada and Y. Tokumaru, "Precise determination of lattice parameter and thermal expansion coefficient of silicon between 300 and 1500 K," J. Appl. Phys. **56**, 314 (1984).

[108] D. D. Cannon, J. Liu, Y. Ishikawa, K. Wada, D. T. Danielson, S. Jongthammanurak, J. Michel, and L. C. Kimerling, "Tensile strained epitaxial Ge films on Si(100) substrates with potential application in L-band telecommunications," Appl. Phys. Lett **84**(6), 906–908 (2004).

[109] X. Liu, Q. Tang, J. S. Harris, and T. I. Kamins, "Arsenic surface segregation during in situ doped silicon and $Si_{1-x}Ge_x$ molecular beam epitaxy," J. Crystal Growth **281**(2-4), 334–343 (2005).

[110] M.-H. Xie, A. K. Lees, J. M. Fernandez, J. Zhang, and B. Joyce, "Arsenic surface segregation and incorporation in Si and $Si_{l-x}Ge_x$ during gas source molecular beam epitaxy," J. Crystal Growth **173**(3-4), 336–342 (1997).

[111] T. Ohno, "Site exchange mechanism in surfactant-mediated epitaxial growth," Phy. Rev. Lett. **73**(3), 460–463 (1991).

[112] B. S. Meyerson and W. L. Olbricht, "phosphorus doped polycrystalline silicon via LPCVD. Paper I. Process characterization," J. Electrochem. Soc. **131**, 2361 (1984).

[113] J. A. Dean, ed., *Lange's Handbook of Chemistry*, chap. 6 (McGraw-Hill, Inc., 1999).

[114] M. L. Yu and B. S. Meyerson, "The adsorption of PH_3 on Si(100) and its effect on the coadsorption of SiH_4," J. Vac. Sci. Tchnol. A **2**, 446–449 (1984).

[115] R. Reif, T. I. Kamins, and K. C. Saraswart, "a model for dopant incorporation into growing silicon epitaxial films I. theory," J. Electrochem. Soc. **126**(4), 644–652 (1979).

[116] R. Reif, T. I. Kamins, and K. C. Saraswart, "a model for dopant incorporation into growing silicon epitaxial films I. comparason of theory and experiment," J. Electrochem. Soc. **126**(4), 653–660 (1979).

[117] V. P. Markevich, I. D. Hawkins, A. R. Peaker, K. V. Emtsev, V. V. Emtsev, V. V. Litvinov, L. I. Murin, and L. Dobaczewski, "Vacancygroup-V-impurity atom pairs in Ge crystals doped with P, As, Sb, and Bi," Phys. Rev. B **70**(23), 235,213 (2004).

[118] W. Klingenstein and H. Schweizer, "Direct gap recombination in germanium at high exciation level and low temperature," Solid-State Elctron. **21**, 1371–1374 (1978).

[119] H. M. van Driel, A. Elci, J. S. Bessey, and M. O. Scully, "Photoluminescence spectra of germanium at high excitation intensities," Solid State Comm. **20**, 837–840 (1976).

[120] J. Weber and M. I. Alonso, "Effect of impurities on free-hole infrared absorption in p-type germanium," Phys. Rev. B **40**(8), 5683–5693 (1989).

[121] S. John, C. Soukoulis, M. H. Cohen, and E. N. Economou, "Theory of electron band tails and the Urbach optical absorption edge," Phys. Rev. Lett. **57**, 1777–1780 (1986).

[122] P. Dobrilla, "A simple technique to evaluate the density of etch pits in GaAs," Mater. Lett. **3**(7,8), 299–301 (1985).

[123] R. Labusch, "Conductivity and photoconductivity at dislocations," J. Phys. III France **7**, 1411–1424 (1997).

[124] S. A. Shevchenko, "Influence of annealing on the dislocation-related electrical conductivity of germanium," Semiconductors **34**(5), 543–549 (1999).

[125] V. A. Goncharov, Y. A. Osipyan, and S. A. Shevchenko, Sov. Phys. Solid State **29**, 1110 (1987).

[126] Y. A. Osipyan and S. A. Shevchenko, "Dislocation conductivity of germanium," JETP Lett. **20**(11), 328 (1974).

[127] J. Hess and R. Labusch, "1D conduction and photoconduction measurements at dislocations in Ge," Phys. Stat. Sol. A **138**, 617 (1993).

[128] M. T. Currie, S. B. Samavedam, T. A. Langdo, C. W. Leitz, and E. A. Fitzgerald, "Controlling Threading Dislocation Densities in Ge on Si Using Graded SiGe Layers and Chemical-Mechanical Polishing," Appl. Phys. Lett. **72**, 1718–1720 (1998).

[129] H.-C. Luan, "Ge photodetectors fo Si microphotonics," Ph.D. thesis, Massachusetts Institute of Technology (2001).

[130] M. M. Rieger and P. Vogl, "Electronic band parameters in strained $Si_{1-x}Ge_x$ alloys on $Si_{1-y}Ge_y$ substrates," Phys. Rev. B **48**, 14,276 (1993).

[131] L. D. Gaspare, G. Capellini, M. Sebastiani, C. Chudoba, and F. Evangelisti, "Ge/Si(100) heterostructures: a photoemission and low-energy yield spectroscopy investigation," Appl. Surf. Sci. **106**, 94 (1996).

[132] P. T. Lansberg, ed., *Recombination in Semiconductors* (Cambridge University Press, Cambridge, UK, 1991).

[133] S. L. Chuang, *Physics of Optoelectronic Devices*, chap. 9, p. 337 (John Wiley & Sons. Inc, 1995).

[134] W. G. Driscoll and W. Vaughan, eds., *Handbook of Optics*, chap. 8, pp. 42–45 (McGraw-Hill Book Company, 1978).

[135] D. W. Johnson, "A Fourier series method for numerical Kramers-Kronig analysis," J. Phys. A: Math. Gen **8**(4), 490–495 (1975).

[136] J. Albertz, H. Ebner, and G. Neukum, in *International Archives of Photogrammetry and Remote Sensing*, vol. 31, Part B4, pp. 58–63 (Vienna, Austria, 1996).

[137] R. Sandau and A. Eckardt, in *International Archives of Photogrammetry and Remote Sensing*, vol. 31, Part B4, pp. 170–175 (Vienna, Austria, 1996).

[138] S. Baronti, A. Casini, F. Lotti, and S.Porcinai, "Multispectral Imaging System for the Mapping of Pigments in Works of Art by use of Principal-Component Analysis," Appl. Optics **37**, 1299 (1998).

[139] S. W. Seo, D. Geddis, , and N. M. Jokerst, "3D Stacked Thin Film Photodetectors for Multispectral Detection Applications," IEEE Photon. Technol. Lett. **15**, 578–580 (2003).

[140] D. Krapf, B. Adoram, J. Shappir, A. Saar, S. G. Thomas, J. L. Liu, and K. L. Wang, "Infrared multispectral detection using Si/Si_xGe_{1x} quantum well infrared photodetectors," Appl. Phys. Lett. **78**(4), 495–497 (2001).

[141] A. Goldberg, S. Kennerly, J. Little, T. Shafer, C. Mears, H. Schaake, M. Winn, M. Taylor, and P. Uppal, "Comparison of HgCdTe and quantum-well infrared photodetector dual-band focal plane arrays," Opt. Eng. **42**, 30–46 (2003).

[142] A. Kock, E. Gornik, G. Abstretier, G. Bhom, M. Walther, and G. Weimann, "Double wavelength selective GaAs/AlGaAs infrared detector device," Appl. Phys. Lett. **60**(16), 2011–2013 (1992).